Chemical Functionalization of Novel Nanocarbons and Formation of Their Clusters and Composites for Light Energy Conversion

Department of Molecular Engineering

Graduate School of Engineering

Kyoto University

Noriyasu Tezuka

Contents

General Introduction

1. Harnessing Solar Energy

Exhaustion of fossil fuels and the global warming caused by massive energy consumption have become one of the most serious problems facing mankind.[1] In this regard, research activities to gain energy from the sun, as a clean and renewable energy source, are being extensively developed.[1b,2] In particular, solar cells have drawn growing attention toward realization of the efficient conversion of solar energy into electric power.[3,4] However, the cost of electricity from standard silicon-based solar cells is much higher than those generated by hydraulic power and nuclear and fossil fuels, thereby seriously hampering the widespread use of solar energy.[3] Therefore, it is highly desirable to develop low-cost solar cells exhibiting high cell performance. In this context, the prospect of utilizing inexpensive materials and the potential compatibility with mass-production processes make organic solar cells fascinating for alternative energy sources.[5–8] Furthermore, they possess other unique advantages of light weight, flexibility and colorfulness over silicon-based solar cells. Although the cell performances of organic solar cells are still lower than those of inorganic-based ones at present, these advantages encourage us to study organic solar cells as a next-generation energy source.

The production of electrical power from sunlight in organic solar cells involves the following processes: (i) sunlight photons are absorbed within a photoactive layer, leading to formation of the locally confined excited states, *i.e.*, excitons, (ii) the excitons migrate to the interface of donor–acceptor heterojunction and subsequently dissociate to form free charges consisting of electrons and holes, and (iii) the charges are transported toward respective electrodes to eventually generate current in an external circuit. To improve the cell performances of organic solar cells, it is essential to elucidate the controlling factors in the processes and optimize each process based on the fundamental information. Thus, extensive efforts have been made in recent years to select suitable donor and acceptor components and organize them on the electrode surface at nanometer scale, aiming for the cell optimization.[5–8]

2. Nanocarbon Materials for Solar Energy Conversion

It has been well established that fullerenes and their derivatives have small reorganization energies of electron transfer (ET), which leads to remarkable acceleration of photoinduced charge separation (CS) and of charge shift as well as deceleration of charge recombination (CR).[9] The excellent ET properties of fullerenes as an acceptor have prompted many researchers to construct fullerene-based solar energy conversion systems.[9–11] For instance, fullerenes and their derivatives have been ubiquitously employed for bulk heterojunction solar

cells, together with small donor molecules or p-type conjugated polymers.[7,12,13] Recent progress in molecular design and device structures has raised the power conversion efficiency (η) of over 7%,[13] which is close to that (~ 10%) of the amorphous silicon solar cells.[14] On the other hand, Imahori and co-workers have successfully combined fullerenes with porphyrins, which are electron donors with excellent light-harvesting properties, to construct a novel photoelectrochemical devices possessing both characters of the dye-sensitized and the bulk heterojuection solar cells (*i.e.*, dye-sensitized bulk heterojunction solar cell).[15–19] In either case, the construction of nanohighways for efficient electron and hole transport within the donor–acceptor multilayer is crucial to attain efficient photocurrent generation.

Recently, the integration of a new class of carbon allotropes (*i.e.*, single-walled carbon nanotubes (SWNTs)) into organic solar cells has attracted much attention in structural analogy with fullerenes.[20] Compared with spherical shape of fullerenes, however, SWNTs are characterized by unique one-dimensional (1-D), nanowire-like structures (Figure 1). The 1-D structures of SWNTs closely associate with an ideal electron- or hole-transporting highway on an electrode, as in the case of 1-D semiconducting materials.[21] Therefore, SWNTs are expected to afford the efficient percolation pathways for photogenerated charge carriers within the active layer of bulk heterojunction solar cells. In this regard, SWNTs exhibit high conductivity, which exceeds those of any conducting polymers by several orders of magnitude.[22] Carrier mobility as high as 100000 $cm^2\ V^{-1}\ s^{-1}$, which is 2 orders higher than that of silicon, is also estimated for SWNTs.[23] Extremely high surface area, ~ 1600 $m^2\ g^{-1}$, reported for purified SWNTs is an another advantage, providing a tremendous opportunity for exciton dissociation with combined donor or acceptor.[24]

Thus, SWNTs are highly promising materials to replace or combine with fullerenes and their derivatives in bulk heterojunction solar cells.[20,25] In the following section, basic

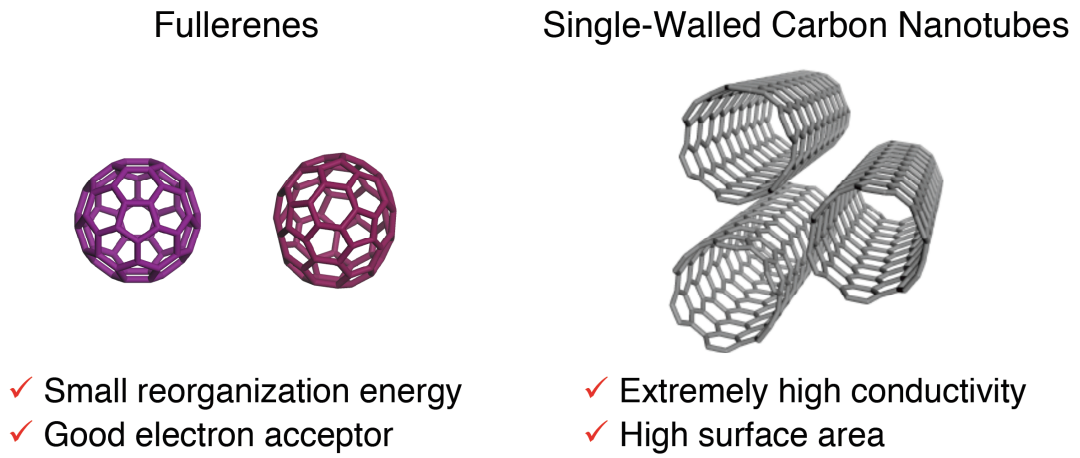

Figure 1. Schematic representations of fullerenes (left: C_{60}, right: C_{70}) and single-walled carbon nanotubes (SWNTs) as a bundle of three tubes.

properties of SWNTs will be briefly summarized to shed light on the detailed functionality of SWNTs in solar energy conversion systems.

3. Basic Structural and Electronic Properties of SWNTs

SWNTs can be regarded as a rolled up graphene sheet, which typically has diameters of *ca.* 1 nm and lengths on the order of micrometers. The role-up vector, which is usually denoted by the pairs of integers (*n*,*m*), determines the "chirality," relating to the electronic nature of SWNTs, *i.e.*, semiconducting or metallic.[26] The electronic structures of both semiconducting and metallic SWNTs (s-SWNTs and m-SWNTs, respectively) are characterized by several pairs of van Hove singularities in the electronic density of states (DOS), as illustrated in Figure 2a,[26,27] and these features bring out the unique optical and electrical properties of SWNTs.[28] For instance, the absorption spectra of SWNTs (*e.g.*, HiPco[29]; Carbon Nanotechnologies, Inc.) dispersed by sodium dodecylbenzenesulfonate (SDBS) in D_2O show absorption peaks arising from transitions of the first and second singularity pairs of s-SWNTs and transition of the first singularity pair of m-SWNTs (Figure 2b). There exist several peaks in the spectra, revealing that the commercially available products consist mixtures of SWNTs bearing various chiralities. It should be noted here that synthesis or isolation of a pure SWNT with a specific (*n*,*m*) chirality is still a challenge at the present stage.[30] Nevertheless, the broad absorption of SWNTs as an ensemble, extending from visible to near infrared (NIR) range, seems to be highly favorable for harvesting the sunlight. Moreover, the divergent nature of van Hove singularities would make it possible to accelerate photoinduced charge separation between suitable donor and s-SWNTs or acceptor and s-SWNTs.[31]

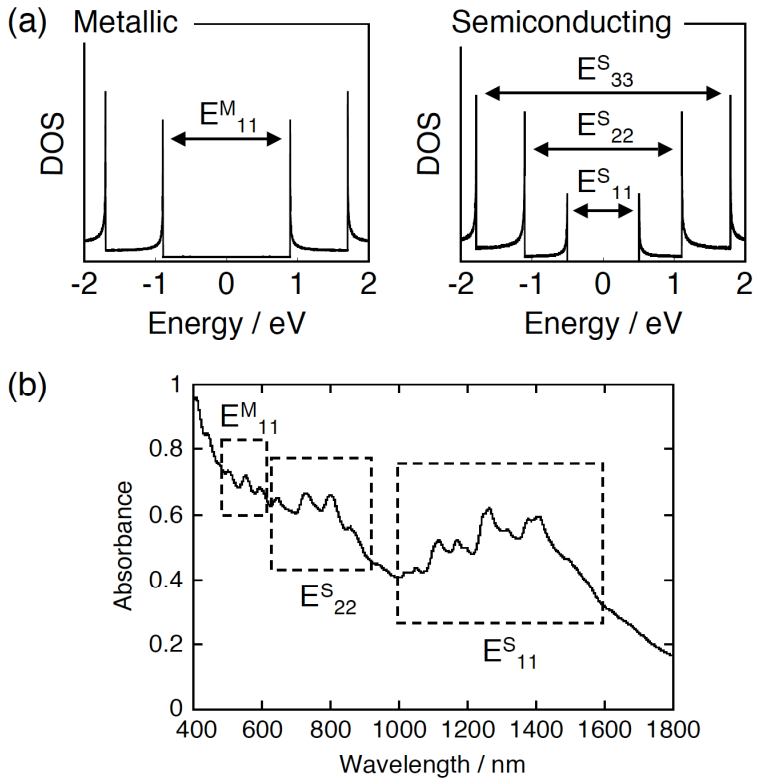

Figure 2. (a) Electronic density of states of metallic and semiconducting SWNTs. (b) Typical absorption spectrum of SWNTs dispersed in D_2O with SDBS.

4. Solubility Limitations of SWNTs

SWNTs have extremely high molecular weight, typically up to $10^5 \sim 10^6$, and tend to interact each other by strong van der Waals binding energy as high as 500 eV per 1 μm of tube–tube contact.[32] As a result, individual SWNTs stack to form aggregated structures, so-called bundles, resulting in extremely poor solubility in any aqueous or organic solvents.[33] This is in striking contrast to fullerenes, which are moderately soluble in typical organic solvents including benzene and toluene. Thus, fullerenes have been successfully incorporated into solar cells and photoelectrochemical devices by using various solution-based deposition processes including spin-coating,[12,13,19] Langmuir-Blodgett (LB) films,[34] layer-by-layer deposition,[35] and electrophoretic deposition.[15–18,36] In contrast, the lack of sufficient solubility has precluded the incorporation of SWNTs into the active layer of such devices. Additionally, the poor solubility of SWNT bundles leads to considerable difficulty in forming interpenetrating networks with donors or acceptors in a composite film, which is critical for efficient exciton dissociation and subsequent charge transport to respective electrodes.[7,37]

The bundle formation of SWNTs gives rise to another drawback. As mentioned above, pristine SWNTs are mixtures of various SWNTs with different (*n*,*m*) chiralities, and roughly speaking, the statistical ratio of s-SWNTs and m-SWNTs is 2:1.[26] For example, a bundle consisting of more than three SWNTs statistically contains one or more metallic tubes, which promote the energy-wasting quenching of photogenerated excitons via inter tube energy transfer and nonradiative relaxation through continuous states near the Fermi level in DOS (Figure 2a).[27] Thus, upon application of SWNTs to solar cells and photoelectrochemical devices, it is of utmost importance to exfoliate the bundle of SWNTs as much as possible.

5. Aim of This Thesis

The needs for environmentally clean energy sources have motivated us to develop highly efficient solar energy conversion systems. In particular, the effective use of organic materials will be a key to achieve the goal, compromising the trade-off between the cell performance and the production costs (Section 1). In such a situation, exploring novel organic materials and related methodology to disclose their functionality is an essential challenge imposed on chemists. As mentioned in Section 2 and 3, nanocarbon materials have notable photophysical and electrical properties, which would be beneficial for the applications to solar energy conversion. **Therefore, the general objective of this thesis is to construct novel light energy conversion systems based on nanocarbon materials, *i.e.*, fullerenes and SWNTs, from which one can draw out valuable information on the design and optimization of organic solar cells. Given that elucidation of the relationship between the morphology and the photovoltaic properties of the active layer is crucial for improving the**

performance of organic solar cells,[7,37] special attention is devoted to understand the correlation among structures, film morphology, and photocurrent generation properties of fullerenes, SWNTs, and their composites. Versatile and rational strategies based on organic and supramolecular chemistry are utilized for preparation of the nanocarbon composites. Specifically, the author fully takes advantage of covalent or noncovalent chemical functionalization of tips, sidewalls, and inside of SWNTs.[38,39] By using such a powerful technique, SWNTs, which are originally insoluble in any solvents due to the bundle formation (Section 4), can be provided with sufficient solubility and processability as well as new functionality. Thus, the former part of this thesis (Chapter 1 – 3) focuses on the structural and electronic properties of the chemically functionalized SWNTs from the perspective of photocurrent generation. In the latter part (Chapter 4 – 8), the cluster formation of the chemically functionalized SWNTs, fullerenes, and their composites in good–poor solvent mixtures is adopted as a viable approach to integrate them into high performance solar energy conversion systems. To access their photocurrent generation properties in the film state, standard three-electrode photoelectrochemical conditions are employed, which are especially suitable to reveal the fundamental photocurrent generation mechanism underlying for the photovoltaic operation of organic solar cells.[15–19]

6. Brief Overview

During the last decade, covalent functionalization of SWNTs has become a well established methodology to exfoliate SWNT bundles.[38] Specifically, the sidewall functionalization is regarded as the most efficient approach to weaken the intertube interaction between SWNTs. It must be noted, however, that the covalent functionalization of the sidewalls tends to alter the electronic properties of SWNTs by disturbing the sp^2 hybridization network of the carbon atoms.[40] Therefore, developing the sidewall reactions that do not deteriorate the electronic states of pristine SWNTs is anticipated for the photoelectrochemical application. In this context, the author investigates in Chapter 1 the impact on the electronic properties of SWNTs by sidewall functionalization with Bingel reaction.[41] Microwave irradiation is utilized to control the degree of the sidewall functionalization. Various spectroscopic techniques are employed to reveal the electronic properties of SWNTs.

As described above, the bundle formation of SWNTs makes it difficult to incorporate SWNTs into photoelectrochemical devices due to the limited solubility as well as impairs device performance by promoting the unfavorable exciton deactivation. In this regard, systematic investigation on the bundle size effect of the photoelectrochemical properties of SWNTs is highly needed for understanding the fundamental aspects of SWNT-based photoelectrochemical devices. With these in mind, in Chapter 2, the author prepares soluble,

covalently functionalized SWNTs with bulky porphyrin moieties on their tips and sidewalls to construct photoelectrochemical devices. By using SWNTs with different degree of covalent functionalization, the relationship between the bundle sizes and the photocurrent generation efficiencies is addressed. In addition, excited state interactions between SWNTs and the attached porphyrin molecules are discussed.

In Chapter 3, the noncovalent functionalization of the inner space of SWNTs is adopted for modulating the electronic structures. Namely, SWNTs offer an unique opportunity for nanoscale engineering of the novel 1-D systems, accomplished by self-assembly of suitably-sized molecules inside the hollow space of SWNT.[42] In particular, fullerene-encapsulated SWNTs, known as fullerene peapods, are highly attractive due to tunable electronic states and doping levels.[42,43] Thus, the author develops the novel nanocarbon hybrids consisting of peapods and conjugated donor polymer, *i.e.*, poly(3-hexylthiophene) (P3HT) for photoelectrochemical devices. Secondary noncovalent functionalization of the outer space of peapods with P3HT via π-π interaction would result in successful dissolution of the hybrids into organic solvent.[39] Ultrafast spectroscopies are conducted to disclose the excited state interactions among P3HT, SWNTs, and the encapsulated fullerenes. Photoelectrochemical properties of the peapod–P3HT hybrids in film state are also compared with the excited state behavior.

In Chapter 4, the author focuses on the shape effects of C_{70} clusters on the electron-transporting and photoelectrochemical properties. Morphological control of the self-assembled clusters was successfully achieved by rapidly injecting a poor solvent (*i.e.*, acetonitrile) into a solution of C_{70} dissolved in various good solvents. Photoelectrochemical properties of semiconducting SnO_2 electrodes modified electrophoretically with C_{70} clusters, which exhibit different morphology, are systematically compared. Relationship between the photocurrent generation efficiency, the electron mobility of the deposited films, and the film morphology are discussed with an emphasis of the comparison with the state-of-the-art bulk heterojunction solar cells.[37]

Combining SWNTs with fullerenes is a fascinating methodology to achieve novel nanocarbon hybrids with both excellent electron-accepting and electron-transporting abilities. Nevertheless, examples of such hybrids are rather limited so far because of the poor solubilizing nature of fullerenes toward SWNTs.[44] Moreover, the correlation between the surface morphology and the photoelectrochemical properties of the fullerene–SWNT hybrids has yet to be elucidated. In such a situation, the author takes advantage of supramolecular approach using the covalently functionalized SWNTs to integrate them with fullerenes. Namely, rapid injection of a poor solvent into the mixed solution of fullerenes and the soluble SWNTs with sterically hindered substituents on their tips affords the composite clusters of

SWNTs and C_{60} (Chapter 5 and 7), C_{70} (Chapter 6 and 7), or C_{84} (Chapter 7). The π-π interaction between fullerenes and the modified SWNTs, as well as the lyophobic interaction between nanocarbons with the poor solvent, would be vital to control the formation of desirable nanocarbon composites. Extensive microscopic and photoelectrochemical inspection on the deposited films of the composites are conducted to reveal the role of SWNTs as 1-D nanoscaffold as well as an electron-transporting pathway. Systematic comparison on the cluster morphology of the fullerene–SWNT hybrids is also performed to correlate the molecular structures of the fullerenes on the hybridizing behavior with the resulting photocurrent generation properties.

In Chapter 8, the author develops a self-assembly method to build up the ordered donor–acceptor networks comprised of the porphyrin–C_{60} dyad molecules for the promoted transport of charge carriers. Semiflexible methylene linkage between the porphyrin and C_{60} is used to assist the formation of donor–acceptor nanoclusters in a good–poor solvent mixture, where the segregated donor–acceptor networks is expected to occur. More importantly, highly soluble covalent-functionalized SWNTs are introduced to bridge between the donor–acceptor nanoclusters for efficient electrical communication. Photocurrent generation properties of the composites are discussed in terms of inter- and intra-cluster charge transport.

7. References

[1] a) M. S. Dresselhaus, I. L. Thomas, *Nature* **2001**, *414*, 332; b) N. Armaroli, V. Balzani, *Angew. Chem. Int. Ed.* **2007**, *46*, 52; c) G. M. Whitesides, G. W. Crabtree, *Science* **2007**, *315*, 796.

[2] a) N. S. Lewis, D. G. Nocera, *Proc. Natl. Acad. Sci. U.S.A.* **2006**, *103*, 15729; b) P. V. Kamat, *J. Phys. Chem. C* **2007**, *111*, 2834.

[3] a) N. S. Lewis, *Science* **2007**, *315*, 798; b) D. Butler, *Nature* **2008**, *454*, 558.

[4] a) R. F. Service, *Science* **2005**, *309*, 548; b) R. F. Service, *Science* **2008**, *319*, 718.

[5] *Organic Photovoltaics*, S. S. Sun, R. S. Sariciftci, Eds., CRC, Boca Raton, 2005.

[6] J.-L. Bredas, J. R. Durrant, *Acc. Chem. Res.* **2009**, *42*, 1689.

[7] a) S. Günes, H. Neugebauer, N. S. Sariciftci, *Chem. Rev.* **2007**, *107*, 1324; b) B. C. Thompson, J. M. Fréchet, *Angew. Chem. Int. Ed.* **2008**, *47*, 58.

[8] a) A. Hagfeldt, M. Grätzel, *Acc. Chem. Res.* **2000**, *33*, 269; b) M. Grätzel, *Nature* **2001**, *414*, 338; c) M. Grätzel, *Acc. Chem. Res.* **2009**, *42*, 1788.

[9] a) H. Imahori, Y. Sakata, *Adv. Mater.* **1997**, *9*, 537; b) H. Imahori, Y. Sakata, *Eur. J. Org. Chem.* **1999**, 2445; c) H. Imahori, *Org. Biomol. Chem.* **2004**, *2*, 1425; d) H. Imahori, *J. Phys. Chem. B* **2004**, *108*, 6130; e) H. Imahori, S. Fukuzumi, *Adv. Funct. Mater.* **2004**, *14*, 525; f) H. Imahori, *Bull. Chem. Soc. Jpn.* **2007**, *80*, 621.

[10] a) M. S. Dresselhaus, G. Dresselhaus, P. C. Eklund, *Science of Fullerenes and Carbon Nanotubes*, Academic Press, San Diego, 1996; b) *Fullerenes*, K. M. Kadish, R. S. Ruoff, Eds., Wiley, New York, 2000; c) *Organic Photovoltaics*, C. Brabec, V. Dyakonov, J. Parisi, N. S. Sariciftci, Eds., Springer, Berlin, 2003.

[11] a) D. M. Guldi, *J. Phys. Chem. B* **2005**, *109*, 11432; b) D. M. Guldi, *Phys. Chem. Chem. Phys.* **2007**, *9*, 1400.

[12] a) G. Yu, J. Gao, J. C. Hummelen, F. Wudl, A. J. Heeger, *Science* **1995**, *270*, 1789; b) R. A. J. Janssen, J. C. Hummelen, N. S. Sariciftci, *MRS Bull.* **2005**, *30*, 33.

[13] a) W. Ma, C. Yang, X. Gong, K. Lee, A. J. Heeger, *Adv. Funct. Mater.* **2005**, *15*, 1617; b) Y. Kim, S. Cook, S. M. Tuladhar, S. A. Choulis, J. Nelson, J. M. Durrant, D. D. C. Bradley, M. Giles, I. Mcculloch, C.-S. Ha, M. Ree, *Nature Mater.* **2006**, *5*, 197; c) J. Peet, J. Y. Kim, N. E. Coates, W. L. Ma, D. Moses, A. J. Heeger, G. C. Bazan, *Nature Mater.* **2007**, *6*, 497; d) S. H. Park, A. Roy, S. Beaupre, S. Cho, N. Coates, J. S. Moon, D. Moses, M. Leclerc, K. Lee, A. J. Heeger, *Nat. Photonics* **2009**, *3*, 297; e) H.-Y. Chen, J. Hou, S. Zhang, Y. Liang, G. Yang, Y. Yang, L. Yu, Y. Wu, G. Li, *Nat. Photonics* **2009**, *3*, 649.

[14] M. A. Green, K. Emery, Y. Hishikawa, W. Warta, *Prog. Photovolt: Res. Appl.* **2010**, *18*, 346.

[15] a) T. Hasobe, Y. Kashiwagi, M. A. Absalom, J. Sly, K. Hosomizu, M. J. Crossley, H. Imahori, P. V. Kamat, S. Fukuzumi, *Adv. Mater.* **2004**, *16*, 975; b) T. Hasobe, P. V. Kamat, M. A. Absalom, Y. Kashiwagi, J. Sly, M. J. Crossley, K. Hosomizu, H. Imahori, S. Fukuzumi, *J. Phys. Chem. B* **2004**, *108*, 12865.

[16] T. Hasobe, P. V. Kamat, V. Troiani, N. Solladie, T. K. Ahn, S. K. Kim, D. Kim, A. Kongkanand, S. Kuwabata, S. Fukuzumi, *J. Phys. Chem. B* **2005**, *109*, 19.

[17] a) T. Hasobe, H. Imahori, P. V. Kamat, S. Fukuzumi, *J. Am. Chem. Soc.* **2003**, *125*, 14962; b) T. Hasobe, H. Imahori, P. V. Kamat, T. K. Ahn, S. K. Kim, D. Kim, A. Fujimoto, T. Hirakawa, S. Fukuzumi, *J. Am. Chem. Soc.* **2005**, *127*, 1216.

[18] a) S. Kang, T. Umeyama, M. Ueda, Y. Matano, H. Hotta, K. Yoshida, S. Isoda, M. Shiro, H. Imahori, *Adv. Mater.* **2006**, *18*, 2549; b) H. Imahori, M. Ueda, S. Kang, H. Hayashi, S. Hayashi, H. Kaji, S. Seki, A. Saeki, S. Tagawa, T. Umeyama, Y. Matano, K. Yoshida, S. Isoda, M. Shiro, N. V. Tkachenko, H. Lemmetyinen, *Chem.-Eur. J.* **2007**, *13*, 10182.

[19] a) A. Kira, M. Tanaka, T. Umeyama, Y. Matano, N. Yoshimoto, Y. Zhang, S. Ye, H. Lehtivuori, N. V. Tkachenko, H. Lemmetyinen, H. Imahori, *J. Phys. Chem. C* **2007**, *111*, 13618; b) A. Kira, T. Umeyama, Y. Matano, K. Yoshida, S. Isoda, J.-K. Park, D. Kim, H. Imahori, *J. Am. Chem. Soc.* **2009**, *131*, 3198.

[20] a) E. Katz, I. Willner, *ChemPhysChem* **2004**, *5*, 1084; b) D. M. Guldi, G. M. A. Rahman, F. Zerbetto, M. Prato, *Acc. Chem. Res.* **2005**, *38*, 871; c) V. Sgobba, D. M. Guldi, *J. Mater.*

Chem. **2008**, *18*, 153; d) T. Umeyama, H. Imahori, *Energy Environ. Sci.* **2008**, *1*, 120; e) V. Sgobba, D. M. Guldi, *Chem. Soc. Rev.* **2009**, *38*, 165.

[21] a) M. Law, L. E. Greene, J. C. Johnson, R. Saykally, P. Yang, *Nature Mater.* **2005**, *4*, 455; b) J. R. Maiolo III, B. M. Kayes, M. A. Filler, M. C. Putnam, M. D. Kelzenberg, H. A. Atwater, N. S. Lewis, *J. Am. Chem. Soc.* **2007**, *129*, 12346; c) O. K. Varghese, M. Paulose, C. A. Grimes, *Nature Nanotech.* **2009**, *4*, 592.

[22] a) T. W. Ebbesen, H. J. Lezec, H. Hiura, J. W. Bennett, H. F. Ghaemi, T. Thio, *Nature* **1996**, *382*, 54; b) R. H. Baughman, A. A. Zakhidov, W. A. de Heer, *Science* **2002**, *297*, 787.

[23] a) T. Dürkop, S. A. Getty, E. Cobas, M. S. Fuhrer, *Nano Lett.* **2004**, *4*, 35; b) P. Avouris, Z. H. Chen, V. Perebeinos, *Nature Nanotech.* **2007**, *2*, 605.

[24] M. Cinke, J. Li, B. Chen, A. Cassell, L. Delzeit, J. Han, M. Meyyappan, *Chem. Phys. Lett.* **2002**, *365*, 69.

[25] a) E. Kymakis, G. A. J. Amaratunga, *Appl. Phys. Lett.* **2002**, *80*, 112; b) E. Kymakis, I. Alexandrou, G. A. J. Amaratunga, *J. Appl. Phys.* **2003**, *93*, 1764; c) C. Li, Y. Chen, Y. Wang, Z. Iqbal, M. Chhowalla, S. Mitra, *J. Mater. Chem.* **2007**, *17*, 2406; d) S. Chaudhary, H. Lu, A. M. Müller, C. J. Bardeen, M. Ozkan, *Nano Lett.* **2007**, *7*, 1973; e) S. Berson, R. de Bettignies, S. Bailly, S. Guillerez, B. Jousselme, *Adv. Funct. Mater.* **2007**, *17*, 3363.

[26] R. Saito, G. Dresselhaus, M. S. Dresselhaus, *Physical Properties of Carbon Nanotubes*, Imperial College Press, London, 1998.

[27] M. J. O'Connell, S. M. Bachilo, C. B. Huffman, V. C. Moore, M. S. Strano, E. H. Haroz, K. L. Rialon, P. J. Boul, W. H. Noon, C. Kittrell, J. Ma, R. H. Hauge, R. B. Weisman, R. E. Smalley, *Science* **2002**, *297*, 593.

[28] It has been demonstrated that the electron–hole binding energies in SWNTs are considerably high, *i.e.*, on the order of 0.3 to 0.5 eV at band gap energies of ~ 1 eV. Thus, general picture of the photoexcited states of SWNTs is excitonic. However, simple band model as shown in Figure 2a does offer qualitative, and quantitative to some extent, description of the excited state event in the SWNT-based photoelectrochemical devices. a) F. Wang, G. Dukovic, L. E. Brus, T. F. Heinz, *Science* **2005**, *308*, 838; b) J. Maultzsch, R. Pomraenke, S. Reich, E. Chang, D. Prezzi, A. Ruini, E. Molinari, M. S. Strano, C. Thomsen, C. Lienau, *Phys. Rev. B* **2005**, *72*, 241402; c) P. Avouris, M. Freitag, V. Perebeinos, *Nat. Photonics* **2008**, *2*, 341.

[29] a) P. Nikolaev, M. J. Bronikowski, R. K. Bradley, F. Rohmund, D. T. Colbert, K. A. Smith, R. E. Smalley, *Chem. Phys. Lett.* **1999**, *313*, 91; b) M. J. Bronikowski, P. A. Willis, D. T. Colbert, K. A. Smith, R. E. Smalley, *J. Vac. Sci. Technol. A* **2001**, *19*, 1800.

[30] a) M. C. Hersam, *Nature Nanotech.* **2008**, *3*, 387; b) X. Tu, S. Manohar, A. Jagota, M. Zheng, *Nature* **2009**, *460*, 250; c) H. Wang, B. Wang, X.-Y. Quek, L. Wei, J. Zhao, L.-J. Li, M. B. Chan-Park, Y. Yang, Y. Chen, *J. Am. Chem. Soc.* **2010**, *132*, 16747.

[31] G. J. Kavarnos, *Fundamentals of Photoinduced Electron Transfer*, Wiley-VCH, New York, 1993.

[32] L. A. Girifalco, M. Hodak, R. S. Lee, *Phys. Rev. B* **2000**, *62*, 13104

[33] A. Thess, R. Lee, P. Nikolaev, H. Dai, P. Petit, J. Robert, C. Xu, Y. H. Lee, S. G. Kim, A. G. Rinzler, D. T. Colbert, G. E. Scuseria, D. Tománek, J. E. Fischer, R. E. Smalley, *Science* **1996**, *273*, 483.

[34] a) D. Zhou, L. Gan, C. Luo, H. Tan, C. Huang, G. Yao, X. Zhao, Z. Liu, X. Xia, B. Zhang, *J. Phys. Chem.* **1996**, *100*, 3150; b) J. Jin, L. S. Li, Y. Li, Y. J. Zhang, X. Chen, D. Wang, S. Jiang, T. J. Li, *Langmuir* **1999**, *15*, 4565; c) N. V. Tkachenko, E. Vuorimaa, T. Kesti, A. S. Alekseev, A. Y. Tauber, P. H. Hynninen, H. Lemmetyinen, *J. Phys. Chem. B* **2000**, *104*, 6371; d) N. V. Tkachenko, V. Vehmanen, J.-P. Nikkanen, H. Yamada, H. Imahori, S. Fukuzumi, H. Lemmetyinen, *Chem. Phys. Lett.* **2002**, *366*, 245.

[35] a) M. Lahav, V. Heleg-Shabtai, J. Wasserman, E. Katz, I. Willner, H. Durr, Y.-Z. Hu, S. H. Bossmann, *J. Am. Chem. Soc.* **2000**, *122*, 11480; b) C. Luo, D. M. Guldi, M. Maggini, E. Menna, S. Mondini, N. A. Kotov, M. Prato, *Angew. Chem., Int. Ed.* **2000**, *39*, 3905; c) F. B. Abdelrazzaq, R. C. Kwong and M. E. Thompson, *J. Am. Chem. Soc.* **2002**, *124*, 4796; d) D. M. Guldi, I. Zilbermann, G. A. Anderson, K. Kordatos, M. Prato, R. Tafuro, L. Valli, *J. Mater. Chem.* **2004**, *14*, 303.

[36] a) P. V. Kamat, S. Barazzouk, K. G. Thomas, S. Hotchandani, *J. Phys. Chem. B* **2000**, ***104***, 4014; b) S. Barazzouk, S. Hotchandani, P. V. Kamat, *Adv. Mater.* **2001**, *13*, 1614; c) H. Imahori, *J. Mater. Chem.* **2007**, *17*, 31.

[37] a) H. Hoppe, N. S. Sariciftci, *J. Mater. Chem.* **2006**, *16*, 45; b) X. Yang, J. Loos, *Macromolecules* **2007**, *40*, 1353.

[38] a) A. Hirsch, *Angew. Chem., Int. Ed.* **2002**, *41*, 1853; b) Y.-P. Sun, K. Fu, Y. Lin, W. Huang, *Acc. Chem. Res.* **2002**, *35*, 1096; c) S. Niyogi, M. A. Hamon, H. Hu, B. Zhao, P. Bhowmik, R. Sen, M. E. Itkis, R. C. Haddon, *Acc. Chem. Res.* **2002**, *35*, 1105; d) C. A. Dyke, J. M. Tour, *J. Phys. Chem. A* **2004**, *108*, 11151; e) D. Tasis, N. Tagmatarchis, A. Bianco, M. Prato, *Chem. Rev.* **2006**, *106*, 1105; f) N. Karousis, N. Tagmatarchis, D. Tasis, *Chem. Rev.* **2010**, *110*, 5366.

[39] a) H. Murakami, N. Nakashima, *J. Nanosci. Nanotechnol.* **2006**, *6*, 16; b) N. Nakashima, T. Fujigaya, *Chem. Lett.* **2007**, *36*, 692; c) Y.-L. Zhao, J. F. Stoddart, *Acc. Chem. Res.* **2009**, *42*, 1161.

[40] a) M. S. Strano, C. A. Dyke, M. L. Usrey, P. W. Barone, M. J. Allen, H. Shan, C. Kittrell,

R. H. Hauge, J. M. Tour, R. E. Smalley, *Science* **2003**, *301*, 1519; b) H. Hu, B. Zhao, M. A. Hamon, K. Kamaras, M. E. Itkis, R. C. Haddon, *J. Am. Chem. Soc.* **2003**, *125*, 14893.

[41] a) K. S. Coleman, S. R. Bailey, S. Fogden, M. L. H. Green, *J. Am. Chem. Soc.* **2003**, *125*, 8722; b) K. A. Worsley, K. R. Moonoosawmy, P. Kruse, *Nano Lett.* **2004**, *4*, 1541.

[42] a) M. Monthioux, *Carbon* **2002**, *40*, 1809; b) A. N. Khlobystov, D. A. Britz, G. A. D. Briggs, *Acc. Chem. Res.* **2005**, *38*, 901; c) R. Kitaura, H. Shinohara, *Jpn. J. Appl. Phys.* **2007**, *46*, 881.

[43] a) J. Lee, H. Kim, S.-J. Kahng, G. Kim, Y.-W. Son, J. Ihm, H. Kato, Z. W. Wang, T. Okazaki, H. Shinohara, Y. Kuk, *Nature* **2002**, *415*, 1005; b) T. Shimada, T. Okazaki, R. Taniguchi, T. Sugai, H. Shinohara, K Suenaga, Y. Ohno, S. Mizuno, S. Kishimoto, T. Mizutani, *Appl. Phys. Lett.* **2002**, *81*, 4067.

[44] a) Y. Takaguchi, M. Tamura, Y. Sako, Y. Yanagimoto, S. Tsuboi, T. Uchida, K. Shimamura, S. Kimura, T. Wakahara, Y. Maeda, T. Akasaka, *Chem. Lett.* **2005**, *34*, 1608; b) D. M. Guldi, E. Menna, M. Maggini, M. Marcaccio, D. Paolucci, F. Paolucci, S. Campidelli, M. Prato, G. M. A. Rahman, S. Schergna, *Chem.-Eur. J.* **2006**, *12*, 3975; c) J. L. Delgado, P. Cruz, A. Urbina, J. T. L. Navarrete, J. Casado, F. Langa, *Carbon* **2007**, *45*, 2250; d) F. D'Souza, R. Chitta, A. S. D. Sandanayaka, N. K. Subbaiyan, L. D'Souza, Y. Araki, O. Ito, *J. Am. Chem. Soc.* **2007**, *129*, 15865; e) W. Wu, H. Zhu, L. Fan, S. Yang, *Chem.-Eur. J.* **2008**, *14*, 5981.

Chapter 1

Retention of Intrinsic Electronic Properties of Soluble Single-Walled Carbon Nanotubes after a Significant Degree of Sidewall Functionalization by the Bingel Reaction

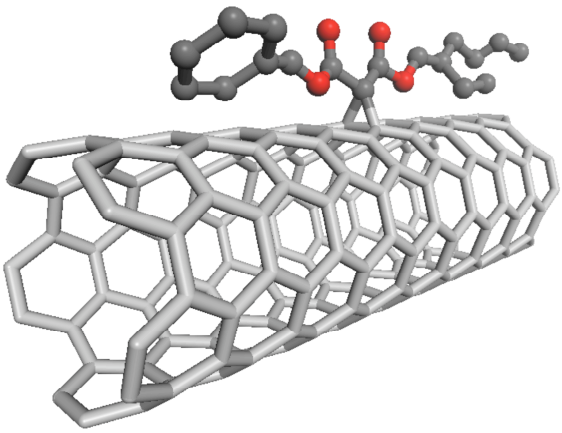

Abstract: Sidewalls of acid-treated, shortened single-walled carbon nanotubes (SWNTs) with long alkyl chains at the open ends and defect sites have been functionalized by Bingel reaction to examine the structures and spectroscopic properties in details. Microwave-assisted Bingel reaction has been successfully applied to the sidewall functionalization of which the reaction rate is *ca.* 50 times faster than that under the conventional conditions. The degree of the sidewall functionalization (one diester unit per 75 – 300 carbon atoms of SWNT) was found to be controllable by changing the output power of microwave under the same temperature. Atomic force microscopy and transmission electron microscopy showed the progressive exfoliation of the SWNT bundles by the double chemical modification. Resonant Raman and UV–vis–near IR absorption spectroscopies revealed that the electronic properties of SWNTs are largely retained after a significant degree of the sidewall modification by Bingel reaction without apparent selective reactivity for metallic and semiconducting SWNTs. This is in remarkable contrast with conventional sidewall functionalization of SWNTs leading to the loss of their electronic properties (one functional group per 10 – 100 carbon atoms on the sidewall). Thus, the covalent functionalization methodology presented here can provide SWNT materials with both excellent solubility and inherent electronic properties which are highly desirable in solution-phase processing for the fabrication of SWNT-based molecular devices.

Introduction

The unique one-dimension structure and extraordinary optical, electrical, thermal, and mechanical properties of single-walled carbon nanotubes (SWNTs) have resulted in an outburst of scientific investigation aiming the applications in various molecular devices.[1] In-situ growth or mechanical manipulation of SWNTs has been applied to integrate SWNTs into molecular devices.[2] Directed assembly of SWNTs from solution is an alternative approach for SWNT-based device. However, solution-phase processing has been hindered by the poor dispersibility of SWNTs in organic and aqueous solvents. Recently, several approaches to the functionalization of SWNTs, including noncovalent interactions[3–9] and covalent bond formation,[10–19] have been developed to overcome the solubility limitations. During the last several years, the noncovalent interactions between SWNTs and surfactants or polymers have been widely employed to prepare individually dispersed SWNTs in aqueous solvents.[3–5] Although the structures and electronic properties of SWNTs are preserved after the solubilization, large excess of surfactants or polymers is required to achieve the functionalization as a result of the weak intermolecular interaction between the adsorbed molecules and SWNTs. Covalent attachment of functional groups to SWNTs leads to the improvement of both solubility and stability of the functionalized SWNTs. For instance, carboxy groups at the open ends and defect sites of shortened SWNTs by oxidation have frequently reacted with amines and alcohols to yield amide and ester linkages, respectively.[11] The sidewalls of SWNTs are also target sites for covalent functionalization. Various direct addition of reactive intermediates, such as 1,3-dipolar cycloaddition of azomethine ylides[12] and arylation with diazonium compounds,[13] to the sidewalls has been reported. It must be noted, however, that the covalent functionalization most significantly alters the structural and electronic properties of pristine SWNTs. Therefore, it is of utmost importance to exploit covalent modification that allows one to achieve the sufficient solubility and retention of the intrinsic electronic properties of SWNTs after a significant degree of functionalization.

The author reports herein the SWNTs doubly functionalized at tips and defect sites with multiple alkyl substituents and on sidewalls with phenyl substituents to give sufficient solubility on the nanotube derivative in organic solvents.[19] Regarding the sidewall functionalization, the author applied Bingel reaction[20] which is one of the most frequently employed methodologies for the functionalization of fullerenes due to the high reactivity under mild reaction conditions. In spite of the favorable situation, only a few reports have appeared for the functionalization of SWNTs by Bingel reaction.[18] As such, the structures and spectroscopic properties of the functionalized SWNTs have not been fully elucidated. Due to the delocalized π-electron and bundled structure, the sidewall functionalization of SWNTs may require severe reaction conditions (*i.e.*, high temperature and long reaction time).[10–19]

Microwave heating, which is known to be faster and more efficient for some organic reactions than conventional heating,[21] is a promising method to avoid the severe conditions. Actually, microwave irradiation has been proved to promote the covalent functionalization of fullerenes[22] and SWNTs[19a,23] more smoothly than conventional heating. Thus, the author also applied the microwave heating to Bingel reaction to obtain SWNTs with a controlled amount of addends on the sidewalls. The effects of the degree of the functionalization on the solubility and the electronic structure of SWNTs after the sidewall modification have been examined in details for the first time.

Results and Discussion

Synthetic Procedure: Synthetic strategy employed for functionalizing SWNTs is shown in Scheme 1. A pristine SWNTs (HiPco, denoted as p-SWNT) is treated with HCl and HNO_3 aqueous solutions to remove catalyst metal particles and various non-nanotube carbon materials.[11] The acid-treatment also cuts SWNTs to yield shortened SWNTs which has carboxylic groups at the open ends and defect sites (denoted as s-SWNT). s-SWNT is reacted first with thionyl chloride, and then octadecylamine is linked to the open ends and the defect sites via formation of the amide functionality (denoted as a-SWNT). This chemical modification at the tips and the defect sites improves the dispersibility in common organic solvents such as chloroform, *o*-dichlorobenzene (ODCB), and THF, which results in higher reactivity for sidewall of a-SWNT than that of s-SWNT (*vide infra*).

SCHEME 1 [a]

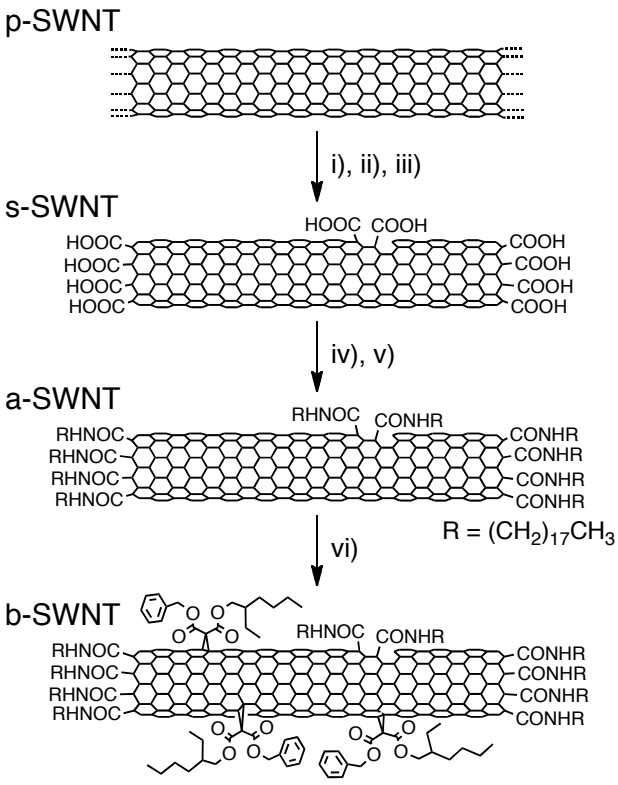

[a] Reagents and conditions: i) in air, 200 °C, 24 h; ii) *conc.* HCl, sonication, 15 min; iii) 2.5 M HNO_3, reflux, 24 h; iv) $SOCl_2$, 70 °C, 2 days; v) $CH_3(CH_2)_{17}NH_2$, 120 °C, 5 days; vi) benzyl 2-ethylhexyl malonate, I_2, DBU, 120 °C (oil bath or microwave).

Initially, Bingel reaction has been applied to fullerenes[20] and recently to SWNTs.[18] The author's attempt to apply Bingel reaction to p-SWNT and s-SWNT in ODCB was unsuccessful

in contrast to the literature,[18] probably due to their low dispersibility in organic solvents (0.1 and 0.05 mg mL^{-1} in ODCB, respectively). On the other hand, the sidewalls of a-SWNT, which has the improved solubility in ODCB (0.4 mg mL^{-1}), showed marked reactivity toward Bingel reaction. The reaction procedure was conducted as follows. Sonication of a-SWNT in ODCB for 30 minutes allowed the black solid of a-SWNT to disperse partially into ODCB. Then, benzyl 2-ethylhexyl malonate, iodine, and 1,8-diaza-bicyclo[5.4.0]undec-7-ene (DBU) were added to the dispersion, and stirred for 24 h at room temperature. The obtained black material (b-SWNT) was purified by reprecipitation and filtration repeatedly. As expected, the solubility of b-SWNT in organic solvents is remarkably improved; for example, the maximum concentration of b-SWNT in $CHCl_3$ (0.15 mg mL^{-1}) is much higher than that of a-SWNT (< 0.02 mg mL^{-1}). Figure 1 displays the photographic images of $CHCl_3$ solutions of a-SWNT and b-SWNT (0.1 mg mL^{-1}) after sonication for 1 h and left for 3 min. b-SWNT forms a clear, dark-brown solution that exhibits no discernable particulate materials and remains stable for a period of at least 1 week.

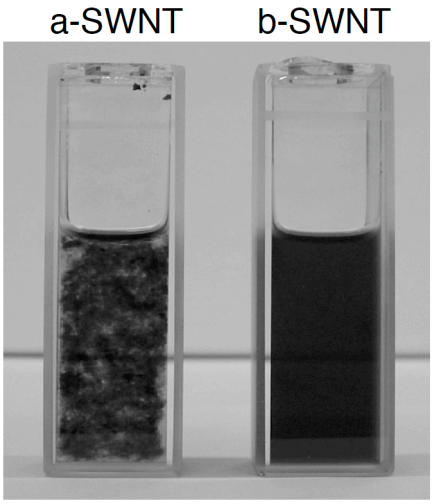

Figure 1. Photographic images of $CHCl_3$ solutions of a-SWNT and b-SWNT (0.1 mg mL^{-1}). The samples were sonicated in a bath sonicator (HONDA W-211, 100W) for 1 h and left for 3 min before the images were taken.

IR and NMR Spectroscopies: Fourier transfer (FT)-infrared (IR) spectra of p-SWNT, s-SWNT, a-SWNT, and b-SWNT measured in the solid state are presented in Figure 2. Intense absorption bands at 2845 cm^{-1} and 2917 cm^{-1}, characteristic of the C-H stretching vibrations,[24] are observed for a-SWNT (Figure 2c) and b-SWNT (Figure 2d), because of introduction of the alkyl substituents into SWNT. The IR spectrum of s-SWNT shows C=O stretching vibration of carboxylic acid at 1746 cm^{-1} together with asymmetrical and symmetrical stretching bands of carboxylate anion at 1602 cm^{-1} and 1402 cm^{-1},[24] respectively (Figure 2b). In contrast, the IR spectrum of a-SWNT reveals a broad peak centered at 1583 cm^{-1} which is attributable to the superposition of C=O stretch (amide I band), N-H deformation vibration (amide II), and C=C stretch of the SWNTs, and a weak peak at 1464 cm^{-1} which is assigned to alkyl chain (C-H bend),[24,25] demonstrating the presence of the alkyl amide group (Figure 2c). The absorption band at 1747 cm^{-1} may stem from the unreacted carboxylic acid. The IR spectrum of b-SWNT (Figure 2d) exhibits C=O and C-O stretching vibrations of the ester group at 1758 cm^{-1} and

1101 cm^{-1},[24] respectively, which supports the sidewall functionalization. The results on the FT-IR spectra are consistent with the expected structures of the functionalized SWNTs (*vide infra*).

^1H NMR spectra of a-SWNT and b-SWNT in $CDCl_3$ exhibit significantly broad peaks for all the protons including aromatic ones due to the restricted mobility caused by the large molecular size and the inherent inhomogeneity of SWNTs, which are typical of ^1H NMR spectra for the covalent substituents on SWNTs (Figure 3).[10–19] A small amount of the residual ferromagnetic metal particles may also contribute to the obscurity of the peaks. The ^1H NMR signals for alkyl chains of the octadecyl amide group at the tips and defects and the 2-ethylhexyl and benzyl groups on the sidewalls that are closer to the surface of SWNTs should be more broadened than those that are toward the middle and terminus of the alkyl chains.[7b,26] Thus, the signals for N*HCH*$_2$ of the alkyl amide group and O*CH*$_2$ of the 2-ethylhexyl and benzyl groups are likely to become considerably broadened. The aromatic protons of the benzyl groups should also be fairly broadened and may be overlapped with the signal of chloroform (7.24 ppm). The small peak around 2.1 ppm, which appears only in the spectrum of b-SWNT, is attributable to OCH_2CH of the 2-ethylhexyl group. The methylene (1.0 – 1.4 ppm) and methyl (0.8 – 1.0 ppm) protons of the 2-ethylhexyl group and the octadecyl group are also overlapped each other, and it is difficult to assign the broad peaks to each component due to the low resolution, resulting in the difficulty to estimate the quantitative content ratio of octadecyl and 2-ethylhexyl groups. However, it can be claimed at least that the ratio of protons of terminal CH_3 groups to those of CH_2 groups that are in the middle of the alkyl chains or close to the terminus of the alkyl chains is higher in the 2-ethylhexyl group with two methyl moieties than in the octadecyl group with one methyl moiety. Thus, the increase of the integral ratio of methyl (0.8 – 1.0 ppm) to methylene (1.0 – 1.4 ppm) protons in b-SWNT (0.3) compared to a-SWNT (0.2) supports the existence of the 2-ethylhexyl group in b-SWNT, which is consistent with the results on the characterization of b-SWNT.

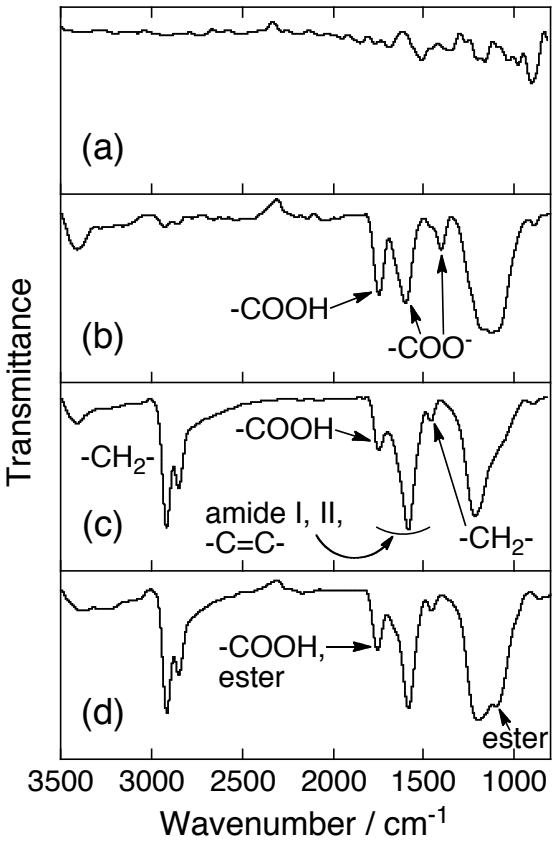

Figure 2. FT-IR spectra of (a) p-SWNT, (b) s-SWNT, (c) a-SWNT, and (d) b-SWNT measured in KBr pellet.

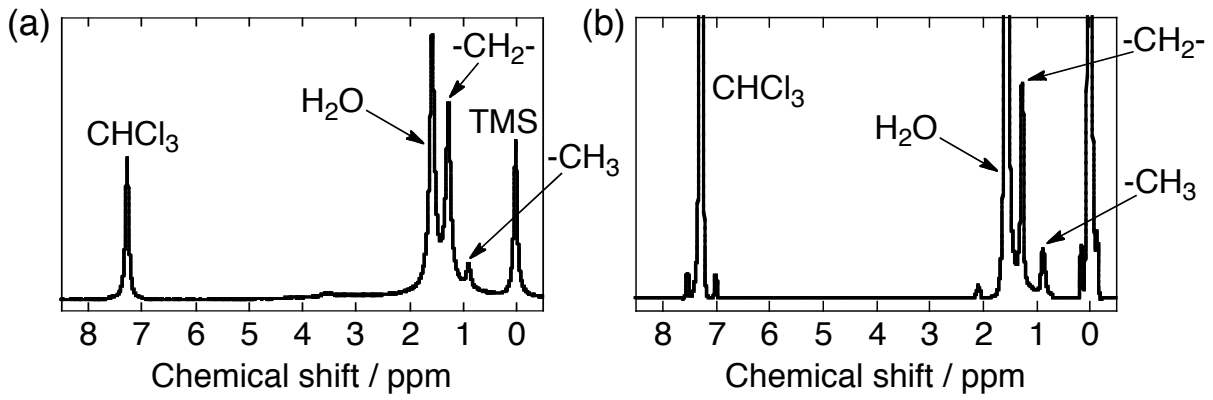

Figure 3. ^{1}H NMR spectra of (a) a-SWNT and (b) b-SWNT in $CDCl_3$.

Microscopic Characterization: Atomic force microscopy (AFM) measurements were performed for all the SWNT samples spin-coated on freshly cleaved mica from the suspension of the SWNTs in $CHCl_3$ (Figure 4). All images exhibit fibrous structures attributed to individual SWNTs and their bundles, and they reveal the progressive exfoliation of SWNT bundles on the mica surfaces in the order of p-SWNT, s-SWNT, a-SWNT, and b-SWNT. Namely, the AFM micrographs of p-SWNT (Figure 4a) and s-SWNT (Figure 4b) exhibit large and thick bundles due to the insolubility in $CHCl_3$. The entanglement of s-SWNT is much reduced compared to that of p-SWNT owing to the short length of the SWNT in s-SWNT. In contrast, the average thickness of the bundles for a-SWNT (Figure 4c) is much smaller than those for p-SWNT and s-SWNT. The AFM image of b-SWNT (Figure 4d) discloses the short, thin rod-like structures with a dramatic decrease in the bundle size, implying that the sidewall functionalization is sufficient for the exfoliation of the bundles. The average length of isolated b-SWNT is determined as 320 nm. Most of b-SWNT on the mica surface still form their bundles which may be present in the cast solution or result from the evaporating process during the spin-coating. The exfoliation of the SWNT bundles after the sidewall modification is also confirmed by the comparison of the transmission electron microscopy (TEM) images of a-SWNT and b-SWNT (Figure 5).

Thermogravimetric Analysis (TGA): Thermogravimetric analysis (TGA) has been widely used to investigate the covalent functionalization of SWNTs.[10–19,27] Figure 6A depicts the thermograms of p-SWNT and the functionalized SWNTs measured in air. The TGA curves of s-SWNT (trace b), a-SWNT (trace c), and b-SWNT (trace d) show almost no end-residue (< 1 wt%) at 700 ^{o}C, whereas *ca.* 15% of the initial weight is left at 700 ^{o}C for p-SWNT (trace a). Thus, most of the metal oxide catalysts are removed by the acid-treatments. In the case of s-SWNT there is a continuous mass loss over a wide range of temperature upon heating. In contrast, two steps of mass loss are observed for the thermograms of a-SWNT and b-SWNT.

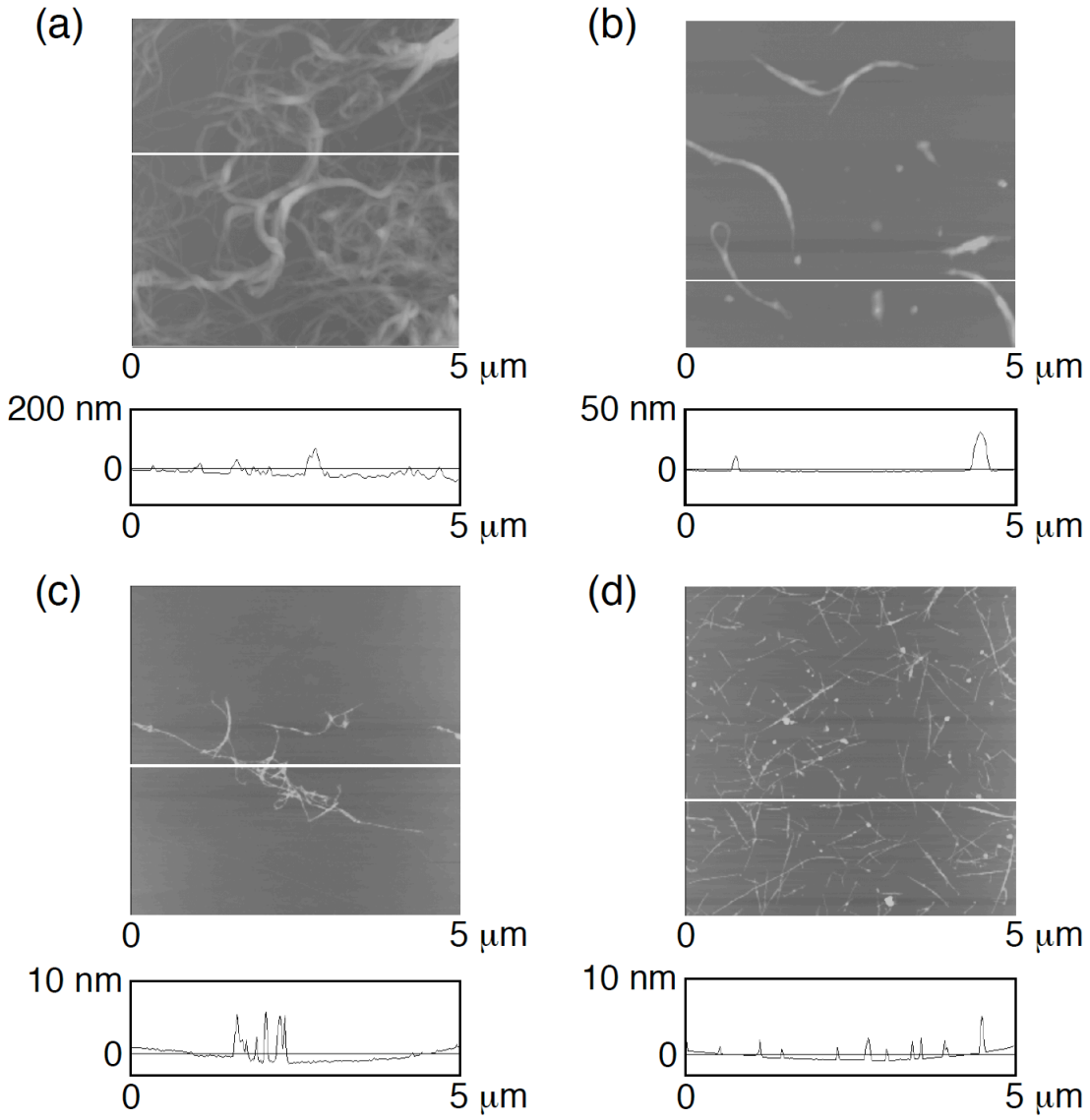

Figure 4. Tapping mode atomic force micrographs of (a) p-SWNT, (b) s-SWNT, (c) a-SWNT, and (d) b-SWNT on mica (Z range: (a) 800 nm, (b) 200 nm, (c), (d) 30 nm) with cross-section profiles. The colour scale represents the height topography, with bright and dark representing the highest and lowest features, respectively.

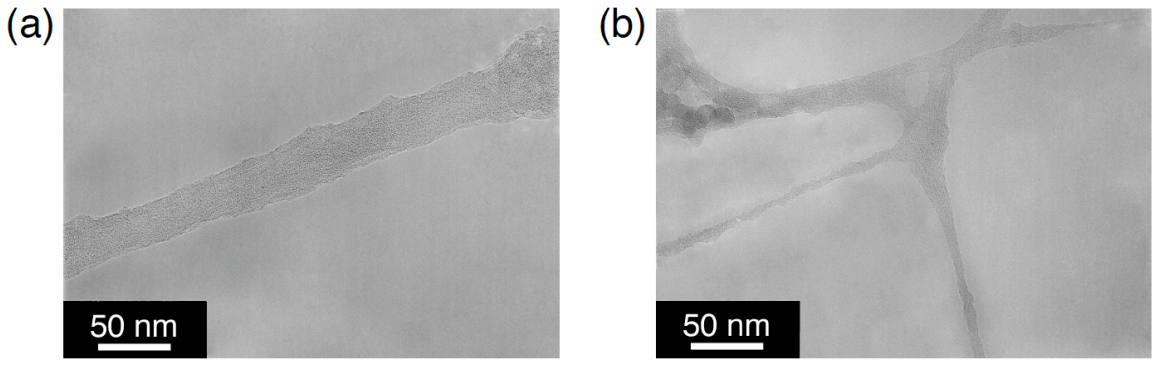

Figure 5. TEM images of (a) a-SWNT and (b) b-SWNT.

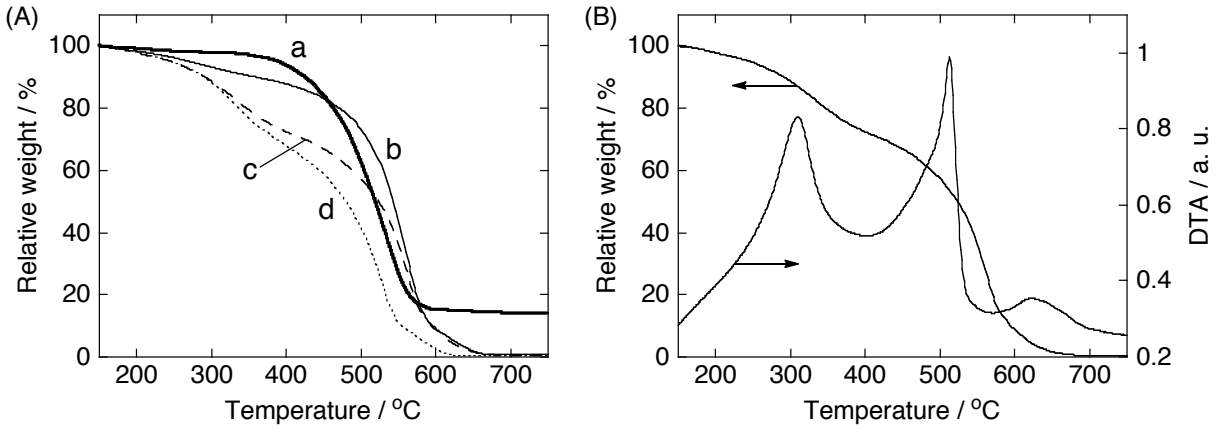

Figure 6. (A) TGA curves of (a) p-SWNT, (b) s-SWNT, (c) a-SWNT, and (d) b-SWNT. The analyses were performed under air with heating rate of 10 °C min^{-1}. (B) TGA curve of a-SWNT with differential thermal analysis (DTA).

This reflects the detachment of the covalently linked groups from the tube terminals and the sidewalls before the combustion of SWNTs. The turning point of the two weight loss processes is determined as 400 °C by differentiating the thermogravimetric analysis curve of a-SWNT (Figure 6B). The weight loses in the temperature ranges of 200 – 400 °C and 400 – 750 °C are assigned to the detachment of the covalently-linked substituents and the combustion of SWNTs, respectively. Weight loss of b-SWNT at 400 °C is larger than that of a-SWNT due to the sidewall functionalization of a-SWNT by the diester unit. Comparison of the relative weight loss of a-SWNT and b-SWNT at 400 °C reveals that b-SWNT contains 26 and 6 wt% of the amide and diester groups, respectively. In other words, one amide group at the terminals and the defect sites and one diester moiety on the sidewalls appear at each *ca.* 65 and 270 carbon atoms of the SWNT, respectively.

Microwave-Assisted Bingel Reaction: As described above and according to the literatures,[18] the Bingel reaction of SWNT at room temperature takes 1 day, while that for fullerene is completed within a few hours.[20] The author carried out Bingel reaction with a-SWNT at elevated temperature (120 °C) to increase the degree of sidewall functionalization with a short reaction time, but the further addition reaction did not proceed. Then, the author focused on microwave heating which has become an important tool for efficient execution of organic reactions; excellent yields are often obtained within reaction times considerably shorter than those with conventional heating.[21] The microwave irradiation was applied to the Bingel reaction of a-SWNT. To avoid the undesired side reaction at high temperature, simultaneous cooling was performed by compressed air.[28] The temperature of the reaction mixture was maintained at 120 °C under microwave irradiation. The reaction with an irradiated microwave

power of 40 W proceeded much faster than that at room temperature without the microwave irradiation, and yielded the expected soluble product (denoted as b-SWNT-MW(40W)) within only 30 min. The solubility and the degree of sidewall functionalization of b-SWNT-MW(40W) is the same as that of b-SWNT obtained by stirring at room temperature for 24 h. The TGA curve for b-SWNT-MW(40W) (Figure 7A(a)) reveals that one diester moieties is attached on each 300 carbon atoms of the SWNT sidewall. The degree of sidewall functionalization of a-SWNT under microwave irradiation increased with increasing the irradation power (*i.e.*, 50 W and 60 W) to give b-SWNTs with one diester unit per 140 carbon atoms of SWNT (denoted as b-SWNT-MW(50W)) and with one diester unit per 75 carbon atoms of SWNT (denoted as b-SWNT-MW(60W)), respectively, which are also calculated from the TGA analyses (Figure 7A(b) and (c)). Note that the temperature of the reaction mixture was kept at 120 ^{o}C by cooling with compressed air flowing. Further increase in the degree of sidewall functionalization of a-SWNT could not be obtained under strong microwave irradiation (> 60 W) for a long reaction time (> 30 min). The integral ratio of methyl to methylene protons in b-SWNT-MW(60W) (0.4) is higher than that of b-SWNT prepared without microwave irradiation (0.3), supporting the higher functionalization ratio in b-SWNT-MW(60W) (Figure 7B). In addition, the solubility of b-SWNT-MW(60W) in $CHCl_3$ (0.25 mg mL^{-1}) is improved compared to that of b-SWNT (0.15 mg mL^{-1}). These results unambiguously demonstrate that the microwave heating is a powerful technique for shortening the reaction time and controlling the degree of sidewall functionalization of SWNTs by changing the irradiation power. Although there have been a few reports on the microwave-assisted functionalization of SWNT sidewalls such as Diels-Alder reaction[19a] and 1,3-dipolar

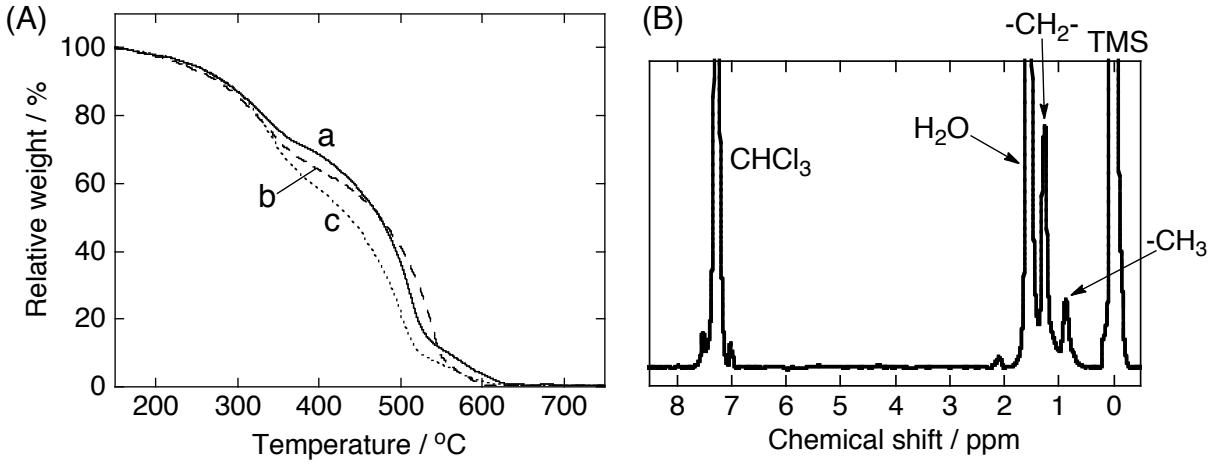

Figure 7. (A) TGA curves of b-SWNTs obtained by microwave irradiation with a power of (a) 40 W (b-SWNT-MW(40W), (b) 50 W (b-SWNT-MW(50W)), and (c) 60 W (b-SWNT-MW(60W)). The analyses were performed under air with heating rate of 10 °C min^{-1}. (B) ^{1}H NMR spectrum of b-SWNT-MW(60W) measured in $CDCl_3$.

TABLE 1: Reaction Conditions and Functionalization Ratios

	microwave power / W	reaction temperature / ^{o}C	reaction time / h	functionalization ratio [a]
b-SWNT	—	25	24	1 / 270
b-SWNT-MW(40W)	40	120	0.5	1 / 300
b-SWNT-MW(50W)	50	120	0.5	1 / 140
b-SWNT-MW(60W)	60	120	0.5	1 / 75

[a] Ratio of a diester group to carbon atoms of SWNT moiety determined by TGA analyses.

cycloaddition of azomethine ylide,[23a] to the best of the author's knowledge, this is the first example of SWNT functionalization by microwave-assisted reaction in which the relationship between the output power of microwave and the functionalization ratio has been examined under the same temperature utilizing compressed-air cooling. The reaction conditions used for microwave syntheses and the resulting functionalization ratios are summerized in Table 1.

Resonant Raman Spectroscopies: Resonant Raman spectroscopy is a valuable tool to characterize SWNTs, since it provides a detailed structural information.[29] Low-wavenumber phonon modes, radial breathing modes (RBMs), are very susceptible to the nanotube diameter and electronic states. Taking into account Kataura plot[30] with diameters of HiPco (0.8 – 1.3 nm),[4] one can monitor semiconducting and metallic SWNTs with diameter of 0.8 – 1.0 and 1.0 – 1.3 nm, respectively, by an excitation energy of 1.96 eV (λ_{ex} = 633 nm), whereas with an excitation energy of 2.54 eV (λ_{ex} = 488 nm) one can probe both metallic and semiconducting SWNTs with diameter of 0.8 – 1.1 and 1.1 – 1.3 nm, respectively, as discussed later. Figure 8 shows the resonant Raman spectra of p-SWNT, s-SWNT, a-SWNT, and b-SWNT prepared under various conditions. The relative peak intensities of tangential mode (G-band) around 1600 cm^{-1} and of disorder mode (D-band) around 1350 cm^{-1} (G/D ratio) reflect the relative amounts of sp^3 carbon, and are used to determine the degree of functionalization.[10–19] The spectra exhibit progressive decrease of G/D ratio by the chemical functionalizations of SWNTs except for s-SWNT. The G/D ratios of a-SWNT (15 and 7.2 for 2.54 and 1.96 eV excitation, respectively) are smaller than those of p-SWNT (19 and 17), which is reasonable considering that the acid treatment increases the terminal and defect sites. The unusual decrease in the G/D ratio of s-SWNT (2.0 and 1.7) may be caused by the residual amorphous carbon, which would be removed during the purification procedures of a-SWNT. The G/D ratios further decrease in the spectra of b-SWNT (10 and 6.7), implying the conversion of sp^2 carbons to sp^3 ones on the sidewalls as a result of the sidewall functionalization by the Bingel reaction. Importantly, the

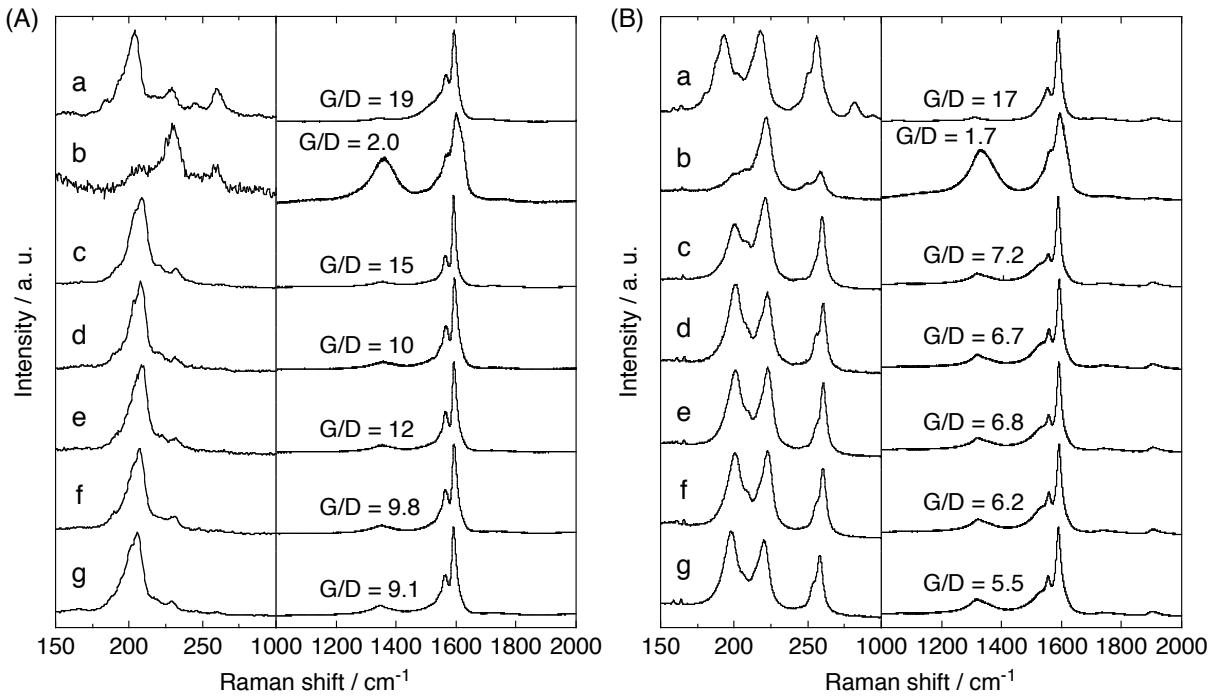

Figure 8. Resonant confocal micro Raman spectra with (A) 2.54 eV and (B) 1.96 eV excitation of (a) p-SWNT, (b) s-SWNT, (c) a-SWNT, (d) b-SWNT, (e) b-SWNT-MW(40W), (f) b-SWNT-MW(50W), and (g) b-SWNT-MW(60W).

spectra of b-SWNT prepared under microwave irradiation show a lower value of G/D ratio as the functionalization ratio determined by TGA becomes higher, which also supports that the sidewall was functionalized more efficiently by using microwave with high output power.

Optical Absorption Spectroscopies: UV–vis–near IR (NIR) spectra of p-SWNT, s-SWNT, a-SWNT, b-SWNT, b-SWNT-MW(40W), b-SWNT-MW(50W), and b-SWNT-MW(60W) dissolved in THF using a tip sonicator in the presence of octylamine[8] are compared to evaluate the effect of the degree of sidewall functionalization by Bingel reaction on their electronic properties (Figure 9). All spectra were measured using the supernatant part after being centrifuged at 8000 *g* for 30 min. The spectrum of p-SWNT (trace a) exhibits characteristic peaks at 450 – 580 nm arising from transitions between the first pair of van Hove singularities in the density of states (DOS) of metallic SWNTs (E^{M}_{11}), as well as those at 600 – 1000 nm and 1100 – 1600 nm arising from transitions of the second and first pairs of semiconducting SWNTs (E^{S}_{22} and E^{S}_{11}).[4] The peak intensities around 1150 nm become smaller after the acid-treatment, suggesting the loss of van Hove singularities in the electronic structure of SWNTs with small diameters (0.8 – 1.0 nm). The overall low peak intensities in the spectrum of s-SWNT is attributable to the lower dispersibility compared to other samples. The comparison of the spectra of a-SWNT (trace c) and b-SWNT (trace d) unambiguously

demonstrates that the peak position and shape stemming from the van Hove singularities are virtually the same between the two spectra. Accordingly, there is little difference in the reactivity of the Bingel reaction for semiconducting and metallic SWNTs.[31] In the diameter-dependent RBMs at 150 – 280 cm^{-1} in the Raman spectra (Figure 8), the peak position and shape are largely similar for a-SWNT and b-SWNT for both excitation energies of 1.96 eV and 2.54 eV. These results are consistent well with the small selectivity of the Bingel reaction for semiconducting and metallic SWNTs. More importantly, the electronic properties of SWNTs are largely retained after the significant degree of sidewall functionalization by Bingel reaction, in spite of the remarkable improvement of the solubility.[13d] The absorption spectra of b-SWNT-MW(50W) (trace f) and b-SWNT-MW(60W) (trace g), of which the sidewalls are functionalized more heavily than those of b-SWNT (trace d) and b-SWNT-MW(40W) (trace e), also show similar peaks from the van Hove singularities. These results imply that the electronic structures of the sidewall-functionalized SWNTs using Bingel reaction can be preserved by up to one diester unit per 75 carbon atoms of the SWNT. This is in remarkable contrast with the conventional sidewall functionalization of SWNTs, resulting in the loss of their electronic properties (one functional group per 10 – 100 carbon atoms on the sidewall).[10–19] For instance, sidewall functionalization of SWNTs by 1,3-dipolar cycloaddition of azomethine ylide leads to structureless absorption spectra, implying the loss of their electronic properties (one functional group per ~ 100 carbon atoms on the sidewall).[12]

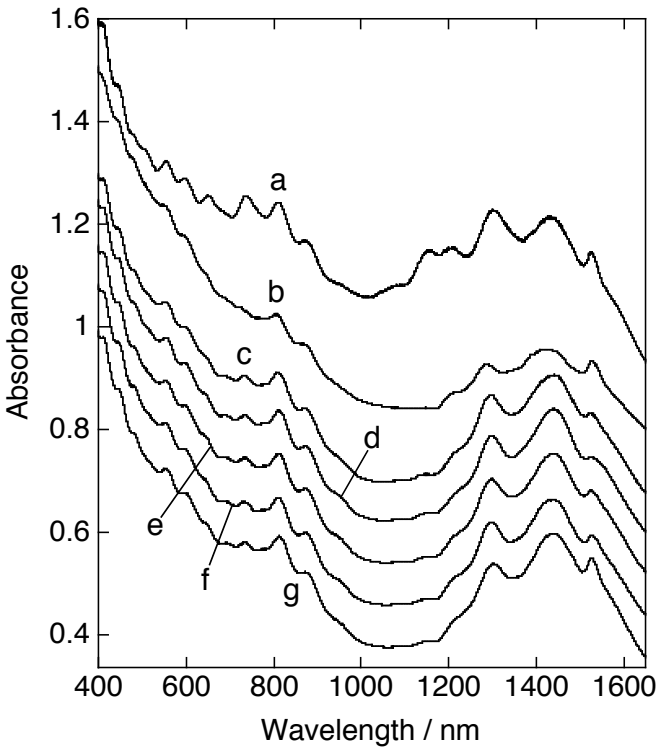

Figure 9. UV–vis–NIR absorption spectra of (a) p-SWNT, (b) s-SWNT, (c) a-SWNT, (d) b-SWNT, (e) b-SWNT-MW(40W), (f) b-SWNT-MW(50W), and (g) b-SWNT-MW(60W) dissolved in THF with the aid of octylamine. The values on y-axis are for line (g) and the other spectra are shown in parallel for comparison.

Interestingly, present results agree well with the theoretical studies by DFT calculations which indicate the electronic structures of SWNTs near the Fermi level are only perturbed modestly by functionalization of the sidewalls with three-membered ring structure at moderate

modification ratios (one functional group per 72 – 96 carbon atoms on the sidewall).[32] Han *et al.* also reported *ab initio* study on SWNTs with various degrees of functionalization using dichlorocarbene (one functional group per 80 – 400 carbon atoms on the sidewall).[33] They found that the electronic properties of SWNTs are significantly modified depending on the site of [2+1] cycloaddition. Specifically, in the type-II geometry of the attached CCl_2 on the sidewall of SWNTs, where the plane of the three-membered ring is perpendicular to the long axis of SWNT, the electronic structures of the functionalized SWNTs are largely maintained compared to those in which the plane of the three-membered ring is parallel to the long axis of SWNT (type-I geometry). Namely, the highly-strained three-membered ring structure on the sidewalls is supposed to result in the products with opened sidewalls in the type-II geometry, leading to the preservation of the sp^2 hybridization network of the carbons on the nanotube sidewall.[32,33] Accordingly, selective addition of the present substituents by Bingel reaction with the type-II arrangement may rationalize the retention of the electronic properties of the sidewall-functionalized SWNTs during Bingel reaction in which the sidewalls are moderately functionalized by the substituents (one functional group per 75 – 300 carbon atoms on the sidewall).

Conclusion

In conclusion, the Bingel reaction has been successfully applied to the sidewall functionalization of SWNTs, yielding sufficiently soluble, functionalized SWNTs in organic solvents. Microwave irradiation was found to reduce the reaction time of up to 30 min and increase the amount of the covalently-linked substituents on the sidewalls with a controlled manner by changing the output power. The structures and the electronic properties of the functionalized SWNTs by Bingel reaction have been examined in detail for the first time. It is noteworthy that the electronic properties of the SWNTs are largely retained after a significant degree of sidewall modification by Bingel reaction without apparent selective reactivity for metallic and semiconducting SWNTs. Thus, the present covalent functionalization exhibiting both excellent solubility and retention of the initial inherent electronic properties is a highly promising methodology for constructing the molecular devices in which SWNTs modified with photoactive and/or electrochemically active chromophores can be employed without losing their intrinsic electronic properties of SWNTs.

Experimental Section

General Information: IR spectra were recorded on a PerkinElmer Spectrum One FT-IR spectrometer using KBr pellets. ^{1}H NMR spectra were obtained by a JEOL JNM-EX400 NMR

spectrometer. UV–vis–NIR spectra were measured with a PerkinElmer Lambda 900 UV/VIS/NIR spectrometer. Resonance Raman spectra were measured using a Horiba JobinYvon LabRAM HR-800 equipped with 2.54 eV (488 nm) and 1.96 eV (633 nm) laser. TEM analyses were carried out by a JEOL JEM2000FX-II. For sample preparation, a $CHCl_3$ solution containing SWNTs was dropped on microgrids and evaporated. AFM images were obtained with a Digital Instruments Nanoscope III in the tapping mode. A $CHCl_3$ solution containing SWNTs was spin-coated on freshly cleaved mica at a rotation speed of 1000 rpm. TGA measurements were conducted on a SHIMADZU TG-60 under a flowing air at a scan rate of 10 ^oC min^{-1}. The microwave-assisted procedures were carried out with a CEM Discover BenchMate microwave synthesizer. a-SWNT was prepared using HiPco (Carbon Nanotechnologies, Inc.) as published elsewhere.[11e] THF was dried and distilled from sodium. ODCB was distilled from calcium hydride before use. All other chemicals purchased from commercial sources were used without further purification.

Preparation of Benzyl 2-Ethylhexyl Malonate: 2,2-Dimethyl-1,3-dioxane-4,6-dione (9.0 g, 62 mmol) and benzyl alcohol (6.5 ml, 63 mmol) were heated at 120 ^oC for 3 h. After cooling to room temperature, resulting acetone was removed by distillation under reduced pressure. The remaining oily yellow residue and triethylamine (7.6 mL, 54 mmol) was dissolved in 170 mL of dry THF. The solution was cooled in an ice bath, and 2-ethylhexyl chloroformate (12 mL, 62 mmol) was added slowly. The mixture was stirred at 0 ^oC for 45 min and then at room temperature for 45 min. After filtration and concentration of the filtrate, column chromatography on silica gel with hexane/ethyl acetate (20:1) as an eluent gave benzyl 2-ethylhexyl malonate as colorless oil (12 g, 39 mmol, 63%). ^1H NMR (400 MHz, $CDCl_3$): δ 7.36 (m, 5H), 5.18 (s, 2H), 4.07 (dd, ^1J = 10.9 Hz, ^2J = 12.8 Hz, 1H), 4.04 (dd, ^1J = 10.9 Hz, ^2J = 13.2 Hz, 1H), 3.43 (s, 2H), 1.56 (m, 1H), 1.38 to 1.26 (m, 8H), 0.86 (m, 6H). ^{13}C NMR (400 MHz, $CDCl_3$): δ 166.4, 166.2, 135.1, 128.4, 123.3, 128.1, 67.8, 67.1, 41.7, 38.6, 30.2, 28.8, 23.6, 22.9, 14.0, 10.9. FTIR (KBr): ν 2960, 2932, 2873, 1737, 1459, 1329, 1271, 1148, 1012, 747 cm^{-1}. HRMS (EI): *m/z* calcd for $C_{18}H_{26}O_4^+$ ($[M]^+$), 306.1831; found 306.1833. $C_{18}H_{26}O_4$ (306.4) calcd, C 70.56, H 8.55, O 20.89; found C 70.78, H 8.46, O 21.12.

Preparation of b-SWNT without Microwave Irradiation: 5.0 mg of a-SWNT was suspended in 5.0 mL of dry ODCB by ultrasonic treatment in an 100 W sonic bath for 30 min. To this suspension, benzyl 2-ethylhexyl malonate (100 mg, 0.33 mmol) and iodine (85 mg, 0.33 mmol) were added under Ar. Then 1,8-diazabicyclo[5.4.0]undec-7-ene (DBU) (0.10 mL, 0.67 mmol) was added dropwise and the mixture was stirred vigorously. After 24 h, the reaction mixture was diluted with ethanol, then filtered using 0.22 μm pore-sized polycarbonate membrane filter. The remaining black paper was dissolved in ODCB by sonication and reprecipitated from acetone. After repeated cycles of reprecipitation from

ODCB/acetone and filtration, the resultant paper was dried at 50 ^{o}C under vacuum for 1 day to afford 5.0 mg of b-SWNT.

Preparation of b-SWNT with Microwave Irradiation: A suspension of a-SWNT (5.0 mg), benzyl 2-ethylhexyl malonate (100 mg, 0.33 mmol), I_2 (85 mg, 0.33 mmol), and DBU (0.10 mL, 0.67mmol) in dry ODCB (5.0 mL) was stirred in the microwave synthesizer at 120 ^{o}C with an average power of 40, 50, and 60 W, respectively, for 30 min under nitrogen flowing condition. After the reaction, the products were purified as described above (final weight: 4.8 (40 W), 4.5 (50 W), and 4.5 mg (60 W)).

References and Notes

[1] a) M. S. Dresselhaus, G. Dresselhaus, P. C. Eklund, *Science of Fullerenes and Carbon Nanotubes*, Academic Press, San Diego, 1996; b) M. Ouyang, J.-L. Huang, C. M. Lieber, *Acc. Chem. Res.* **2002**, *35*, 1018; c) S. Reich, C. Thomsen, J. Maultzsch, *Carbon Nanotubes*, Wiley-VCH, Weinheim, 2004; d) *Applied Physics of Carbon Nanotubes*, S. V. Rotkin, S. Subramoney, Eds., Springer, Berlin, 2005.

[2] a) T. Rueckes, K. Kim, E. Joselevich, G. Y. Tseng, C. L. Cheung, C. M. Lieber, *Science* **2000**, *289*, 94; b) H. J. Dai, *Surf. Sci.* **2002**, *500*, 218; c) L. Dai, A. Patil, X. Gong, Z. Guo, L. Liu, Y. Liu, D. Zhu, *ChemPhysChem* **2003**, *4*, 1150.

[3] a) J. Liu, A. G. Rinzler, H. Dai, J. H. Hafner, R. K. Bradley, P. J. Boul, A. Lu, T. Iverson, K. Shelimov, C. B. Huffman, F. Rodriguez-Macias, Y.-S Shon, T. R. Lee, D. T. Colbert, R. E. Smalley, *Science* **1998**, *280*, 1253; b) V. C. Moore, M. S. Strano, E. H. Haroz, R. H. Hauge, R. E. Smalley, J. Schmidt, Y. Talmon, *Nano Lett.* **2003**, *3*, 1379; c) M. F. Islam, E. Rojas, D. M. Bergey, A. T. Johnson, A. G. Yodh, *Nano Lett.* **2003**, *3*, 269.

[4] a) M. J. O'Connell, S. M. Bachilo, C. B. Huffman, V. C. Moore, M. S. Strano, E. H. Haroz, K. L. Rialon, P. J. Boul, W. H. Noo, C. Kittrell, J. Ma, R. H. Hauge, R. B. Weisman, R. E. Smalley, *Science* **2002**, *297*, 593; b) S. M. Bachilo. M. S. Strano, C. Kittrell, R. H. Hauge, R. E. Smalley, R. B. Weisman, *Science* **2002**, *298*, 2361.

[5] a) M. J. O'Connell, P. Boul, L. M. Ericson, C. Huffman, Y. Wang, E. Haroz, C. Kuper, J. Tour, K. D. Ausman, R. E. Smalley, *Chem. Phys. Lett.* **2001**, *342*, 265; b) M. Zheng, A. Jagota, E. D. Semke, B. A. Diner, R. S. Mclean, S. R. Lustig, R. E. Richardson, N. G. Tassi, *Nature Mater.* **2003**, *2*, 338; c) A. Star, D. W. Steuerman, J. R. Heath, J. F. Stoddart, *Angew. Chem. Int. Ed.* **2002**, *41*, 2508; d) M. Numata, M. Asai, K. Kaneko, A.-H. Bae, T. Hasegawa, K. Sakurai, S. Shinkai, *J. Am. Chem. Soc.* **2005**, *127*, 5875; e) M. Shigeta, M. Komatsu, N. Nakashima, *Chem. Phys. Lett.* **2006**, *418*, 115.

[6] a) R. J. Chen, Y. Zhang, D. Wang, H. Dai, *J. Am. Chem. Soc.* **2001**, *123*, 3838; b) N.

Nakashima, Y. Tomonari, H. Murakami, *Chem. Lett.* **2002**, *31*, 638; c) H. Murakami, T. Nomura, N. Nakashima, *Chem. Phys. Lett.* **2003**, *378*, 481; d) H. Li, B. Zhou, Y. Lin, L. Gu, W. Wang, K. A. S. Fernando, S. Kumar, L. F. Allard, Y.-P. Sun, *J. Am. Chem. Soc.* **2004**, *126*, 1014; e) T. Hasobe, S. Fukuzumi, P. V. Kamat, *J. Am. Chem. Soc.* **2005**, *127*, 11884.

[7] a) S. A. Curran, P. M. Ajayan, W. J. Blau, D. L. Carroll, J. N. Coleman, A. B. Dalton, A. P. Davey, A. Drury, B. McCarthy, S. Maier, A. Strevens, *Adv. Mater.* **1998**, *10*, 1091; b) A. Star, J. F. Stoddart, D. Steuerman, M. Diehl, A. Boukai, E. W. Wong, X. Yang, S.-W. Chung, H. Choi, J. R. Heath, *Angew. Chem. Int. Ed.* **2001**, *40*, 1721; c) D. W. Steuerman, A. Star, R. Narizzano, H. Choi, R. S. Ries, C. Nicolini, J. F. Stoddart, J. R. Heath, *J. Phys. Chem. B* **2002**, *106*, 3124; d) J. Chen, H. Liu, W. A. Weimer, M. D. Halls, D. H. Ealdeck, G. C. Walker, *J. Am. Chem. Soc.* **2002**, *124*, 9034; e) A. Ikeda, K. Nobusawa, T. Hamano, J.-i. Kikuchi, *Org. Lett.* **2006**, *8*, 5489.

[8] a) Y. Maeda, S.-i. Kimura, Y. Hirashima, M. Kanda, Y. Lian, T. Wakahara, T. Akasaka, T. Hasegawa, H. Tokumoto, T. Shimizu, H. Kataura, Y. Miyauchi, S. Maruyama, K, Kobayashi, S. Nagase, *J. Phys. Chem. B* **2004**, *108*, 18395; b) Y. Maeda, S.-i. Kimura, M. Kanda, Y. Hirashima, T. Hasegawa, T. Wakahara, Y. Lian, T. Nakahodo, T. Tsuchiya, T. Akasaka, J. Lu, X. Zhang, Z. Gao, T. Shimizu, H. Tokumoto, R. Saito, *J. Am. Chem. Soc.* **2005**, *127*, 10287; c) Y. Maeda, M. Kanda, M. Hashimoto, T. Hasegawa, S.-i. Kimura, Y. Lian, T. Wakahara, T. Akasaka, S. Kazaoui, N. Minami, T. Okazaki, Y. Hayamizu, K. Hata, J. Lu, S. Nagase, *J. Am. Chem. Soc.* **2006**, *128*, 12239.

[9] a) J. Lee, H. Kim, S.-J. Kahng, G. Kim, Y.-W. Son, J. Ihm, H. Kato, Z. W. Wang, T. Okazaki, H. Shinohara, Y. Kuk, *Nature* **2002**, *415*, 1005; b) H. Kataura, Y. Maniwa, M. Abe, A. Fujiwara, T. Kodama, K. Kikuchi, H. Imahori, Y. Misaki, S. Suzuki, Y. Achiba, *Appl. Phys. A* **2002**, *74*, 349; c) T. Takenobu, T. Takano, M. Shiraishi, Y. Murakami, M. Ata, H. Kataura, Y. Achiba, Y. Iwasa, *Nature Mater.* **2003**, 2, 683; d) L. J. Li, A. N. Khlobystov, J. G. Wiltshire, G. A. D. Briggs, R. J. Nicholas, *Nature Mater.* **2005**, *4*, 481; e) K. Yanagi, Y. Miyata, H. Kataura, *Adv. Mater.* **2006**, *18*, 437.

[10] a) S. Niyogi, M. A. Hamon, H. Hu, B. Zhao, P. Bhowmik, R. Sen, M. E. Itkis, R. C. Haddon, *Acc. Chem. Res.* **2002**, *35*, 1105; b) Y.-P. Sun, K. Fu, Y. Lin, W. Huang, *Acc. Chem. Res.* **2002**, *35*, 1096; c) C. A. Dyke, J. M. Tour, *J. Phys. Chem. A* **2004**, *108*, 11151; d) C. A. Dyke, J. M. Tour, *Chem.-Eur. J.* **2004**, *10*, 812; e) S. Banerjee, T. Hemraj-Benny, S. S. Wong, *Adv. Mater.* **2005**, *17*, 17; f) D. M. Guldi, G. M. A. Rahman, F. Zerbetto, M. Prato, *Acc. Chem. Res.* **2005**, *38*, 871; g) D. Tasis, N. Tagmatarchis, A. Bianco, M. Prato, *Chem. Rev.* **2006**, *106*, 1105.

[11] a) J. Chen, M. A. Hamon, H. Hu, Y. Chen, M. A. Rao, P. C. Eklund, R. C. Haddon,

Science **1998**, *282*, 95; b) J. E. Riggs, Z. Guo, D. L. Carroll, Y.-P. Sun, *J. Am. Chem. Soc.* **2000**, *122*, 5879; c) Y.-P. Sun, W. Huang, Y. Lin, K. Fu, A. Kitaygorodskiy, L. A. Riddle, Y. J. Yu, D. L. Carroll, *Chem. Mater.* **2001**, *13*, 2864; d) Y. Lian, Y. Maeda, T. Wakahara, T. Akasaka, S. Kazaoui, N. Minami, N. Choi, H. Tokumoto, *J. Phys. Chem. B* **2003**, *107*, 12082; e) H. Hu, B. Zhao, M. A. Hamon, K. Kamaras, M. E. Itkis, R. C. Haddon, *J. Am. Chem. Soc.* **2003**, *125*, 14893.

[12] a) V. Georgakilas, K. Kordatos, M. Prato, D. M. Guldi, M. Holzinger, A. Hirsch, *J. Am. Chem. Soc.* **2002**, *124*, 760; b) V. Georgakilas, D. Voulgaris, E. Vazquez, M. Prato, D. M. Guldi, A. Kukovecz, H. Kuzmany, *J. Am. Chem. Soc.* **2002**, *124*, 14318; c) D. M. Guldi, M. Marcaccio, D. Paolucci, F. Pallucci, N. Tagmatarchis, D. Tasis, E. Vazquez, M. Prato, *Angew. Chem. Int. Ed.* **2003**, *42*, 4206; d) M. Melle-Franco, M. Marcaccio, D. Paolucci, F. Paolucci, V. Georgakilas, D. M. Guldi, M. Prato, F. Zerbetto, *J. Am. Chem. Soc.* **2004**, *126*, 1646; e) N. Tagmatarchis, M. Prato. *J. Mater. Chem.* **2004**, *14*, 437.

[13] a) J. L. Bahr, J. Yang, D. V. Kosynkin, M. J. Bronikowski, R. E. Smalley, J. M. Tour, *J. Am. Chem. Soc.* **2001**, *123*, 6536; b) J. L. Bahr, J. M. Tour, *Chem. Mater.* **2001**, *13*, 3823; c) J. L. Bahr, J. M. Tour, *J. Mater. Chem.* **2002**, *12*, 1952; d) M. S. Strano, C. A. Dyke, M. L. Usrey, P. W. Barone, M. J. Allen, H. Shan, C. Kittrell, R. H. Hauge, J. M. Tour, R. E. Smalley, *Science* **2003**, *301*, 1519; e) J. J. Stephenson, J. L. Hudson, S. Azad, J. M. Tour, *Chem. Mater.* **2006**, *18*, 374.

[14] a) A. Hamwi, H. Alvergnat, S. Bonnamy, F. Béguin, *Carbon* **1997**, *35,* 723; b) E. T. Mickelson, I. W. Chiang, J. L. Zimmerman, P. J. Boul, J. Lozano, J. Liu, R. E. Smalley, R. H. Hauge, J. L. Margrave, *Chem. Phys. Lett.* **1998**, *296*, 188; c) V. N. Khabashesku, W. E. Billups, J. L. Margrave, *Acc. Chem. Res.* **2002**, *35*, 1087; d) J. L. Steves, A. Y. Huang, H. Peng, I. W. Chiang, V. N. Khabashesku, J. L. Margrave, *Nano Lett.* **2003**, *3*, 331.

[15] a) Y. Ying, R. K. Saini, F. Liang, A. K. Sadana, W. E. Billups, *Org. Lett.* **2003**, *5*, 1471; b) H. Peng, L. B. Alemany, J. L. Margrave, V. N. Khabashesku, *J. Am. Chem. Soc.* **2003**, *125*, 15174; c) T. Nakamura, M. Ishihara, T. Ohana, A. Tanaka, Y. Koga, *Chem. Commun.* **2004**, 1336.

[16] a) F. Liang, A. K. Sadana, A. Peera, J. Chattopadhyay, Z. Gu, R. H. Hauge, W. E. Billups, *Nano Lett.* **2004**, *4*, 1257; b) F. Liang, L. B. Alemany, J. M. Beach, W. E. Billups, *J. Am. Chem. Soc.* **2005**, *127*, 13941; c) R. Graupner, J. Abraham, D. Wunderlich, A. Vencelova, P. Lauffer, J. Rohrl, M. Hundhausen, L. Ley, A. Hirsch, *J. Am. Chem. Soc.* **2006**, *128*, 6683; d) J. J. Stephenson, A. K. Sadana, A. L. Higginbotham, J. M. Tour, *Chem. Mater.* **2006**, *18*, 4658.

[17] a) M. Holzinger, O. Vostrowsky, A. Hirsch, F. Hennrich, M. Kappes, R. Weiss, F. Jellen, *Angew. Chem. Int. Ed.* **2001**, *40*, 4002; b) M. Holzinger, J. Abraham, P. Whelan, R.

Graupner, L. Ley, F. Hennrich, M. Kappes, A. Hirsch, *J. Am. Chem. Soc.* **2003**, *125*, 8566; c) M. Holzinger, J. Steinmetz, D. Samaille, M. Glerup, M. Paillet, P. Bernier, L. Ley, R. Graupner, *Carbon* **2004**, *42*, 941; d) Z. Yinghuai, A. T. Peng, K. Carpenter, J. A. Maguire, N. S. Hosmane, M. Takagaki, *J. Am. Chem. Soc.* **2005**, *127*, 9875.

[18] a) K. S. Coleman, S. R. Bailey, S. Fogden, M. L. H. Green, *J. Am. Chem. Soc.* **2003**, *125*, 8722; b) K. A. Worsley, K. R. Moonoosawmy, P. Kruse, *Nano Lett.* **2004**, *4*, 1541.

[19] a) J. L. Delgado, P. Cruz, F. Langa, A. Urbina, J. Casado, J. T. L. Navarrete, *Chem. Commun.* **2004**, 1734; b) M. Alvaro, P. Atienzar, P. de la Cruz, J. L. Delgado, H. Garcia, F. Langa, *J. Phys. Chem. B* **2004**, *108*, 12691; c) M. Alvaro, P. Atienzar, P. de la Cruz, J. L. Delgado, V. Troiani, H. Garcia, F. Langa, A. Palkar, L. Echegoyen, *J. Am. Chem. Soc.* **2006**, *128*, 6626.

[20] a) C. Bingel, *Chem. Ber.* **1993**, *126*, 1957; b) X. Camps, A. Hirsch, *J. Chem. Soc., Perkin Trans. 1* **1997**, 1595.

[21] B. L. Hayes, *Microwave Synthesis: Chemistry at the Speed of Light*, CEM Publishing, North Carolina, 2002.

[22] a) U. M. Fernandez-Paniagua, B. Illescas, N. Martin, C. Seoane, P. de la Cruz, A. de la Hoz, F. Langa, *J. Org. Chem.* **1997**, *62*, 3705; b) F. Langa, P. de la Cruz, A. de la Hoz, E. Espildora, F. P. Cossio, B. Lecea, *J. Org. Chem.* **2000**, *65*, 2499; c) F. Langa, P. de la Cruz, E. Espildora, A. Gonzalez-Cortes, A. de la Hoz, V. Lopez-Arza, *J. Org. Chem.* **2000**, *65*, 8675; d) F. Langa, P. de la Cruz, E. Espildora, A. de la Hoz, J. L. Bourdelande, L. Sanchez, N. Martin, *J. Org. Chem.* **2001**, *66*, 5033.

[23] a) Y. Wang, Z. Iqbal, S. Mitra, *Carbon* **2005**, *43*, 1015; b) K. Kubota, M. Sano, T. Masuko, *Jpn. J. Appl. Phys.* **2005**, *44*, 465; c) Y. Wang, Z. Iqbal, S. Mitra, *J. Am. Chem. Soc.* **2006**, *128*, 95; d) J. Li, H. Grennberg, *Chem. Eur. J.* **2006**, *12*, 3869; e) Y. Wang, Z. Iqbal, S. Mitra, *Carbon* **2006**, *44*, 2804.

[24] *Spectrometric Identification of Organic Compounds*, R. M. Silverstein, G. C. Bassler, T. C. Morrill, Eds., John Wiley & Sons, New York, 1991.

[25] M. A. Hamon, H. Hu, P. Bhowmik, S. Niyogi, B. Zhao, M. E. Itkis, R. C. Haddon, *Chem. Phys. Lett.* **2001**, *347*, 8.

[26] M. A. Hamon, J. Chen, H. Hu, Y. Chen, M. E. Itkis, A. M. Rao, P. C. Eklund, R. C. Haddon, *Adv. Mater.* **1999**, *11*, 834.

[27] a) E. V. Basiuk, M. Monroy-Pelaez, I. Puente-Lee, V. A. Basiuk, *Nano Lett.* **2004**, *4*, 863; b) D. Baskaran, J. W. Mays, X. P. Zhang, M. S. Bratcher, *J. Am. Chem. Soc.* **2005**, *127*, 6916.

[28] a) J. J. Chen, S. V. Deshpande, *Tetrahedron Lett.* **2003**, *44*, 8873; b) C. E. Humphrey, M. A. M. Easson, J. P. Tierney, N. J. Turner, *Org. Lett.* **2003**, *5*, 849.

[29] M. S. Dresselhaus, G. Dresselhaus, R. Saito, A. Jorio, *Phys. Rep.* **2005**, *409*, 47.

[30] H. Kataura, Y. Kumazawa, Y. Maniwa, I. Umezu, S. Suzuki, Y. Ohtsuka, Y. Achiba, *Synth. Metals* **1999**, *103*, 2555.

[31] The author could not detect significant emission at 900 – 1500 nm from b-SWNT dispersed in THF with the aid of octylamine.

[32] a) J. Zhao, Z. Chen, Z. Zhou, H. Park, P. R. Schleyer, J. P. Lu, *ChemPhysChem* **2005**, *6*, 598; b) J. Lu, D. Wang, S. Nagase, M. Ni, X. Zhang, Y. Maeda, T. Wakahara, T. Nakahodo, T. Tsuchiya, T. Akasaka, Z. Gao, D. Yu, H. Ye, Y. Zhou, W. N. Mei, *J. Phys. Chem. B* **2006**, *110*, 5655.

[33] E. Cho, H. Kim, C. Kim, S. Han, *Chem. Phys. Lett.* **2006**, *419*, 134.

Chapter 2

Electrophoretic Deposition of Single-Walled Carbon Nanotubes Covalently Modified with Bulky Porphyrins on Nanostructured SnO_2 Electrodes for Photoelectrochemical Devices

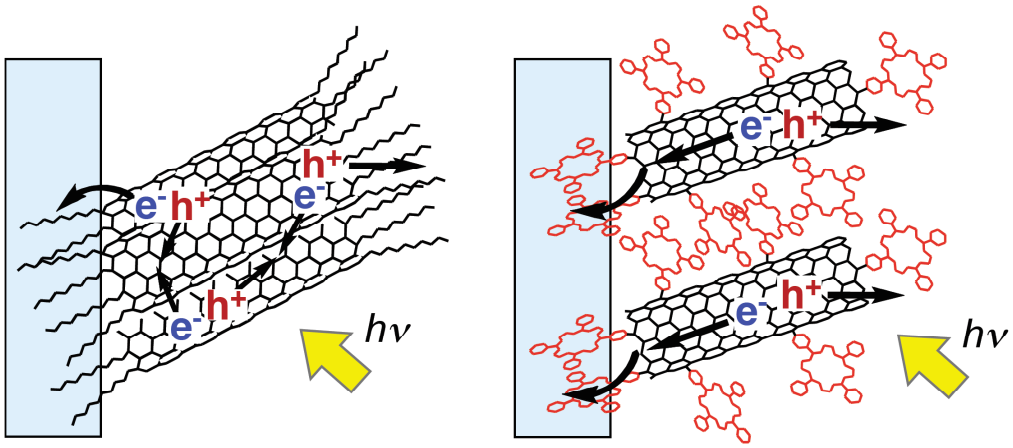

Abstract: Single-walled carbon nanotubes (SWNTs) covalently modified with large porphyrin molecules have been prepared to construct photoelectrochemical devices with nanostructured SnO_2 electrodes on which the multiporphyrin-linked SWNTs are deposited electrophoretically. The film of the porphyrin-linked SWNTs on the nanostructured SnO_2 electrode exhibited an incident photon-to-current efficiency up to 4.9% under an applied potential of 0.08 V *vs.* SCE. The more uniform film formation and the moderate photocurrent generation in the porphyrin-linked SWNT devices can be rationalized by the exfoliation abilities of the bulky porphyrins that yield large steric hindrance around the SWNTs. Direct electron injection from the excited states of the SWNTs to the conduction band of the SnO_2 electrode is responsible for the photocurrent generation. In spite of efficient quenching of the porphyrin excited singlet state by the SWNTs in the porphyrin-linked SWNTs, the photocurrent action spectra revealed that the excitation of the porphyrin moieties makes no contribution to the photocurrent generation. The evolution of exciplex between the porphyrin excited singlet state and the SWNTs and the subsequent rapid decay to the ground state without generating the charge-separated state is proposed to explain the unusual photoelectrochemical behavior. The results obtained here will provide valuable information on the design of SWNT-based photoelectrochemical devices.

Introduction

Nanometer scale carbon materials (*i.e.*, fullerenes and carbon nanotubes) have enormous potential as components of energy conversion devices due to their fascinating optical and electrical properties as well as their robustness.[1,2] In particular, it has been well established that fullerenes have small reorganization energies of electron transfer (ET), which leads to remarkable acceleration of photoinduced charge separation (CS) and of charge shift as well as deceleration of charge recombination (CR).[3] The excellent ET properties of fullerenes as acceptors have prompted us to construct fullerene-based photoelectrochemical devices and solar cells.[1,2] In this context, control of donor–acceptor nanostructures on electrodes is prerequisite for achieving high device performance. For instance, electrophoretic deposition is a unique method to fabricate fullerene films or fullerene-containing composite films for photoelectrochemical devices.[4,5] As has been shown by Imahori and co-workers, supramolecular fullerene–porphyrin composite films, prepared by electrophoretic deposition, on nanostructured SnO_2 electrodes have exhibited efficient photocurrent generation.[5–10] The systems have been regarded as a novel type of supramolecular organic solar cells (*i.e.*, dye-sensitized bulk heterojunction type). Namely, initial CS takes place at the blend interface between donor (D) and acceptor (A) in the D–A multilayers, which is similar to that in bulk heterojunction solar cells. In contrast, the separated electrons are injected into the conduction band (CB) of semiconducting electrodes, as seen in dye-sensitized solar cells. Thus, both characteristics are involved in dye-sensitized bulk heterojunction solar cells of which the cell performance would be further improved by modulating the D–A multilayer-structures on electrodes. Specifically, the photocurrent generation efficiency can be increased remarkably by preorganizing porphyrin units on various nanoscaffolds including dendrimers,[7] oligomers,[8] and nanoparticles,[9] or by preprogramming porphyrin units with self-assembling substituents.[10] These studies have demonstrated experimentally that the construction of nanohighways for efficient electron and hole transport in D–A multilayers on electrodes is highly important to attain efficient photocurrent generation.

One-dimensional, nanowire-like structures of carbon nanotubes (CNTs) provide potential possibilities to construct such ideal nanohighways for efficient electron and hole transport on electrodes. Thus, CNTs have been applied to photovoltaic and photoelectrochemical devices based on the concept.[11–15] Most widely studied CNT-based photovoltaic devices involve bulk heterojunction structures, where CNTs are blended with electron-donating π-conjugated polymers such as poly(*p*-phenylenevinylene) and polythiophene.[11,12] In such cases CNTs are expected to act as electron pathways as well as electron acceptors. In addition, individual CNTs would provide large surface area at the polymer–CNT interface, which is favorable for efficient dissociation of exciton. However, incorporation of debundled CNTs into photovoltaic

systems has been hindered by their poor dispersibility in organic and aqueous solvents as a result of their strong π-π interaction between the individual CNTs.[11,12] Hence, the bundle structures of CNTs remain intact in the blend films of bulk heterojunction solar cells even after a pretreatment of ultrasonication in the presence of the π-conjugated polymers. Overall, the bundle structures preclude the formation of interpenetrating, D–A bicontinuous nanohighways and thus enhance self-quenching of the excited state of CNTs due to the intertube interaction, leading to poor photocurrent generation. To surmount the poor dispersibility of CNTs in solvents, several approaches, including noncovalent interactions[16–18] and covalent bond formation,[19–24] have been developed. During the last decade, noncovalent interactions of single-walled carbon nanotubes (SWNTs) with hydrophilic polymers,[16] surfactants[17] or π-conjugated compounds[18] have been widely used to prepare individually dispersed SWNTs in aqueous solvents or organic solvents. Recently, Kamat *et al.* reported fabrication of the uniform film of SWNTs by electrophoretic deposition from the THF suspension of SWNTs with the aid of tetrabutylammonium bromide (TOAB) as a dispersant to exfoliate SWNT bundles.[14] SWNTs dispersed with protonated porphyrins in acidified THF have also been deposited electrophoretically onto nanostructured SnO_2 electrodes.[15] The SWNTs–porphyrin nanohybrid electrodes exhibited incident photon-to-current efficiency (IPCE) of up to 13% at an applied potential of 0.2 V *vs.* SCE. They proposed dual role of SWNTs in promoting photoinduced CS between the protonated porphyrins and SWNTs and facilitating charge transport to the CB of semiconducting electrode. On the other hand, there have been a few reports on photovoltaic systems utilizing covalently functionalized SWNTs.[12d,13b] Nevertheless, no large donor molecules have been covalently linked to SWNTs to exfoliate SWNT bundles and enhance photocurrent generation efficiency in SWNT-based photo-electrochemical devices. As such, electrophoretic deposition of SWNTs, covalently linked with large functional molecules, onto nanostructured semiconducting electrodes has yet to be reported for photoelectrochemical devices.

Here the author reports the first electrophoretic deposition of SWNTs, covalently linked with large porphyrin molecules at the terminals, defect sites, and sidewalls, onto nanostructured SnO_2 electrodes for photoelectrochemical devices (Scheme 1). Bulky porphyrin units with *tert*-butyl groups at the *meta* positions of the *meso*-phenyl rings are employed as a large chromophore for the covalent functionalization, since they are highly soluble in organic solvents and exhibit efficient light-harvesting property in the visible region. Sequential covalent modification of SWNTs is used to disentangle large bundles of SWNTs and yield stable suspension of SWNTs in organic solvents. Namely, acid-treated, shortened single-walled carbon nanotubes (NT-CO_2H) with carboxyl groups at the open ends and defect sites are reacted with thionyl chlorode and then aminoporphyrins to yield multiporphyrin-linked

SWNTs with amido linkage (NT-CONHH$_2$P).[20] Then, the sidewalls of NT-CONHH$_2$P are further functionalized with aminoporphyrins utilizing *in situ* generated diazonium intermediate to give H$_2$P-NT-CONHH$_2$P.[21] As a result, the author can expect effective suppression of the bundle formation by covalent introduction of the bulky porphyrin moieties into the terminals, defect sites, and sidewalls of SWNTs, resulting in the improvement of the solubility in organic solvents. More importantly, self-quenching of the excited SWNTs as well as of the excited porphyrins would be suppressed considerably by avoiding the association between the SWNTs and/or the porphyrins. The structures, the film morphology on the electrodes, and the photo-electrochemical properties of each SWNT (NT-AR, NT-CO$_2$H, NT-ref, NT-CONHH$_2$P, and H$_2$P-NT-CONHH$_2$P) are investigated by using various spectroscopic and surface analyses and photoelectrochemical measurements to disclose the relationship.

SCHEME 1 [a]

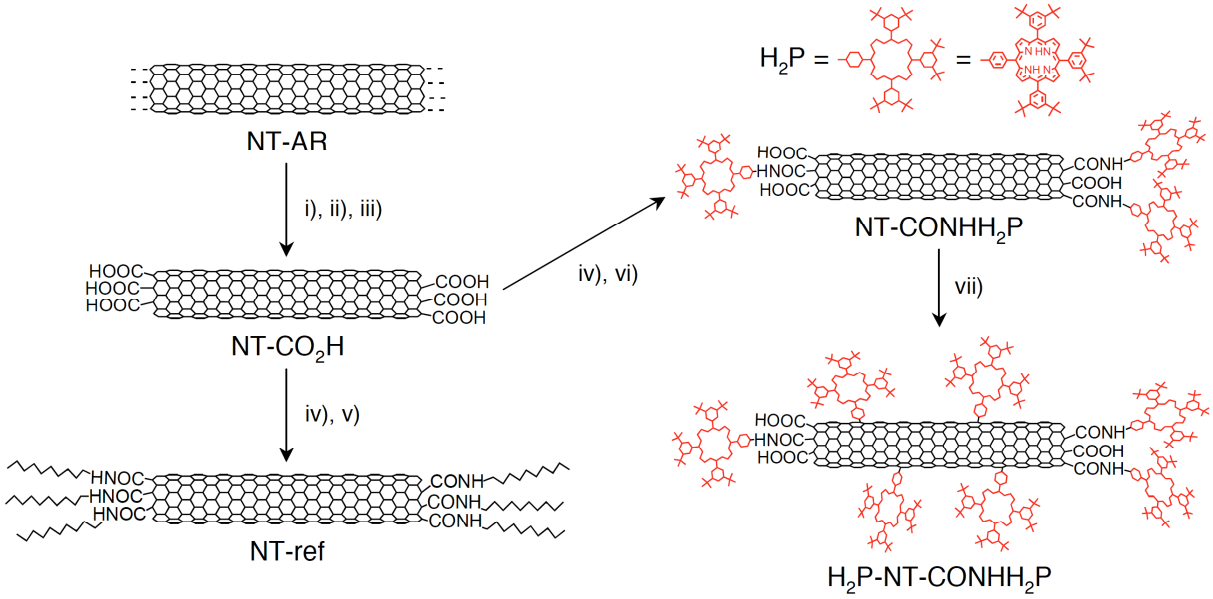

[a] Reagents and conditions: i) 200 °C, air, 24 h; ii) *conc.* HCl, sonication, 15 min; iii) 2.6 M HNO$_3$, reflux, 24 h; iv) SOCl$_2$, reflux, 24 h; v) *n*-C$_{10}$H$_{21}$NH$_2$, 130 °C, 3 days; vi) H$_2$P-NH$_2$, DMF, 80 °C, 3 days, vii) H$_2$P-NH$_2$, isoamyl nitrite, ODCB, microwave, 100 °C, 30 min.

Results and Discussion

Covalent Modification of SWNTs: Synthetic strategy employed for functionalizing SWNTs is shown in Scheme 1. As-received SWNTs (HiPco, denoted as NT-AR) was treated with HCl and HNO$_3$ aqueous solutions to remove metal catalysts and amorphous carbon.[25] The acid-treatment also cuts SWNTs to yield shortened SWNTs which have carboxyl groups at the open ends and defect sites (NT-CO$_2$H).[25] The carboxyl groups at the terminals and the defect sites of NT-CO$_2$H were used to attach the aminoporphyrin, *i.e.*, 5-(4-aminophenyl)-

10,15,20-tris(3,5-di-*tert*-butylphenyl)porphyrin (H_2P-NH_2), via amide linkage formation.[20,26] NT-CO_2H treated with thionyl chloride was further reacted with excess amount of H_2P-NH_2 in DMF under argon atmosphere to afford NT-$CONHH_2P$. For the sidewall functionalization of NT-$CONHH_2P$, the author employed *in situ* generated aryl diazonium intermediate from H_2P-NH_2 to obtain H_2P-NT-$CONHH_2P$.[21,27] In the synthesis of H_2P-NT-$CONHH_2P$, the author utilized microwave irradiation for heating.[28] Microwave heating is known to facilitate various covalent modification of CNTs such as Diels-Alder reaction, 1,3-dipolar cycloaddition, and amide-linkage formation.[24a,29] Under microwave irradiation the reaction mixture was cooled simultaneously by compressed air[30] to transmit the energy to the reaction mixture efficiently and to maintain the reaction temperature at *ca.* 100 ^oC. The arylation reaction of SWNTs was completed within 30 minutes. The reaction rate is *ca.* 100 times faster than that under conventional heating. Thus, microwave irradiation of SWNTs can facilitate the addition of the aryl radical, arising from diazotization of H_2P-NH_2 and subsequent N_2 releasing, to double bonds on the sidewalls. NT-ref with long alkyl chains at the terminals and the defect sites was also prepared by the same method as that described for NT-$CONHH_2P$.

As expected, the solubility of SWNTs in organic solvents is improved by the attachment of bulky porphyrin units at the terminals, defect sites, and sidewalls. H_2P-NT-$CONHH_2P$ is dissolved into DMF (0.2 g L^{-1}) to yield a clear, yellowish-brown solution without discernable particulates. The solution remains stable for a period of at least 2 weeks. The maximum concentration of each SWNT after sonication for 30 min in DMF is in the order of NT-AR (< 0.001 g L^{-1}) << NT-ref (0.1 g L^{-1}) < NT-CO_2H (0.15 g L^{-1}) < NT-$CONHH_2P$ (0.3 g L^{-1}) < H_2P-NT-$CONHH_2P$ (0.5 g L^{-1}). The solubility of each SWNT increases with increasing the degree of functionalization except the case of NT-CO_2H. Carboxy groups at the terminals and the defect sites may assist the solubilization of NT-CO_2H in polar DMF. The trend of the solubility corroborates that the double functionalization of SWNTs with the bulky porphyrin units at the terminals, defect sites, and sidewalls is highly effective for the exfoliation of SWNT bundles.

Characterization of Modified SWNTs: The functionalized SWNTs were characterized by using atomic force microscopy (AFM), transmission electron microscopy (TEM), FT-IR and resonant Raman spectroscopies, thermogravimetric analysis (TGA), and UV–vis–near IR (NIR) absorption and fluorescence spectroscopies.

Figure 1 displays AFM images of NT-AR, NT-CO_2H, NT-ref, NT-$CONHH_2P$, and H_2P-NT-$CONHH_2P$, of which the DMF suspension after sonication for 2 h is spin-coated onto freshly cleaved mica. All images exhibit fibrous structures attributed to individual SWNTs and their bundles. They reveal the progressive exfoliation of SWNT bundles on the mica surfaces

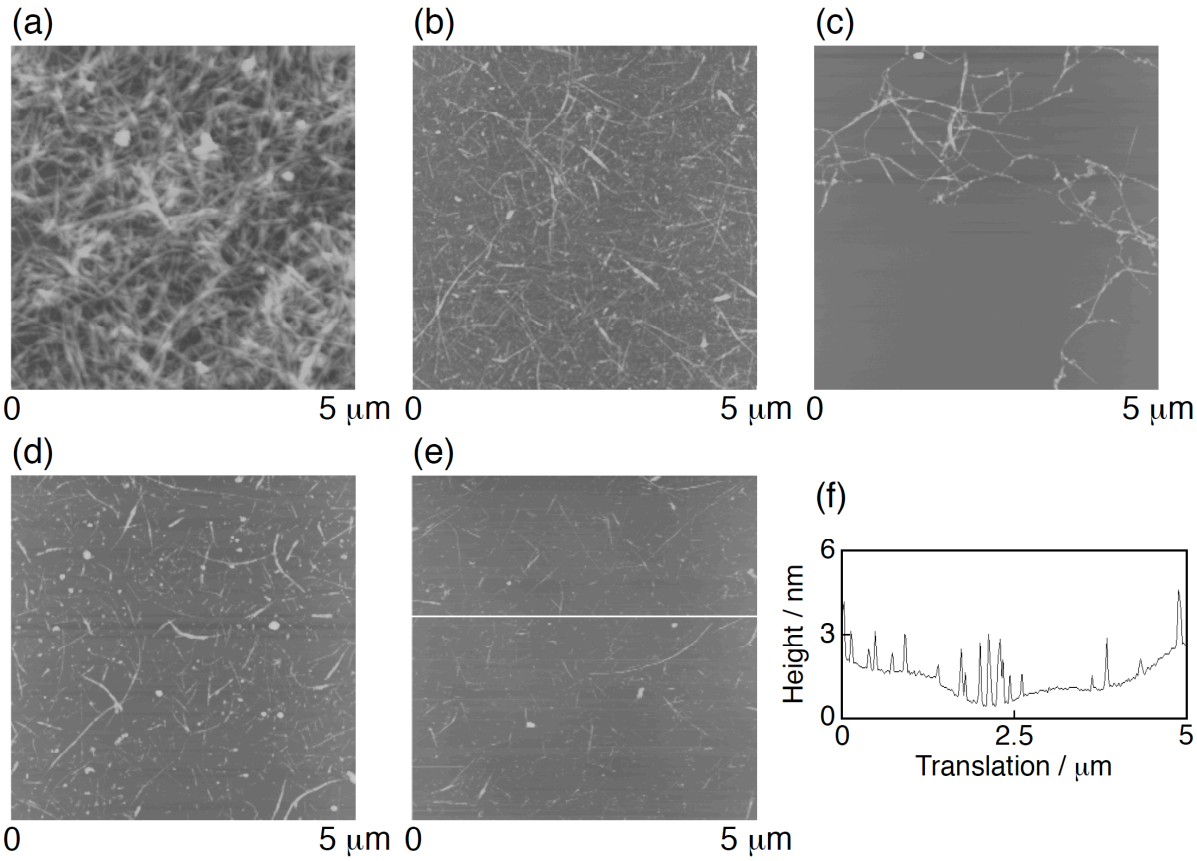

Figure 1. Tapping mode AFM images of (a) NT-AR, (b) NT-CO_2H, (c) NT-ref, (d) NT-$CONHH_2P$, and (e) H_2P-NT-$CONHH_2P$ on mica (Z range: (a) 100 nm, (b) – (e) 50 nm) and (f) section profile of H_2P-NT-$CONHH_2P$. The color scale represents the height topography, with bright and dark representing the highest and lowest features, respectively.

in the order of NT-AR, NT-ref, NT-CO_2H, NT-$CONHH_2P$, and H_2P-NT-$CONHH_2P$, which is consistent with the trend of the solubility (*vide supra*). Namely, the AFM image of NT-AR exhibits large bundles owing to the extremely low solubility in DMF (Figure 1a). NT-CO_2H (Figure 1b) forms bundles with reduced thickness (1.5 – 8 nm) relative to the values of NT-ref (3 – 12 nm, Figure 1c) because of the higher compatibility of NT-CO_2H with DMF (*vide supra*). The bundle sizes of NT-$CONHH_2P$ (1 – 8 nm) and H_2P-NT-$CONHH_2P$ (1 – 3 nm) are further decreased with increasing the degree of the functionalization, as a result of attachment of the large porphyrin molecules to the SWNTs (Figure 1d – f). The average length of isolated H_2P-NT-$CONHH_2P$ is determined as 320 nm. Most of the SWNTs on the mica surface still form their bundles, which may be present in the cast solution or result from the evaporating process during the spin-coating.

The FT-IR spectra of the SWNTs as well as 5,10,15,20-tetrakis(3,5-di-*tert*-butylphenyl)-porphyrin (H_2P-ref) measured in the solid state are presented in Figure 2. Although the peaks at 1500 – 1750 cm^{-1} support the existence of carbonyl groups including carboxylic acid,

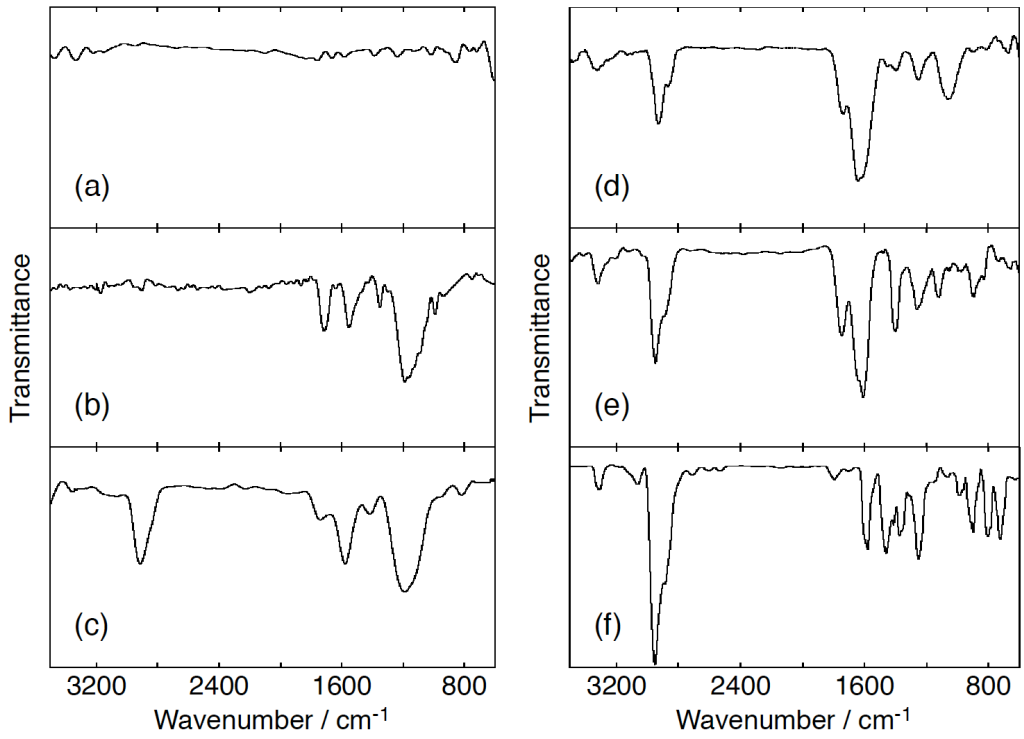

Figure 2. FT-IR spectra of (a) NT-AR, (b) NT-CO_2H, (c) NT-ref, (d) NT-$CONHH_2P$, (e) H_2P-NT-$CONHH_2P$, and (f) H_2P-ref measured in KBr pellet.

carboxylate anion, and amide group[31] in NT-CO_2H, NT-ref, NT-$CONHH_2P$, and H_2P-NT$CONHH_2P$ (Figure 2b – e), extensive overlapping of the bands with others due to the porphyrin moieties does not allow the author to assign each band accurately.[32] Nevertheless, the author can confirm the covalent attachment of the functional moieties (*i.e.*, alkyl chains and porphyrins) to SWNTs. For instance, the band at 2900 cm^{-1} in the spectrum of NT-ref is attributed to C–H stretching vibration of the long alkyl chain (Figure 2c). The spectra of NT-$CONHH_2P$ (Figure 2d) and H_2P-NT-$CONHH_2P$ (Figure 2e) as well as H_2P-ref (Figure 2f) exhibit characteristic absorption bands at 3300 cm^{-1} and 2900 cm^{-1} which are assigned to the stretching vibration of N–H of the pyrrole rings and of C–H of the *tert*-butyl group of the porphyrin moiety, respectively. These FT-IR data are in good agreement with the structures of functionalized SWNTs in Scheme 1.

Resonance Raman spectroscopy is widely used for characterization of SWNTs, since it provides detailed information on the structures of SWNTs.[33] The ratio of peak intensities of tangential mode (G-band) around 1600 cm^{-1} and disorder mode (D-band) around 1350 cm^{-1} (G/D ratio) reflects the relative amount of sp^3 carbon, and is used to determine the degree of functionalization. The Raman spectra of NT-AR, NT-CO_2H, NT-ref, NT-$CONHH_2P$, and H_2P-NT-$CONHH_2P$ were measured with a laser excitation energy of 2.54 eV or 1.96 eV (Figure 3). The Raman signals arising from the porphyrin and alkyl moieties are negligible

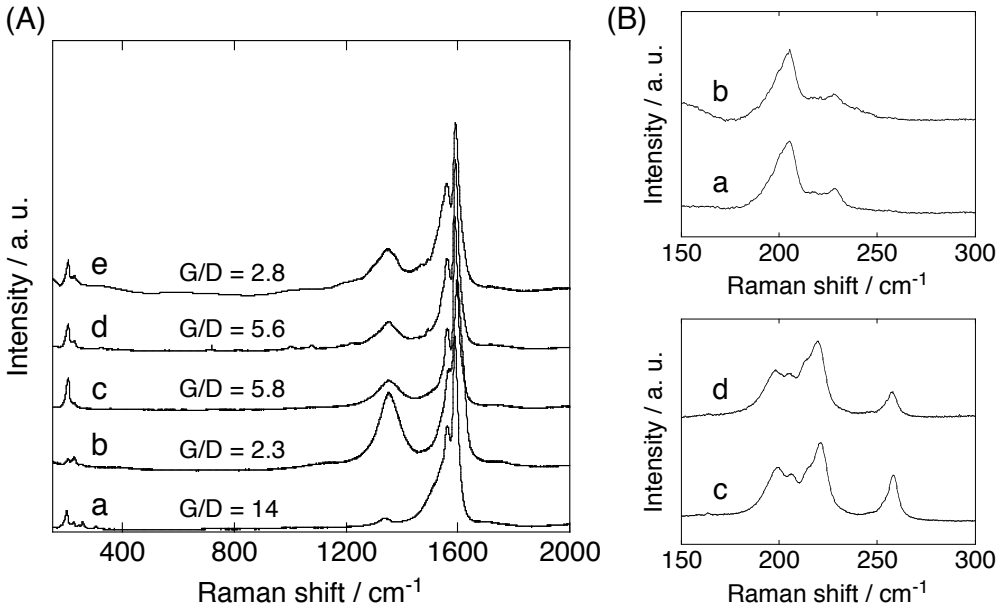

Figure 3. (A) Resonant Raman spectra of (a) NT-AR, (b) NT-CO_2H, (c) NT-ref, (d) NT-$CONHH_2P$, and (e) H_2P-NT-$CONHH_2P$ with an excitation energy of 2.54 eV. Each spectrum is normalized at 1590 cm^{-1}. (B) Resonant Raman spectra in the RBM region of (a) NT-$CONHH_2P$ and (b) H_2P-NT-$CONHH_2P$ with an excitation energy of 2.54 eV and (c) NT-$CONHH_2P$ and (d) H_2P-NT-$CONHH_2P$ with an excitation energy of 1.96 eV.

compared to those of the carbon nanotubes under the experimental conditions. The G/D ratios of NT-ref (5.8) and NT-$CONHH_2P$ (5.6) are almost identical (Figure 3A), but the values are smaller than that of NT-AR (14). This observation is reasonable, considering that the acid treatment increases the terminal and defect sites. The G/D ratio further decreases in the spectrum of H_2P-NT-$CONHH_2P$ (2.8), implying the conversion of sp^2 carbons to sp^3 ones on the sidewalls as a result of the sidewall functionalization by the arylation. The unusual decrease in the G/D ratio of NT-CO_2H (2.3) may be caused by the residual amorphous carbon, which would be generated by the acid-treatment of NT-AR and removed during the purification procedures for NT-ref and NT-$CONHH_2P$. Taking into account Kataura plot[34] with diameters of HiPco (0.8 – 1.3 nm), in the diameter-dependent radial breathing modes (RBMs) at 150 – 280 cm^{-1} (Figure 3B), one can monitor both metallic and semiconducting SWNTs with diameters of 0.8 – 1.1 nm and 1.1 – 1.3 nm with the excitation energy of 2.54 eV, whereas 1.0 – 1.3 nm and 0.8 – 1.0 nm with the excitation energy of 1.96 eV, respectively. The peak position and shape of the spectra are largely similar for NT-$CONHH_2P$ and H_2P-NT-$CONHH_2P$ for the excitation energies of 2.54 eV and 1.96 eV. These results suggest little selectivity of the arylation for semiconducting and metallic SWNTs under the microwave-assisted conditions. This is in marked contrast with exclusive reactivity of arylation using *in situ* generated diazonium intermediate for metallic SWNTs over semiconducting ones under

conventional heating.[21d]

TGA provides further evidence for the covalent functionalization of SWNTs. The TGA curves of the SWNTs and H_2P-ref measured in air are depicted in Figure 4. NT-CO_2H, NT-ref, NT-$CONHH_2P$, and H_2P-NT-$CONHH_2P$ show little end-residue (< 1 wt%) at 750 °C, whereas *ca.* 15% of the initial weight is left at 750 °C for NT-AR. Thus, most of the metal catalysts are removed by the acid-treatment. The curve of NT-ref exhibits two steps for the mass loss, reflecting detachment of covalently-linked long alkyl groups from the SWNTs before the combustion of SWNTs. Accordingly, the weight loses in the temperature ranges of 200 – 380 °C and 380 – 600 °C are assigned to the detachment of the alkyl groups and the combustion of SWNTs, respectively. The TGA reveals that 25 wt% corresponds to the alkyl groups with the amido linkage. In other words, one alkyl group appears at each *ca.* 70 carbon atoms of the SWNT. In the TGA curves of NT-$CONHH_2P$ and H_2P-NT-$CONHH_2P$, in contrast, there are continuous mass losses over a wide range of temperature (200 – 600 °C) upon heating. Unlike the alkyl groups, the thermally stable porphyrin moieties do not lose their whole weight before the combustion of SWNTs so that the TGA curves would not be reliable to estimate the degree of porphyrin functionalization for the SWNTs. However, the rapid weight losses for NT-$CONHH_2P$ and H_2P-NT-$CONHH_2P$ relative to NT-CO_2H in the temperature range of 200 – 600 °C certainly agree with the covalent functionalization of SWNTs.

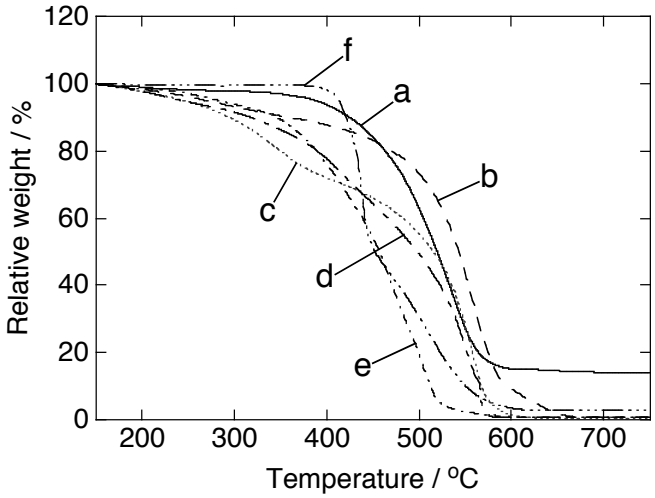

Figure 4. TGA curves of (a) NT-AR, (b) NT-CO_2H, (c) NT-ref, (d) NT-$CONHH_2P$, (e) H_2P-NT-$CONHH_2P$, and (f) H_2P-ref measured in air with heating rate of 10 °C min^{-1}.

Absorption and Fluorescence Spectra of Modified SWNTs: Figure 5 shows the UV–vis–NIR spectra of NT-$CONHH_2P$ and H_2P-NT-$CONHH_2P$ in THF. The spectra exhibit intense Soret band around 420 nm and weak Q bands around 500 – 650 nm, in addition to the broad absorption extending into the NIR region. The spectra largely match the combination of the spectra of NT-ref and H_2P-ref. This provides unambiguous evidence for the presence of the porphyrin units on the SWNTs. The Soret bands are also compared for H_2P-ref, NT-$CONHH_2P$, and H_2P-NT-$CONHH_2P$ (inset of Figure 5). The Soret bands in the absorption spectra of NT-$CONHH_2P$ and H_2P-NT-$CONHH_2P$ are red-shifted by 2 nm and broadened

compared to that of H_2P-ref. The Soret band of H_2P-NT-$CONHH_2P$ is more broadened than that of NT-$CONHH_2P$, reflecting that there is notable electronic communication between the SWNTs and the porphyrin units on the sidewalls in the ground state, owing to the short phenyl spacer between the two units (*vide infra*). The degree of porphyrin functionalization in NT-$CONHH_2P$ and H_2P-NT-$CONHH_2P$ is estimated by comparing the integrated values of absorbance of the SWNT and porphyrin moieties for all frequencies at 20000 – 32000 cm^{-1}, assuming that the integrated values of molar absorption coefficients of the porphyrin moieties for H_2P-ref, NT-$CONHH_2P$, and H_2P-NT-$CONHH_2P$ and those of SWNT moieties for NT-ref, NT-$CONHH_2P$, and H_2P-NT-$CONHH_2P$ are identical, respectively. Consequently, one porphyrin unit at the terminals and defect sites in NT-$CONHH_2P$ is calculated to appear at 720 carbon atoms of the SWNT. Because of the low reactivity of the aminoporphyrin with the bulky *tert*-butyl groups, the degree of porphyrin functionalization at the terminals and defect sites is lower than that of the alkyl functionalization in NT-ref estimated by TGA (*vide supra*). On the other hands, one porphyrin unit at the terminals and defect sites and on the sidewall in H_2P-NT-$CONHH_2P$ is estimated to appear at 240 carbon atoms of the SWNT. This also corresponds to the estimation that one porphyrin unit linked to the sidewall by the short phenyl spacer appears at every 360 carbon atoms of the SWNT. This calculation leads to the conclusion that the degree of the sidewall functionalization by the porphyrin is 2 times higher than that of the terminal and defect functionalization. Assuming that the average diameter of SWNTs employed here is 1.0 nm, there is one porphyrin at each 3.2 nm length on average,[35] suggesting that each porphyrin on the sidewall is well-separated to suppress the intramolecular interaction between the porphyrins in the ground and excited states.

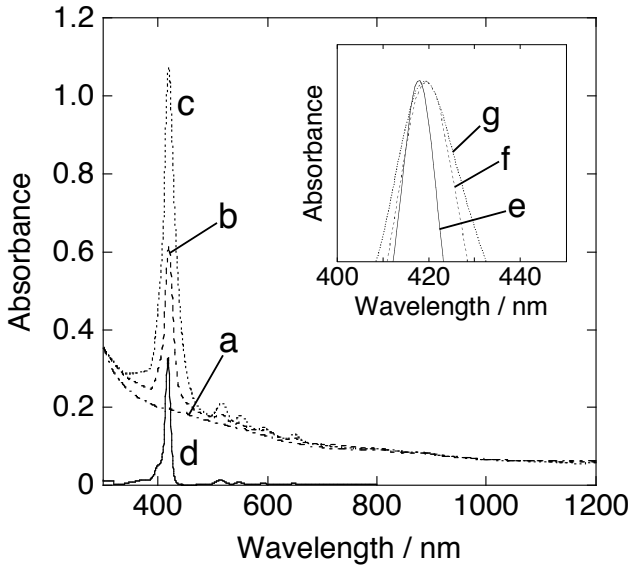

Figure 5. Absorption spectra of (a) NT-ref (0.020 g L^{-1}), (b) NT-$CONHH_2P$, (c) H_2P-NT-$CONHH_2P$, and (d) H_2P-ref (9.5×10^{-7} M) in THF. Spectra (b) and (c) are normalized to spectrum (a) at 1000 nm for comparison. Inset shows (e) absorption spectrum of H_2P-ref and differential absorption spectra of (f) NT-$CONHH_2P$ and NT-ref and (g) H_2P-NT-$CONHH_2P$ and NT-ref. The absorbances are normalized at the peak positions of Soret band.

To compare the absorption due to the SWNT moiety, the absorption spectra of NT-$CONHH_2P$, H_2P-NT-$CONHH_2P$, and NT-ref were also measured in DMF (Figure 6).

NT-ref exhibits characteristic peaks at 500 – 650 nm arising from transitions between the first pair of van Hove singularities in the density of states (DOS) of metallic SWNTs (E^{M}_{11}), and those at 800 – 1000 nm arising from transitions of the second pair of semiconducting SWNTs (E^{S}_{22}).[36] The spectra of NT-CONHH$_2$P and H$_2$P-NT-CONHH$_2$P reveal the four Q bands which overlap with the peaks stemming from the metallic SWNTs extensively. The peaks resulting from the semiconducting SWNTs are virtually the same for NT-CONHH$_2$P and NT-ref, but the peaks in H$_2$P-NT-CONHH$_2$P are significantly broadened in comparison with those in NT-CONHH$_2$P and NT-ref. This broadening can be rationalized by the fact that the sidewall functionalization generally causes the peak broadening owing to the loss of the highly symmetric structure of DOS.[19–24]

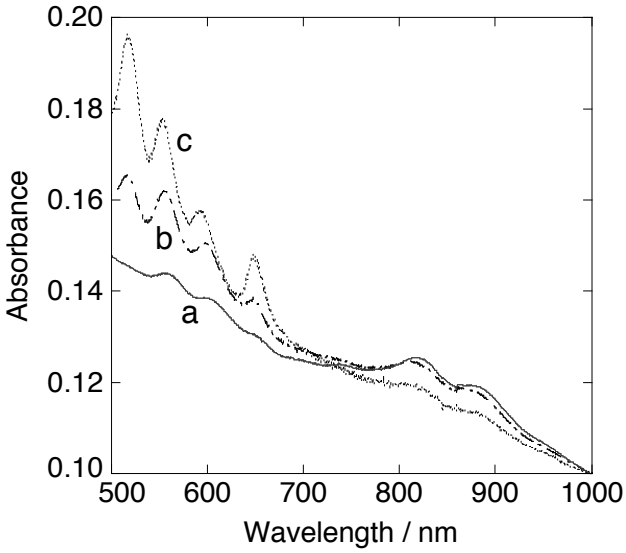

Figure 6. Absorption spectra of (a) NT-ref (0.020 g L^{-1}), (b) NT-CONHH$_2$P, and (c) H$_2$P-NT-CONHH$_2$P in DMF. Spectra (b) and (c) are normalized to the spectrum (a) at 1000 nm for comparison.

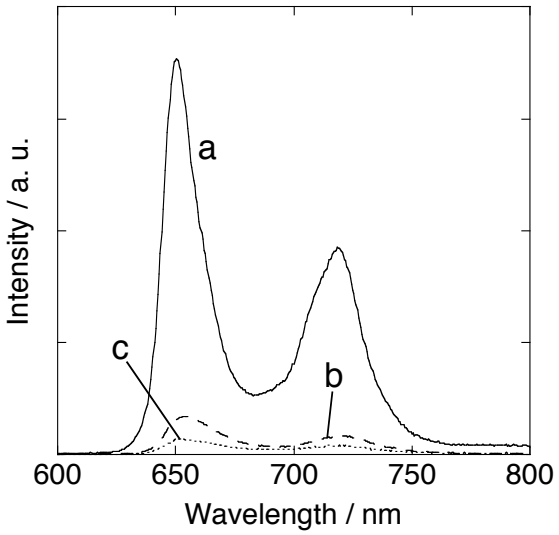

Figure 7. Steady-state fluorescence spectra of (a) H$_2$P-ref, (b) NT-CONHH$_2$P, and (c) H$_2$P-NT-CONHH$_2$P in THF. For excitation, absorbances of the porphyrin moieties in NT-CONHH$_2$P and H$_2$P-NT-CONHH$_2$P were adjusted to be identical to that of H$_2$P-ref at respective peak positions of the Soret band.

The excited state interactions between the SWNTs and the porphyrins were examined by measuring steady-state fluorescence spectra of H$_2$P-ref, NT-CONHH$_2$P, and H$_2$P-NT-CONHH$_2$P in THF (Figure 7). Upon excitation of the porphyrin moiety at the Soret band, where the absorbances of the porphyrin were adjusted to be identical, similar shape of the fluorescence from the porphyrin moiety is observed. The author could not detect significant emission from the SWNT moiety under the present conditions.[37] It is noteworthy that the fluorescence intensities of NT-CONHH$_2$P (12%) and H$_2$P-NT-CONHH$_2$P (7.0%) are reduced considerably compared to that of H$_2$P-ref. The strong quenching of the

porphyrin moieties by the SWNTs suggests that the porphyrin excited singlet state is quenched by the SWNTs via energy transfer (EN), ET or charge transfer (CT), which will be discussed later. The more efficient quenching of H_2P-NT-$CONHH_2P$ relative to that of NT-$CONHH_2P$ is in good agreement with the broadening of the Soret band in H_2P-NT-$CONHH_2P$ due to the short phenyl spacer between the porphyrin and SWNT moieties. The fluorescence lifetimes of NT-$CONHH_2P$, H_2P-NT-$CONHH_2P$, and H_2P-ref were measured in THF–triethylamine (10:1, v/v) by the time-correlated single photon counting technique at emission wavelength of 650 nm with excitation at 400 nm. The decay curves of the fluorescence intensity could be fitted as a single exponential for all cases. The fluorescence lifetimes are similar for NT-$CONHH_2P$ (9.4 ns), H_2P-NT-$CONHH_2P$ (10.8 ns), and H_2P-ref (10.9 ns). However, the fluorescence intensities of NT-$CONHH_2P$ (9.4 ns) and H_2P-NT-$CONHH_2P$ (10.8 ns) are much smaller than that of H_2P-ref, suggesting the occurence of ultrafast quenching of the porphyrin moieties by the SWNT. Because such a fast process is beyond the time resolution (10 ps) of the present system employed, the components of the fluorescence lifetimes in NT-$CONHH_2P$ and H_2P-NT-$CONHH_2P$ may be originate from the minor deactivation pathways of the porphyrin excited singlet state.

Electrophoretic Deposition: The electrophoretic deposition was carried out to fabricate films of the SWNTs from the DMF solution (1.5 mL) in which the same concentration of the SWNTs (0.10 g L^{-1}) is suspended. Upon subjecting the DMF suspension of the functionalized SWNTs to a high electric direct current (dc) field (80 V for NT-CO_2H and NT-ref and 100 V for NT-$CONHH_2P$ and H_2P-NT-$CONHH_2P$), the SWNTs are deposited onto a fluorine-doped tin oxide (FTO) electrodes with nanostructured SnO_2 modification (denoted as FTO/SnO_2) to give the modified electrode (denoted as FTO/SnO_2/SWNTs). As the electrophoretic deposition proceeds, the author can observe discoloration of the suspension and simultaneous coloration of the FTO/SnO_2 electrode that is connected to the positive terminal of the dc supply. The absorbance of the electrodes is increased with increasing the duration time of the electrophoretic deposition and becomes

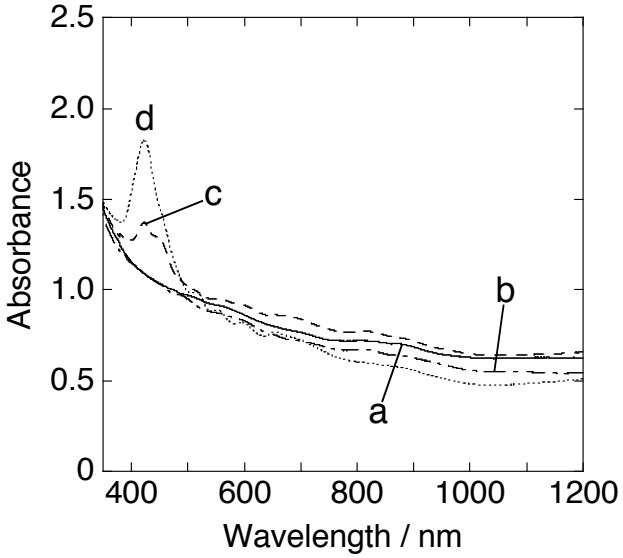

Figure 8. Absorption spectra of (a) FTO/SnO_2/NT-CO_2H, (b) FTO/SnO_2/NT-ref, (c) FTO/SnO_2/NT-$CONHH_2P$, and (d) FTO/SnO_2/H_2P-NT-$CONHH_2P$ electrodes.

saturated within 120 s, implying the completion of the SWNT deposition on the SnO_2 electrode. The electrophoretically deposited films are robust enough for photoelectrochemical measurements (*vide infra*). It should be noted that NT-AR could not be deposited on the electrode due to its extremely low dispersibility in DMF. For all the measurements described later, the author used electrodes prepared by the electrophoretic deposition of the DMF suspension of the functionalized SWNTs for the duration time of 120 s. Figure 8 depicts the absorption spectra of the SWNT modified electrodes. FTO/SnO_2/NT-CO_2H and FTO/SnO_2/NT-ref reveal featureless SWNT absorption that decreases monotonically from UV to NIR regions. In contrast, FTO/SnO_2/NT-$CONHH_2P$ and FTO/SnO_2/H_2P-NT-$CONHH_2P$ exhibit the characteristic absorption due to the porphyrin moieties at 400 – 650 nm, together with the SWNT absorption. All the spectra show strong absorption over UV to NIR regions, ensuring that they absorb incident light effectively.

Surface Characterization of Deposited SWNT Films: To shed light on the film morphology of functionalized SWNTs on the electrodes, optical microscopic measurements were performed (Figure 9). Although FTO/SnO_2/NT-CO_2H and FTO/SnO_2/NT-ref exhibit uniformly black films visibly, the microscopic images reveal the irregularly distributed black spots, which are agglomerates of the SWNTs, on the colorless SnO_2 substrate. The more uniformly distributed films of NT-$CONHH_2P$ and H_2P-NT-$CONHH_2P$ on the electrodes are slightly yellowish black, arising from the color of porphyrin moieties. The film of FTO/SnO_2/H_2P-NT-$CONHH_2P$ shows the most uniform film, suggesting that the exfoliated bundle structures in DMF result in the formation of the more regularly spread film. The author also employed AFM equipped with the optical microscope to characterize the film structure in nano- to micrometer scale (Figure 10). The AFM images for the light black parts of the films disclose the fibrous rod-like structures on the SnO_2 layer, suggesting that SWNT bundles are packed loosely in these regions. On the other hand, the AFM images for the dark black parts of

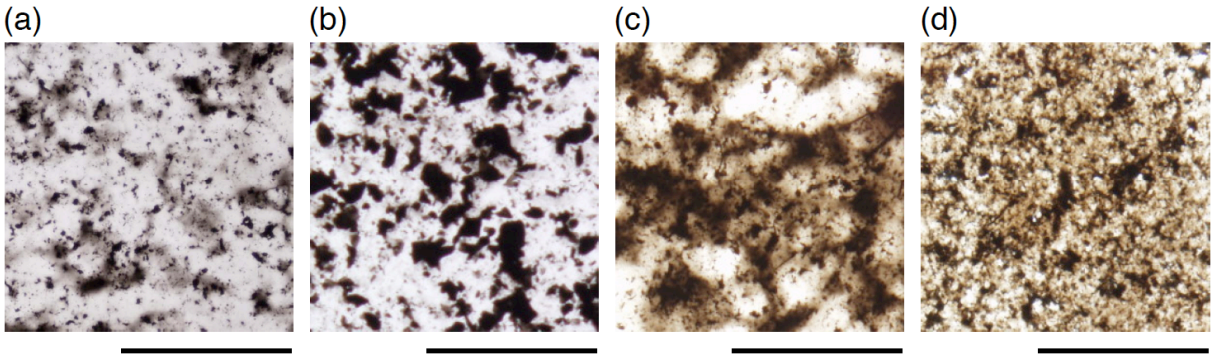

Figure 9. Optical microscopic images of (a) FTO/SnO_2/NT-CO_2H, (b) FTO/SnO_2/NT-ref, (c) FTO/SnO_2/NT-$CONHH_2P$, and (d) FTO/SnO_2/H_2P-NT-$CONHH_2P$. Scale bar: 500 μm.

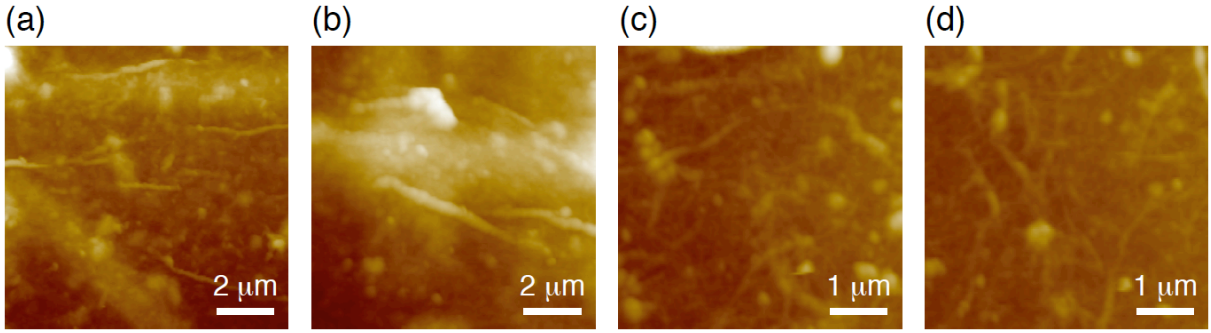

Figure 10. Tapping mode AFM images of (a) FTO/SnO_2/NT-CO_2H, (b) FTO/SnO_2/NT-ref, (c) FTO/SnO_2/NT-$CONHH_2P$, and (d) FTO/SnO_2/H_2P-NT-$CONHH_2P$ electrodes (Z range: (a), (b) 600 nm, (c), (d) 400 nm). The color scale represents the height topography, with bright and dark representing the highest and lowest features, respectively.

the films show extensive overlapping of the SWNT bundles, making it difficult to evaluate the size of each bundle. The height of the bundles on the electrodes is in the order of NT-ref (100 ± 20 nm) > NT-CO_2H (60 ± 20 nm) > NT-$CONHH_2P$ (30 ± 10 nm) > H_2P-NT-$CONHH_2P$ (23 ± 7 nm). This trend is the same as that for the height of the bundles prepared by spin-coating the DMF solution of the modified SWNTs onto mica (*vide supra*). Although the size of SWNT bundles on FTO/SnO_2 is much larger than that on the mica, it is evident that the large porphyrin molecules with the bulky *tert*-butyl groups have large impact on the exfoliation of the SWNT bundles, leading to the small bundle size in NT-$CONHH_2P$ and H_2P-NT-$CONHH_2P$ relative to that in NT-CO_2H and NT-ref.

Photoelectrochemical Measurements: Photoelectrochemical measurements were performed in acetonitrile containing 0.5 M LiI and 0.01 M I_2 with FTO/SnO_2/NT-CO_2H, FTO/SnO_2/NT-ref, FTO/SnO_2/NT-$CONHH_2P$, or FTO/SnO_2/H_2P-NT-$CONHH_2P$ as a working electrode, a Pt wire counter electrode, and an I^-/I_3^- reference electrode. The inset of Figure 11 displays the photoelectrochemical response of FTO/SnO_2/H_2P-NT-$CONHH_2P$ device for the on/off light illumination cycles with an excitation wavelength of 400 nm with input power of 1.10 μW cm^{-2} at an applied potential of 0.08 V *vs.* SCE. The photoelectrochemical response is prompt, steady, and reproducible during repeated on/off cycles. Blank experiments of FTO/SnO_2 electrode without SWNT films exhibited much smaller photocurrent responses under the same conditions. These results confirm the role of the functionalized SWNT films toward harvesting light energy and generating photocurrent during the operation of the photoelectrochemical device. Figure 11 shows current–applied potential curve of FTO/SnO_2/H_2P-NT-$CONHH_2P$ device under white light illumination (λ > 380 nm, input power: 2.16 mW cm^{-2}). With increasing positive bias up to 0.08 V *vs.* SCE, the photocurrent increases

compared to the dark current. Increased CS and the facile transportation of charge carriers under positive bias are responsible for the enhanced photocurrent generation. Similar photoelectrochemical behavior is noted for NT-CO_2H-, NT-ref-, and NT-$CONHH_2P$-based devices.

To evaluate the photoelectrochemical response of the films of SWNTs toward photocurrent generation, the author examined the wavelength dependence of the incident photon-to-current efficiency (IPCE) of the SWNT films on FTO/SnO_2 electrodes (Figure 12A). The IPCE values are calculated by normalizing the photocurrent densities for incident light energy and intensity and by use of the expression:

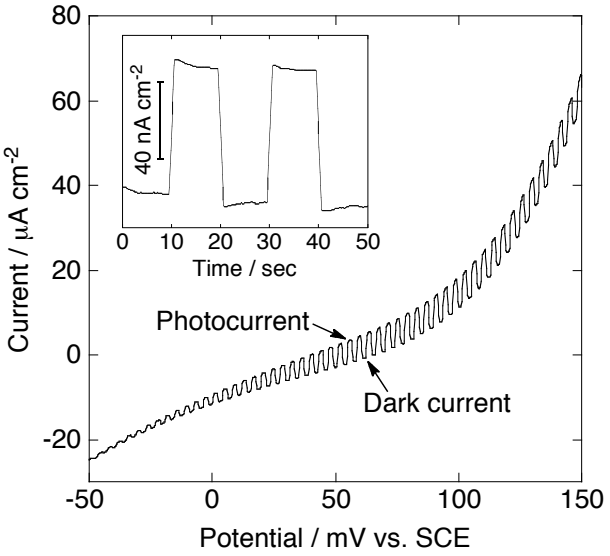

Figure 11. Current *vs.* potential curve of FTO/SnO_2/H_2P-NT-$CONHH_2P$ device under illumination with white light (λ > 380 nm, input power: 2.16 mW cm^{-2}). Inset shows photocurrent response at an excitation wavelength of 400 nm (input power: 1.10 μW cm^{-2}, applied potential: +0.08 V *vs.* SCE). Electrolyte: 0.5 M LiI and 0.01 M I_2 in acetonitrile.

$$\text{IPCE (\%)} = 100 \times 1240 \times i/(W_{in} \times \lambda)$$

where i is the photocurrent density (A cm^{-2}), W_{in} is the incident light intensity (W cm^{-2}), and λ is the excitation wavelength (nm). The overall responses of FTO/SnO_2/NT-CO_2H and FTO/SnO_2/NT-ref devices parallel the broad absorption features, showing the involvement of SWNT films in photocurrent generation. They exhibited anodic photocurrent generation with maximum IPCE values of 2.6% and 2.3% at 400 nm, respectively. These results are in sharp contrast with those of the similar photoelectrochemical device using a nanostructured SnO_2 electrode modified with SWNTs with the aid of TOAB.[14b] The device generated opposite, cathodic photocurrent with a maximum IPCE of *ca.* 0.15%, which is one order of magnitude lower than the IPCE values in the present system under the similar conditions. The presence of insulating TOAB around SWNTs may hamper the efficient electron and hole transport in the deposited film, resulting in poorer photocurrent generation.

On the other hand, the photocurrent action spectra of FTO/SnO_2/NT-$CONHH_2P$ and FTO/SnO_2/H_2P-NT-$CONHH_2P$ show the photocurrent response only from the SWNT moieties. The absorption due to the porphyrin moieties does not contribute to the photocurrent generation (*vide infra*). Accordingly, the maximum IPCE values at an excitation wavelength of 400 nm

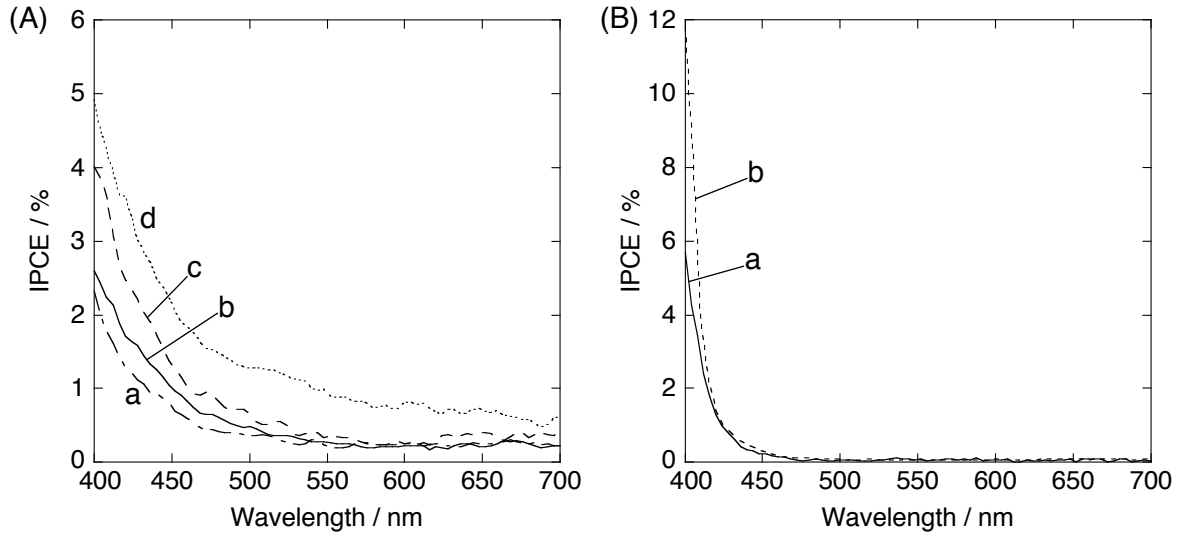

Figure 12. (A) Photocurrent action spectra of (a) FTO/SnO_2/NT-ref, (b) FTO/SnO_2/NT-CO_2H, (c) FTO/SnO_2/NT-$CONHH_2P$, and (d) FTO/SnO_2/H_2P-NT-$CONHH_2P$ devices. (B) Photocurrent action spectra of (a) FTO/TiO_2/H_2P-NT-$CONHH_2P$ and (b) FTO/TiO_2 devices. Applied potential: +0.08 V *vs.* SCE. Electrolyte: 0.5 M LiI and 0.01 M I_2 in acetonitrile.

are as follows: FTO/SnO_2/NT-ref (2.3%) < FTO/SnO_2/NT-CO_2H (2.6%) < FTO/SnO_2/NT-$CONHH_2P$ (4.0%) < FTO/SnO_2/H_2P-NT-$CONHH_2P$ (4.9%). This trend for the photocurrent generation efficiency correlates well with the order of the bundle size of the SWNTs deposited on the electrode (*vide supra*). The correlation suggests that the suppression of the bundle formation decreases self-quenching of the excited SWNTs by the intertube interaction, resulting in the efficient photocurrent generation. The more uniform structures of the deposited films in FTO/SnO_2/NT-$CONHH_2P$ and FTO/SnO_2/H_2P-NT-$CONHH_2P$ devices also explain the higher photocurrent generation efficiency.

The author also prepared nanostructured TiO_2 film on FTO electrode (FTO/TiO_2) to deposit H_2P-NT-$CONHH_2P$ electrophoretically (denoted as FTO/TiO_2/H_2P-NT-$CONHH_2P$). The photoelectrochemical measurements for FTO/TiO_2/H_2P-NT-$CONHH_2P$ and FTO/TiO_2 devices were performed under the same experimental conditions as those for the nanostructured SnO_2 devices. On the contrary to the SnO_2-based devices, the maximum IPCE value (5.6% at 400 nm) of FTO/TiO_2/H_2P-NT-$CONHH_2P$ device is much smaller than that (12% at 400 nm) of FTO/TiO_2 device (Figure 12B). According to the experimentally determined, relational expressions for the Fermi level and the diameter of SWNTs[38] and the diameter and the bandgap energy of semiconducting SWNTs (s-SWNT),[36] the CB of s-SWNTs with diameter of 0.9 – 1.1 nm is in the range of –0.5 – 0 V *vs.* NHE. Such energetics of the s-SWNTs make it possible to inject electrons from the CB of the s-SWNTs to the CB of SnO_2 (E_{CB} (SnO_2) = 0 V *vs.* NHE) due to the exothermic process,[4] but do not from the CB of the s-SWNTs to the CB

of TiO_2 (E_{CB} (TiO_2) = –0.5 V *vs.* NHE) due to the endothermic one.[4] In other words, the s-SWNTs of which the CB lie between 0 and –0.5 V *vs.* NHE are responsible for the photocurrent generation in the present system. Note that the s-SWNTs with the CB level of < –0.5 V *vs.* NHE can inject electrons to the CB of TiO_2, whereas I^- cannot give electrons to the valence band (VB) of the same s-SWNTs in which the energy levels of the VB (< 0.5 V *vs.* NHE) are higher than the level (0.5 V *vs.* NHE) of I_3^-/I^- in the electrolyte solution.[4,38] Although the electronic structure of H_2P-NT-$CONHH_2P$ is perturbed significantly by the sidewall functionalization, the positions of the CB and VB would not be affected, as seen in similar peak positions (E^S_{22}) in the absorption spectra of NT-ref, NT-$CONHH_2P$, and H_2P-NT-$CONHH_2P$ (Figure 6).[36]

Photocurrent Generation Mechanism: On the basis of the photoelectrochemical properties together with the spectroscopic studies, photocurrent generation diagram is illustrated in Scheme 2. As a representative example, (8,6) s-SWNT, which is the highest distribution of (*n*,*m*) species in the present SWNTs, is given in the scheme. The primary step in the photocurrent generation is initiated by electron injection from the CB of the excited states of the s-SWNTs with the diameter of 0.9 – 1.1 nm (–0.5 – 0 V *vs.* NHE) to the SnO_2 nanocrystallites (E_{CB} = 0 V *vs.* NHE). Electron is also transferred from I^- (I_3^-/I^- = 0.5 V *vs.* NHE) in the electrolyte solution to the VB of the s-SWNTs (0.5 – 1.2 V *vs.* NHE).[38] The electron transferred to the semiconductor nanocrystallines is driven to the counter electrode via external circuit to regenerate the redox couple. The bulky porphyrin moieties attached covalently to the tips, defects, and sidewalls inhibit the SWNT bundle formation that causes self-deactivation of the excited states by the intertube interaction.

SCHEME 2

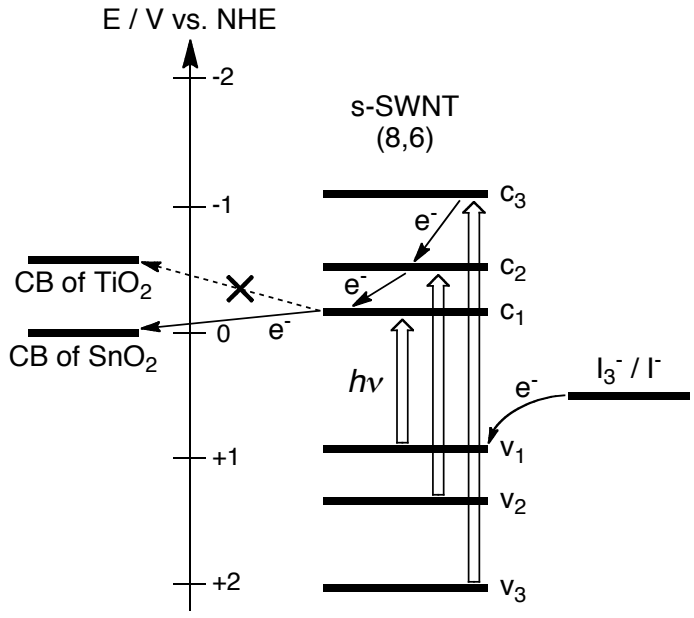

It should be noted here that the absence of photocurrent response from the porphyrin moiety is not consistent with the strong quenching of the porphyrin excited singlet state by the attached SWNTs. The author can consider some possibilities for the relationship between the strong quenching and no photocurrent response from the porphyrin moieties. First, EN from

the porphyrin excited singlet state to the s-SWNT and the metallic SWNTs (m-SWNT) is possible. The EN to the m-SWNT may deactivate the porphyrin and m-SWNT, resulting in no contribution to photocurrent generation. On the other hand, the EN to the s-SWNT yields the excited s-SWNT state, which would be expected to generate photocurrent in the present system. Thus, the EN quenching mechanism is unlikely to occur in the present system. Second, ET from the porphyrin excited singlet state to the s-SWNT is plausible. However, if fast CS and slow CR between the porphyrin and the SWNT moieties take place,[15b,19e] as seen in the porphyrin–fullerene systems,[3] the author would expect highly efficient photocurrent generation in the present system. Accordingly, the ET quenching mechanism may be ruled out in the present system. Finally, CT quenching mechanism is proposed to explain the experimental results. Tkachenko *et al.* have demonstrated that porphyrin–fullerene linked dyads with a short spacer form an exciplex state from the CT interaction between the porphyrin excited singlet state and fullerene.[39] The exciplex state decays to the ground state or to the charge-separated state, depending on the nature of the spacer and the surrounding environment. Therefore, as in the cases of the porphyrin–fullerene system, CT would occur from the porphyrin excited singlet state to the s-SWNTs to generate the exciplex state, which rapidly decays to the ground state rather than to the charge-separated state, resulting in no contribution to the photocurrent generation.

It is interesting to compare the photoelectrochemical properties of covalently- and noncovalently-linked porphyrin–SWNT devices.[15b] In the present system where the porphyrin units are covalently linked to the terminals, defect sites, and sidewalls of the SWNTs, the electronic structure of SWNTs may be disrupted, especially around the porphyrin units. Thus, the photoinduced charge separation between SWNTs and porphyrins is impeded, leading to the rather lower IPCE value (4.9%) relative to the value (13%) in the noncovalently-linked porphyrin–SWNT device. The difference in SWNTs (HiPco *vs.* Nanocs Inc.)[40] may also influence the photoelectrochemical properties. Kamat *et al.* used SWNTs with diameters of 2 – 10 nm (Nanocs Inc.) for the formation of the composite film with protonated porphyrins, which caused anodic photocurrent generation. The author employed SWNTs (HiPco) with small diameters of 0.8 – 1.3 nm. The work function of SWNTs is known to become larger in a manner inversely proportional to the diameter of SWNTs.[38a] Although the absolute potentials of the Fermi level of the functionalized SWNTs are not clear, the electronic interaction between excited porphyrins and SWNTs here is different from that of the previous system. The efficient EN in the *J*-aggregate like porphyrin arrays on SWNTs and similar exciplex formation between the porphyrin excited singlet state and the SWNTs may also accommodate the efficient photocurrent generation in the noncovalently-linked porphyrin–SWNT device.

Conclusion

In conclusion, the author has successfully constructed photoelectrochemical devices with nanostructured SnO_2 electrodes modified with the covalently-linked porphyrin–SWNT hybrids. The film of porphyrin-linked SWNTs on the nanostructured SnO_2 electrode exhibited an incident photon-to-current efficiency as high as 4.9% under an applied potential of 0.08 V *vs.* SCE. The more uniform film and moderate photocurrent generation in the porphyrin–linked SWNT devices can be rationalized by the exfoliation abilities of the porphyrins due to the large steric hindrance. Direct electron injection from the excited states of the SWNTs to the conduction band of the SnO_2 electrode is responsible for the photocurrent generation. It is noteworthy that the absence of photocurrent response from the porphyrin moiety is not consistent with the strong quenching of the porphyrin excited singlet state by the attached SWNTs. Occurrence of charge transfer from the porphyrin excited singlet state to the semiconducting SWNTs to generate the exciplex states, which rapidly decay to the ground state rather than to the charge-separated state, is proposed to explain the discrepancy. The results obtained here will provide basic and valuable information on the design of SWNT-based photoelectrochemical devices.

Experimental Section

General Procedure: The microwave-assisted syntheses were carried out with a CEM Discover BenchMate microwave synthesizer. FT-IR spectra were recorded on a JASCO FT/IR-470 Plus spectrometer using KBr pellets. Resonance Raman spectra were measured using a Horiba JobinYvon LabRAM HR-800 equipped with 2.54 eV (488 nm) and 1.96 eV (633 nm) laser. The solid samples of the SWNTs were mounted on a slideglass. TGA curves were obtained by a SHIMADZU TG-60 under a flowing air at a scan rate of 10 ^{o}C min^{-1}. AFM observations of the SWNT samples spin-coated on mica were performed with a Digital Instruments Nanoscope III in the tapping mode. DMF suspension of SWNTs (0.10 g L^{-1}) was sonicated for 120 min and spin-coated on freshly cleaved mica at a rotation speed of 1000 rpm. AFM images of the SWNT samples deposited on the electrodes were obtained using a Keyence VN-8000 in the tapping mode. TEM analyses were conducted with a JEOL JEM2000FX-II. For sample preparation, a THF solution containing SWNTs was dropped on microgrids and dried under vacuum. UV–vis–NIR absorption spectra were measured by a PerkinElmer Lambda 900 UV/VIS/NIR spectrometer. For a typical sample preparation, 0.020 g L^{-1} suspension of a SWNT sample in THF or DMF was sonicated for 1 h. Steady-state fluorescence spectra were recorded on a Horiba SPEX Fluoromax-3 spectrofluorometer. Fluorescence lifetimes were determined by the single-photon counting method using a second

harmonic generation (SHG, 400 nm) of a Ti:sapphire laser (Spectra-Physics, Tsunami 3950-L2S, full width at half maximum (FWHM): 150 fs) and a streakscope (Hamamatsu Photonics, C4334-01) equipped with a polychromator (Acton Research, SpectraPro 150) as an excitation source and a detector, respectively. An optically transparent FTO electrode (Asahi Glass) was washed by sonication in 2-propanol and cleaned in an O_3 atmosphere in advance. A 15% SnO_2 colloidal solution (particle size = 15 nm; Chemat Technology, Inc.) was deposited on the FTO electrode using doctor blade technique.[9d,e] The electrode was annealed at 673 K to yield 1.3 μm thick SnO_2 film (denoted as FTO/SnO_2). NT-AR is Purified HiPco SWNTs purchased from Carbon Nanotechnologies, Inc., and used as-received. NT-COOH and NT-ref were prepared as described elsewhere.[25] 5-(4-Aminophenyl)-10,15,20-tris(3,5-di-*tert*-butyl-phenyl)porphyrin (H_2P-NH_2) and 5,10,15,20-tetrakis(3,5-di-*tert*-butylphenyl)porphyrin (H_2P-ref) were prepared according to the literature.[41] *o*-Dichlorobenzene (ODCB) was distilled from calcium hydride before use. All other chemicals purchased from commercial sources were used without further purification.

Preparation of NT-CONHH_2P: A suspension of 5.0 mg of NT-COOH in 5.0 mL of $SOCl_2$ was refluxed for 24 h under a nitrogen atmosphere. $SOCl_2$ was removed under vacuum, and then 50 mg of H_2P-NH_2 (0.052 mmol) in 20 mL of dehydrated DMF was added to the residue. After stirring at 130 ^oC for 3 days, the reaction mixture was diluted with ethanol, then filtered using 0.22 μm pore-sized polycarbonate membrane filter. The filtrate was blackish purple, implying the involvement of amorphous carbon and excess H_2P-NH_2 in the filtrate. After being washed with THF and dichloromethane to remove the excess H_2P-NH_2 completely, the black solid was dried under vacuum to afford 5.2 mg of NT-CONHH_2P.

Preparation of H_2P-NT-CONHH_2P: A mixture of 2.5 mg of NT-CONHH_2P and 250 mg of H_2P-NH_2 (0.26 mmol) in 5.0 mL of ODCB was sonicated using 100 W sonic bath for 30 min under a nitrogen atmosphere. After addition of 63 μL of isoamyl nitrite (0.47 mmol), the reaction mixture was stirred in the microwave synthesizer at 100 ^oC for 30 min under nitrogen flowing conditions. The simultaneous cooling by compressed air was conducted during the reaction. The product was purified as described above to yield 3.0 mg of H_2P-NT-CONHH_2P.

Electrophoretic Deposition of SWNTs: DMF suspension of SWNTs (0.10 g L^{-1}) was sonicated for 2 h and 1.5 mL of the suspension was transferred to a 1 cm cuvette in which two electrodes (*i.e.*, FTO and FTO/SnO_2) were kept at a distance of 6.0 mm by a Teflon spacer. A dc voltage (80 V for NT-COOH and NT-ref, 100 V for NT-CONHH_2P and H_2P-NT-CONHH_2P) for 2 min was applied between these two electrodes using a power supply (ATTO, model AE-8750). The deposition of the film could be confirmed visibly as the suspension becomes colorless with simultaneous colorization of the FTO/SnO_2 electrode.

Photoelectrochemical Measurements: All electrochemical measurements were carried

out in a standard three-electrode system using an ALS 630A electrochemical analyzer.[9d,e] The SWNT film as a working electrode was immersed into the electrolyte solution containing 0.5 M LiI and 0.01 M I_2 in acetonitrile. A Pt wire covered with a glass ruggin capillary, whose tip was located near the working electrode, and a Pt coil were used as quasi-reference and counter electrodes, respectively. The potential measured was converted to the saturated calomel electrode (SCE) scale by adding +0.05 V. The stability of the reference electrode potential was confirmed under the experimental conditions. A 500 W xenon lamp (USHIO, XB-50101AAA) was used as a light source. Potential versus current characteristics were measured with controlled-potential scan (1 mV s^{-1}) under 0.5 Hz chopped white light (λ > 380 nm, input power: 2.16 mW cm^{-2}). Monochromatic light through a monochrometer (Ritsu, MC-10N) was illuminated on the modified area of the working electrode (0.20 cm^2) from the backside. The light intensity was monitored by an optical power meter (Anritsu, ML9002A).

References and Notes

[1] a) M. S. Dresselhaus, G. Dresselhaus, P. C. Eklund, *Science of Fullerenes and Carbon Nanotubes*, Academic Press, San Diego, 1996; b) *Fullerenes*, K. D. Kadish, R. S. Ruoff, Eds., Wiley, New York, 2000; c) S. Reich, C. Thomsen, J. Maultzsch, *Carbon Nanotubes*, Wiley-VCH, Weinheim, 2004; d) *Applied Physics of Carbon Nanotubes*, S. V. Rotkin, S. Subramoney, Eds., Springer, Berlin, 2005; e) *Organic Photovoltaics*, C. Brabec, V. Dyakonov, J. Parisi, N. S. Sariciftci, Eds., Springer, Berlin, 2003.

[2] a) E. Katz, I. Willner, *ChemPhysChem* **2004**, *5*, 1084; b) D. M. Guldi, *J. Phys. Chem. B* **2005**, *109*, 11432; c) P. V. Kamat, *J. Phys. Chem. C* **2007**, *111*, 2834.

[3] a) H. Imahori, Y. Sakata, *Adv. Mater.* **1997**, *9*, 537: b) H. Imahori, Y. Sakata, *Eur. J. Org. Chem.* **1999**, 2445; c) H. Imahori, *Org. Biomol. Chem.* **2004**, *2*, 1425; d) H. Imahori, *J. Phys. Chem. B* **2004**, *108*, 6130; e) H. Imahori, S. Fukuzumi, *Adv. Funct. Mater.* **2004**, *14*, 525.

[4] a) P. V. Kamat, S. Barazzouk, K. G. Thomas, S. Hotchandani, *J. Phys. Chem. B* **2000**, *104*, 4014; b) P. V. Kamat, S. Barazzouk, S. Hotchandani, K. G. Thomas, *Chem.-Eur. J.* **2000**, *6*, 3914.

[5] H. Imahori, *J. Mater. Chem.* **2007**, *17*, 31.

[6] a) H. Imahori, T. Hasobe, H. Yamada, P. V. Kamat, S. Barazzouk, M. Fujitsuka, O. Ito, S. Fukuzumi, *Chem. Lett.* **2001**, 784; b) T. Hasobe, H. Imahori, S. Fukuzumi, P. V. Kamat, *J. Phys. Chem. B* **2003**, *107*, 12105.

[7] a) T. Hasobe, Y. Kashiwagi, M. A. Absalom, J. Sly, K. Hosomizu, M. J. Crossley, H. Imahori, P. V. Kamat, S. Fukuzumi, *Adv. Mater.* **2004**, *16*, 975; b) T. Hasobe, P. V.

Kamat, M. A. Absalom, Y. Kashiwagi, J. Sly, M. J. Crossley, K. Hosomizu, H. Imahori, S. Fukuzumi, *J. Phys. Chem. B* **2004**, *108*, 12865.

[8] T. Hasobe, P. V. Kamat, V. Troiani, N. Solladie, T. K. Ahn, S. K. Kim, D. Kim, A. Kongkanand, S. Kuwabata, S. Fukuzumi, *J. Phys. Chem. B* **2005**, *109*, 19.

[9] a) T. Hasobe, H. Imahori, P. V. Kamat, S. Fukuzumi, *J. Am. Chem. Soc.* **2003**, *125*, 14962; b) T. Hasobe, S. Hattori, P. V. Kamat, Y. Urano, N. Umezawa, T. Nagano, S. Fukuzumi, *Chem. Phys.* **2005**, *319*, 243; c) T. Hasobe, H. Imahori, P. V. Kamat, T. K. Ahn, S. K. Kim, D. Kim, A. Fujimoto, T. Hirakawa, S. Fukuzumi, *J. Am. Chem. Soc.* **2005**, *127*, 1216; d) H. Imahori, A. Fujimoto, S. Kang, H. Hotta, K. Yoshida, T. Umeyama, Y. Matano, S. Isoda, M. Isosomppi, N. V. Tkachenko, H. Lemmetyinen, *Chem.-Eur. J.* **2005**, *11*, 7265; e) H. Imahori, K. Mitamura, Y. Shibano, T. Umeyama, Y. Matano, K. Yoshida, S. Isoda, Y. Araki, O. Ito, *J. Phys. Chem. B* **2006**, *110*, 11399.

[10] S. Kang, T. Umeyama, M. Ueda, Y. Matano, H. Hotta, K. Yoshida, S. Isoda, M. Shiro, H. Imahori, *Adv. Mater.* **2006**, *18*, 2549.

[11] a) D. B. Romero, M. Carrard, W. De Heer, L. Zuppiroli, *Adv. Mater.* **1996**, *8*, 899; b) H. Ago, K. Petritsch, M. S. P. Shaffer, A. H. Windle, R. H. Friend, *Adv. Mater.* **1999**, *11*, 1281; c) A. Star, J. F. Stoddart, D. Steuerman, M. Diehl, A. Boukai, E. W. Wong, X. Yang, S.-W. Chung, H. Choi, J. R. Heath, *Angew. Chem. Int. Ed.* **2001**, *40*, 1721.

[12] a) E. Kymakis, G. A. J. Amaratunga, *Appl. Phys. Lett.* **2002**, *80*, 112; b) S. Bhattacharyya, E. Kymakis, G. A. J. Amaratunga, *Chem. Mater.* **2004**, *16*, 4819; c) B. J. Landi, R. P. Raffaelle, S. L. Castro, S. G. Bailey, *Prog. Photovoltaics* **2005**, *13*, 165; d) B. Pradhan, S. K. Batabyal, A. J. Pal, *Appl. Phys. Lett.* **2006**, *88*, 093106.

[13] a) W. Wu, J. Li, L. Liu, L. Yanga, Z.-X. Guo, L. Dai, D. Zhu, *Chem. Phys. Lett.* **2002**, *364*, 196; b) S.-R. Jang, R. Vittal, K.-J. Kim, *Langmuir* **2004**, *20*, 9807; c) G. M. A. Rahman, D. M. Guldi, R. Cagnoli, A. Mucci, L. Schenetti, L. Vaccari, M. Prato, *J. Am. Chem. Soc.* **2005**, *127*, 10051; d) L. Sheeney-Haj-Ichia, B. Basnar, I. Willner, *Angew. Chem. Int. Ed.* **2005**, *44*, 78; e) V. Sgobba, G. M. A. Rahman, D. M. Guldi, N. Jux, S. Campidelli, M. Prato, *Adv. Mater.* **2006**, *18*, 2264.

[14] a) P. V. Kamat, K. G. Thomas, S. Barazzouk, G. Girishkumar, K. Vinodgopal, D. Meisei, *J. Am. Chem. Soc.* **2004**, *126*, 10757; b) S. Barazzouk, S. Hotchandani, K. Vinodgopal, P. V. Kamat, *J. Phys. Chem. B* **2004**, *108*, 17015.

[15] a) T. Hasobe, S. Fukuzumi, P. V. Kamat, *J. Am. Chem. Soc.* **2005**, *127*, 11884; b) T. Hasobe, S. Fukuzumi, P. V. Kamat, *J. Phys. Chem. B* **2006**, *110*, 25477.

[16] a) M. J. O'Connell, P. Boul, L. M. Ericson, C. Huffman, Y. Wang, E. Haroz, C. Kuper, J. Tour, K. D. Ausman, R. E. Smalley, *Chem. Phys. Lett.* **2001**, *342*, 265; b) M. Zheng, A. Jagota, E. D. Semke, B. A. Diner, R. S. Mclean, S. R. Lustig, R. E. Richardson, N. G.

Tassi, *Nature Mater.* **2003**, *2*, 338; c) A. Star, D. W. Steuerman, J. R. Heath, J. F. Stoddart, *Angew. Chem. Int. Ed.* **2002**, *41*, 2508; d) M. Numata, M. Asai, K. Kaneko, A.-H. Bae, T. Hasegawa, K. Sakurai, S. Shinkai, *J. Am. Chem. Soc.* **2005**, *127*, 5875.

[17] a) J. Liu, A. G. Rinzler, H. Dai, J. H. Hafner, R. K. Bradley, P. J. Boul, A. Lu, T. Iverson, K. Shelimov, C. B. Huffman, F. Rodriguez-Macias, Y.-S. Shon, T. R. Lee, D. T. Colbert, R. E. Smalley, *Science* **1998**, *280*, 1253; b) V. C. Moore, M. S. Strano, E. H. Haroz, R. H. Hauge, R. E. Smalley, J. Schmidt, Y. Talmon, *Nano Lett.* **2003**, *3*, 1379; c) M. F. Islam, E. Rojas, D. M. Bergey, A. T. Johnson, A. G. Yodh, *Nano Lett.* **2003**, *3*, 269.

[18] a) R. J. Chen, Y. Zhang, D. Wang, H. Dai, *J. Am. Chem. Soc.* **2001**, *123*, 3838; b) N. Nakashima, Y. Tomonari, H. Murakami, *Chem. Lett.* **2002**, *31*, 638; c) H. Murakami, T. Nomura, N. Nakashima, *Chem. Phys. Lett.* **2003**, *378*, 481; d) H. Li, B. Zhou, Y. Lin, L. Gu, W. Wang, K. A. S. Fernando, S. Kumar, L. F. Allard, Y.-P. Sun, *J. Am. Chem. Soc.* **2004**, *126*, 1014.

[19] a) S. Niyogi, M. A. Hamon, H. Hu, B. Zhao, P. Bhowmik, R. Sen, M. E. Itkis, R. C. Haddon, *Acc. Chem. Res.* **2002**, *35*, 1105; b) Y.-P. Sun, K. Fu, Y. Lin, W. Huang, *Acc. Chem. Res.* **2002**, *35*, 1096; c) C. A. Dyke, J. M. Tour, *J. Phys. Chem. A* **2004**, *108*, 11151; d) C. A. Dyke, J. M. Tour, *Chem.-Eur. J.* **2004**, *10*, 812; e) D. M. Guldi, G. M. A. Rahman, F. Zerbetto, M. Prato, *Acc. Chem. Res.* **2005**, *38*, 871; f) D. Tasis, N. Tagmatarchis, A. Bianco, M. Prato, *Chem. Rev.* **2006**, *106*, 1105.

[20] a) J. Chen, M. A. Hamon, H. Hu, Y. Chen, M. A. Rao, P. C. Eklund, R. C. Haddon, *Science* **1998**, *282*, 95; b) Y.-P. Sun, W. Huang, Y. Lin, K. Fu, A. Kitaygorodskiy, L. A. Riddle, Y. J. Yu, D. L. Carroll, *Chem. Mater.* **2001**, *13*, 2864; c) Y. Lian, Y. Maeda, T. Wakahara, T. Akasaka, S. Kazaoui, N. Minami, N. Choi, H. Tokumoto, *J. Phys. Chem. B* **2003**, *107*, 12082; d) M. A. Herranz, N. Martin, S. Campidelli, M. Prato, G. Brehm, D. M. Guldi, *Angew. Chem. Int. Ed.* **2006**, *45*, 4478.

[21] a) J. L. Bahr, J. Yang, D. V. Kosynkin, M. J. Bronikowski, R. E. Smalley, J. M. Tour, *J. Am. Chem. Soc.* **2001**, *123*, 6536; b) J. L. Bahr, J. M. Tour, *Chem. Mater.* **2001**, *13*, 3823; c) J. L. Bahr, J. M. Tour, *J. Mater. Chem.* **2002**, *12*, 1952; d) M. S. Strano, C. A. Dyke, M. L. Usrey, P. W. Barone, M. J. Allen, H. Shan, C. Kittrell, R. H. Hauge, J. M. Tour, R. E. Smalley, *Science* **2003**, *301*, 1519; e) J. J. Stephenson, J. L. Hudson, S. Azad, J. M. Tour, *Chem. Mater.* **2006**, *18*, 374.

[22] a) V. Georgakilas, K. Kordatos, M. Prato, D. M. Guldi, M. Holzinger, A. Hirsch, *J. Am. Chem. Soc.* **2002**, *124*, 760; b) V. Georgakilas, D. Voulgaris, E. Vazquez, M. Prato, D. M. Guldi, A. Kukovecz, H. Kuzmany, *J. Am. Chem. Soc.* **2002**, *124*, 14318; c) D. M. Guldi, M. Marcaccio, D. Paolucci, F. Pallucci, N. Tagmatarchis, D. Tasis, E. Vazquez, M. Prato, *Angew. Chem. Int. Ed.* **2003**, *42*, 4206; d) M. Melle-Franco, M. Marcaccio, D. Paolucci, F.

Paolucci, V. Georgakilas, D. M. Guldi, M. Prato, F. Zerbetto, *J. Am. Chem. Soc.* **2004**, *126*, 1646; e) N. Tagmatarchis, M. Prato. *J. Mater. Chem.* **2004**, *14*, 437.

[23] a) K. S. Coleman, S. R. Bailey, S. Fogden, M. L. H. Green, *J. Am. Chem. Soc.* **2003**, *125*, 8722; b) K. A. Worsley, K. R. Moonoosawmy, P. Kruse, *Nano Lett.* **2004**, *4*, 1541.

[24] a) J. L. Delgado, P. Cruz, F. Langa, A. Urbina, J. Casado, J. T. L. Navarrete, *Chem. Commun.* **2004**, 1734; b) M. Alvaro, P. Atienzar, P. de la Cruz, J. L. Delgado, H. Garcia, F. Langa, *J. Phys. Chem. B* **2004**, *108*, 12691; c) M. Alvaro, P. Atienzar, P. de la Cruz, J. L. Delgado, V. Troiani, H. Garcia, F. Langa, A. Palkar, L. Echegoyen, *J. Am. Chem. Soc.* **2006**, *128*, 6626.

[25] H. Hu, B. Zhao, M. A. Hamon, K. Kamaras, M. E. Itkis, R. C. Haddon, *J. Am. Chem. Soc.* **2003**, *125*, 14893.

[26] Similar esterification of acid-treated SWNTs with hydroxyporphyrins has already been reported. a) H.-P. Li, R. B. Martin, B. A. Harruff, R. A. Carino, L. F. Allard, Y.-P. Sun, *Adv. Mater.* **2004**, *16*, 896; b) D. Baskaran, J. W. Mays, X. P. Zhang, M. S. Bratcher, *J. Am. Chem. Soc.* **2005**, *127*, 6916.

[27] Arylation using *in situ* generated diazonium intermediates was applied to attach porphyrin units onto the sidewalls of SWNTs produced by arc-discharge method without any pretreatment. Z. Guo, F. Du, D. Ren, Y. Chen, J. Zheng, Z. Liu, J. Tian, *J. Mater. Chem.* **2006**, *16*, 3021.

[28] B. L. Hayes, *Microwave Synthesis: Chemistry at the Speed of Light*, CEM Publishing, North Carolina, 2002.

[29] a) Y. Wang, Z. Iqbal, S. Mitra, *Carbon* **2005**, *43*, 1015; b) K. Kubota, M. Sano, T. Masuko, *Jpn. J. Appl. Phys.* **2005**, *44*, 465; c) J. Li, H. Grennberg, *Chem.-Eur. J.* **2006**, *12*, 3869.

[30] a) J. J. Chen, S. V. Deshpande, *Tetrahedron Lett.* **2003**, *44*, 8873; b) C. E. Humphrey, M. A. M. Easson, J. P. Tierney, N. J. Turner, *Org. Lett.* **2003**, *5*, 849.

[31] *Spectrometric Identification of Organic Compounds*, R. M. Silverstein, G. C. Bassler, T. C. Morrill, Eds., John Wiley & Sons, New York, 1991.

[32] The author could not obtain significant ^{1}H NMR signals of H_2P-NT-CONHH_2P for all the protons including aromatic ones due to the restricted mobility caused by the large molecular size and the inherent inhomogeneity of SWNTs, which are typical of ^{1}H NMR spectra for the covalent substituents on SWNTs.[19–24]

[33] M. S. Dresselhaus, G. Dresselhaus, R. Saito, A. Jorio, *Phys. Rep.* **2005**, *409*, 47.

[34] H. Kataura, Y. Kumazawa, Y. Maniwa, I. Umezu, S. Suzuki, Y. Ohtsuka, Y. Achiba, *Synth. Metals* **1999**, *103*, 2555.

[35] R. Saito, G. Dresselhaus, M. S. Dresselhaus, *Physical Properties of Carbon Nanotubes*,

Imperial College Press, London, 1998.

[36] R. B. Weisman, S. M. Bachilio, *Nano Lett.* **2003**, *3*, 1235.

[37] a) J. E. Riggs, Z. Guo, D. L. Carroll, Y.-P. Sun, *J. Am. Chem. Soc.* **2000**, *122*, 5879; b) Y.-P. Sun, B. Zhou, K. Henbest, K. Fu, W. Huang, Y. Lin, S. Taylor, D. L. Carroll, *Chem. Phys. Lett.* **2002**, *351*, 349; c) B. Zhou, Y. Lin, L. M. Veca, K. A. S. Fernando, B. A. Harruff, Y.-P. Sun, *J. Phys. Chem. B* **2006**, *110*, 3001.

[38] Murakoshi and co-workors[38a] reported the relational expression, $\Phi_s = 1.2 \times 10^{-2}\omega_{RBM} - 2.85$ (V *vs.* NHE), where Φ_s is work function of isolated s-SWNTs and ω_{RBM} is Raman shift in the RBM region of s-SWNTs. Using an equation, $d = 248/\omega_{RBM}$,[38b] where d represents the diameter of SWNTs, Φ_s can be determined. The author added 0.2 V to the value of Φ_s obtained by the Murakoshi's equation, according to the theoretical study by Zhao *et al.*,[38c] since the electrophoretically deposited SWNTs form bundle structures. Accordingly, the author can derive the following equation to estimate the CB and VB of the s-SWNTs used in this study: $\Phi_s = (2.98/d) - 2.65$ (V *vs.* NHE). a) K.-i. Okazaki, Y. Nakato, K. Murakoshi, *Phys. Rev. B* **2003**, *68*, 035434; b) A. Jorio, R. Saito, J. H. Hafner, C. M. Lieber, M. Hunter, T. McClure, G. Dresselhaus, M. S. Dresselhaus, *Phys. Rev. Lett.* **2001**, *86*, 1118; c) J. J. Zhao, J. Han, J. P. Lu, *Phys. Rev. B* **2002**, *65*, 193401.

[39] a) N. V. Tkachenko, L. Rantala, A. Y. Tauber, J. Helaja, P. H. Hynninen, H. Lemmetyinen, *J. Am. Chem. Soc.* **1999**, *121*, 9378; b) T. J. Kesti, N. V. Tkachenko, V. Vehmanen, H. Yamada, H. Imahori, S. Fukuzumi, H. Lemmetyinen, *J. Am. Chem. Soc.* **2002**, *124*, 8067; c) N. V. Tkachenko, H. Lemmetyinen, J. Sonoda, K. Ohkubo, T. Sato, H. Imahori, S. Fukuzumi, *J. Phys. Chem. A* **2003**, *107*, 8834.

[40] Nanocs, Inc. http://www.nanocs.com/nanotube.htm (accessed 03/06/07).

[41] H. Imahori, K. Hagiwara, M. Aoki, T. Akiyama, S. Taniguchi, T. Okada, M. Shirakawa, Y. Sakata, *J. Am. Chem. Soc.* **1996**, *118*, 11771.

Chapter 3

Photophysics and Photoelectrochemical Properties of Nanohybrids Consisting of Fullerene-Encapsulated Single-Walled Carbon Nanotubes and Poly(3-hexylthiophene)

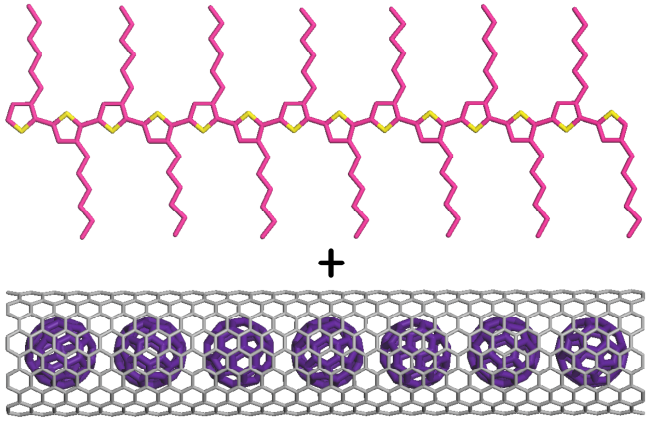

Abstract: Novel nanohybrids of single-walled carbon nanotubes (SWNTs) encapsulating C_{60} or C_{70} with poly(3-hexylthiophene) (P3HT) have been prepared and their photophysics and photoelectrochemical properties are studied in detail. Strong π-π interaction between the SWNT sidewalls and P3HT afforded successful dissolution of the so-called fullerene peapods into an organic solvent, as in the case of empty SWNTs (p-SWNT). Fluorescence emission of P3HT in the SWNT–P3HT hybrids was completely quenched by the SWNTs regardless of the fullerenes insertion. Transient absorption and fluorescence up-conversion technique revealed the excited state dynamics of the nanohybrids, where exciplex forms from the short-lived P3HT singlet excited state (~ 0.2 ps) with the fullerene peapods and subsequently relaxes to the ground state within ~ 1 ps. Significant difference in the photodynamics upon encapsulation of C_{60} or C_{70} was not detected, implying little participation of the fullerenes in the excited state event and thus the inability of the encapsulated fullerenes to generate the charge-separated state between the fullerene peapods and P3HT. Photoelectrochemical devices based on the peapod–P3HT nanohybrids showed almost the same incident photon-to-current efficiencies as those for the p-SWNT–P3HT-based device, which is in good agreement with the results of the time-resolved spectroscopies. Thus, the results obtained here will give a deep insight into the photophysics and photoelectrochemical properties of fullerene peapod–conjugated polymer as well as SWNT–conjugated polymer hybrids.

Introduction

Producing highly efficient organic photovoltaics (OPVs) is a desirable goal toward realization of the large-area, light-weight, and flexible solar cells at low cost. The state of the art in the field of OPVs is represented by bulk heterojunction (BHJ) solar cells based on electron-donating conjugated polymers and electron-accepting fullerene derivatives.[1] In particular, the BHJ solar cells consisting of poly(3-hexylthiophene) (P3HT) and [6,6]-phenyl-C_{61}-butyric acid methyl ester ([60]PCBM) have shown a power conversion efficiency (η) over 5%, which is among the highest values ever reported for polymer-based OPVs.[2] Although this system still has significant importance as a prototypical benchmark for comparison of the device performance or investigation of the basic operation mechanism, recent focus has turned to replacing the components by novel materials with excellent optical, electronic, and morphological properties in film state.[3] Specifically, given that the poorly built percolation network for charges in the BHJ structure and the resulting low charge mobilities are one of the major factors limiting the performance of OPVs,[4] exploring other photoactive materials which can yield more efficient network structure is essential for highly efficient OPVs.[3f]

Single-walled carbon nanotubes (SWNTs) are mechanically strong, high modulus graphitic fibers with a diameter of 1 – 2 nanometers and a length of a few micrometers.[5] Particularly, their high electron mobility and the large aspect ratio provide the potential to construct an ideal percolation pathway for electron transport in the deposited film.[5,6] In this context, the use of SWNTs instead of PCBM as well as the combination of SWNTs and PCBM is promising for improving the device performance.[7,8] Indeed, several authors have reported that the blend of SWNTs with P3HT or other conjugated polymers exhibited an increase in the photoresponse compared to the pristine polymer device.[8] However, the η values of the SWNT–polymer devices are typically below 1%, which seldom exceed the η values of current high-performance devices based on the [60]PCBM–P3HT system as well as [6,6]-phenyl-C_{71}-butyric acid methyl ester ([70]PCBM)–low bandgap conjugated polymer systems (η = 5 – 7%).[2,3] One plausible reason for the poor performance of the SWNT-based devices is the involvement of metallic SWNTs (m-SWNTs), which provide a nonradiative relaxation channel for photogenerated excitons and act as an efficient recombination pathway for charge carriers.[9,10] Thus, the isolation of semiconducting SWNTs (s-SWNTs) from a mixture of s-SWNTs and m-SWNTs may offer a fundamental approach toward harnessing the potential of SWNTs.[11] Another main reason is an insufficient electron-accepting ability of SWNTs compared to the fullerenes. In fact, some groups have suggested a lack of electron transfer (ET) between the photoexcited P3HT and SWNTs because of the exclusive occurrence of energy transfer,[12,13] whereas other groups have concluded that photoinduced ET from the hybridized donor polymers to SWNTs would take place on the basis of intense quenching of

the polymer fluorescence or the faster fluorescence decay, without observing the formation of charged species directly.[14] Therefore, the photophysics of the donor polymer–SWNT hybrids is still a controversial issue.[15]

One of the most unique characteristics of SWNTs is their capability to accommodate suitable-sized organic molecules like tetrathiafulvalene (TTF), tetracyanoquinodimethane (TCNQ), and fullerenes inside the hollow space.[16] Such an inner space doping of SWNTs affords a practical opportunity to alter the electronic properties of SWNTs, *i.e.*, bandgap energies[17,18] and carrier concentrations,[19] retaining their intrinsic 1-dimensional (1-D) structure without introducing defects or chemical bonds to the outer surface. This is crucial when hybridizing SWNTs with conjugated donor polymers through non-covalent π-π interactions between the SWNT sidewalls and the polymer backbone. With this regard, fullerene-encapsulated SWNTs, known as fullerene peapods, are an important class of the dopant-encapsulated SWNTs. Indeed, the encapsulation of various fullerenes into SWNTs has produced functionalized SWNTs with controlled doping states and their electronic characteristics have been investigated both experimentally and theoretically.[20–22]

Recently, Hatakeyama *et al.* reported the infrared photovoltaic solar cells based on the configuration of SWNT/Si heterojunction.[23] Importantly, C_{60} encapsulation into the SWNTs (denoted as C_{60}@SWNT) resulted in enhanced device performance under infrared light illumination (1550 nm), as compared to that obtained with empty SWNTs. According to their claim, such an enhancement can be ascribed to ground state charge transfer (CT) interaction between C_{60} and SWNTs, which would enhance the p-type character of SWNTs, causing higher build-in potential in the SWNT/Si junction. The higher build-in potential was directly reflected to the higher open circuit voltage (100 mV *vs.* 57 mV) in the C_{60}@SWNT-based device.[23]

On the other hand, the enhanced p-type character due to the CT interaction implies that the SWNT sidewalls become more electronically positive upon encapsulating C_{60}, which would promote the ET from excited donor polymers to the C_{60}@SWNT. Hence, the author envisaged that encapsulating fullerenes into SWNTs inner space would control the ET behavior of the SWNTs. Despite the successful introduction of fullerene peapods into the photovoltaic devices by Hatakeyama *et al.*,[23] nanohybrids comprised of peapods and donor polymers have not been prepared to examine the photophysics and photoelectrochemical properties of such hybrids.

In this study, the author has prepared novel nanohybrids comprised of C_{60}@SWNT or C_{70} encapsulated SWNTs (denoted as C_{70}@SWNT) with P3HT for the first time. In addition, their photophysics and photoelectrochemical properties have been investigated and compared systematically with the composite of P3HT and SWNTs without the encapsulation of fullerenes

(p-SWNT). Specifically, π-π interaction between SWNTs and P3HT was harnessed to dissolve the peapods in an organic solvent. Various experimental techniques including the transient absorption and fluorescence up-conversion measurements were employed to disclose the interaction between P3HT and the fullerene peapods in the excited state. Moreover, the direct interaction between SWNTs and the bound P3HT was addressed by eliminating any effect from unbound polymers, which gave an insight into the reported ET behavior of SWNT–P3HT systems. Finally, thin films of the peapod–P3HT hybrids were fabricated on transparent conductive electrodes to access their photoelectrochemical properties. To the best of the author's knowledge, this is the first study reporting the preparation, photodynamics, and photoelectrochemical properties of the hybrid material comprised of peapods and conjugated donor polymer.

Results and Discussion

Characterization of C_{60} and C_{70} Fullerene Peapods: Figure 1a shows a typical transmission electron microscopy (TEM) image of the synthesized C_{60}@SWNT (see Experimental Section). The image reveals that C_{60} molecules are closely packed inside the SWNT cage. Encapsulation of C_{60} inside the SWNTs is further confirmed by reduction of the (10) peak of SWNT bundles observed in X-ray diffraction (XRD) patterns, similar to the previous reports[24] (Figure 2b). Also, appearance of the Ag(2) mode of C_{60} at 1470 cm^{-1} in the resonance Raman spectrum is another evidence of the encapsulation[24] (Figure 3b). These results collaborate successful preparation of the C_{60} peapods. C_{70}@SWNT was also fully

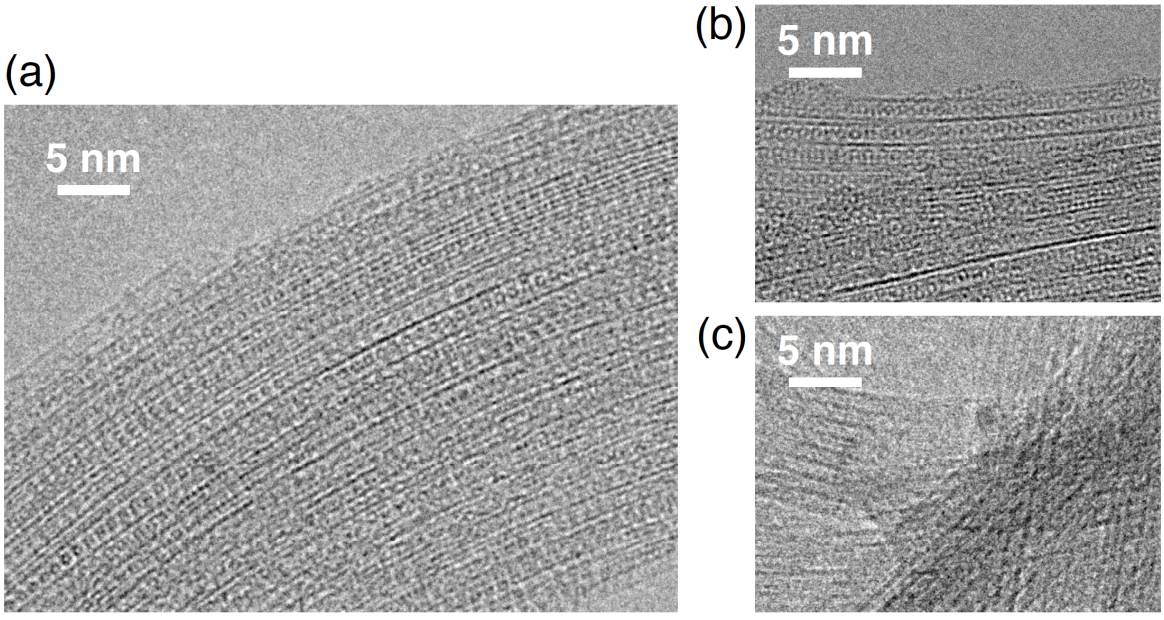

Figure 1. TEM images of (a) C_{60}@SWNT, (b) C_{70}@SWNT, and (c) p-SWNT.

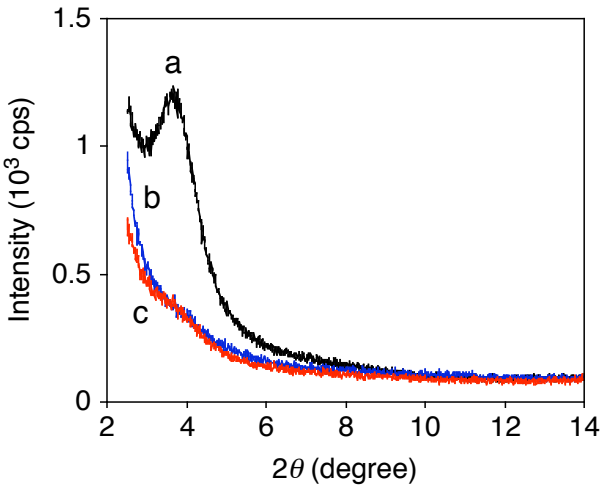

Figure 2. XRD patterns of (a) p-SWNT, (b) C_{60}@SWNT, and (c) C_{70}@SWNT.

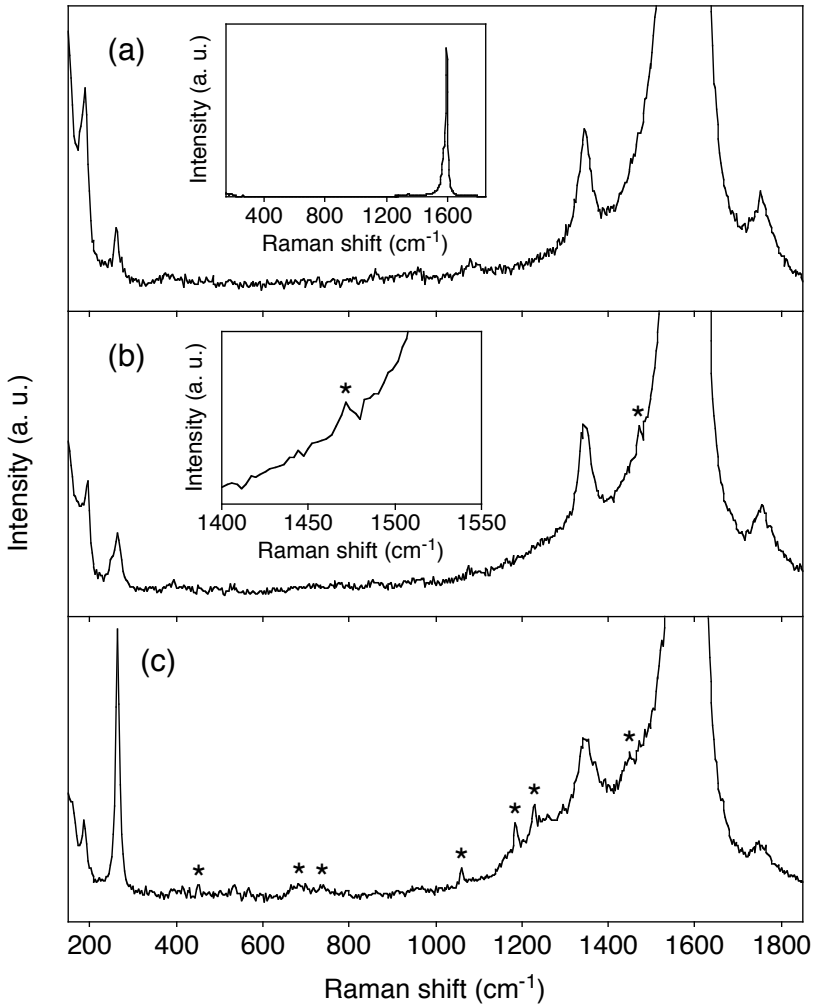

Figure 3. Resonance Raman spectra of (a) p-SWNT, (b) C_{60}@SWNT, and (c) C_{70}@SWNT measured with an excitation of 2.33 eV (531.95 nm). Inset in panel (a) shows contracted view of whole spectrum for p-SWNT, whereas that in (b) shows enlarged view of 1400 – 1550 cm^{-1} region for C_{60}@SWNT. Peaks marked with asterisk are assigned as signals from the encapsulated C_{60} (in (b)) or C_{70} (in (c)).

characterized by TEM, XRD, and Raman scattering measurements as in the case of C_{60}@SWNT (Figure 1b, 2c, and 3c). The filling yields of the fullerenes inside SWNTs are roughly estimated as > 80% for both cases from the TEM observations.

Characterization and Optical Properties of Peapod–P3HT Hybrids: Nanohybrids of P3HT with C_{60}@SWNT or C_{70}@SWNT were successfully prepared by sonicating the respective peapods with P3HT according to the procedure reported for p-SWNT–P3HT hybrids[14a] (see Experimental Section). The excess, unbound P3HT was removed by filtration and washing process to eliminate the effect of the unbound P3HT. The obtained blackish purple dispersions were quite stable and exhibited no discernible agglomeration for at least 1 month. Figure 4 depicts atomic force microscopy (AFM) images of the peapod–P3HT hybrids as well as p-SWNT–P3HT spin-coated on mica. Fibrous structures of SWNTs are clearly observed for the samples. Furthermore, even isolated SWNTs with a height of 1 – 2 nm are seen, implying efficient debundling of the SWNTs by P3HT regardless of the fullerene encapsulation. The height profiles display that the average diameters of the hybrids are virtually the same, *i.e.*, 4.0 nm for C_{60}@SWNT–P3HT, 4.2 nm for C_{70}@SWNT–P3HT, and 4.1 nm for p-SWNT–P3HT hybrids, respectively. Influence of the encapsulated fullerenes on the bundle sizes is not recognized distinctly.

Figure 5A shows UV–vis–near infrared (NIR) absorption spectra of the peapod–P3HT hybrids in chlorobenzene, together with those of p-SWNT–P3HT and pure P3HT solutions. Most distinctive feature in the spectra is the absorption peak corresponding to the HOMO–LUMO transition of P3HT, which is broadened and shifted from ~ 460 nm in the pure P3HT solution (Figure 5A(d)) to ~ 590 nm (Figure 5A(a) – (c)) upon hybridization with the SWNTs. On the other hand, absorption due to the peapods is discernible as featureless band extending to the NIR region with small bump around 1500 nm.[25] The observed broadening and red-shift of P3HT absorption band are analogous to previous SWNT–conjugated polymer hybrids without encapsulated fullerenes and thus can be attributed to the directly enhanced ordering of polymer chains on the SWNT sidewalls and/or SWNT-induced polymer/polymer ordering.[13c]

The important finding to note here is that the similar trend is observed for the peapod–P3HT (Figure 5A(a) and (b)) and p-SWNT–P3HT hybrids (Figure 5A(c)). This means that the degree of interaction between the SWNTs and P3HT would not be changed significantly by the encapsulation of C_{60} or C_{70}. On the other hand, a relative intensity of the P3HT absorption band, hence a relative amount of the bound P3HT in the hybrids, is slightly decreased for the C_{60}@SWNT–P3HT and C_{70}@SWNT–P3HT hybrids as compared to the p-SWNT–P3HT hybrid. Although the origin of this difference is unclear at present, the partial positive charge on the outer surface of the peapods due to the ground state charge transfer from

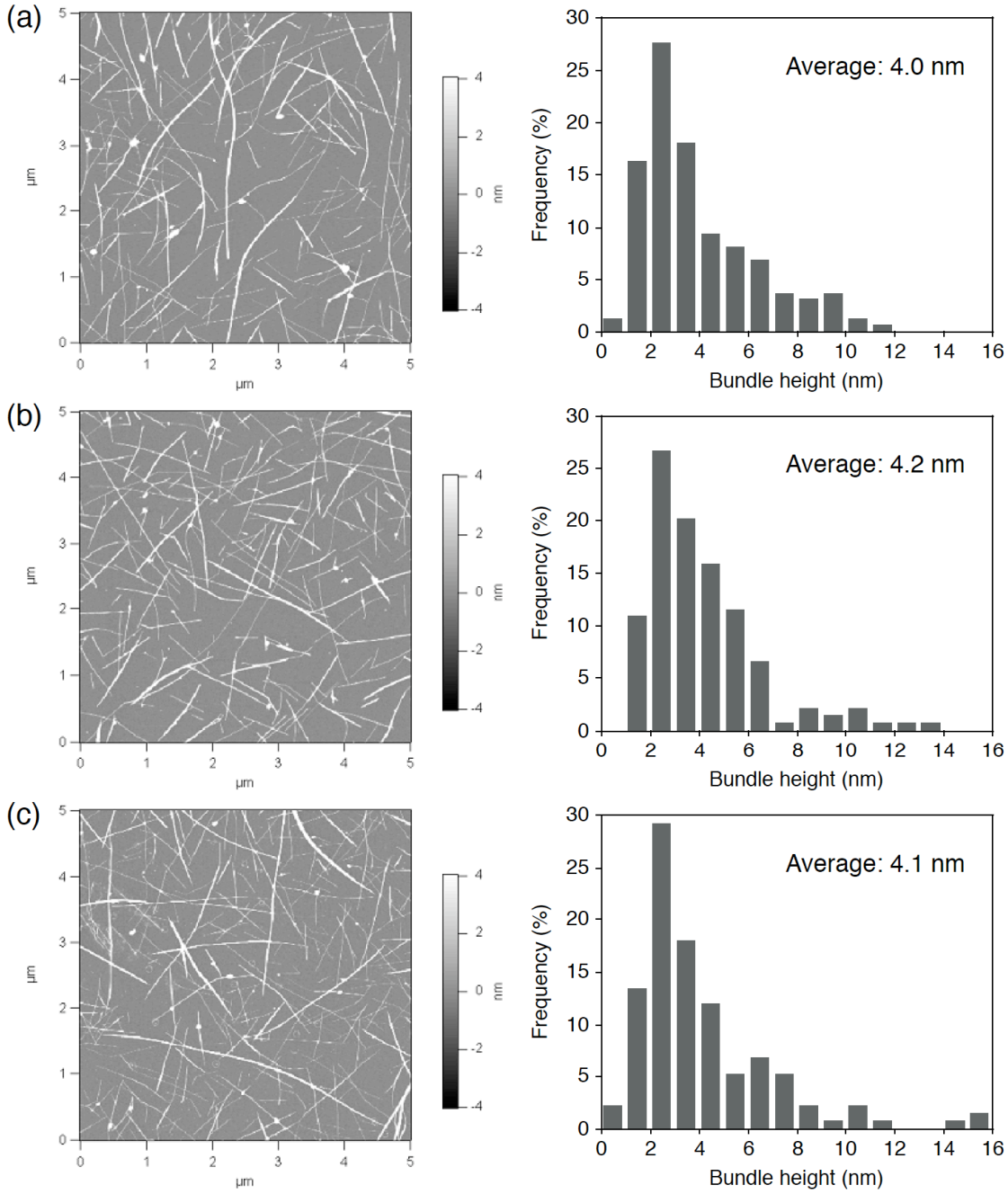

Figure 4. AFM images of (a) C_{60}@SWNT–P3HT, (b) C_{70}@SWNT–P3HT, and (c) p-SWNT–P3HT hybrids spin-coated on mica from respective dispersions in chlorobenzene. Corresponding diameter distributions for isolated bundles are shown in right panels.

SWNT to fullerenes may affect the binding energies for the complexation, leading to somewhat lower incorporation of P3HT into the hybrids.[26] Thermogravimetric analysis (TGA) on the p-SWNT–P3HT hybrid (Figure 5B) show that the hybrid contains P3HT of nearly 50 wt%. By comparing the integrated absorption cross-section of the P3HT absorption (430 – 710 nm) as a function of wavenumber, amounts of incorporated P3HT in the C_{60}@SWNT–P3HT and C_{70}@SWNT–P3HT hybrids are estimated as 71% and 61% of that in the p-SWNT–P3HT.

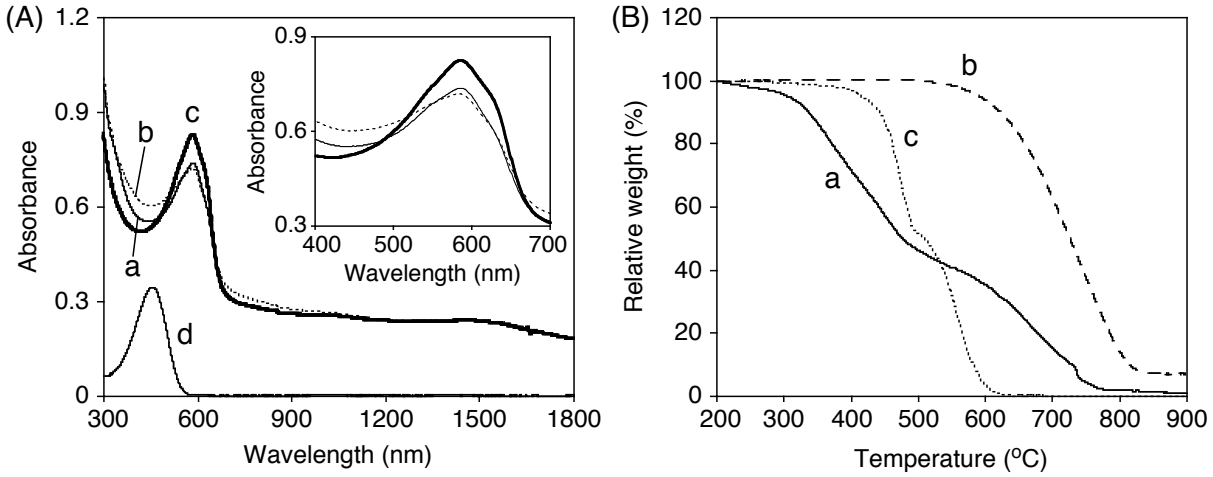

Figure 5. (A) UV–vis–NIR absorption spectra of (a) C_{60}@SWNT–P3HT, (b) C_{70}@SWNT– P3HT, (c) p-SWNT–P3HT, and (d) P3HT in chlorobenzene. Inset shows an enlarged view of visible region (400 – 700 nm) for comparison of P3HT-derived absorption of the SWNT– P3HT hybrids. (B) TGA curves of (a) p-SWNT–P3HT hybrid, (b) p-SWNT, and (c) P3HT obtained under a flowing air at a scan rate of 10 ^{o}C min^{-1}.

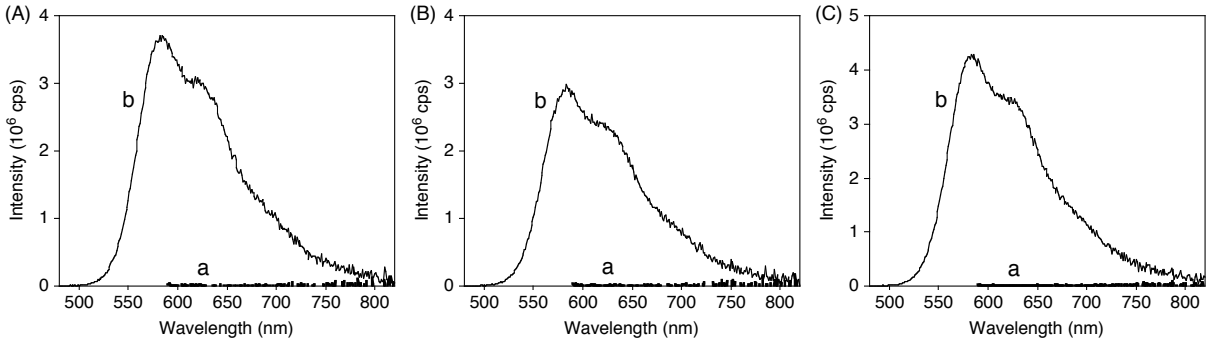

Figure 6. (A) Fluorescence emission spectra of (a) C_{60}@SWNT–P3HT and (b) P3HT. (B) Fluorescence emission spectra of (a) C_{70}@SWNT–P3HT and (b) P3HT. (C) Fluorescence emission spectra of (a) p-SWNT–P3HT and (b) P3HT. Excitation wavelength (λ_{ex}) was set at the peak position of P3HT-derived absorption, *i.e.*, 586 nm for the SWNT–P3HT hybrids and 457 nm for P3HT. Absorbances of the P3HT moieties of the SWNT–P3HT hybrids were adjusted to be identical (~ 0.1) to that of P3HT at the respective peak positions. Solvent: chlorobenzene.

Figure 6 compares the fluorescence emission spectra of pure P3HT (λ_{ex} = 457 nm) and the SWNT–P3HT hybrids (λ_{ex} = 586 nm) in chlorobenzene. Note that the fluorescence emission from P3HT is completely quenched upon association with the peapods as well as p-SWNT. Such quenching of P3HT emission is indicative of strong interaction between the excited states of P3HT and SWNTs, leading to the efficient relaxation of the P3HT excited singlet state other than radiative decay, as disclosed by the time-resolved study below. Complete quenching of the P3HT fluorescence in the C_{60}@SWNT–P3HT, C_{70}@SWNT–P3HT, and p-SWNT–P3HT

hybrids infers similar strength of interaction between the excited P3HT and the SWNTs irrespective of the fullerene encapsulation.

Excited State Dynamics of Peapod–P3HT Hybrids: Information on the ultrafast photodynamics of the p-SWNT–P3HT hybrid was provided by the pump-probe study in the subpicosecond time domain. Figure 7a displays transient absorption component spectra and corresponding decay kinetics at 580 and 700 nm (inset) for the p-SWNT–P3HT hybrid in chlorobenzene obtained with a laser excitation at 600 nm, where absorption of the P3HT moiety becomes nearly maximal. The two components (0.14 ps and 0.74 ps) are reasonably derived from the global analysis. The reconstructed time-resolved spectrum at 0 ps is roughly characterized by the ground state bleaching of P3HT absorption, thus confirming that the absorption majority of the photoexcited species arises from the P3HT moiety in the hybrid. The fast decaying component with a lifetime of 0.14 ps exhibits broad bleaching at 500 – 800 nm together with gradually increasing absorption with increasing wavelength at 900 – 1100 nm. This NIR absorption is close to that observed for the P3HT excited singlet state.[3c,27,28] Thus, the author assigned this component as the P3HT excited singlet state.

On the other hand, the slow decaying component with a lifetime of 0.74 ps has a negative peak at 590 nm, a positive peak at 690 nm, and a broad shoulder at 800 – 1000 nm. According to the previous studies on the excited state dynamics of regioregular P3HT in the film state, these positive signals could be attributed to the one-electron oxidized radical cation of P3HT, generated by ET from the P3HT excited singlet state to p-SWNT.[3c,27,28] However, given the extremely fast formation and relaxation behavior, it is rather dangerous to conclude that this component corresponds to the charge-separated state. Another insight into the slow decaying component arose from the fluorescent up-conversion measurement (Figure 7b). The sample solution containing the p-SWNT–P3HT hybrid was excited at 400 nm and the emission at 690 nm was monitored, on the assumption that fluorescence from the P3HT moiety in the hybrid resembles that from a pure P3HT film, emitting around 700 nm. The obtained decay trace disclosed an ultrafast component with a lifetime of 0.75 ps, which is in good agreement with that of the slow decaying component (0.74 ps) obtained by the transient absorption component spectra.[29] Hence, the slow decaying component in the transient absorption component spectra is emissive, ruling out the possibility of formation of the charge-separated state. Instead, an emissive exciplex state is likely to be formed as the transient species. In fact, exciplex formation in the excited donor–acceptor systems interacting in very close proximity has been seen frequently.[30] For instance, Tkachenko and co-workers have demonstrated that porphyrin–fullerene linked dyads with a short spacer generate an exciplex state between the porphyrin and fullerene from their excited states.[30b] The exciplex state decays to the ground

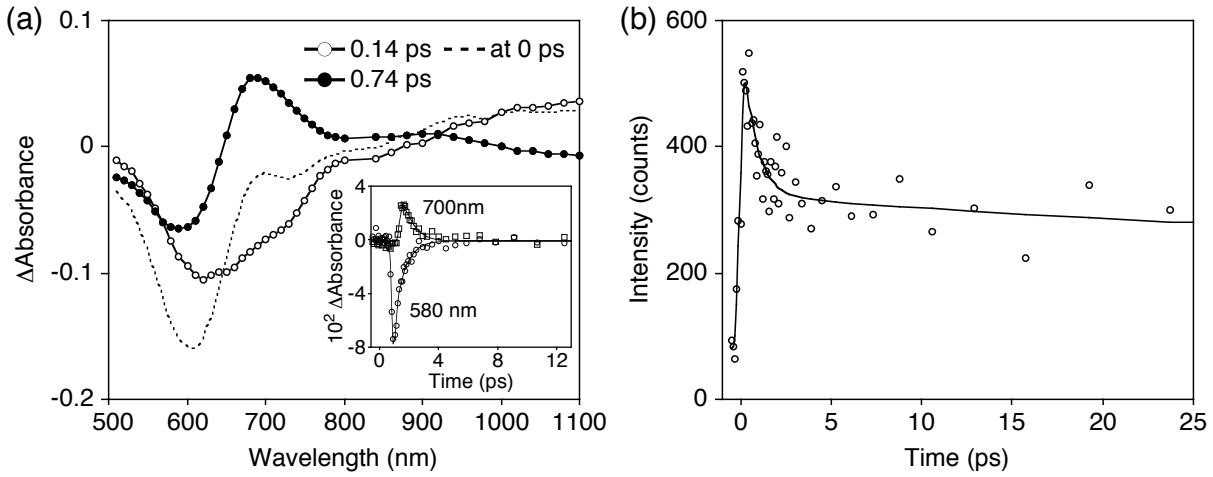

Figure 7. (a) Transient absorption decay component spectra of p-SWNT–P3HT in chlorobenzene obtained with global two-component fit of the data. The sample was excited at 600 nm. The fitted time constants are displayed in the figure. Dotted line shows recalculated time-resolved spectrum at 0 delay. Inset displays time traces of transient signals at 580 (circle) and 700 nm (square). Solid lines represent the results of bi-exponential fitting. (b) Fluorescence decay of p-SWNT–P3HT in chlorobenzene. The sample was excited at 400 nm and emission at 690 nm was monitored. Solid line shows the result of bi-exponential fit of the data, from which two time constants (0.75 ps (54%) and > 100 ps (46%)) are reasonably derived. The slow decay component (> 100 ps) probably originates from the emission of trace amount of unbound P3HT, which could not be detected by UV–vis absorption spectroscopy.

state or to the charge-separated state, depending on the nature of the spacer and the surrounding environment. Therefore, as in the cases of the porphyrin–fullerene systems, partial charge transfer would occur from the excited P3HT to p-SWNT to generate the exciplex, which rapidly decays to the ground state rather than to the complete charge-separated state because of the strong interaction between the P3HT and p-SWNT.[31]

The results obtained here are in stark contrast to several reports on the SWNT–P3HT hybrids where the occurrence of ET from the P3HT excited state to SWNTs is claimed.[14,15] In this regard, the author has to point out that in almost all of those reports, excess, unbound P3HT is not removed from the solutions or composite films, whereas in the present study excess P3HT is removed by filtration and washing procedure (*vide supra*). Accordingly, to the best of the author's knowledge, this is the first photophysical measurement to evaluate the interaction between SWNTs and bound conjugated polymers in the excited state. In contrast, interaction between SWNTs and P3HT by indirect contact would influence the excited state event, if the excess polymers were not removed. Therefore, the asserted ET behavior in the previous reports could originate from direct ET from the unbound, but weakly coupled P3HT to SWNTs. Another plausible explanation is that the involvement of the unbound, surrounding

P3HT may promote the conversion of exciplex, formed at the interfaces of SWNTs and attached P3HT, into charge-separated state.[1d,13b] Meanwhile, D'Souza *et al.* have recently revealed that the ET dynamics of noncovalently linked SWNT–donor hybrids considerably depends on the chirality of SWNTs.[32] Also, Nicholas *et al.* have pointed out the inability of SWNTs with a thick diameter of > 1 nm to form the staggered band alignment (type-II heterojunction) with conjugated donor polymers including P3HT, based on their elaborated spectroscopic studies on the SWNT–conjugated polymer hybrids dispersed in chloroform.[13b] The SWNTs used in this work possess an average diameter of *ca.* 1.4 nm, indicating the inability to form desirable type II heterojunction with bound P3HT. Absence of the type II heterojunction means that the photogenerated excitons cannot be dissociated efficiently at the interface between SWNTs and P3HT. Thus, these recent findings may rationalize the aforementioned results of the time-resolved measurements.

It is noteworthy that similar behavior of the time-resolved transient absorption spectra is noted for the C_{60}@SWNT–P3HT and C_{70}@SWNT–P3HT hybrids (Figure 8). Namely, one can see the fast decaying component with a lifetime of ~ 0.1 – 0.3 ps, assigned as the P3HT excited singlet state, and the slow decaying component with a lifetime of ~ 0.8 ps, assigned as the exciplex state. Note that the characteristic absorption due to C_{60} and C_{70} radical anion (1080 and 880 nm, respectively) is not detected.[33] These results suggest little participation of the encapsulated fullerenes in the excited state event and their inability to form the charge-separated state, contrary to the author's expectation. Rather, the results obtained here are

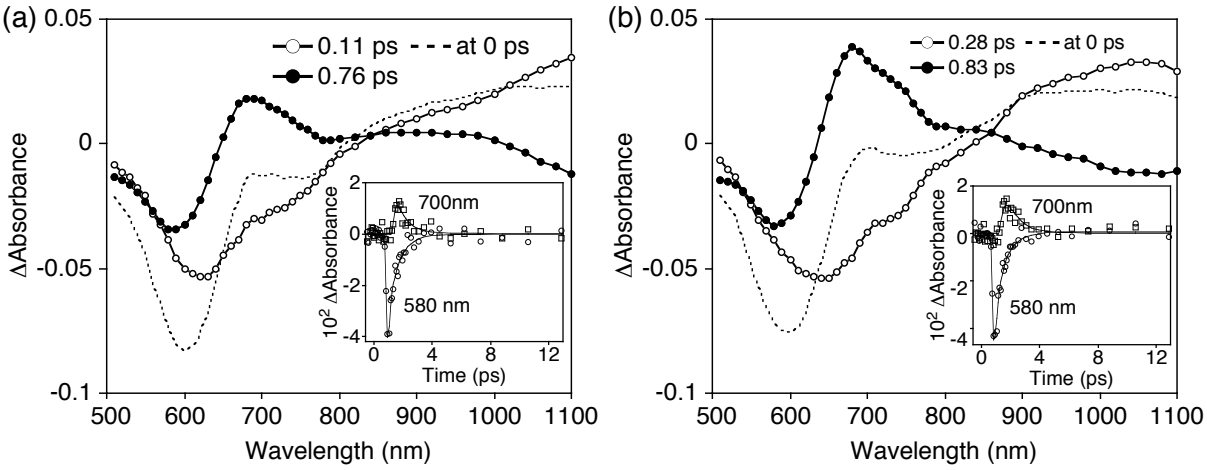

Figure 8. Transient absorption decay component spectra of (a) C_{60}@SWNT–P3HT and (b) C_{70}@SWNT–P3HT in chlorobenzene obtained with global two-component fit of the data. The samples were excited at 600 nm. The fitted time constants are displayed in the respective figures. Dotted lines show recalculated time-resolved spectra at 0 delay. Insets display time traces of transient signals at 580 (circle) and 700 nm (square). Solid lines represent the results of bi-exponential fitting.

consistent with those of the electrochemical studies by Kataura *et al.* on the C_{60} and C_{70} peapods, where no fullerene-related faradaic processes are detected and the electrochemical process is dominated by the capacitive double-layer charging of the outer wall.[34]

Thin-film Fabrication of Peapod–P3HT Hybrids: Thin films of C_{60}@SWNT–P3HT, C_{70}@SWNT–P3HT, and p-SWNT–P3HT hybrids were prepared on the indium tin oxide (ITO) electrodes using the filtration method (denoted as ITO/C_{60}@SWNT–P3HT, ITO/C_{70}@SWNT–P3HT, and ITO/p-SWNT–P3HT).[35] Figure 9A depicts a representative AFM image of the film surface of C_{60}@SWNT–P3HT hybrid, which reveals the entangled bundles of SWNTs lying horizontally on the ITO electrode. The thickness of the film was determined as ~ 250 nm by analyzing the AFM height profile of the edge part of the film. Films of C_{70}@SWNT–P3HT and p-SWNT–P3HT hybrids showed similar surface morphology and thickness.

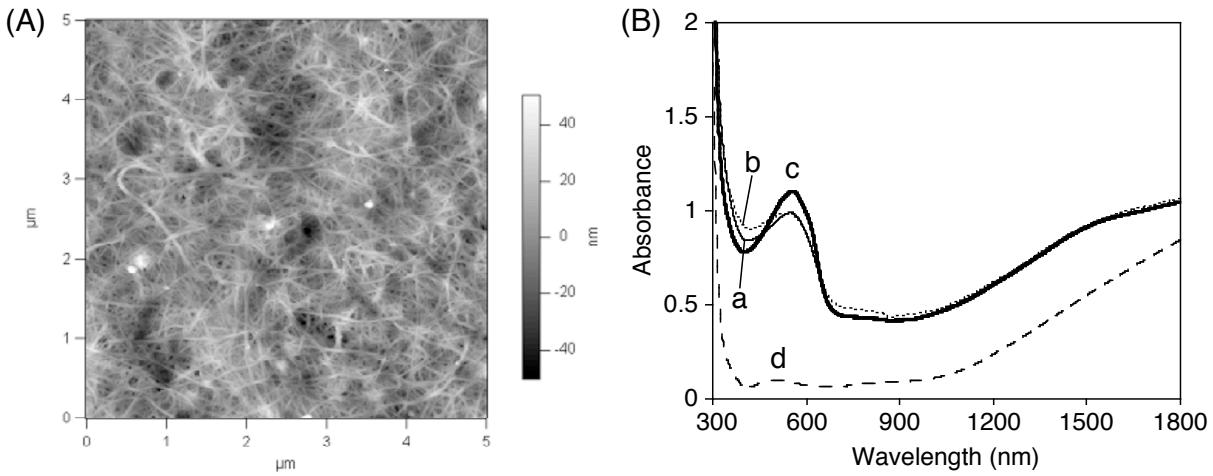

Figure 9. (A) AFM image of the ITO/C_{60}@SWNT–P3HT electrode. (B) UV–vis–NIR absorption spectra of (a) ITO/C_{60}@SWNT–P3HT, (b) ITO/C_{70}@SWNT–P3HT, (c) ITO/p-SWNT–P3HT, and (d) ITO electrodes.

The UV–vis–NIR absorption spectra of the modified ITO electrodes are illustrated in Figure 9B. In general, the absorption features of the thin films are largely similar to those in the corresponding chlorobenzene solutions (Figure 5A). Slight broadening of the P3HT absorption bands is discernible and is attributed to further interaction between P3HT and SWNTs and between the P3HT polymers in the film states. The broad absorption of the fabricated films in addition to the relatively high absorptivity in the visible to NIR region makes these films suitable for harvesting the solar energy. Additionally, the deposited films are sufficiently robust for the photoelectrochemical measurements (*vide infra*).

Photoelectrochemical Measurements: Photoelectrochemical measurements were performed in deaerated acetonitrile containing 0.5 M LiI and 0.01 M I_2 with the modified ITO electrodes as a working electrode, a platinum wire as a counter electrode, and an I^-/I_3^- reference electrode. Figure 10A displays representative photocurrent response of the ITO/C_{60}@SWNT–P3HT electrode illuminated with white light ($\lambda > 380$ nm) at an applied potential of 0 V *vs.* SCE. The repeated on-off cycles of illumination corroborate the immediacy, stability, and reproducibility of the photocurrent response of the electrode. A control experiment of the unmodified ITO electrode exhibited much smaller photocurrents under the same condition, confirming the role of the C_{60}@SWNT–P3HT film toward harvesting incident light and generating electron flow from the ITO electrode to the electrolyte solution through the C_{60}@SWNT–P3HT film during the operation of the photoelectrochemical devices.[36] Importantly, the ITO/C_{60}@SWNT–P3HT electrode did not show any degradation behavior during the measurements, indicating sufficient photostability of peapod–P3HT hybrids toward photoelectrochemical application. Applying a negative bias potential of –50 mV *vs.* SCE yields 1.3 times higher photocurrent (2.1 μA cm^{-2}) than that obtained without applying the bias potential (1.6 μA cm^{-2}), while photocurrent is decreased by a factor of 2.7 under a positive bias potential of 50 mV *vs.* SCE (0.6 μA cm^{-2}). Increased charge separation and the facilitated transport of charge carriers under negative bias potential are responsible for the enhanced photocurrent generation. Similar photoelectrochemical properties were obtained for the ITO/C_{70}@SWNT–P3HT and ITO/p-SWNT–P3HT devices.

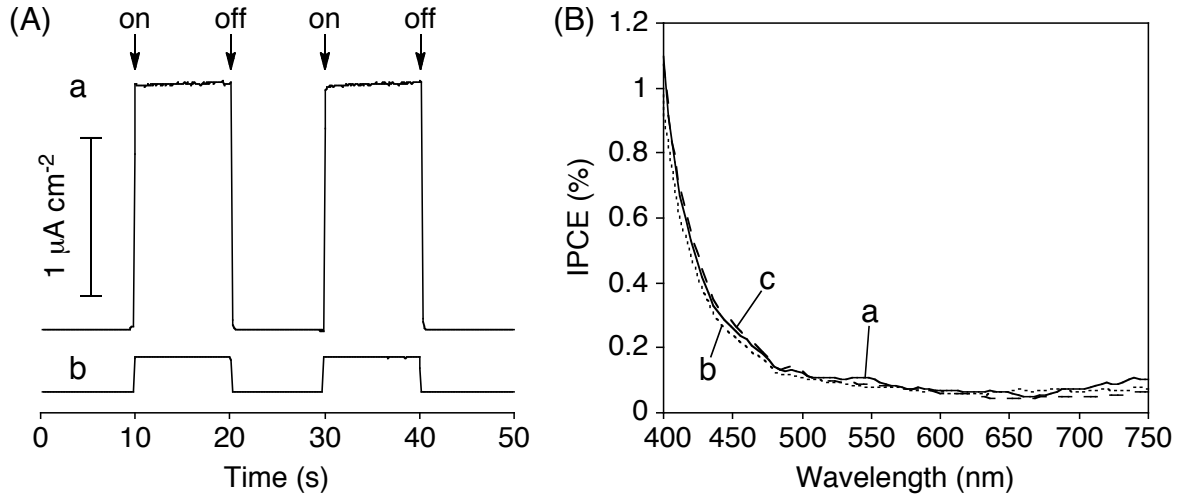

Figure 10. (A) Photocurrent response of (a) ITO/C_{60}@SWNT–P3HT and (b) ITO electrodes under an applied potential of 0 V *vs.* SCE. Illuminated with white light ($\lambda > 380$ nm, input power: 32 mW cm^{-2}). (B) Photocurrent action spectra of (a) ITO/C_{60}@SWNT–P3HT (solid line), (b) ITO/C_{70}@SWNT–P3HT (dotted line), and (c) ITO/p-SWNT–P3HT (dashed line) electrodes. Applied potential: –0.05 V *vs.* SCE. Electrolyte: 0.5 M LiI and 0.01 M I_2 in acetonitrile.

To gain further insights into the photoelectrochemical properties of the SWNT–P3HT hybrids, the author measured the wavelength dependent incident photon-to-current efficiency (IPCE) spectra. The IPCE values are calculated by normalizing the photocurrent densities for incident light energy and intensity and by use of the expression:

$$\text{IPCE (\%)} = 100 \times 1240 \times i/(W_{\text{in}} \times \lambda)$$

where i is the photocurrent density (A cm^{-2}), W_{in} is the incident light intensity (W cm^{-2}), and λ is the excitation wavelength (nm).

Figure 10B depicts the photocurrent action spectra of the ITO electrodes modified with the SWNT–P3HT hybrids. All the devices exhibit similar spectral features, where the IPCE value decreases with increasing the wavelength. Of particular interest to note here is that photocurrent response resulting from the absorption due to the P3HT moieties is totally absent in all cases. In other words, the absorption due to the P3HT moieties does not contribute to the photocurrent generation. This agrees well with the results of the time-resolved spectroscopies, where the photoexcited P3HT rapidly relaxes to yield the emissive partial CT state, *i.e.*, exciplex, and subsequently decays to the ground state (< 1 ps), without generating the charge-separated state. Therefore, the photocurrent generation is triggered by the direct excitation of s-SWNTs and subsequent hole transfer to the ITO electrode and electron transfer to the I^-/I_3^- couple in the electrolyte as proposed for analogous photoelectrochemical devices using the SWNT-modified semiconductor electrodes.[36] Note that the excitation of m-SWNTs leads to the rapid relaxation from the excited state without generating the photocurrent.[9] In fact, the shapes of the action spectra shown in Figure 10B parallel those of the absorption and action spectra obtained for the ITO/C_{60}@SWNT, ITO/C_{70}@SWNT, and ITO/p-SWNT electrodes, which are fabricated from respective sodium dodecylbenzenesulfonate (SDBS) dispersions in D_2O with similar procedure (Figure 11). These results corroborate that the photoexcitation of s-SWNTs is responsible for the photocurrent generation.

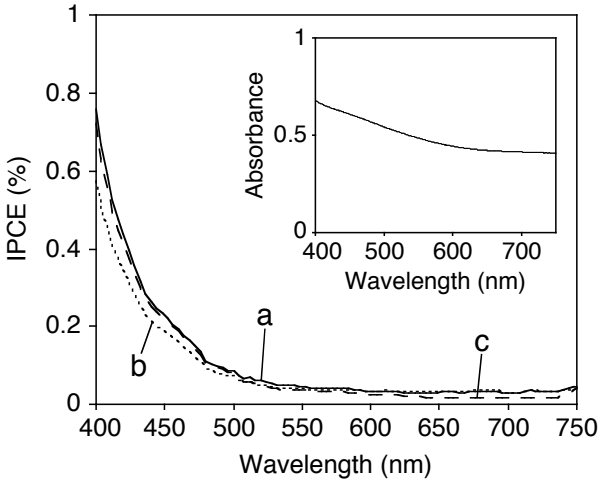

Figure 11. Photocurrent action spectra of (a) ITO/C_{60}@SWNT (solid line), (b) ITO/C_{70}@SWNT (dotted line), and (c) ITO/p-SWNT (dashed line) electrodes. Applied potential: –0.05 V *vs.* SCE. Electrolyte: 0.5 M LiI and 0.01 M I_2 in acetonitrile. Inset shows absorption spectrum of ITO/C_{60}@SWNT electrode.

It is interesting to mention the similarity between the present results with those obtained for the covalently linked SWNT–porphyrin hybrids.[37] Namely, when deposited on semiconductor electrodes, the hybrids did not show photocurrent response corresponding to the absorption of the porphyrin moieties, despite the considerable quenching of the fluorescence emission from the porphyrin moieties. The author has concluded that the exciplex formation between porphyrin singlet excited state and SWNTs and the subsequent decay to the ground state is most probable reason for the absence of porphyrin-related photocurrent generation, as in the present case. Thus, these two works concertedly offer an implication that SWNTs do not act as an excellent electron acceptor, supporting the claim from several groups.[12,13]

Maximum IPCE values obtained at 400 nm are 1.1%, 1.0%, and 1.1% for the ITO/C_{60}@SWNT–P3HT, ITO/C_{70}@SWNT–P3HT, and ITO/p-SWNT–P3HT devices (Figure 10B). Rather low IPCE values (~ 1%) may be at least partially ascribed to the presence of unseparated m-SWNTs, which promote nonradiative relaxation of the photogenerated excitons in s-SWNTs and offer an efficient recombination site for the separated charge carriers at the SWNT–ITO and/or SWNT–electrolyte solution interfaces.[9,10] On the other hand, almost the same IPCE values for the three systems show that the encapsulation of fullerene molecules does not improve the photocurrent generation. This matches the fact that the encapsulated C_{60} and C_{70} do not alter the excited state dynamics of the SWNT–P3HT hybrids, where fast exciplex formation between the SWNT shell and P3HT and subsequent rapid relaxation to the ground state are dominant (Figure 7 and 8). Also, the encapsulated fullerenes are not likely to exert significant impact on the electronic states of SWNTs so that they do not affect the photoelectrochemical properties significantly. This is in remarkable contrast to the recent Hatakeyama's report where encapsulating C_{60} into SWNTs leads to the improved photovoltaic performance of the SWNTs/Si heterojunction cells through adjusting the Fermi level of SWNTs.[23] Difference in the interaction between the encapsulated fullerene molecules and DIPS[38] SWNTs employed here or their SWNTs prepared with arc-discharge method would account for the contrasting results. Additionally, the difference may result from the excitation source (400 – 750 nm *vs.* 1550 nm) and the device configurations (three-electrode wet cell *vs.* two-electrode dry cell).

Conclusion

Novel nanocarbon hybrids of C_{60}- and C_{70}-peapods with P3HT have been prepared and their excited state dynamics and photoelectrochemical properties have been studied for the first time. The AFM observation disclosed successful dissolution of the fullerene peapods into an organic solvent by π-π interaction with P3HT, as in the case of p-SWNT. The steady state

fluorescence emission measurements showed the complete quenching of the P3HT fluorescence by incorporating SWNTs, regardless of the fullerene encapsulation. The transient absorption and fluorescence up-conversion technique revealed the excited state dynamics of the hybrids, where the short-lived P3HT singlet excited state (~ 0.2 ps) relaxes to yield the exciplex state with the SWNTs and then rapidly decays to the ground state (< 1 ps). Significant difference in the photodynamics upon the encapsulation of C_{60} or C_{70} was not detected, implying that the electronic structures of the SWNTs are retained irrespective of the encapsulation of C_{60} or C_{70} inside the SWNTs. The photoelectrochemical devices consisting of the peapod–P3HT hybrids exhibited almost the same IPCE values as those for the p-SWNT–P3HT-based device, which is consistent with the results of the time-resolved spectroscopic measurements. Thus, the results obtained here corroborate that the encapsulation of C_{60} or C_{70} has no significant impact on the photodynamics and the photoelectrochemical properties of the intrinsic SWNTs. Such a fundamental information on the fullerene peapod–conjugated polymer hybrids may be important to develop photoactive molecular devices in which the encapsulated molecules can be used for other functions (*i.e.*, charge transport) without affecting the intrinsic properties of the carbon nanotubes.

Experimental Section

General Procedure: UV–vis–NIR absorption spectra of solutions and films were measured with a Perkin-Elmer Lambda 900 UV/vis/NIR spectrometer. Steady-state fluorescence spectra were recorded on a HORIBA SPEX Fluoromax-3 spectrofluorometer. Resonance Raman spectra were measured using a Horiba JobinYvon LabRAM HR-800 equipped with 2.33 eV (531.95 nm) laser. XRD analyses were conducted by a Rigaku A2 diffractometer using Cu K_a radiation. TEM images were obtained from a JEOL JEM-2200FS. For sample preparation, SWNT dispersions in ethanol were dropped on microgrids (Cu mesh) and dried under vacuum. AFM analyses were carried out with an Asylum Technology MFP-3D-SA in the AC mode. SWNT dispersions were spin-coated on freshly cleaved mica at 1400 rpm. TGA measurements were conducted on a SHIMADZU DTG-60H under a flowing air at a scan rate of 10 ^{o}C min^{-1}.

Materials: SWNT soot produced by the direct-injection-pyrolytic-synthesis (DIPS)[38] method was supplied by NIKKISO CO., LTD. As-received soot was refluxed in 15% H_2O_2 *aq.*, stirred in *conc.* HCl *aq.*, and oxidized in air at 450 ^{o}C, affording purified, open-ended SWNTs (p-SWNT). Diameter range of p-SWNT was estimated as 1.3 – 1.6 nm from TEM observation. C_{60} (99.98%) and C_{70} (99.5%) were obtained from MTR Ltd. and used as-received. Encapsulation of fullerenes into p-SWNT was conducted through gas-phase reaction.[24]

Namely, p-SWNT (3 mg) and either C_{60} or C_{70} (15 mg) were sealed in a Pyrex tube under vacuum at 1.5×10^{-5} Torr and heated to 530 °C for 72 h. The raw materials were washed with toluene and CS_2 to remove excess fullerenes, giving C_{60}@SWNT and C_{70}@SWNT. P3HT was purchased from Sigma-Aldrich with publicized regioregularity (RR) of 98%, number-average molecular weight (M_n) of 41000, and polydispersity index (PDI) of 1.5. All other solvents and chemicals were of reagent-grade quality, purchased commercially, and used without further purification.

Preparation of SWNT–P3HT Hybrids: SWNTs (0.3 mg) and P3HT (3 mg) in chlorobenzene (10 mL) were sonicated using a tip-type sonicator (Astrason, XL2020; 140 W) for 10 min with continuous cooling by water flowing. The resultant dispersions were filtered through a 0.1 μm PTFE filter and washed with a copious amount of chlorobenzene to remove excess, unbound P3HT. Removal of unbound P3HT was confirmed by UV–vis absorption spectra of the final filtrate, showing negligible absorption due to P3HT. The resulting SWNT–P3HT hybrids without excess P3HT on the filter were redispersed in 10 mL of chlorobenzene with the aid of tip-sonication (140 W, 10 min). Finally, the prepared dispersions were diluted with chlorobenzene to exhibit absorbance of 0.24 at 1500 nm and stored for further analyses.

Thin Film Fabrication of SWNT–P3HT Hybrids: A thin film of the SWNT–P3HT hybrids on an ITO electrode (GEOMATEC, R_s = 7 ~ 10 W/□) was prepared by the filtration method[35] with slight modification. In short, 1 mL of the SWNT–P3HT dispersion in chlorobenzene was filtered with 0.1 μm polyvinylidene difluoride filter (ϕ = 25 mm). The remaining SWNT–P3HT film on the filter was first cut to suitable size (typically 7 × 14 mm) together with the attached filter paper and then put and clamped for a while on the ITO electrode, which was washed by sonication in 2-propanol and cleaned in an O_3 atmosphere in advance. Finally, the filter was removed by drying the whole assembly with hair drier, leaving the dark purple film of SWNT–P3HT hybrids on ITO.

Thin Film Fabrication from SWNT Dispersions in D_2O: SWNTs (0.3 mg) and SDBS (10 mg) in D_2O (10 mL) were sonicated using a tip-type sonicator (Astrason, XL2020; 140 W) for 10 min with continuous cooling by water flowing. A thin film of the SWNTs on an ITO electrode (GEOMATEC, R_s = 7 ~ 10 W/□) was prepared by the filtration method.[35] In short, 1 mL of the SWNT dispersion in D_2O was filtered with 0.05 μm mixed cellulose ester (MCE) filter (ϕ = 25 mm). The remaining SWNT film was washed with a copious amount of deionized water to remove SDBS. Then, the film on the filter was first cut to suitable size (typically 7 × 14 mm) together with the attached filter paper and then put and clamped for a while on the ITO electrode, which was washed by sonication in 2-propanol and cleaned in an O_3 atmosphere in advance. Finally, the filter was dissolved by immersing the whole assembly

in acetone bath for 1 day, affording the blackish, semi-transparent film of SWNTs on ITO. AFM observation revealed a film thickness of *ca.* 200 nm.

Time-resolved Spectroscopy: Sub-picosecond to nanosecond time-resolved absorption spectra were collected using a pump-probe technique as described elsewhere.[30a] The femtosecond pulses of the Ti:sapphire generator (CDP Corp., TiF-50) were amplified by using a multipass amplifier (CDP Corp.) pumped by a second harmonic of the Nd:YAG Q-switched laser (SOLAR TII, LF-114). The amplified pulses were used to generate an excitation pulse (600 nm) through an optical parametric amplifier (CDP Corp., CDP2017) for sample excitation (pump beam) and a white continuum for time-resolved spectrum detection (probe beam). An average of 100 pulses at 10 Hz repetition rate was used to improve the signal-to-noise ratio. The transient spectra were recorded by a charge-coupled device (CCD) detector (Andor Technology, Newton) coupled with a monochromator in the visible and near-infrared ranges. The wavelength range for a single measurement was 296 nm and typically two regions were studied, *i.e.*, 506 – 802 and 810 – 1106 nm. The typical response time of the instrument was 150 fs (full width at half-maximum (FWHM)). A global multi-exponential fitting procedure was applied to process the data. The procedure takes into account the instrument time response function and the group velocity dispersion of the white continuum, and allows one to calculate the decay time constants and dispersion-compensated transient absorption spectra. An up-conversion method for fluorescence was employed to detect the ultrafast dynamics of emissive intermediates with a time resolution of *ca.* 200 fs.[30a] The second harmonic (400 nm) of Ti:sapphire laser was used as excitation source and the emission at 690 nm was monitored. The fluence of excitation beam was taken to below 1 mJ cm^{-2} for both pump-probe and up-conversion studies. The SWNT–P3HT hybrids remained intact under the employed conditions, which was confirmed by the negligible change in UV–vis–NIR absorption spectra before and after the measurements. All measurements were carried out using a rotating cuvette with 1 mm path at room temperature in air.

Photoelectrochemical Measurements: All photoelectrochemical measurements were carried out in a standard three-electrode system using an ALS 630A electrochemical analyzer.[37] The fabricated film as a working electrode was immersed into an electrolyte solution containing 0.5 M LiI and 0.01 M I_2 in acetonitrile. A Pt wire covered with a glass Luggin capillary, whose tip was located near the working electrode, was used as a quasi-reference electrode. A Pt coil was employed as a counter electrode. The potential measured was converted to the saturated calomel electrode (SCE) scale by adding +0.05 V. The cathodic current direction with respect to the working electrode was set as positive polarity. A 500 W xenon lamp (USHIO, XB-50101AAA) was used as a light source. White light (λ > 380 nm, input power: 32 mW cm^{-2}) or monochromatic light through a monochromator (Ritsu, MC-

10N) was illuminated on the modified area of the working electrode (0.20 cm^2) from the backside. The light intensity was monitored by an optical power meter (Anritsu, ML9002A) and corrected for calculation of IPCE values.

References and Notes

[1] a) S. Günes, H. Neugebauer, N. S. Sariciftci, *Chem. Rev.* **2007**, *107*, 1324; b) B. C. Thompson, J. M. Fréchet, *Angew. Chem. Int. Ed.* **2008**, *47*, 58; c) J. L. Delgado, P.-A. Bouit, S. Filippone, M. Á. Herranz, N. Martín, *Chem. Commun.* **2010**, *46*, 4853; d) R. D. Pensack, J. B. Asbury, *J. Phys. Chem. Lett.* **2010**, *1*, 2255.

[2] a) W. Ma, C. Yang, X. Gong, K. Lee, A. J. Heeger, *Adv. Funct. Mater.* **2005**, *15*, 1617; b) G. Li, V. Shrotriya, J. Huang, Y. Yao, T. Moriarty, K. Emery, Y. Yang, *Nature Mater.* **2005**, *4*, 864; c) Y. Kim, S. Cook, S. M. Tuladhar, S. A. Choulis, J. Nelson, J. M. Durrant, D. D. C. Bradley, M. Giles, I. Mcculloch, C.-S. Ha, M. Ree, *Nature Mater.* **2006**, *5*, 197.

[3] a) J. Peet, J. Y. Kim, N. E. Coates, W. L. Ma, D. Moses, A. J. Heeger, G. C. Bazan, *Nature Mater.* **2007**, *6*, 497; b) C.-P. Chen, S.-H. Chan, T.-C. Chao, C. Ting, B.-T. Ko, *J. Am. Chem. Soc.* **2008**, *130*, 12828; c) R. B. Ross, C. M. Cardona, D. M. Guldi, S. G. Sankaranarayanan, M. O. Reese, N. Kopidakis, J. Peet, B. Walker, G. C. Bazan, E. V. Keuren, B. C. Holloway, M. Drees, *Nature Mater.* **2009**, *8*, 208; d) S. H. Park, A. Roy, S. Beaupre, S. Cho, N. Coates, J. S. Moon, D. Moses, M. Leclerc, K. Lee, A. J. Heeger, *Nat. Photonics* **2009**, *3*, 297; e) H.-Y. Chen, J. Hou, S. Zhang, Y. Liang, G. Yang, Y. Yang, L. Yu, Y. Wu, G. Li, *Nat. Photonics* **2009**, *3*, 649; f) T. Sagawa, S. Yoshikawa, H. Imahori, *J. Phys. Chem. Lett.* **2010**, *1*, 1020.

[4] a) H. Hoppe, N. S. Sariciftci, *J. Mater. Chem.* **2006**, *16*, 45; b) X. Yang, J. Loos, *Macromolecules* **2007**, *40*, 1353.

[5] a) M. S. Dresselhaus, G. Dresselhaus, P. C. Eklund, *Science of Fullerenes and Carbon Nanotubes*, Academic Press, San Diego, 1996; b) *Carbon Nanotubes and Related Structures*, D. M. Guldi, N. Martín, Eds., Wiley-VCH, Weinheim, 2010.

[6] a) P. Avouris, Z. H. Chen, V. Perebeinos, *Nature Nanotech.* **2007**, *2*, 605; b) P. Avouris, M. Freitag, V. Perebeinos, *Nat. Photonics* **2008**, *2*, 341.

[7] a) T. Umeyama, H. Imahori, *Energy Environ. Sci.* **2008**, *1*, 120; b) V. Sgobba, D. M. Guldi, *Chem. Soc. Rev.* **2009**, *38*, 165.

[8] a) E. Kymakis, G. A. J. Amaratunga, *Appl. Phys. Lett.* **2002**, *80*, 112; b) E. Kymakis, I. Alexandrou, G. A. J. Amaratunga, *J. Appl. Phys.* **2003**, *93*, 1764; c) S. Kazaoui, N. Minami, B. Nalini, Y. Kim, K. Hara, *J. Appl. Phys.* **2005**, *98*, 084314; d) E. Kymakis, E. Koudoumas, I. Franghiadakis, G. A. J. Amaratunga, *J. Phys. D: Appl. Phys.* **2006**, *39*,

1058; e) J. Geng, T. Zeng, *J. Am. Chem. Soc.* **2006**, *128*, 16827; f) S. Berson, R. de Bettignies, S. Bailly, S. Guillerez, B. Jousselme, *Adv. Funct. Mater.* **2007**, 17, 3363; g) A. T. Mallajosyula, S. S. K. Lyer, B. Mazhari, *Jpn. J. Appl. Phys.* **2009**, *48*, 011503; h) C.-K. Chang, J.-Y. Hwang, W.-J. Lai, C.-W. Chen, C.-I. Huang, K.-H. Chen, L.-C. Chen, *J. Phys. Chem. C* **2010**, *114*, 10932.

[9] Y. Kanai, J. C. Grossman, *Nano Lett.* **2008**, *8*, 908.

[10] L. Liu, W. E. Stanchina, G. Li, *Appl. Phys. Lett.* **2009**, *94*, 233309.

[11] M. C. Hersam, *Nature Nanotech.* **2008**, *3*, 387.

[12] a) M. S. Arnold, J. D. Zimmerman, C. K. Renshaw, X. Xu, R. R. Lunt, C. M. Austin, S. R. Forrest, *Nano. Lett.* **2009**. *9*. 3354; b) C. J. Collison, S. Pellizzeri, F. Ambrosio, *J. Phys. Chem. B* **2009**, *113*, 5809.

[13] a) A. Nish, J.-Y. Hwang, J. Doig, R. J. Nicholas, *Nanotechnology* **2008**, *19*, 095603; b) T. Schuettfort, A. Nish, R. J. Nicholas, *Nano Lett.* **2009**, *9*, 3871; c) T. Schuettfort, H. J. Snaith, A. Nish, R. J. Nicholas, *Nanotechnology* **2010**, *21*, 025201.

[14] a) J. Tsukamoto, J. Mata, *Jpn. J. Appl. Phys.* **2004**, *43*, L214; b) A. Ikeda, K. Nobusawa, T. Hamano, J.-i. Kikuchi, *Org. Lett.* **2006**, *8*, 24; c) J. Zou, L. Liu, H. Chen, S. I. Khondaker, R. D. McCullough, Q. Huo, L. Zhai, *Adv. Mater.* **2008**, *20*, 2055; d) S. Chu, W. Yi, S. Wang, F. Li, W. Feng, Q. Gong, *Chem. Phys. Lett.* **2008**, *451*, 116; e) J. Geng, B.-S. Kong, S. B. Yang, S. C. Youn, S. Park, T. Joo, H.-T. Jung, *Adv. Funct. Mater.* **2008**, *18*, 2659; f) E. Lioudakis, A. Othonos, I. Alexandrou, *Nanoscale Res. Lett.* **2008**, *3*, 278; g) I. Alexandrou, E. Lioudakis, D. Delaportas, C. Z. Zhao, A. Othonos, *Nanoscale Res. Lett.* **2009**, *4*, 635.

[15] A. J. Ferguson, J. L. Blackburn, J. M. Holt, N. Kopidakis, R. C. Tenent, T. M. Barnes, M. J. Heben, G. Rumbles, *J. Phys. Chem. Lett.* **2010**, *1*, 2406.

[16] a) M. Monthioux, *Carbon* **2002**, *40*, 1809; b) A. N. Khlobystov, D. A. Britz, G. A. D. Briggs, *Acc. Chem. Res.* **2005**, *38*, 901; c) R. Kitaura, H. Shinohara, *Jpn. J. Appl. Phys.* **2007**, *46*, 881.

[17] J. Lee, H. Kim, S.-J. Kahng, G. Kim, Y.-W. Son, J. Ihm, H. Kato, Z. W. Wang, T. Okazaki, H. Shinohara, Y. Kuk, *Nature* **2002**, *415*, 1005.

[18] T. Okazaki, S. Okubo, T. Nakanishi, S.-K. Joung, T. Saito, M. Otani, S. Okada, S. Bandow, S. Iijima, *J. Am. Chem. Soc.* **2008**, *130*, 4122.

[19] T. Takenobu, T. Takano, M. Shiraishi, Y. Murakami, M. Ata, H. Kataura, Y. Achiba, Y. Iwasa, *Nature Mater.* **2003**, *2*, 683.

[20] a) T. Shimada, T. Okazaki, R. Taniguchi, T. Sugai, H. Shinohara, K Suenaga, Y. Ohno, S. Mizuno, S. Kishimoto, T. Mizutani, *Appl. Phys. Lett.* **2002**, *81*, 4067; b) T. Shimada, Y. Ohno, T. Okazaki, T. Sugai, K. Suenaga, S. Kishimoto, T. Mizutani, T. Inoue, R.

Taniguchi, N. Fukui, H. Okubo, H. Shinohara, *Phys. E* **2004**, *21*, 1089.

[21] a) G. Pagona, G. Rotas, A. N. Khlobystov, T. W. Chamberlain, K. Porfyrakis, N. Tagmatarchis, *J. Am. Chem. Soc.* **2008**, *130*, 6062; b) Y. Iizumi, T. Okazaki, Z. Liu, K. Suenaga, T. Nakanishi, S. Iijima, G. Rotas, N. Tagmatarchis, *Chem. Commun.* **2010**, *46*, 1293.

[22] a) Y. F. Li, T. Kaneko, R. Hatakeyama, *Appl. Phys. Lett.* **2008**, *92*, 183115; b) Y. F. Li, T. Kaneko, R. Hatakeyama, *Nanotechnology* **2008**, *19*, 415201; c) Y. Li, T. Kaneko, J. Kong, R. Hatakeyama, *J. Am. Chem. Soc.* **2009**, *131*, 3412.

[23] R. Hatakeyama, Y. F. Li, T. Y. Kato, T. Kaneko, *Appl. Phys. Lett.* **2010**, *97*, 013104.

[24] a) H. Kataura, Y. Maniwa, T. Kodama, K. Kikuchi, K. Hirahara, K. Suenega, S. Iijima, S. Suzuki, Y. Achiba, W. Krätschmer, *Synth. Metals* **2001**, *121*, 1195; b) H. Kataura, Y. Maniwa, M. Abe, A. Fujiwara, T. Kodama, K. Kikuchi, H. Imahori, Y. Misaki, S. Suzuki, Y. Achiba, *Appl. Phys. A* **2002**, *74*, 349.

[25] This bump can be assigned as the first van Hove transitions in s-SWNTs (E^{S}_{11}) with diameter of *ca.* 1.3 nm. In present study, peaks arising from transitions between the second van Hove transitions in s-SWNTs (E^{S}_{22}) and the first van Hove transitions in m-SWNTs (E^{M}_{11}) are hardly resolved, probably due to incomplete isolation of SWNT bundles. R. B. Weisman, S. M. Bachilo, *Nano. Lett.* **2003**, *3*, 1235.

[26] Difference in the amounts of P3HT in the SWNT–P3HT hybrids is not likely to affect the degree of the debundling of SWNTs, judging from the results of AFM observations.

[27] a) O. J. Korovyanko, R. Österbacka, X. M. Jiang, Z. V. Vardeny, R. A. J. Janssen, *Phys. Rev. B* **2001**, *64*, 235122; b) X. M. Jiang, R. Österbacka, O. Korovyanko, C. P. An, B. Horovitz, R. A. J. Janssen, Z. V. Vardeny, *Adv. Funct. Mater.* **2002**, *12*, 587; c) J. Piris, T. E. Dykstra, A. A. Bakulin, P. H. M. van Loosdrecht, W. Knulst, M. T. Trinh, J. M. Schins, L. D. A. Siebbeles, *J. Phys. Chem. C* **2009**, *113*, 14500.

[28] a) H. Ohkita, S. Cook, Y. Astuti, W. Duffy, S. Tierney, W. Zhang, M. Heeney, I. McCulloch, J. Nelson, D. D. C. Bradley, J. R. Durrant, *J. Am. Chem. Soc.* **2008**, *130*, 3030; b) S. Cook, A. Furube, R. Katoh, *Energy Environ. Sci.* **2008**, *1*, 294; c) S. Cook, R. Katoh, A. Furube, *J. Phys. Chem. C* **2009**, *113*, 2547; d) J. Guo, H. Ohkita, H. Benten, S. Ito, *J. Am. Chem. Soc.* **2009**, *131*, 16869.

[29] Decay of P3HT fluorescence seems to be beyond the time resolution (~ 0.2 ps).

[30] a) N. V. Tkachenko, L. Rantala, A. Y. Tauber, J. Helaja, P. H. Hynninen, H. Lemmetyinen, *J. Am. Chem. Soc.* **1999**, *121*, 9378. b) N. V. Tkachenko, H. Lemmetyinen, J. Sonoda, K. Ohkubo, T. Sato, H. Imahori, S. Fukuzumi, *J. Phys. Chem. A* **2003**, *107*, 8834.

[31] Energy transfer (EN) from the P3HT singlet state to SWNTs is also a plausible quenching

mechanism, as reported by several groups.[13,15] However, the author could not obtain any evidence of EN in the present system.

[32] a) E. Maligaspe, A. S. D. Sandanayaka, T. Hasobe, O. Ito, F. D'Souza, *J. Am. Chem. Soc.* **2010**, *132*, 8158; b) F. D'Souza, A. S. D. Sandanayaka, O. Ito, *J. Phys. Chem. Lett.* **2010**, *1*, 2586.

[33] a) D. M. Guldi, H. Hungerbühler, E. Janata, K.-D. Asmus, *J. Phys. Chem.* **1993**, *97*, 11258; b) D. M. Guldi, H. Hungerbühler, M. Wilhelm, K.-D. Asmus, *J. Chem. Soc., Faraday Trans.* **1994**, *90*, 1391.

[34] a) L. Kavan, L. Dunsch, H. Kataura, *Chem. Phys. Lett.* **2002**, *361*, 79; b) L. Kavan, L. Dunsch, H. Kataura, A. Oshiyama, M. Otani, S. Okada, *J. Phys. Chem. B* **2003**, *107*, 7666.

[35] Z. Wu, Z. Chen, X. Du, J. M. Logan, J. Sippel, M. Nikolou, K. Kamaras, J. R. Reynolds, D. B. Tanner, A. F. Hebard, A. G. Rinzler, *Science* **2004**, *305*, 1273.

[36] S. Barazzouk, S. Hotchandani, K. Vinodgopal, P. V. Kamat, *J. Phys. Chem. B* **2004**, *108*, 17015.

[37] T. Umeyama, M. Fujita, N. Tezuka, N. Kadota, Y. Matano, K. Yoshida, S. Isoda, H. Imahori, *J. Phys. Chem. C* **2007**, *111*, 11484.

[38] a) H. Ago, S. Ohshima, K. Uchida, M. Yumura, *J. Phys. Chem. B* **2001**, *105*, 10453; b) T. Saito, S. Ohshima, W.-C. Xu, H. Ago, M. Yumura, S. Iijima, *J. Phys. Chem. B* **2005**, *109*, 10647; c) T. Saito, W.-C. Xu, S. Ohshima, H. Ago, M. Yumura, S. Iijima, *J. Phys. Chem. B* **2006**, *110*, 5849.

Chapter 4

Good Solvent Effects of C_{70} Cluster Formations and Their Electron-Transporting and Photoelectrochemical Properties

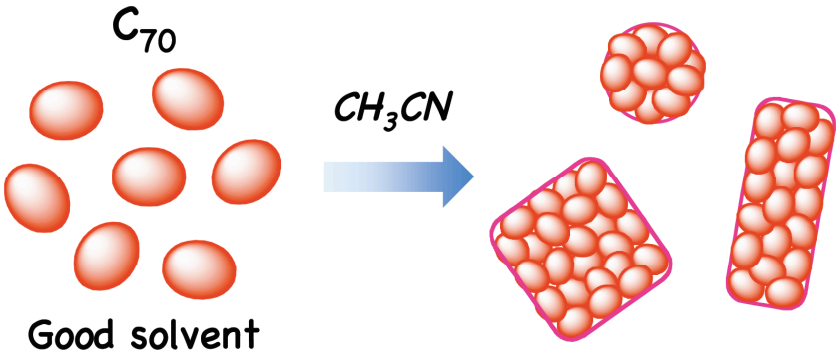

Abstract: Good solvent effects of C_{70} cluster formations and their electron-transporting and photoelectrochemical properties have been systematically examined. Nano-to-micrometer scale assemblies of C_{70} with different morphologies were prepared by rapidly injecting poor solvent (*i.e.*, acetonitrile) into a solution of C_{70} dissolved in various good solvents (*i.e.*, benzene, toluene, chlorobenzene, *etc.*). The cluster morphology engineering was successfully achieved by changing the good solvent, yielding the spherical, rod-like, or plate-like clusters in the mixed solvents. The clusters of C_{70} were electrophoretically deposited onto a nanostructured SnO_2 electrode to examine the photoelectrochemical properties under the white light or monochromatic light illumination. The maximum incident photon-to-current efficiency (IPCE) varied from 0.8% to 10% depending on the combinations of the poor–good solvents. The differences in the IPCE values are discussed in terms of the surface area, thickness, and electron mobility of the deposited cluster films. The electron mobility is found to be the most predominant factor for the IPCE, indicating the importance of the electron-transporting process in the overall photocurrent generation. In addition, the electron mobility is closely correlated with the underlying molecular alignment and the resultant cluster structure. Thus, these results will provide basic clue for the design of C_{70}-based molecular devices including the organic photovoltaics.

Introduction

Self-assembled molecular architectures have attracted considerable attention due to their promising application toward bottom-up approaches to nanotechnology.[1] In particular, shape-defined assemblies with nano-to-micrometer dimensions can be potentially harnessed as building blocks of next-generation optoelectronic devices.[1,2] One of the key components to construct such molecular nanostructures is fullerenes and their derivatives. So far, the preparation of fullerene-based assemblies like nanorod,[3,4] nanofiber (or nanowhisker),[5,6] nanotube,[7] nanosheet,[8] nanoflower,[9] nanoparticle,[10] and others[11] have been reported, all of which deserve special interests from a perspective of material research because of their unique morphologies. On the other hand, those nanostructures of fullerenes provoke another interest relating to the state-of-the-art bulk heterojunction (BHJ) solar cells, where the morphological control of fullerene nanodomains in the blend film with conjugated polymers is essential to achieve high cell performance.[12,13] Indeed, elucidation of the photoelectrochemical properties of fullerene-based nanostructures would offer fundamental information toward designing highly efficient BHJ devices. However, there are limited number of studies focusing on the photoelectrochemical properties of nanostructured fullerene assemblies.[11d,14,15] As such, systematic comparison of the photoelectrochemical properties of fullerene-based assemblies and/or their composite films with different nano-to-micrometer scale morphologies has yet to be conducted.

One of the most frequently employed approaches to prepare fullerene assemblies is rapid injection technique first demonstrated by Sun and Bunker, where a poor solvent (*e.g.*, acetonitrile) is rapidly injected into a solution of fullerene dissolved in good solvent (*e.g.*, benzene, toluene, *etc*.) or *vice versa*.[15–19] The lyophobic interaction between the mixed solvent and fullerene molecules as well as the π-π interaction between fullerene molecules is responsible for formation of the metastable colloidal aggregates in the mixed solvent. Most prominent advantage of the rapid injection method is its capability to be followed by subsequent electrophoretic deposition, which results in film deposition on an electrode from colloidal dispersions.[18] In fact, various films of the aggregated fullerene nanoclusters have been fabricated using this rapid injection-electrophoretic deposition protocol.[15,18] Considering that the integrative properties of film state is more informative than respective properties of nanocluster itself in terms of device application including BHJ solar cells, the ability to fabricate homogeneous thin films affords a substantial benefit. In addition, this protocol can be completed within a few minutes under an ambient atmosphere. Obviously, the simplicity and convenience of the rapid injection-electrophoretic deposition protocol to prepare fullerene-based films are advantageous over other preparation methods of fullerene assemblies, *e.g.*, reprecipitation technique[3d,10e,11f] and liquid–liquid interfacial precipitation (LLIP),[6,7c,8b–d]

which are regarded as useful methods to prepare the crystalline assemblies of fullerenes with varying shapes. In those methods, fullerene crystals are obtained as gradually growing precipitates. Thus, there is no chance for one-pot fabrication of thin films with sufficient uniformity by the following electrophoretic deposition. In this context, it can be affirmed that the rapid injection-electrophoretic deposition methodology is most suitable for systematic investigation on the photoelectrochemical properties of thin films composed of the fullerene assemblies.

In contrast to the reprecipitation, LLIP and other methodologies, the rapid injection technique typically affords fullerene aggregates with spherical shapes, which are difficult to be altered.[15–18] This always happens when C_{60} and its derivatives are used, as has been intensively studied by several groups.[15b,c,17b–f,18] On the other hand, the low symmetrical molecular structure of C_{70} leads to aggregation behavior different from C_{60}. Nath and coworkers have reported that C_{70} clusters prepared by the rapid injection method can vary its shape depending on the preparation condition, *i.e.*, fullerene concentration or solvents.[19] In their study, spherical[19a] and rod-like[19b] structures of C_{70} aggregates have been obtained by varying the concentration of C_{70} in benzonitrile prior to mixing with acetonitrile, or varying the volume ratio of benzonitrile and acetonitrile. However, photoelectrochemical investigations on the deposited films of the different-shaped clusters have not been conducted in the study. In addition, there still exists a possibility of further shape modulation of C_{70} aggregates. Given that the shape of the fullerene assemblies can be controlled by selecting the appropriate solvents in the cases of reprecipitation, LLIP and other methods,[3–11] it is reasonable to presume that the cluster shape can be also modulated by selecting the good solvent for the rapid injection method. Recently, the author fabricated C_{70} cluster films electrophoretically deposited on the nanostructured SnO_2 electrodes from mixed solvents of toluene–acetonitrile[15a] and *o*-dichlorobenzene–acetonitrile.[20] The author found a notable difference in the photocurrent generation efficiencies as well as in the film surface structures of the two electrodes modified with different C_{70} clusters. This is in sharp contrast with similar spherical shapes and comparable photocurrent generation efficiencies for the cases of the clusterization of C_{60} in toluene–acetonitrile and *o*-dichlorobenzene–acetonitrile mixtures.[15,18] However, the underlying correlation between the photoelectrochemical properties and the cluster structures of C_{70} as well as the resultant film morphologies has remained unclear.

Here the author reports the first systematic studies on the electrophoretically deposited film structures, photoelectrochemical properties, and charge carrier mobilities of C_{70} clusters with different shapes (*i.e.*, particles, rods, and plates) prepared by rapid injection method. The successful morphology engineering of the clusters was accomplished by changing the good solvents, in which C_{70} was dissolved before injection of acetonitrile (poor solvent).

Morphologies of cluster and the resulting film were correlated with the photocurrent generation in terms of the light-absorption, carrier generation, and carrier transport properties by using various experimental techniques including the time-resolved microwave conductivity and transient absorption measurements. The charge carrier mobility is found to be the most predominant factor determining the photocurrent generation efficiency.

Results and Discussion

Spectroscopic Characterization on Clusterization of C_{70}: The C_{70} cluster solution (0.14 mM) was prepared by rapidly injecting acetonitrile (denoted as AN, poor solvent) into a solution of C_{70} dissolved in various good solvents (0.68 mM). For the good solvent, the author chose benzene (denoted as BZ), toluene (TL), *o*-xylene (XY), chlorobenzene (CB), *o*-dichlorobenzene (DCB),[20] benzonitrile (BZN), nitrobenzene (NB), and anisole (ANS), all of which have reasonably high solubilities for C_{70} ranging from 1.5 mM for BZ to 43 mM for DCB (Table 1).[21] For all the solvent combinations, volume ratio of good solvent–acetonitrile (1:4) and C_{70} concentration (0.14 mM in the mixed solvents) were kept constant.[22]

TABLE 1: Boiling Point and C_{70} Solubility of Solvents Employed in This Study

solvent	boiling point [a] / °C	C_{70} solubility [b] / mM
benzene (BZ)	80	1.5 [c]
toluene (TL)	110 – 111	1.7 [c]
o-xylene (XY)	143 – 145	14 ± 1
chlorobenzene (CB)	132	3.0 ± 0.1
o-dichlorobenzene (DCB)	178 – 180	43 [c]
benzonitrile (BZN)	191	1.6 ± 0.1
nitrobenzene (NB)	210 – 211	1.7 ± 0.1
anisole (ANS)	154	3.0 ± 0.1
acetonitrile (AN)	81 – 82	—

[a] From Aldrich's chemicals catalog, 2009. [b] Estimated with pre-determined molar absorptivity and the absorbance of saturated solution in solvent of interest. [c] From ref 21.

The clusterization behaviors of C_{70} in the solvent mixtures were first investigated by using UV–vis–near IR (NIR) absorption spectroscopy. Figure 1a illustrates the UV–vis–NIR absorption spectra measured in BZ (dotted line) and BZ–AN mixture (solid line). In neat BZ, the absorption feature with maximum at 470 nm and shoulders around 550 – 680 nm agrees

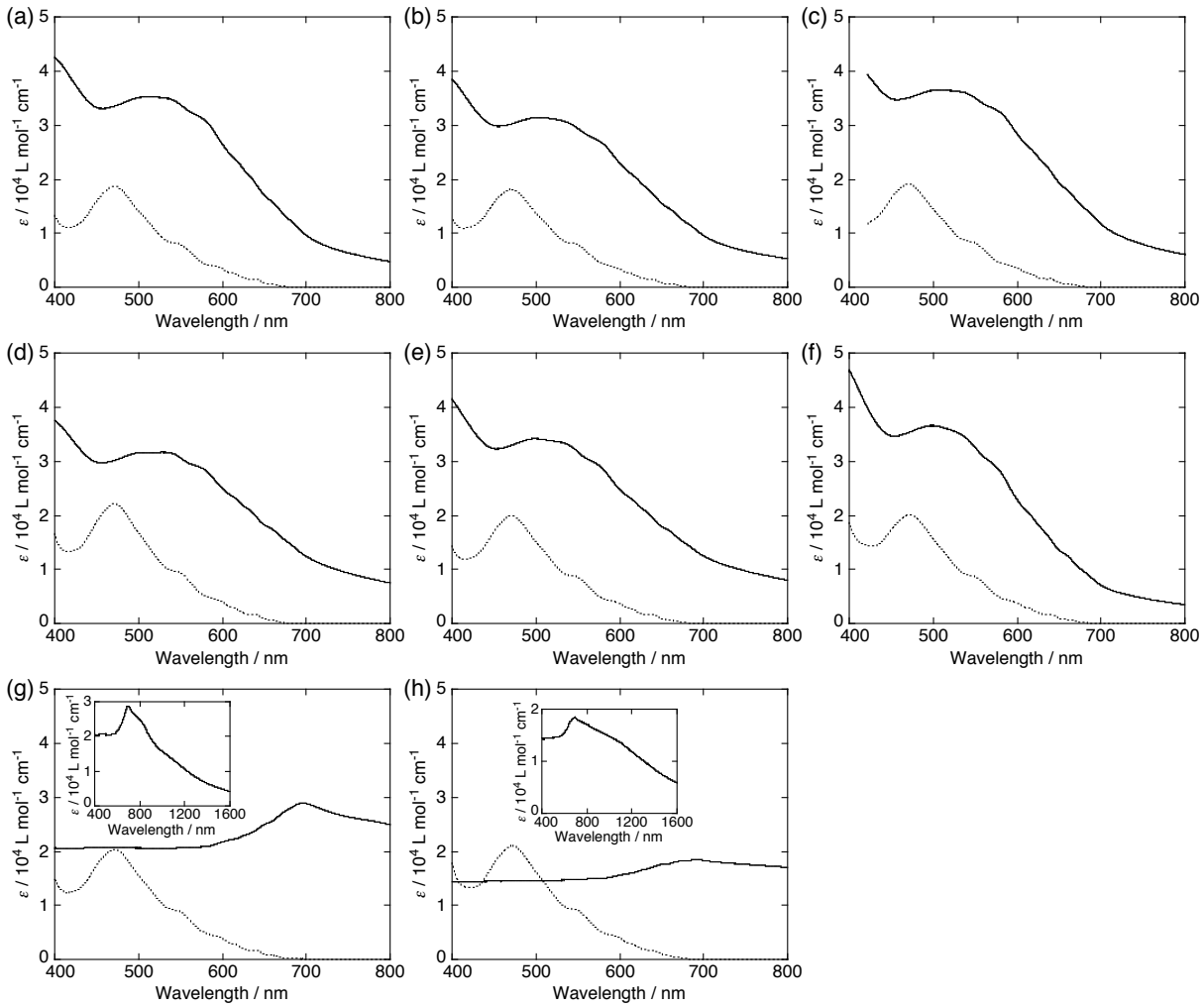

Figure 1. UV–vis–NIR absorption spectra of C_{70} measured in neat solvent ([C_{70}] = 0.68 mM, path length 1 mm) (dotted lines) and solvent mixture with AN (80 vol% of AN, [C_{70}] = 0.14 mM, path length 3 mm) (solid lines). The good solvents are (a) BZ, (b) BZN, (c) NB, (d) TL, (e) CB, (f) ANS, (g) DCB, and (h) XY. Insets in (g) and (h) show the spectra for respective solvent mixtures with wider wavelength range.

well with the characteristics of the monomeric C_{70} absorption.[23] In BZ–AN mixture, the intense peak around 470 nm observed in neat BZ solution is red-shifted to ~ 520 nm and significantly broadened exhibiting an absorption tail extending to NIR region (> 800 nm). Such a drastic change in the absorption spectrum is ascribed to the formation of clusterized species of C_{70} (denoted as $(C_{70})_m$) due to the lyophobic interaction between the mixed solvent and C_{70} molecules in addition to the π-π interaction between C_{70} molecules, as reported by several groups.[16,17a,g,19] Likewise, absorption spectra in other neat solvents (BZN, NB, TL, CB, and ANS) reveal monomeric features of C_{70} and the spectral changes largely similar to Figure 1a are discernible upon injection of AN (Figure 1b – f). Thus, C_{70} exists as its monomeric form without AN and as cluster form with AN in these solvents. On the other hand,

albeit the absorption spectra in DCB and XY display typical monomer characteristics, those in DCB–AN[20] and XY–AN mixtures disclose totally different features from the behavior in other mixed solvents (Figure 1g and h). Namely, the intense peak at 470 nm observed in neat solvents disappears and a new broad band around 700 nm emerges with retaining absorption over 1600 nm. Taking into account the high solubilities of C_{70} in DCB and XY as good solvents relative to the other good solvents, DCB and XY molecules may interact so strongly with C_{70} molecules as to be incorporated into $(C_{70})_m$ upon the clusterization in the mixed solvents. The incorporated solvents would affect the local environments of $(C_{70})_m$, altering the electronic structure of C_{70} and/or the electronic coupling interaction between C_{70} molecules within the cluster.

Microscopic Observations of C_{70} Clusters: Field emission scanning electron microscopy (FE-SEM) measurements were conducted to evaluate the structures of the $(C_{70})_m$ (Figure 2). The samples for the FE-SEM observations were prepared by spin-coating the cluster solutions onto silicon wafer. In parallel, dynamic light scattering (DLS) measurements were also performed to complement the FE-SEM results (Figure 3). The FE-SEM image of $(C_{70})_m$ prepared from BZ–AN mixture reveals granular aggregates with a size of ~ 250 nm (Figure 2a). Correspondingly, DLS measurement of the cluster solution in BZ–AN shows a monomodal size distribution with an average diameter (D_{av}) of 240 nm (Figure 3A(a)). Likewise, $(C_{70})_m$ formed in BZN-AN (Figure 2b) and NB–AN (Figure 2c) are found to be granular aggregates with sizes of ~ 170 nm and ~ 180 nm, which are consistent with the D_{av} values obtained from the DLS measurements (Figure 3A(b) and (c)). In contrast, Figure 2d displays rod-like structures of $(C_{70})_m$ prepared from TL–AN mixture with length of 200 – 400 nm, accompanying small particles with a diameter of ~ 100 nm.[24] The FE-SEM image of $(C_{70})_m$ formed in CB–AN exhibits analogous rod-like assemblies with sizes of 200 – 500 nm in length (Figure 2e). DLS measurements on the cluster solutions in TL–AN and CB–AN show rather broad distributions with D_{av} of 230 nm and 290 nm, respectively, which agree with the FE-SEM observations (Figure 3B(a) and (b)). On the other hand, the FE-SEM image of $(C_{70})_m$ prepared from ANS–AN mixture depicts fragile, plate-like structures with sizes over 1 μm (Figure 2f). Consistently, DLS experiment on the cluster solution exhibited bimodal broad distribution with maxima at 340 nm and ~ 2.5 μm, which may be correlated with the plate-like structures with the large aspect ratio of the thin thickness and the large two-dimensional size (Figure 3B(c)). To the best of the author's knowledge, this is the first example of the plate-like cluster of C_{70} prepared by the rapid injection method. Figure 2g illustrates cuboidal particles of $(C_{70})_m$ formed in DCB–AN mixture with sizes of 260 – 360 nm, which is in good agreement with the estimated D_{av} of 330 nm (Figure 3C(a)).[20] Similar cuboidal particles (Figure 2h) are

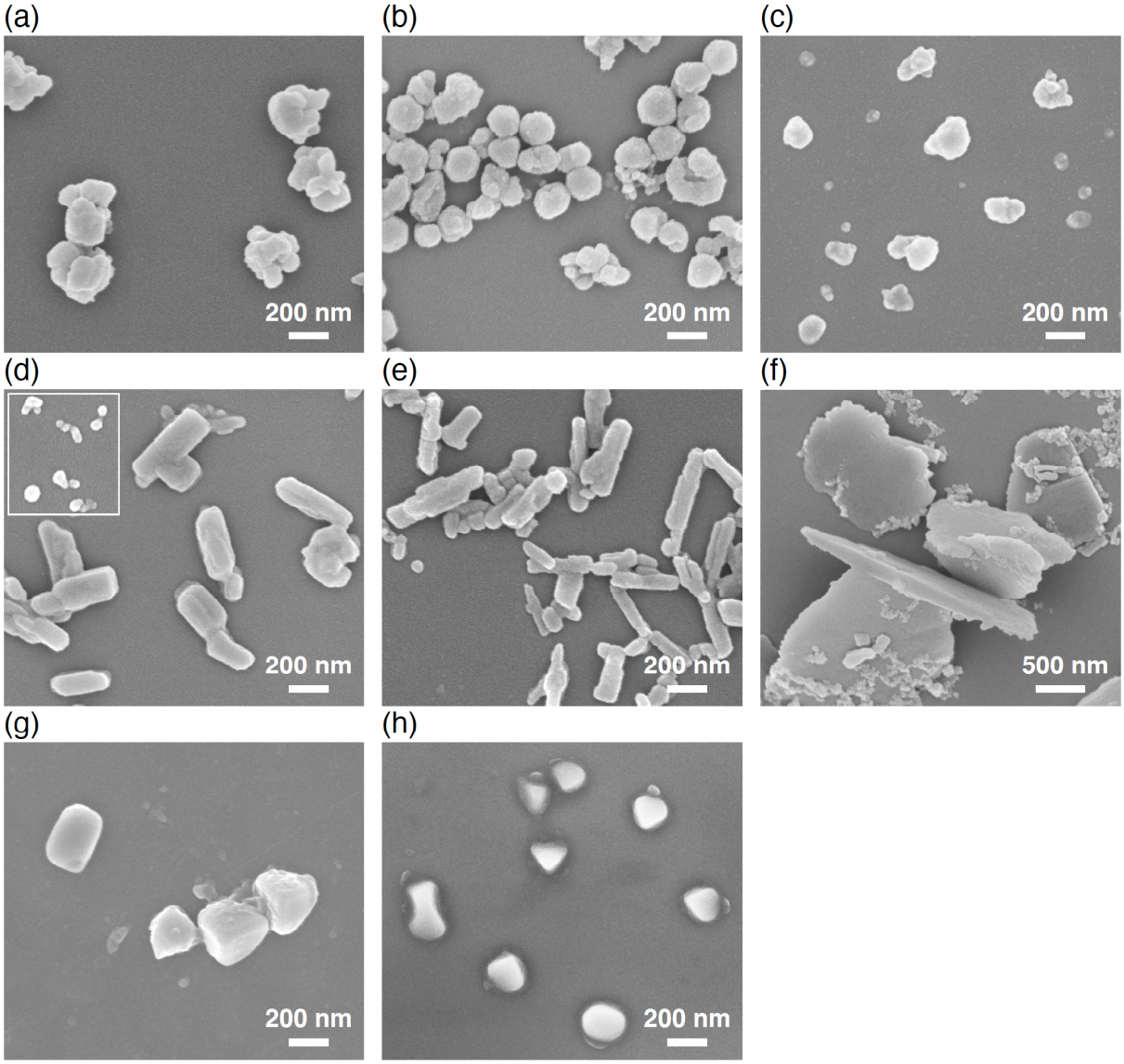

Figure 2. FE-SEM images of $(C_{70})_m$ prepared from mixed solvents of (a) BZ–AN, (b) BZN–AN, (c) NB–AN, (d) TL–AN, (e) CB–AN, (f) ANS–AN, (g) DCB–AN, and (h) XY–AN. The samples were spin-coated on Si wafer from corresponding cluster solutions (good solvent:AN = 1:4, v/v; $[C_{70}]$ = 0.14 mM). Inset in Figure 2d shows particulate clusters observed at a different position on the same substrate.

observed for $(C_{70})_m$ prepared from XY–AN (D_{av} = 170 nm, Figure 3C(b)). Thus, emphasis should be placed on the successful cluster morphology engineering of $(C_{70})_m$ by altering the good solvents, affording particulate, rod-like, and plate-like structures with controllable size distributions ranging from ~ 100 nm to over micrometer scale. It should be noted here that various other factors, such as the volume ratio of good and poor solvents, concentration, and poor solvent used, would also influence the cluster morphology prepared by the rapid injection. In fact, it was reported by Nath and coworkers that BZN–AN could selectively afford both

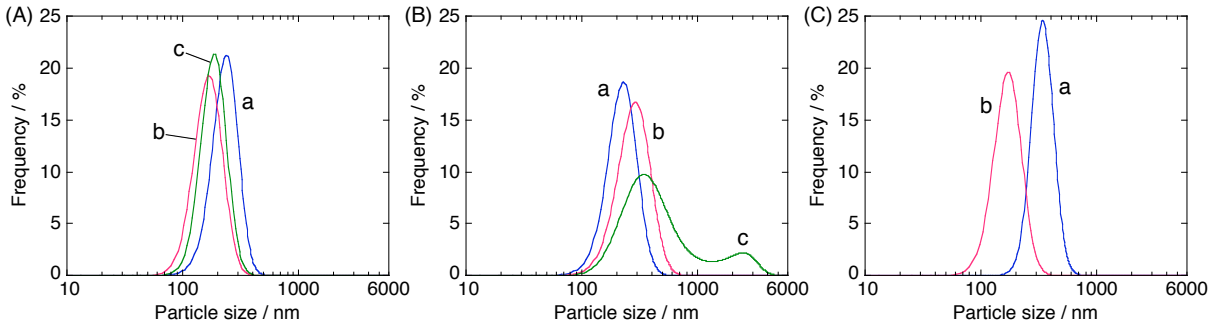

Figure 3. Particle size distribution of $(C_{70})_m$ measured in the solvent mixtures with AN (good solvent:AN = 1:4, v/v; $[C_{70}]$ = 0.14 mM). The good solvents are (A) (a) BZ, (b) BZN, and (c) NB; (B) (a) TL, (b) CBZ, and (c) ANS; (C) (a) DCB and (b) XY.

spherical particles and rod-like aggregates of C_{70} depending on the volume ratio of the solvents (volume (%) of AN < 75% for sphere and > 75% for rod, respectively) at relatively low concentration ($[C_{70}]$ = 0.0126 mM).[19] Although more detailed, extensive studies on the cluster morphology engineering are necessary, the author can conclude that intermolecular interaction between C_{70} molecules and good solvents at least has a large impact on the shape and size of $(C_{70})_m$ clusters prepared by the rapid injection method.

Of another interest to note here is the correlation between the cluster shapes and the absorption spectra. For instance, the absorption spectra of $(C_{70})_m$ prepared in BZ–AN, BZN–AN, NB–AN, TL–AN, CB–AN, and ANS–AN reveal similar spectral features as represented by Figure 1a, despite the remarkable variation of the cluster shapes and sizes. This result implies resemblance in the microscopic environments surrounding C_{70} molecules in the respective clusters, although the eventual cluster shapes are not necessarily the same. Moreover, the notably different absorption spectra of $(C_{70})_m$, prepared in DCB–AN as well as XY–AN, from those prepared in the other solvent–AN mixtures, may result from the altered electronic states of C_{70} induced by the different local environments around C_{70} molecules in the clusters incorporating the good solvents (*vide supra*), whereas the difference does not have correlation with their shape of cuboidal clusters.

Electrophoretic Deposition: For the photoelectrochemical measurements and the other experiments, the clusters of C_{70} were electrophoretically deposited from the corresponding solvent mixtures onto the fluorine-doped tin oxide (FTO) electrodes with nanostructured SnO_2 modification (denoted as FTO/SnO_2/$(C_{70})_m$). Under an application of the high DC electric field (200 V), the clusters, which were negatively charged in the mixed solvent, were driven toward the positively charged electrode (*i.e.*, FTO/SnO_2). The film formation was probed by monitoring the changes in absorbance of the electrophoretically deposited electrodes as a

function of the deposition time. The film formation reached completion within 120 s for all cases. Hence, the author used electrodes prepared with the deposition time of 120 s for all the following measurements.

Absorption Spectroscopy of the Deposited Films: The UV–vis–NIR absorption spectra of the FTO/SnO_2/$(C_{70})_m$ electrodes are shown in Figure 4. Apparently, all of the modified electrodes exhibit analogous spectra with noticeable shoulder around 500 nm, which are largely similar to those of the typical cluster solution (solid lines in Figure 1a – f). It is noteworthy that the absorption spectra of the electrodes deposited from DCB–AN[20] (Figure 4A(d)) and XY–AN (Figure 4B(d)) are different from those of the respective cluster solutions (solid lines in Figure 1g and h). Namely, the broad absorption around 700 nm observed in the cluster solutions disappeared and the prominent shoulder at 450 – 700 nm became apparent. Such a spectral change is indicative of the structural alteration of $(C_{70})_m$ on the electrodes (*vide infra*). Note that the position of the absorption maximum at 480 nm in the case of FTO/SnO_2/$(C_{70})_m$ electrodes prepared from DCB–AN is close to that of the characteristic peak at 470 nm arising from the monomeric C_{70} (dotted lines in Figure 1). The broad absorption of these films as well as their high absorption in the visible region makes these films suitable for harvesting solar energy.

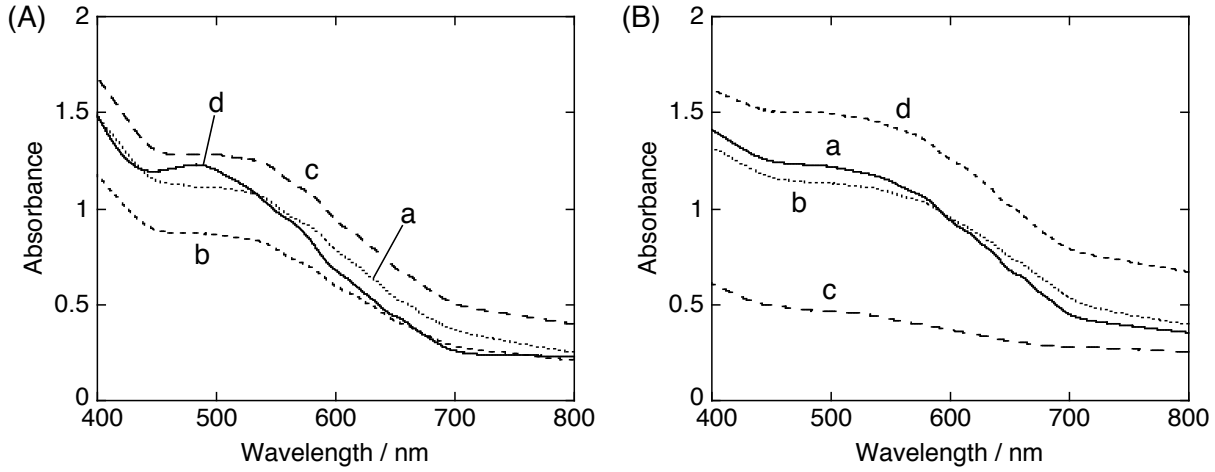

Figure 4. (A) UV–vis–NIR absorption spectra of FTO/SnO_2/$(C_{70})_m$ electrodes prepared from cluster solutions of C_{70} in (a) BZ–AN, (b) TL–AN, (c) CB–AN, and (d) DCB–AN mixtures. (B) UV–vis–NIR absorption spectra of FTO/SnO_2/$(C_{70})_m$ electrodes prepared from cluster solutions of C_{70} in (a) BZN–AN, (b) NB–AN, (c) ANS–AN, and (d) XY–AN mixtures.

Surface Characterization of the Deposited Films: FE-SEM was employed to evaluate the surface morphology of the electrophoretically deposited films (Figure 5). The FE-SEM image of the FTO/SnO_2/$(C_{70})_m$ electrode prepared from BZ–AN (Figure 5a) shows densely

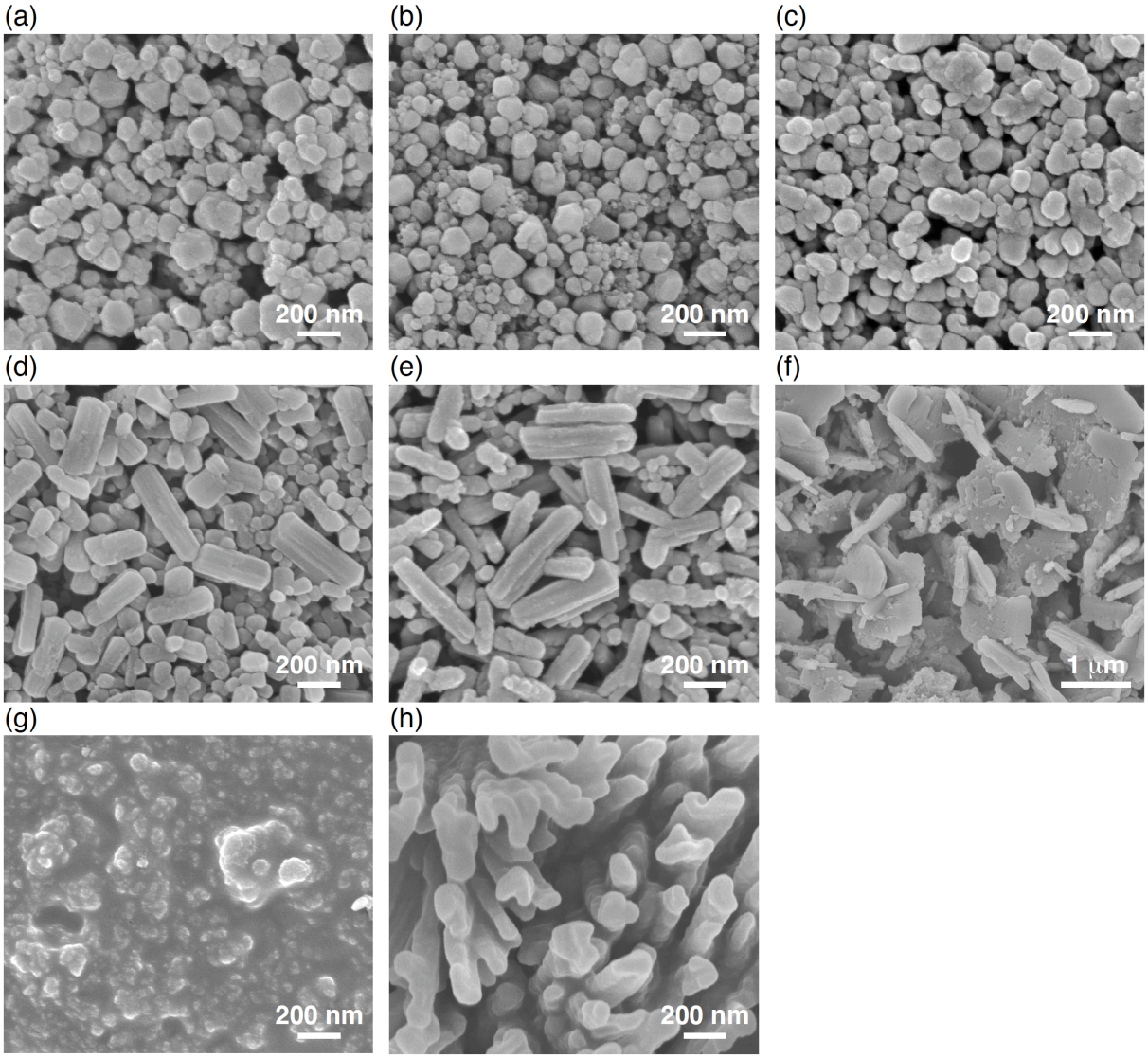

Figure 5. FE-SEM images of FTO/SnO_2/$(C_{70})_m$ electrodes prepared from mixed solvents of (a) BZ–AN, (b) BZN–AN, (c) NB–AN, (d) TL–AN, (e) CB–AN, (f) ANS–AN, (g) DCB–AN, and (h) XY–AN. All samples were coated with *ca.* 5 nm thick Pt layer prior to the measurements.

packed particles with sizes of 100 – 250 nm, which resemble those observed in the spin-coated sample (Figure 2a). Thus, the author concludes that the $(C_{70})_m$ formed in the mixed solvent was successfully deposited onto the FTO/SnO_2 electrode without significant change in its structure. Similarly, FTO/SnO_2/$(C_{70})_m$ electrodes, prepared from BZN–AN (Figure 5b), NB–AN (Figure 5c), TL–AN (Figure 5d), CB–AN (Figure 5e), and ANS–AN (Figure 5f), exhibit closely packed clusters which are virtually the same as those observed in the corresponding FE-SEM images of the spin-coated samples. In contrast, FTO/SnO_2/$(C_{70})_m$ electrode, deposited from DCB–AN mixture, discloses blurred structureless surface morphology from which small grains are protruded (Figure 5g).[20] The cuboidal clusters observed in the spin-coated sample (Figure 2g) are totally absent. Given the fact that the absorption spectral shape of the deposited film is

close to that arising from the monomeric C_{70} in DCB rather than that arising from the $(C_{70})_m$ in DCB–AN mixture (*vide supra*), it is most likely that the aggregated state of C_{70} is transformed into the monomeric C_{70} on the electrode, yielding an amorphous-like film with granulous remnants of aggregated C_{70}.[20] Meanwhile, the FE-SEM image of FTO/SnO_2/$(C_{70})_m$ electrode prepared from XY–AN depicts unique nanostructures protruding from the bottom of the SnO_2 electrode (Figure 5h). Note that the angular-shaped particles observed on Si wafer (Figure 2h) are not seen. These micrographic observations together with the spectroscopic change upon electrophoretic deposition (Figures 1h and Figure 4B(d)) obviously manifest the regeneration of C_{70} monomers from C_{70} aggregate. Such behavior of $(C_{70})_m$ may be explained by the extraordinary high solubility of C_{70} in DCB and XY (Table 1), as well as the difference in boiling points (bp) of good and poor solvents. That is, during drying process of the deposited electrode by dryer, AN with low bp of 82 ^oC vaporizes much faster than DCB with high bp of 180 ^oC and XY with high bp of 143 ^oC. The resultant good solvent-rich environment on the electrode would dissociate aggregated C_{70} to regenerate the monomeric C_{70} without especial stimulation like sonication, owing to the high solubilities of C_{70} in DCB and XY. Furthermore, the vaporization of solvent molecules incorporated in the clusters may facilitate the collapse of the cuboidal clusters. The dissolution of aggregated C_{70} did not occur in the cases of BZN–AN and NB–AN systems, where good solvents possess even higher bp (BZN: 191 ^oC; NB: 210 ^oC), but exhibit one-order lower solubilities of C_{70} in BZN and NB than in DCB and XY.

The structures of $(C_{70})_m$ on the FTO/SnO_2 electrodes are summarized in Table 2. It is expected that the morphological difference of the fabricated films, as well as the morphological change upon electrophoretic deposition in the cases of DCB–AN and XY–AN systems, should affect the photoelectrochemical properties.

Photoelectrochemical Properties: Photoelectrochemical measurements were performed in deaerated acetonitrile containing 0.5 M LiI and 0.01 M I_2 with the FTO/SnO_2/$(C_{70})_m$ electrodes as a working electrode, a platinum wire as a counter electrode, and an I^-/I_3^- reference electrode. Figure 6a displays representative photocurrent response of the electrode prepared from BZ–AN mixture illuminated with white light (λ > 380 nm) at an applied potential of 0.05 V *vs*. SCE. The photocurrent response is prompt, steady, and reproducible during the repeated on/off cycles of the visible light illumination. Blank experiment of the FTO/SnO_2 electrode without deposited films exhibited negligible photocurrent responses under the same conditions, demonstrating the role of the deposited clusters toward harvesting light energy and generating electron flow from the electrolyte to the FTO/SnO_2 electrode through the film. Figure 6b illustrates current *vs.* potential curve of the same device. With increasing positive bias up to 0.05 V *vs*. SCE, the photocurrent is increased compared to the dark current.

TABLE 2: Cluster Structure, IPCE value, Surface Area, Film Thickness, and Electron Mobility of FTO/SnO_2/$(C_{70})_m$ electrodes Prepared from Various Solvent Mixtures

solvent	structure of $(C_{70})_m$	IPCE at 400 nm / %	surface area [a] / $m^2\ g^{-1}$	film thickness [b] / nm	$\Sigma\mu$ [c] / $cm^2\ V^{-1}\ s^{-1}$
DCB–AN	amorphism [d]	10	22	400 ± 130	1.9 [e]
NB–AN	particle	4.8	58	700 ± 210	0.38
BZ–AN	particle	4.6	88	830 ± 310	0.21
BZN–AN	particle	4.5	114	670 ± 240	0.15
ANS–AN	plate	2.5	50	1450 ± 260	0.098
TL–AN	rod + particle [f]	1.7	65	680 ± 230	0.048
XY–AN	protruding structure [g]	1.0	69	820 ± 530	0.037
CB–AN	rod	0.82	87	560 ± 170	0.043

[a] Calculated by subtracting the contribution from the bare FTO/SnO_2 electrode. [b] Determined by subtracting thickness of SnO_2 base layer (~ 540 nm) from total thickness. [c] $\Sigma\mu$: sum of mobilities of all the transient-charge carriers calculated by maximum value of transient conductivity upon photoexcitation at 355 nm and quantum efficiency of carrier generation determined for DCB–AN sample (0.031) with conventional DC-current integration. [d] Rearranged from cuboidal particle. [e] From ref 20. [f] The ratio of rod and particle structures was estimated as ~ 1:2 from the FE-SEM image of deposited film. [g] Rearranged from angulated particle.

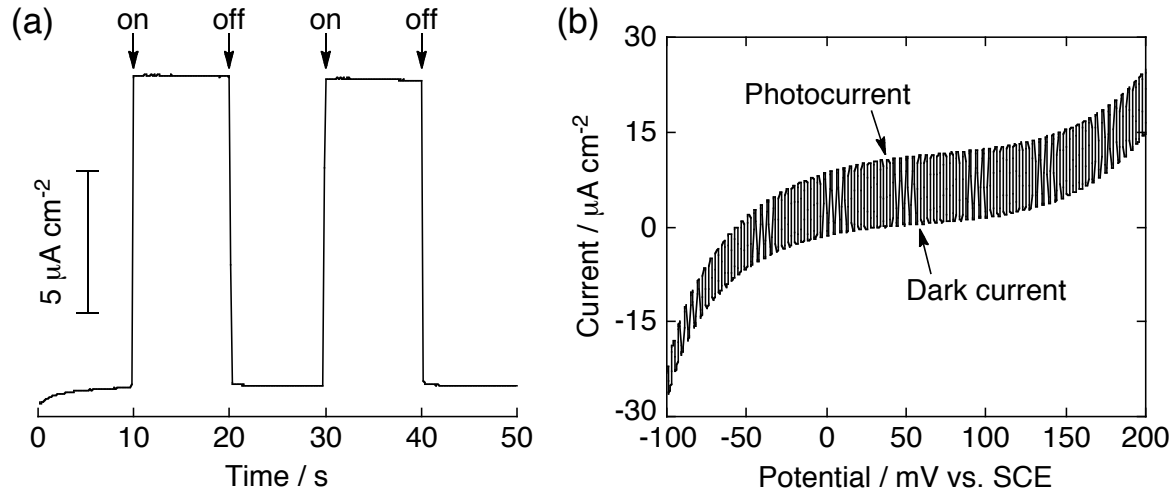

Figure 6. (a) Photocurrent response and (b) current *vs.* potential curve of FTO/SnO_2/$(C_{70})_m$ electrode prepared from cluster solution in BZ–AN mixture. Illuminated with white light (λ > 380 nm, input power: 37 mW cm^{-2}). Electrolyte: 0.5 M LiI and 0.01 M I_2 in acetonitrile. The photo-response was measured under an applied potential of +0.05 V *vs.* SCE

The increased charge separation and the facile transport of the generated charge carriers under positive bias are responsible for the enhanced photocurrent generation. Similar photoelectrochemical behaviors were observed for the other FTO/SnO_2/$(C_{70})_m$ electrodes.

For further insights into the photoelectrochemical properties of the deposited films, the author evaluated the wavelength dependent incident photon-to-current efficiency (IPCE) spectra. The IPCE values are calculated by normalizing the photocurrent densities for incident light energy and intensity and by use of the expression:

$$\text{IPCE (\%)} = 100 \times 1240 \times i/(W_{\text{in}} \times \lambda)$$

where i is the photocurrent density (A cm^{-2}), W_{in} is the incident light intensity (W cm^{-2}), and λ is the excitation wavelength (nm).

Figure 7 depicts the photocurrent action spectra of the FTO/SnO_2/$(C_{70})_m$ electrodes. The photocurrent action spectra largely parallel the absorption spectra of the deposited electrodes (Figure 4). The IPCE values are compared at 400 nm where the values are maximal and most of the incident light is absorbed by the films (Table 2). The maximum IPCE (10%)[20] of the electrode prepared from DCB–AN mixture outperforms the corresponding values of the electrodes prepared from NB–AN (4.8%), BZ–AN (4.6%), BZN–AN (4.5%), ANS–AN (2.5%), TL–AN (1.7%), XY–AN, (1.0%), and CB–AN (0.82%) mixtures. Considering the sufficiently high light-harvesting property at 400 nm (absorbance > 1), the difference in the maximum IPCE values originates from those in charge separation efficiency and charge collection efficiency (*vide infra*).[25] The author emphasizes that the different shapes of $(C_{70})_m$, thereby different morphologies of the electrophoretically deposited films, lead to different photocurrent generation efficiencies ranging from 0.8% to 10%. This is in stark contrast to the results for C_{60} clusters prepared by the same rapid

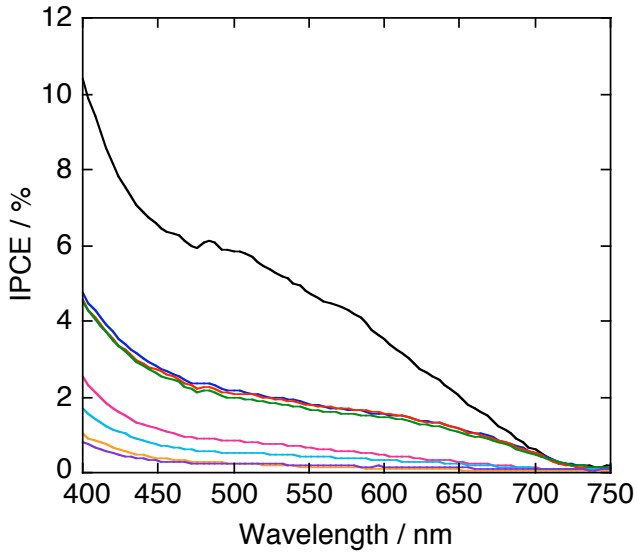

Figure 7. Photocurrent action spectra of FTO/SnO_2/$(C_{70})_m$ electrodes prepared from mixed solvents of, from top to bottom, DCB–AN (black), NB–AN (blue), BZ–AN (red), BZN–AN (green), ANS–AN (pink), TL–AN (light blue), XY-AN (orange), and CB-AN (purple). Applied potential: +0.05 V *vs.* SCE. Electrolyte: 0.5 M LiI and 0.01 M I_2 in acetonitrile.

injection method, where spherical assemblies are formed irrespective of the clusterization conditions and maximum IPCE around 3 – 5% are obtained when the clusters are deposited onto the SnO_2 electrodes.[15,18]

Photocurrent Generation Mechanism: Before focusing the correlation between the film morphologies and the photoelectrochemical properties, the author presents the photocurrent generation mechanism of the FTO/SnO_2/$(C_{70})_m$ electrodes on the basis of the previously studied C_{60}-based devices (Scheme 1).[15,18]

SCHEME 1. Schematic diagram of photocurrent generation in FTO/SnO_2/$(C_{70})_m$ device.

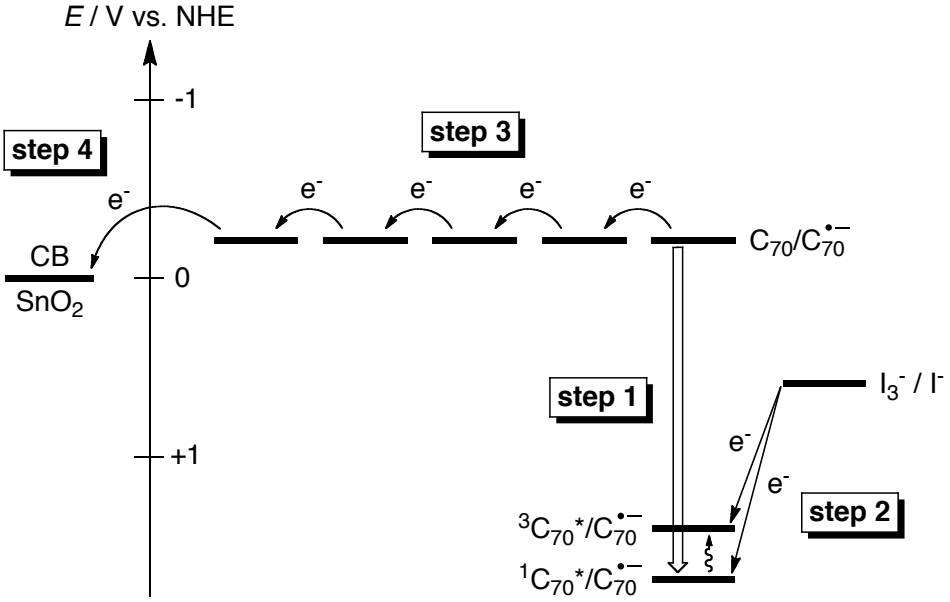

Photocurrent generation is initiated by absorption of the incident light by C_{70} (step 1), yielding the highly energetic excited states of C_{70} (lowest singlet energy ≈ 1.9 eV; lowest triplet energy ≈ 1.5 eV).[26] Then, electron transfer (ET) from iodide ion (I_3^-/I^- = 0.5 V *vs.* NHE)[15,18] in the electrolyte to the excited C_{70} ($^1C_{70}^*/C_{70}^{\bullet-}$ ≈ 1.7 V *vs.* NHE; $^3C_{70}^*/C_{70}^{\bullet-}$ ≈ 1.3 V *vs.* NHE)[26,27] occurs as in the case of analogous photoelectrochemical devices utilizing C_{60} clusters (step 2).[15,18] Next, the reduced C_{70} ($C_{70}/C_{70}^{\bullet-}$ ≈ –0.2 V *vs.* NHE)[27] mediates its electron toward the SnO_2 layer through the C_{70} arrays via electron hopping (step 3). Finally, C_{70} radical anion, which is closest to the SnO_2 surface, injects electron into the conduction band of SnO_2 (E_{CB} = 0 V *vs.* NHE) (step 4).[15,18] The electrons injected into the SnO_2 electrode are driven to the counter electrode via external circuit to regenerate the redox couple. Thus, photocurrent generation mechanism is basically divided into four steps (steps 1 – 4) and the IPCE is a product of the efficiencies of the respective steps. Of these, step 1, *i.e.*, light absorption, is unlikely a key factor yielding the difference in the IPCE values (*vide supra*).

Therefore, the author has to consider the efficiencies of steps 2 – 4. As for step 2, the charge separation (CS) efficiency from I^- to the C_{70} excited states depends on the exciton diffusion lengths and lifetimes of the C_{70} excited states, the thickness and the surface area of the deposited films, and diffusion process of I^- to the C_{70} excited states at the interface of the film surface and the electrolyte solution. Assuming that the exciton diffusion lengths and the lifetimes of the C_{70} excited states and the diffusion process of I^- to the C_{70} excited states in the interface are similar in the present systems, the thickness and the surface area of the deposited films are responsible for difference in the CS efficiency of step 2.[28] The CS efficiency would increase if the film thickness becomes smaller or the surface area becomes larger, but the larger surface area may also induce the unfavorable carrier recombination between $C_{70}^{\bullet-}$ and I_3^-. On the other hand, the electron-transporting efficiency of step 3 would be enhanced as the film thickness is smaller or the electron mobility within the film is larger. Finally, the electron injection efficiency of step 4 can be discussed in terms of the reduction potential of C_{70}. Here, the reduction potential of C_{70} can be regarded as independent on the cluster structures.[18a] Therefore, surface area, film thicknesses, and electron mobility are the subjects of further investigation.

Surface Area and Film Thickness: The surface areas of the FTO/SnO_2/$(C_{70})_m$ electrodes were evaluated by BET analyses with N_2 adsorption protocol at 77 K. The BET surface area was calculated by subtracting the contribution from the bare FTO/SnO_2 electrode. It should be noted that the value determined for the film prepared from ANS–AN mixture represents the lower limits since the deposited film partially exfoliates after the electrophoretic process in this case.[25] The BET surface areas of the FTO/ SnO_2/$(C_{70})_m$ electrodes are listed in Table 2 and plotted as a function of the maximum IPCE values (Figure 8). It is evident that there is no apparent correlation between the two parameters. Thus, the surface area of the deposited films has no significant impact on the difference in the IPCE values.

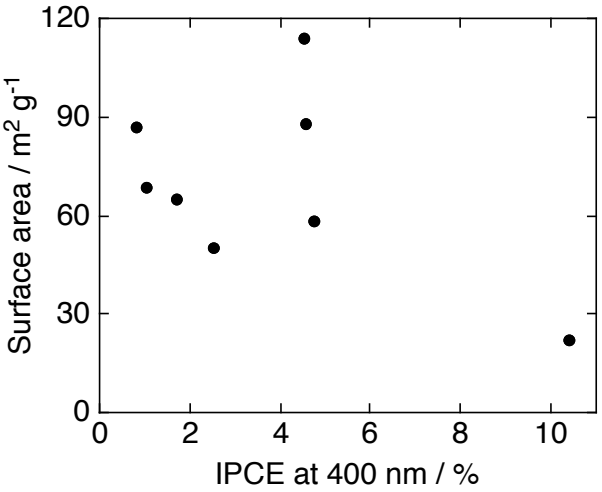

Figure 8. Plot of BET surface areas *vs.* IPCE values at 400 nm.

The thickness of the deposited film was determined by analyzing the AFM height profile of the intentionally grooved trenches on the film (Figure 9). To assess the cluster layer only,

average thickness of the SnO_2 layer (540 nm) was subtracted from that of the whole film. The thicknesses are summarized in Table 2 and plotted *vs.* the maximum IPCE (Figure 10). There is no systematic change in the IPCE values as a function of the film thickness. Therefore, the film thickness is not a decisive parameter for the difference in the IPCE values. The alignment of C_{70} molecules in the cluster may influence more significantly the photocurrent generation efficiency (*vide infra*).

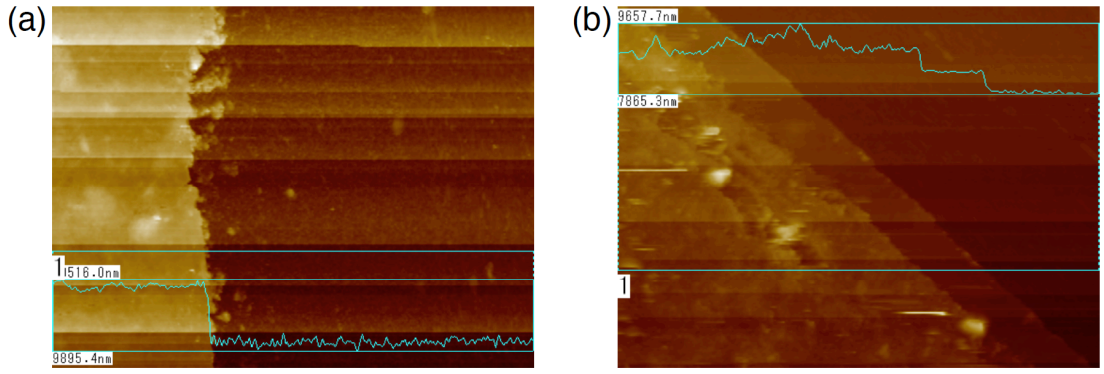

Figure 9. Representative AFM images (20 μm × 15 μm) of (a) bare FTO/SnO_2 electrode and (b) FTO/SnO_2/$(C_{70})_m$ electrode prepared from TL–AN mixture. Height profiles corresponding to the light-blue lines are also shown for comparison. Steps observed in the figures represent one parts of the walls of intentionally grooved trenches. In Figure b, the SnO_2 base layer and deposited $(C_{70})_m$ layer can be recognized as steps.

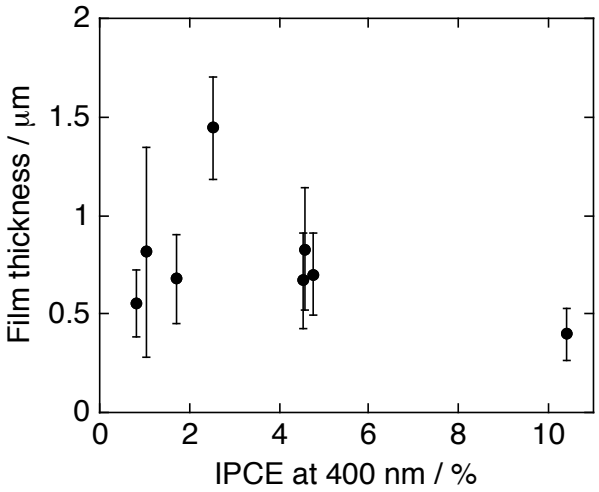

Figure 10. Plot of film thicknesses *vs.* IPCE values at 400 nm. Error bar denotes the corresponding standard deviation of thickness.

Transient Microwave Conductivity: Flash-photolysis time-resolved microwave conductivity (TRMC) measurements[29] were performed on the deposited films of $(C_{70})_m$ to evaluate the charge carrier mobility (μ). For the sample preparation, the films were peeled off

from the FTO substrate and fixed on quartz plates with poly(methyl methacrylate) matrices. Upon exposure to a laser pulse with an excitation wavelength of 355 nm, all samples exhibit a rise of the transient conductivity $<\phi\Sigma\mu>$, in which ϕ is the quantum efficiency of charge carrier generation and $\Sigma\mu$ is the sum of the mobility of all the transient charge carriers (Figure 11A). The $\Sigma\mu$ values are calculated using the maximum values of $<\phi\Sigma\mu>$ and the ϕ value (0.031)[20] determined for the film prepared from DCB–AN mixture with conventional DC-current integration technique, assuming that the ϕ value is independent of the cluster structures and the film morphologies. This assumption is likely to be reasonable considering the similarity of the excited state dynamics of the deposited films.[28] Additionally, it should be mentioned that the major charge carriers stem from electrons as indicated by effective accumulation of negative charges into the integrator under negative bias mode, whereas negligible positive charges are observed under positive bias mode. The $\Sigma\mu$ values are listed in Table 2 and the plot of the $\Sigma\mu$ values *vs.* the maximum IPCE values is illustrated in Figure 11B.

Figure 11B manifests that the IPCE value is increased with increasing the $\Sigma\mu$ value. Thus, the electron-transporting process of step 3 turns out to have a large influence on the IPCE values in the present systems. The largest maximum IPCE value (10%) of the FTO/SnO_2/$(C_{70})_m$ electrode prepared from DCB–AN mixture mainly results from the remarkably high electron mobility (1.9 $cm^2\ V^{-1}\ s^{-1}$). Then, one fundamental question arises; what factor determines the mobility?[30] This seems to be closely related to the packing pattern of C_{70} molecules in the respective clusters, as have been demonstrated in the previous studies on

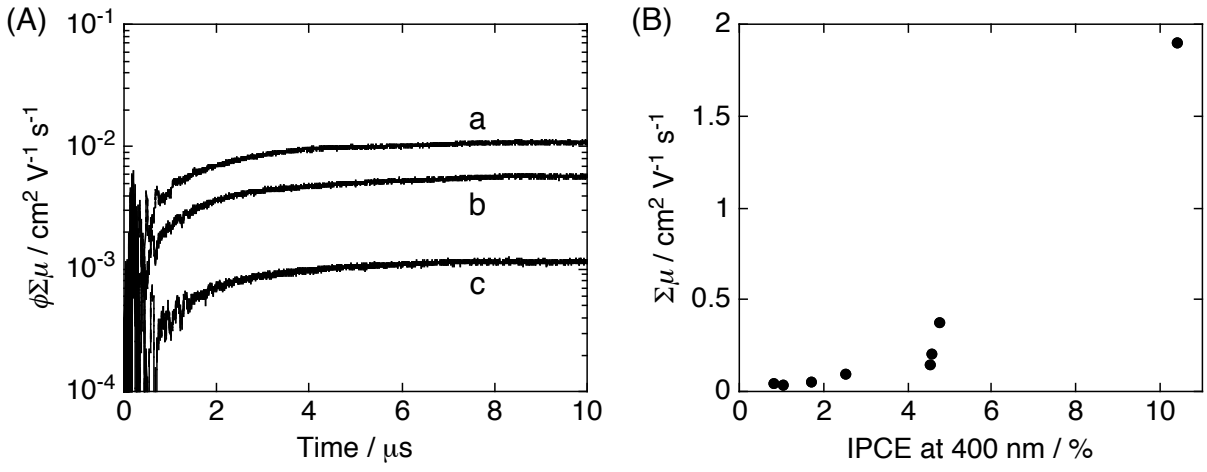

Figure 11. (A) Flash-photolysis TRMC transients for FTO/SnO_2/$(C_{70})_m$ electrodes prepared from mixed solvents of (a) NB–AN, (b) BZ–AN, and (c) CB–AN. The transients were recorded at an excitation wavelength of 355 nm with a photon density of 3.3×10^{15} cm^{-2}. All samples were fixed on quartz substrates with poly(methyl methacrylate) matrices. (B) Plot of microwave electron mobilities *vs.* IPCE values at 400 nm.

porphyrin–C_{60} assembly.[2e,f,31] Given the fact that the TRMC mobilities are higher for the films with particulate clusters, prepared from BZ–AN, BZN–AN, and NB–AN, than those for the films with rod-like clusters, prepared from TL–AN and CB–AN, and plate-like clusters, prepared from ANS–AN, there seems to be connection among the cluster structure, molecular packing, and carrier mobility (Table 2). To shed light on the inner structures of $(C_{70})_m$, the author conducted X-ray diffraction (XRD) analyses on the cluster films. However, no XRD patterns arising from the crystalline packing of C_{70}[32] are observed for all the samples, indicating that any existing crystallites in $(C_{70})_m$ are too small to be detected or inner structures of $(C_{70})_m$ are rather amorphous.

The turn-over period of the microwave is about ~ 110 ps at 9.1 GHz used in the TRMC measurement, suggesting the perturbation length of the negative charge carriers as ~ 2 nm with the values of observed mobilities (~ 0.5 $cm^2\ V^{-1}\ s^{-1}$), under the averaged strength of the employed electric field ($3 - 4 \times 10^2$ V cm^{-1}). This implies that the TRMC measurements probe the AC-field induced oscillating motion of the electrons within a few molecules of C_{70}.[33] Hence, the author could postulate that the tiny stacks comprised of several C_{70} molecules affects strongly the TRMC mobility and the eventual cluster shape, without showing observable signals in the XRD pattern.[17f,g,34] For instance, the small stacks of C_{70} molecules with desirable structure for the efficient electron hopping may lead to the spherical shaped clusters, while other types of stacks, which are undesirable for the efficient electron hopping, result in the rod-like or plate-like clusters. In the case of the film deposited from DCB–AN, the melting behavior of the deposited clusters by the drying process would be responsible for the formation of favorable pathway for efficient electron hopping, whereas for the formation of unfavorable pathway in the film from XY–AN.

Conclusion

The author has systematically examined the good solvent effects of C_{70} clusterization behavior in the good–poor solvent mixtures as well as of their electron-transporting and photo-electrochemical properties for the first time. The successful cluster morphology engineering of C_{70} was achieved by changing the good solvent, affording the spherical, rod-like, and plate-like clusters. The C_{70} clusters were electrophoretically deposited onto the nanostructured SnO_2 electrodes and their photoelectrochemical properties were examined. The incident photon-to-current efficiency (IPCE) varied dramatically from 0.8% to 10% depending on the solvent combination for the cluster formation. The origin of the variation in the IPCE values was discussed in terms of the surface area, film thickness, and electron mobility. The electron mobility was found to be the most predominant factor for the difference in the IPCE values,

implying the importance of the electron-transporting process in the C_{70} films. The underlying molecular packing and the resultant cluster structure were suggested to correlate with the electron mobility. Accordingly, these results will provide basic information on the supramolecular chemistry of fullerenes as well as the design of the fullerene-based molecular devices including the organic photovoltaics.

Experimental Section

General Procedures: UV–vis–NIR absorption spectra of solutions and films were recorded on a Perkin-Elmer Lambda 900 UV/vis/NIR spectrometer. FE-SEM observation was carried out with a JEOL JSM-6705F. For preparation of the cluster samples, a mixture of good solvent–acetonitrile containing C_{70} was spin-coated on Si wafer (polished wafer; SUMCO TECHXIV) at a rotation speed of 1200 rpm. Prior to the observation, both spin-coated samples and electrophoretically deposited films were coated with 5 nm thick Pt layer using a JEOL JFC-1600 auto fine coater. DLS measurements of the cluster solutions were performed by a Horiba LB550 particle size analyzer. AFM images were obtained with a KEYENCE VN-8000 hybrid microscope in the tapping mode. Thickness of the deposited film was estimated by averaging the height of steps (over 80 points) at intentionally grooved trenches. XRD analyses were conducted on a Rigaku A2 diffractometer using Cu K_α radiation. X-ray photoelectron spectroscopy (XPS) on film samples was carried out with a SHIMADZU ESCA750S electron spectrometer. C_{70} (99.5%) was purchased from MTR Ltd. and used as-received. An optically transparent FTO electrode (Asahi Glass) was washed by sonication in 2-propanol and cleaned in an O_3 atmosphere in advance. A 15% SnO_2 colloidal solution (particle size = 15 nm; Chemat Technology, Inc.) was deposited on the FTO electrode using doctor blade technique.[15c,20] The electrode was annealed at 673 K to yield 0.5 μm thick SnO_2 film (denoted as FTO/SnO_2). All of the solvents employed (benzene, toluene, *o*-xylene, chlorobenzene, *o*-dichlorobenzene, benzonitrile, nitrobenzene, and anisole as a good solvent, and acetonitrile as a poor solvent) were of reagent-grade quality, purchased commercially, and used without further purification.

Solubility Evaluation of C_{70}: Solubility of C_{70} in various good solvents was estimated by using pre-determined molar absorptivity of C_{70} and the absorbance of the saturated solution of C_{70} in the respective solvents.[21] Saturated solution was prepared by suspending excess C_{70} (~ 40 mg) in 2 mL of neat solvent by vigorous bath-sonication for 2 h then removing undissolved sediment by Millipore Millex-FG (pore size: 0.20 μm) syringe-driven filter unit. For accurate measurement of the absorption spectrum, the saturated solution was diluted appropriately with known amount of neat solvent.

Preparation of Cluster Solutions and Films: The cluster solutions of C_{70} (0.14 mM) were prepared in a 1 cm cuvette by quickly injecting 1.6 mL of acetonitrile into a solution of C_{70} (0.68 mM) in 0.4 mL of good solvent (good solvent:acetonitrile = 1:4, v/v).[20] Then, two electrodes (*i.e.*, FTO and FTO/SnO_2) were inserted into the cuvette with keeping at a distance of 0.6 cm by a Teflon spacer. A DC voltage (200 V) was applied for 120 s between these two electrodes using a power supply (ATTO, model AE-8750). The deposition of the film could be visibly confirmed as the suspension became colorless with simultaneous colorization of the FTO/SnO_2 electrode. After the deposition, the deposited film was dried immediately with a hair dryer.

Photoelectrochemical Measurements: All electrochemical measurements were carried out in a standard three-electrode system using an ALS 630A electrochemical analyzer.[15c,20] The deposited film as a working electrode was immersed into an electrolyte solution containing 0.5 M LiI and 0.01 M I_2 in acetonitrile. A Pt wire covered with a glass Luggin capillary, whose tip was located near the working electrode, was used as a quasi-reference electrode. A Pt coil was employed as a counter electrode. The potential measured was converted to the saturated calomel electrode (SCE) scale by adding +0.05 V. A 500 W xenon lamp (USHIO, XB-50101AAA) was used as a light source. Potential versus current characteristics were measured with controlled-potential scan (1 mV s^{-1}) under 0.5 Hz chopped white light ($\lambda > 380$ nm, input power: 37 mW cm^{-2}). The light was passed through a monochromator (Ritsu, MC-10N) and focused on the modified area of the working electrode (0.20 cm^2) from the backside. The light intensity was monitored by an optical power meter (Anritsu, ML9002A) and the corrected values were used for calculation of incident photon-to-current efficiencies.

BET Surface Area Analyses: BET surface areas of the deposited film samples were obtained with a BEL JAPAN BELSORP28SA according to the nitrogen adsorption protocol at 77 K. Appropriately cut FTO/SnO_2 electrodes with deposited cluster films were inserted in the sample tube and dried under reduced pressure (< 10^{-3} Torr) for 3 h before the measurements. The contribution from the bare FTO/SnO_2 electrode was subtracted from the whole surface areas and the specific surface areas of the deposited films were calculated based on the mass of C_{70} used for the film formation (0.23 mg).

Time-resolved Microwave Conductivity Measurements: The instruments setup as descrived in the previous studies[20,29] were used for the measurements. Namely, nanosecond laser pulses at 355 nm (full width at half maximum (FWHM): 3 – 5 ns) with photon density of 3.3×10^{15} cm^{-2} were used as an excitation source. A microwave frequency of 9.1 GHz and a power of 3 – 20 mW were employed. Other experimental details are described elsewhere.[29]

Time-resolved Spectral Measurements: A pump-probe method was used to measure transient absorption spectra in sub-picosecond to nanosecond time domain. The measurements

were carried out using the instrument described previously.[35] Briefly, the transient spectra were recorded by a CCD detector coupled with a monochromator in the visible and near infrared ranges and a second harmonic (410 nm) of Ti:sapphire laser was used for excitation. A typical time resolution of the instrument was 150 fs (FWHM). The excitation energy was adjusted to the highest value at which the degradation of the samples during measurements is negligible. All measurements were carried out at room temperature in air.

References and Notes

[1] a) G. M. Whitesides, J. P. Mathias, C. T. Seto, *Science* **1991**, *254*, 1312; b) S. Zhang, *Nat. Biotechnol.* **2003**, *21*, 1171; c) K. Ariga, T. Nakanishi, J. P. Hill, *Curr. Opin. Colloid Interface Sci.* **2007**, *12*, 106; d) K. Ariga, J. P. Hill, M. V. Lee, A. Vinu, R. Charvet, S. Acharya, *Sci. Technol. Adv. Mater.* **2008**, *9*, 014109; e) S. Mann, *Nature Mater.* **2009**, *8*, 781.

[2] a) T. Hasobe, H. Imahori, P. V. Kamat, S. Fukuzumi, *J. Am. Chem. Soc.* **2003**, *125*, 14962; b) J. P. Hill, W. Jin, A. Kosaka, T. Fukushima, H. Ichihara, T. Shimomura, K. Ito, T. Hashizume, N. Ishi, T. Aida, *Science* **2004**, *304*, 1481; c) N. I. Kovtyukhova, T. E. Mallouk, *Adv. Mater.* **2005**, *17*, 187; d) Y. Yamamoto, T. Fukushima, Y. Suna, N. Ishii, A. Saeki, S. Seki, S. Tagawa, M. Taniguchi, T. Kawai, T. Aida, *Science* **2006**, *314*, 1761; e) H. Imahori, *J. Mater. Chem.* **2007**, *17*, 31; f) H. Imahori, T. Umeyama, *J. Phys. Chem. C* **2009**, *113*, 9029.

[3] a) A. M. Cassell, C. L. Asplund, J. M. Tour, *Angew. Chem. Int. Ed.* **1999**, *38*, 2403; b) P. Brough, D. Bonifazi, M. Prato, *Tetrahedron* **2006**, *62*, 2110; c) L. Wang, B. Liu, D. Liu, M. Yao, Y. Hou, S. Yu, T. Cui, D. Li, G. Zou, A. Iwasiewicz, B. Sundqvist, *Adv. Mater.* **2006**, *18*, 1883; d) Z. Tan, A. Masuhara, H. Kasai, H. Nakanishi, H. Oikawa, *Jpn. J. Appl. Phys.* **2008**, *47*, 1426.

[4] a) Y. Jin, R. J. Curry, J. Sloan, R. A. Hatton, L. C. Chong, N. Blanchard, V. Stolojan, H. W. Kroto, S. R. P. Silva, *J. Mater. Chem.* **2006**, *16*, 3715; b) H.-X. Ji, J.-S.; Hu, Q.-X. Tang, W.-G. Song, C.-R. Wang, W.-P. Hu, L.-J. Wan, S.-T. Lee, *J. Phys. Chem. C* **2007**, *111*, 10498; c) H.-X. Ji, J.-S. Hu, L.-J. Wan, Q.-X. Tang, W.-P. Hu, *J. Mater. Chem.* **2008**, *18*, 328; d) L. C. Chong, J. Sloan, G. Wagner, S. R. P. Silva, R. J. Curry, *J. Mater. Chem.* **2008**, *18*, 3319.

[5] a) H. Murakami, M. Shirakusa, T. Sagara, N. Nakashima, *Chem. Lett.* **1999**, 815; b) Y.-G. Guo, C.-J. Li, L.-J. Wan, D.-M. Chen, C.-R. Wang, C.-L. Bai, Y.-G. Wang, *Adv. Funct. Mater.* **2003**, *13*, 626; c) C.-J. Li, Y.-G. Guo, B.-S. Li, C.-R. Wang, L.-J. Wan, C.-L. Bai, *Adv. Mater.* **2005**, *17*, 71; d) J. Geng, W. Zhou, P. Skelton, W. Yue, I. A. Kinloch, A. H.

Windle, B. F. G. Johnson, *J. Am. Chem. Soc.* **2008**, *130*, 2527.

[6] a) K. Miyazawa, Y. Kuwasaki, A. Obayashi, M. Kuwabara, *J. Mater. Res.* **2002**, *17*, 83; b) K. Miyazawa, *J. Am. Ceram. Soc.* **2002**, *85*, 1297; c) K. Miyazawa, K. Hamamoto, S. Nagata, T. Suga, *J. Mater. Res.* **2003**, *18*, 1096; d) M. Sathish, K. Miyazawa, T. Sasaki, *Chem. Mater.* **2007**, *19*, 2398.

[7] a) V. Georgakilas, F. Pellarini, M. Prato, D. M. Guldi, M. Melle-Franco, F. Zerbetto, *Proc. Natl. Acad. Sci. U.S.A.* **2002**, *99*, 5075; b) H. Liu, Y. Li, L. Jiang, H. Luo, S. Xiao, H. Fang, H. Li, D. Zhu, D. Yu, J. Xu, B. Xiang, *J. Am. Chem. Soc.* **2002**, *124*, 13370; c) K. Miyazawa, J. Minato, T. Yoshii, M. Fujino, T. Suga, *J. Mater. Res.* **2005**, *20*, 688; d) D. M. Guldi, A. Gouloumis, P. Vázquez, T. Torres, V. Georgakilas, M. Prato, *J. Am. Chem. Soc.* **2005**, *127*, 5811; e) S. I. Cha, K. Miyazawa, J.-D. Kim, *Chem. Mater.* **2008**, *20*, 1667.

[8] a) L. Wang, B. Liu, D. Liu, M. Yao, S. Yu, Y. Hou, B. Zou, T. Cui, G. Zou, B. Sundqvist, Z. Luo. H. Li, Y. Li, J. Liu, S. Chen, G. Wang, Y. Liu, *Appl. Phys. Lett.* **2007**, *91*, 103112; b) M. Sathish, K. Miyazawa, *J. Am. Chem. Soc.* **2007**, *129*, 13816; c) M. Sathish, K. Miyazawa, J. P. Hill, K. Ariga, *J. Am. Chem. Soc.* **2009**, *131*, 6372; d) T. Wakahara, M. Sathish, K. Miyazawa, C. Hu, Y. Tateyama, Y. Nemoto, T. Sasaki, O. Ito, *J. Am. Chem. Soc.* **2009**, *131*, 9940.

[9] a) T. Nakanishi, K. Ariga, T. Michinobu, K. Yoshida, H. Takahashi, T. Teranishi, H. Möhwald, D. G. Kurth, *Small* **2007**, *3*, 2019; b) T. Nakanishi, T. Michinobu, K. Yoshida, N. Shirahata, K. Ariga, H. Möhwald, D. G. Kurth, *Adv. Mater.* **2008**, *20*, 443.

[10] a) A. D. Bokare, A. Patnaik, *J. Phys. Chem. B* **2003**, *107*, 6079; b) N. Fujita, T. Yamashita, M. Asai, S. Shinkai, *Angew. Chem. Int. Ed.* **2005**, *44*, 1257; c) S. Deguchi, S. Mukai, *Chem. Lett.* **2006**, *35*, 396; d) T. Kawauchi, J. Kumaki, E. Yashima, *J. Am. Chem. Soc.* **2006**, *128*, 10560; e) B. Li, X. Tao, H. Kasai, H. Oikawa, H. Nakanishi, *Mater. Lett.* **2007**, *61*, 1738.

[11] a) M. Brettreich, S. Burghardt, C. Böttcher, T. Bayerl, S. Bayerl, A. Hirsh, *Angew. Chem. Int. Ed.* **2000**, *39*, 1845; b) S. Zhou, C. Burger, B. Chu, M. Sawamura, N. Nagahama, M. Toganoh, U. E. Hackler, H. Isobe, E. Nakamura, *Science* **2001**, *291*, 1944; c) M. Sawamura, K. Kawai, Y. Matsuo, K. Kanie, T. Kato, E. Nakamura, *Nature* **2002**, *419*, 702; d) H. Hotta, S. Kang, T. Umeyama, Y. Matano, K. Yoshida, S. Isoda, H. Imahori, *J. Phys. Chem. B* **2005**, *109*, 5700; e) T. Nakanishi, W. Schmitt, T. Michinobu, D. G. Kurth, K. Ariga, *Chem. Commun.* **2005**, 5982; f) A. Masuhara, Z. Tan, H. Kasai, H. Nakanishi, H. Oikawa, *Jpn. J. Appl. Phys.* **2009**, *48*, 050206.

[12] a) H. Hoppe, N. S. Sariciftci, *J. Mater. Chem.* **2006**, *16*, 45; b) X. Yang, J. Loos, *Macromolecules* **2007**, *40*, 1353; c) S. Günes, H. Neugebauer, N. S. Sariciftci, *Chem. Rev.*

2007, *107*, 1324; d) B. C. Thompson, J. M. J. Fréchet, *Angew. Chem., Int. Ed.* **2008**, *47*, 58.

[13] a) H. Hoppe, M. Niggemann, C. Winder, J. Kraut, R. Hiesgen, A. Hinsch, D. Meissner, N. S. Sariciftci, *Adv. Funct. Mater.* **2004**, *14*, 1005; b) X. Yang, J. K. J. van Duren, R. A. J. Janssen, M. A. J. Michels, J. Loos, *Macromolecules* **2004**, *37*, 2151; c) X. Yang, J. Loos, S. C. Veenstra, W. J. H. Verhees, M. M. Wienk, J. M. Kroon, M. A. J. Michels, R. A. J. Janssen, *Nano. Lett.* **2005**, *5*, 579; d) A. Swinnen, I. Haeldermans, M. vande Ven, J. D'Haen, G. Vanhoyland, S. Aresu, M. D'Olieslaeger, J. Manca, *Adv. Funct. Mater.* **2006**, *16*, 760; e) J. Peet, J. Y. Kim, N. E. Coates, W. L. Ma, D. Moses, A. J. Heeger, G. C. Bazan, *Nature Mater.* **2007**, *6*, 497; f) J. K. Lee, W. L. Ma, C. J. Brabec, J. Yuen, J. S. Moon, J. Y. Kim, K. Lee, G. C. Bazan, A. J. Heeger, *J. Am. Chem. Soc.* **2008**, *130*, 3619.

[14] a) Y. J. Xing, G. Y. Jing, J. Xu, D. P. Yu, H. B. Liu, Y. L. Li, *Appl. Phys. Lett.* **2005**, *87*, 263117; b) P. R. Somani, S. P. Somani, M. Umeno, *Appl. Phys. Lett.* **2007**, *91*, 173503; c) H. S. Shin, S. M. Yoon, Q. Tang, B. Chon, T. Joo, H. C. Choi, *Angew. Chem. Int. Ed.* **2008**, *47*, 693; d) G. Lu, L. Li, X. Yang, *Small* **2008**, *4*, 601; e) R. Bai, M. Ouyang, Z.-Z. Li, L.-G. Yang, M.-M. Shi, G. Wu, M. Wang, H.-Z. Chen, *J. Mater. Chem.* **2008**, *18*, 4318; f) T. Hasobe, A. S. D. Sandanayaka, T. Wada, Y. Araki, *Chem. Commun.* **2008**, 3372.

[15] a) T. Hasobe, H. Imahori, P. V. Kamat, T. K. Ahn, S. K. Kim, D. Kim, A. Fujimoto, T. Hirakawa, S. Fukuzumi, *J. Am. Chem. Soc.* **2005**, *127*, 1216; b) K. Hosomizu, H. Imahori, U. Hahn, J.-F. Nierengarten, A. Listorti, N. Armaroli, T. Nemoto, S. Isoda, *J. Phys. Chem. C* **2007**, *111*, 2777; c) T. Umeyama, N. Tezuka, M. Fujita, S. Hayashi, N. Kadota, Y. Matano, H. Imahori, *Chem.-Eur. J.* **2008**, *14*, 4875.

[16] a) Y.-P. Sun, C. E. Bunker, *Nature* **1993**, *365*, 398; b) Y.-P. Sun, C. E. Bunker, *Chem. Mater.* **1994**, *6*, 578; c) Y.-P. Sun, B. Ma, C. E. Bunker, B. Liu, *J. Am. Chem. Soc.* **1995**, *117*, 12705.

[17] a) H. N. Ghosh, A. V.; Sapre, J. P. Mittal, *J. Phys. Chem.* **1996**, *100*, 9439; b) M. Fujitsuka, H. Kasai, A. Masuhara, S. Okada, H. Oikawa, H. Nakanishi, A. Watanabe, O. Ito, *Chem. Lett.* **1997**, 1211; c) K. G. Thomas, V. Biju, D. M. Guldi, P. V. Kamat, M. V. George, *J. Phys. Chem. B* **1999**, *103*, 8864; d) S. Nath, H. Pal, A. V. Sapre, *Chem. Phys. Lett.* **2000,** *327*, 143; e) R. G. Alargova, S. Deguchi, K. Tsujii, *J. Am. Chem. Soc.* **2001**, *123*, 10460; f) A. Saha, A. K. Mukherjee, *J. Chem. Phys.* **2005**, *122*, 184504; g) K. Datta, A. K. Mukherjee, *J. Chem. Phys.* **2006**, *124*, 144509.

[18] a) P. V. Kamat, S. Barazzouk, K. G. Thomas, S. Hotchandani, *J. Phys. Chem. B* **2000**, *104*, 4014; b) P. V. Kamat, S. Barazzouk, S. Hotchandani, K. G. Thomas, *Chem.-Eur. J.* **2000**, *6*, 3914; c) S. Barazzouk, S. Hotchandani, P. V. Kamat, *Adv. Mater.* **2001**, *13*, 1614; d) W.

Kutner, P. Pieta, R. Nowakowski, J. W. Sobczak, Z. Kaszkur, A. L. McCarty, F. D'Souza, *Chem. Mater.* **2005**, *17*, 5635.

[19] a) S. Nath, H. Pal, A. V. Sapre, *Chem. Phys. Lett.* **2002**, *360*, 422; b) S. Nath, H. Pal, A. V. Sapre, *Chem. Phys. Lett.* **2003,** *369*, 394.

[20] a) T. Umeyama, N. Tezuka, S. Seki, Y. Matano, M. Nishi, K. Hirao, H. Lehtivuori, N. V. Tkachenko, H. Lemmetyinen, Y. Nakao, S. Sakaki, H. Imahori, *Adv. Mater.* **2010**, *22*, 1767; b) N. Tezuka, T. Umeyama, S. Seki, Y. Matano, M. Nishi, K. Hirao, H. Imahori, *J. Phys. Chem. C* **2010**, *114*, 3235.

[21] N. Sivaraman, R. Dhamodaran, I. Kaliappan, T. G. Srinivasan, P. R. Vasudeva Rao, C. K. Mathews, *Fullerene Sci. Technol.* **1994**, *2*, 233.

[22] The author examined the effects of volume ratio of good solvent–acetonitrile on the incident photon-to-current efficiency (IPCE) value. The volume ratio (1:4) was found to be an optimized condition with respect to the IPCE value.

[23] H. Ajie, M. M. Alvarez, S. J. Anz, R. D. Beck, F. Diederich, K. Fostiropoulos, D. R. Huffman, W. Krätschmer, Y. Rubin, K. E. Schriver, D. Sensharma, R. L. Whetten, *J. Phys. Chem.* **1990**, *94*, 8630.

[24] The ratio of rod-like and particulate clusters is estimated to be ~ 1:2 by counting the numbers of the clusters in the FE-SEM image of the deposited film (Figure 5d).

[25] In case of the electrode deposited from ANS–AN mixture, absorbance at 400 nm is relatively low (0.61) compared to the films prepared from the other solvent mixtures, because some parts of the deposited film inevitably exfoliate when pulled up from the cluster solution after completion of the electrophoretic process. However, the photocurrent generation efficiency based on the number of absorbed photons is calculated to be 3.3%, which is smaller than the IPCE value of the electrode prepared from BZN–AN (4.5%). Hence, given the high light-harvesting efficiency at 400 nm in the other deposited films, the light-harvesting efficiency is not a major factor determining the photocurrent generation in the present systems.

[26] a) J. W. Arbogast, C. S. Foote, *J. Am. Chem. Soc.* **1991**, *113*, 8886; b) M. R. Wasielewski, M. P. O'Neil, K. R. Lykke, M. J. Pellin, D. M. Gruen, *J. Am. Chem. Soc.* **1991**, *113*, 2774.

[27] P.-M. Allemand, A. Koch, F. Wudl, Y. Rubin, F. Diederich, M. M. Alvarez, S. J. Anz, R. L. Whetten, *J. Am. Chem. Soc.* **1991**, *113*, 1050.

[28] To shed light on the excited state dynamics, the author performed the sub-picosecond to nanosecond time-resolved transient absorption measurements on the FTO/SnO_2/$(C_{70})_m$ electrodes prepared from BZ–AN and CB–AN. Both of them showed ground-state bleaching around 550 nm and excited state absorption at > 650 nm. Although the maximum IPCE values are significantly different (4.6 and 0.8%, respectively), there

seemed to be no considerable difference in the excited state lifetimes of C_{70}. Therefore, the excited state lifetimes of C_{70} do not affect the difference in the IPCE values.

[29] a) F. C. Grozema, L. D. A. Siebbeles, J. M. Warman, S. Seki, S. Tagawa, U. Scherf, *Adv. Mater.* **2002**, *14*, 228; b) A. Saeki, S. Seki, Y. Koizumi, T. Sunagawa, K. Ushida, S. Tagawa, *J. Phys. Chem. B* **2005**, *109*, 10015; c) T. Amaya, S. Seki, T. Moriuchi, K. Nakamoto, T. Nakata, H. Sakane, A. Saeki, S. Tagawa, T. Hirao, *J. Am. Chem. Soc.* **2009**, *131*, 408.

[30] X-ray photoelectron spectroscopy measurements on the deposited film samples did not reveal any peaks originating from remaining solvents (*e.g.*, Cl, in the case of the sample prepared from DCB–AN mixture). Therefore, the author can rule out any possible effects of residual solvents on electron mobility.

[31] a) S. Kang, T. Umeyama, M. Ueda, Y. Matano, H. Hotta, K. Yoshida, S. Isoda, M. Shiro, H. Imahori, *Adv. Mater.* **2006**, *18*, 2549; b) H. Imahori, M. Ueda, S. Kang, H. Hayashi, S. Hayashi, H. Kaji, S. Seki, A. Saeki, S. Tagawa, T. Umeyama, Y. Matano, K. Yoshida, S. Isoda, M. Shiro, N. V. Tkachenko, H. Lemmetyinen, *Chem.-Eur. J.* **2007**, *13*, 10182.

[32] G. B. M. Vaughan, P. A. Heiney, J. E. Fischer, D. E. Luzzi, D. A. Ricketts-Foot, A. R. McGhie, Y.-W. Hui, A. L. Smith, D. E. Cox, W. J. Romanow, B. H. Allen, N. Coustel, J. P. McCauley, Jr., A. B. Smith III, *Science* **1991**, *254*, 1350.

[33] Time-of-flight (TOF) technique is suitable to evaluate the electron mobility of the entire film with thickness of more than several hundreds of nanometer. However, intense surface roughness of the deposited films did not allow the author to apply TOF method to the electrophoretically deposited $(C_{70})_m$ films.

[34] a) T. P. Martin, U. Näher, H. Schaber, U. Zimmermann, *Phys. Rev. Lett.* **1993**, *70*, 3079; b) W. Branz, N. Malinowski, H. Schaber, T. P. Martin, *Chem. Phys. Lett.* **2000**, *328*, 245; c) W. Branz, N. Malinowski, A. Enders, T. P. Martin, *Phys. Rev. B* **2002**, *66*, 094107.

[35] N. V. Tkachenko, L. Rantala, A. Y. Tauber, J. Helaja, P. H. Hynninen, H. Lemmetyinen, *J. Am. Chem. Soc.* **1999**, *121*, 9378.

Chapter 5

Clusterization, Electrophoretic Deposition, and Photoelectrochemical Properties of Fullerene-Functionalized Carbon Nanotube Composites

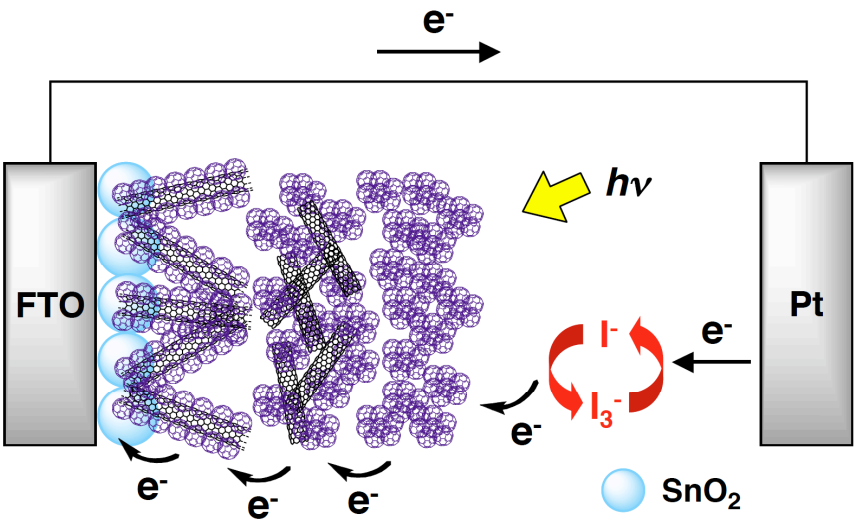

Abstract: The author has successfully developed a new methodology for the self-organization of C_{60} molecules on the sidewall of carbon nanotubes for photoelectrochemical devices. Novel nanocarbon composites of fullerene (*i.e.*, C_{60}) and highly soluble, chemically functionalized single-walled carbon nanotube (f-SWNT) have been prepared by rapid injection of poor solvent (*i.e.*, acetonitrile) into the mixed solution of C_{60} and f-SWNT in *o*-dichlorobenzene. Measurements of scanning electron microscopy for cast samples revealed that the composites are categorized into three groups; i) f-SWNT bundles covered with layers of C_{60} molecules, ii) round, large C_{60} clusters (sizes of 500 – 1000 nm) containing f-SWNT, and iii) typical, round C_{60} clusters (sizes of 150 – 250 nm). The electrophoretic deposition of the composites onto a nanostructured SnO_2 electrode yielded the hierarchical film with gradient composition depending on the difference in the mobilities of C_{60} and f-SWNT during the electrophoretic process. The composite film exhibited an incident photon-to-current efficiency as high as 18% at 400 nm under an applied potential of 0.05 V *vs.* SCE. The photocurrent generation efficiency is the highest value among carbon nanotube-based photoelectrochemical devices in which carbon nanotubes are deposited electrophoretically, electrostatically or covalently onto semiconducting electrodes. The highly aligned structure of C_{60} molecules on f-SWNT can rationalize the efficient photocurrent generation. The results obtained here will provide valuable information on the design of carbon nanotube-based molecular devices.

Introduction

Single-walled carbon nanotubes (SWNTs) have been regarded as potential materials for highly efficient transportation of charges in optoelectronic and photovoltaic devices owing to their one-dimensional structure and unique electronic and photophysical properties. However, the poor solubility of SWNTs in aqueous or organic solvents due to the extremely strong π-π interaction has resulted in a marked impediment to their applications. Covalent chemical functionalization is one of the promising approaches to impart sufficient solubility to SWNTs.[1–7] Extensive sidewall functionalization is known to disrupt the conjugated π-systems of SWNTs.[1,3–7] On the other hand, shortened SWNTs by acid treatment largely preserve the characteristic electronic structure, since the chemical functionalization (*i.e.*, carboxylic group) localizes at terminals and defect sites of the nanotube structure and in turn most of the sidewall remains intact.[2] Noncovalent functionalization using hydrophobic interaction[8–10] in aqueous solvents and π-π interaction in aqueous or organic solvents[11–13] is an alternative approach because it can provide a general method of dissolving SWNTs without altering the electronic structure. Various π electron-donating compounds including pyrenes,[11] porphyrins,[12] and π-conjugated polymers[13] have been employed to interact with SWNTs, leading to formation of supramolecular complexes in aqueous or organic media under ultrasonication. Thus, the complexation of π electron-rich compounds with SWNTs imparts moderate solubility to SWNTs. Nevertheless, integration of such complexes into photoelectrochemical and photovoltaic devices has not given satisfactory results due to the insufficient debundling of SWNTs by the π electron-rich compounds.[14]

Three-dimensional structural fullerenes are carbon allotropes that exhibit peculiar electron transfer (ET) properties. There has been intensive research on photovoltaic systems utilizing fullerenes and their derivatives as acceptors,[15,16] because the small reorganization energies of fullerenes in ET lead to remarkable acceleration of photoinduced charge separation (CS) and of charge shift as well as deceleration of charge recombination (CR).[17] With these in mind, arrangement of fullerene molecules along SWNTs is an attractive strategy to attain efficient transportation of charges in photoelectrochemical and photovoltaic devices. Examples of such arrangement, however, are almost limited to the fullerene-encapsulated SWNTs (bucky-peapods),[18,19] which are insoluble in organic solvents, making it difficult to apply them to molecular devices. No fullerene–SWNT composites utilizing π-π interaction between fullerene and the external sidewall of SWNTs have been isolated and investigated owing to the poor solubility of the composites in organic solvents. Although there are several examples of the ternary composites comprising of C_{60}, SWNTs, and other π-conjugated compounds,[20] the interaction between C_{60} and SWNTs has attracted rather less attention in the complicated ternary systems.

Recently, Mitra *et al.* reported the formation of C_{60}–SWNT supramolecular complex in toluene–H_2O or toluene–EtOH (v/v = 1/25) by microwave irradiation.[21] They spin-coated the composite solution with poly(3-hexylthiophene) (P3HT) to an ITO electrode to fabricate bulk heterojunction solar cells. The power conversion efficiency (0.57%) was found to be improved compared to the reference cell comprising of P3HT and C_{60} without SWNTs under their experimental conditions, but is much smaller than the typical value (3 – 5%) of P3HT–C_{60} bulk heterojunction solar cells.[22] Thus, the relationship between the structure and photovoltaic properties of C_{60}–SWNT composites remains elusive.

Here the author reports on a novel strategy for the arrangement of C_{60} molecules on the external surface of SWNTs (Scheme 1). First, acid treatment cuts pristine SWNTs (denoted as p-SWNT) to yield shortened SWNTs (denoted as s-SWNT) with carboxylic groups at the open ends and defect sites (Scheme 1, step 1).[2] Then, s-SWNT is functionalized with sterically hindered amine (*i.e.*, swallow-tailed secondary amine) to yield soluble, functionalized SWNTs (denoted as f-SWNT) in organic solvents (step 2). Finally, poor solvent (*i.e.*, acetonitrile) is rapidly injected into a mixture of C_{60} and f-SWNT in good solvent (*o*-dichlorobenzene (ODCB)), resulting in formation of the composite clusters of C_{60} and f-SWNT (denoted as $(C_{60}$+f-SWNT$)_m$).[23] The author expected that lyophobic interaction between C_{60}–f-SWNT and the mixed solvent as well as the π-π interaction between C_{60} molecules and between C_{60} and f-SWNT would lead to the desirable arrangement of C_{60} molecules on the external surface of SWNTs in the mixed solvent (step 3). The author also describes the photoelectrochemical properties of the C_{60}–f-SWNT composites electrophoretically deposited onto a nanostructured SnO_2 electrode.[24,25] A series of microscopic and photoelectrochemical studies on the deposited composite films has been performed to elucidate the relationship between the structures and the photoelectrochemical properties of the novel C_{60}–f-SWNT composites.

SCHEME 1

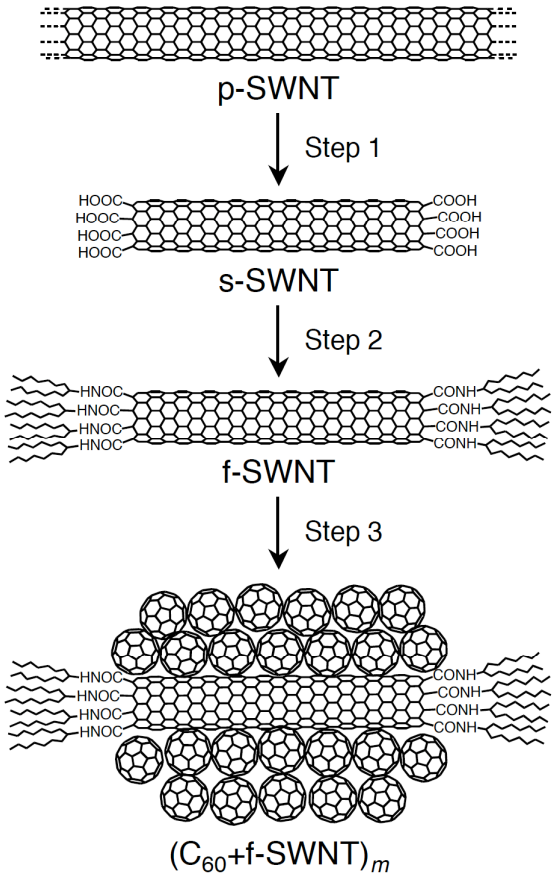

Results and Discussion

Preparation of Functionalized SWNTs: f-SWNT was prepared by purification and oxidation of p-SWNT (HiPco, purified grade) and subsequent reaction of s-SWNT with thionyl chloride and 8-aminopentadecane.[2] f-SWNT is soluble in common organic solvents including *o*-dichlorobenzene, chloroform, THF, and toluene and shows the solubility of up to ~ 1.0 g L^{-1} in ODCB after sonication for 30 min. The solution is stable during at least one month. It is noteworthy that the solubility of f-SWNT is remarkably improved relative to that of similar SWNTs (0.4 g L^{-1} in ODCB)[5c] functionalized with the long alkyl amine (*i.e.*, octadecylamine) instead of the swallow-tailed secondary amine. The atomic force microscopy (AFM) image of f-SWNT (Figure 1a), which is obtained for the sample spin-coated on freshly cleaved mica

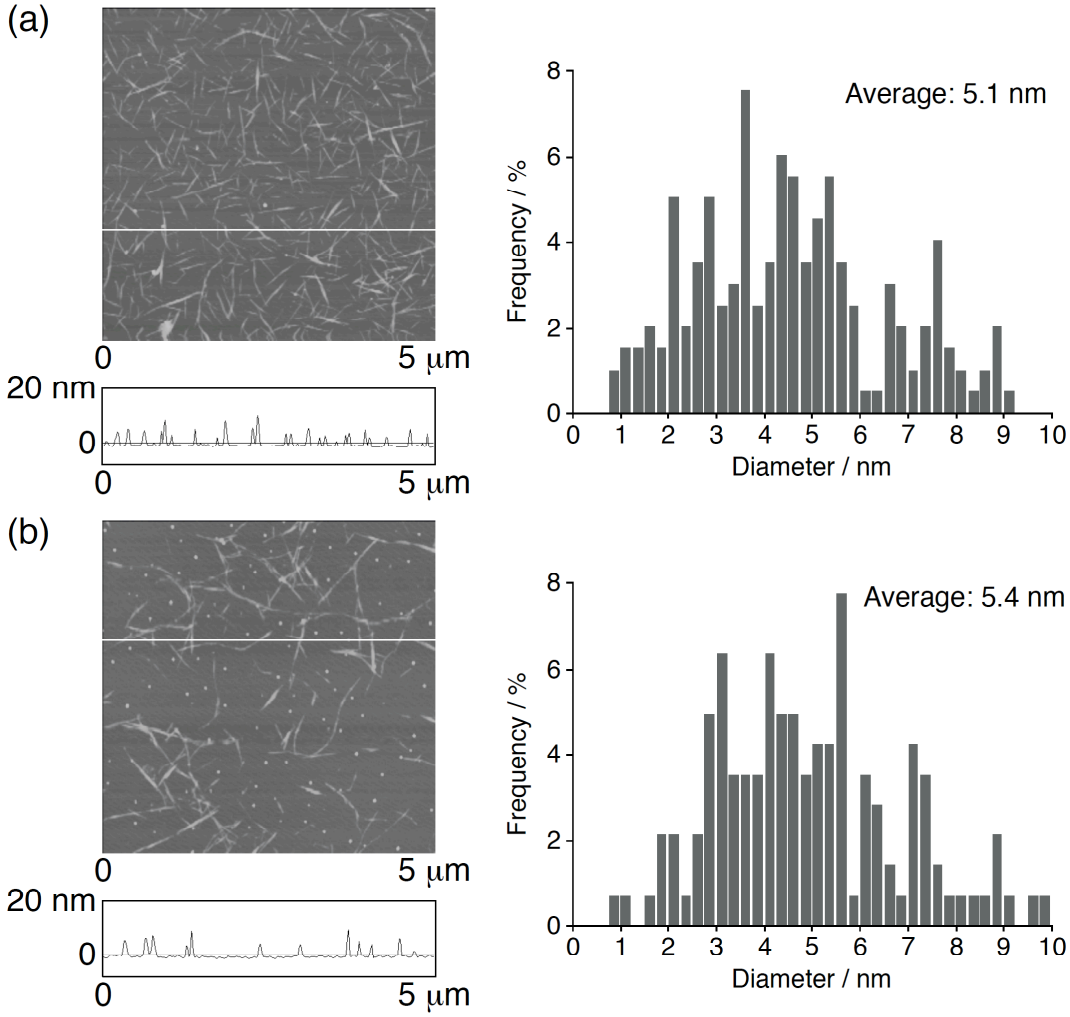

Figure 1. AFM images and section profiles of f-SWNT (*Z* range: 60 nm). The samples were prepared by spin-coating (a) ODCB solution (0.098 g L^{-1}) and (b) ODCB–acetonitrile solution (1:3, v/v; 0.024 g L^{-1}) of f-SWNT on freshly cleaved mica. The color scale represents the height topography, with bright and dark representing the highest and lowest features, respectively. Corresponding Diameter distributions for the isolated bundles are shown in the right panels.

from the ODCB solution of f-SWNT, discloses the short, thin rod-like structures attributed to the bundles of f-SWNT. The average diameter of isolated bundles of f-SWNT is determined to be 5.1 nm. These results demonstrate that the author's strategy is useful for the solubilization of SWNTs which allows π electron-rich compounds to interact with the sidewalls, making the supramolecular complex in organic solvents (*vide infra*).

Clusterization: UV–vis–near IR (NIR) absorption spectra of C_{60}, f-SWNT, and the composite were measured in ODCB and ODCB–acetonitrile mixture (1:3, v/v). The absorption spectrum of f-SWNT (Figure 2A(a)) in ODCB (0.024 g L^{-1}) shows characteristic peaks associated with the transitions between symmetric van Hove singularities in the density of states for SWNTs, implying that the electronic structure of SWNTs is retained after the chemical modification.[2] The appearance of the moderately sharp peaks discloses that f-SWNT is dispersed modestly in ODCB, since the sharpness of these peaks is widely considered to be a measure for the level of exfoliation of SWNT bundles. To examine the clusterization behavior of f-SWNT by lyophobic interaction, acetonitrile (poor solvent) was added rapidly to an ODCB (good solvent) solution of f-SWNT (0.098 g L^{-1}). The absorption spectrum of the resulting pale black, transparent solution in the ODCB–acetonitrile mixture (1:3, v/v) (Figure 2A(b)) is largely similar to that of f-SWNT in ODCB under the same concentration. The similarity in the sharpness of the absorption peaks in the two spectra suggests that the size of the bundles is largely preserved after the injection of acetonitrile.

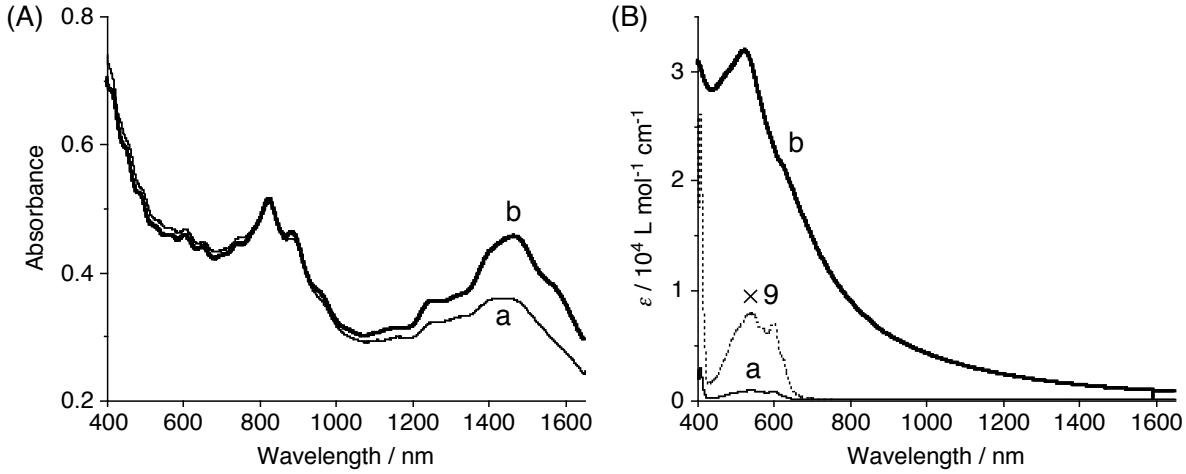

Figure 2. (A) UV–vis–NIR absorption spectra of f-SWNT (0.024 g L^{-1}) in (a) ODCB and (b) ODCB–acetonitrile (1:3, v/v). Path length: 1 cm. (B) UV–vis–NIR absorption spectra of C_{60} in (a) ODCB (0.56 mM) and (b) ODCB–acetonitrile (1:3, v/v; 0.070 mM). To measure the absorption spectrum in the mixed solvent accurately, acetonitrile was injected into the ODCB solution of C_{60} (0.56 mM) to give an ODCB–acetonitrile (1:3, v/v) solution of C_{60} (0.14 mM). Then, the solution was diluted to yield an ODCB–acetonitrile (1:3, v/v) solution of C_{60} (0.070 mM).

However, there is a slight difference in the absorption intensity of f-SWNT in the mixed solvent relative to that in ODCB, which may be attributed to a small increase in the bundle size in the mixed solvent or difference in the solvent polarity or light scattering. Small vibration of the cuvette caused the precipitation of f-SWNT, making the solution transparent, thereby showing that the clusters of f-SWNT (denoted as $(\text{f-SWNT})_m$) are unstable in the mixed solvent (*vide infra*). The AFM image of f-SWNT (Figure 1b), which is obtained for the sample spin-coated on freshly cleaved mica from the ODCB–acetonitrile (1:3, v/v) solution of f-SWNT, also reveals the short, thin rod-like structures, but the average diameter (5.4 nm) of the isolated bundles is slightly larger than that from the ODCB solution. Thus, the author can conclude that the size of the bundles of f-SWNT in the mixed solvent is slightly larger than that in ODCB due to the lyophobic interaction with the mixed solvent.

In contrast, the clusterization behavior of C_{60} is different from that of f-SWNT. An ODCB–acetonitrile solution of C_{60} (1:3, v/v) was prepared by rapid injection of acetonitrile to an ODCB solution of C_{60} (0.56 mM). Compared with the absorption spectrum of C_{60} in ODCB (Figure 2B(a)), that in the mixed solvent (Figure 2B(b)) exhibits broad absorption with a maximum at 520 nm and the molar extinction coefficient in the mixed solvent is much larger than that in ODCB. The absorption behavior of C_{60} in the mixed solvent is attributed to the formation of stable C_{60} clusters (denoted as $(C_{60})_m$) by lyophobic interaction in the mixed solvent.[23] Dynamic light scattering (DLS) measurement of the cluster solution revealed that the size distribution of the $(C_{60})_m$ cluster is relatively narrow with an average diameter of 200 nm. Similar clusterization behavior of C_{60} is noted in toluene–acetonitrile mixture.[23]

The absorption spectrum of a mixture of C_{60} (0.56 mM, 0.40 g L^{-1}) and f-SWNT (0.098 g L^{-1}) in ODCB, together with the single component spectra of C_{60} and f-SWNT in ODCB is depicted in Figure 3A. The absorption spectrum of the mixture in ODCB (Figure 3A(c)) matches the sum of the absorption spectra of C_{60} and f-SWNT in ODCB (Figure 3A(d)), implying that there is no significant interaction between C_{60} and f-SWNT in ODCB. The clusterization behavior of C_{60}–f-SWNT composite is also different from that of C_{60} and f-SWNT. The absorption spectrum of the mixture of C_{60} and f-SWNT in ODCB–acetonitrile (1:3, v/v) (Figure 3B(c))[26] shows structureless, broad absorption, which is different from those of C_{60} (Figure 3B(a)) and f-SWNT (Figure 3B(b)) in the same mixed solvents. Moreover, the absorption spectrum of the mixture of C_{60} and f-SWNT in the mixed solvent does not match the sum of the absorption spectra of f-SWNT and C_{60} in the same mixed solvents (Figure 3B(d)). These results indicate that C_{60} molecules interact with f-SWNT to form the composite clusters of $(C_{60}+\text{f-SWNT})_m$ in the mixed solvent.

Field emission scanning electron microscopy (FE-SEM) measurements were performed to evaluate the shapes and morphology of C_{60}, f-SWNT, and the composite of C_{60} and f-SWNT in

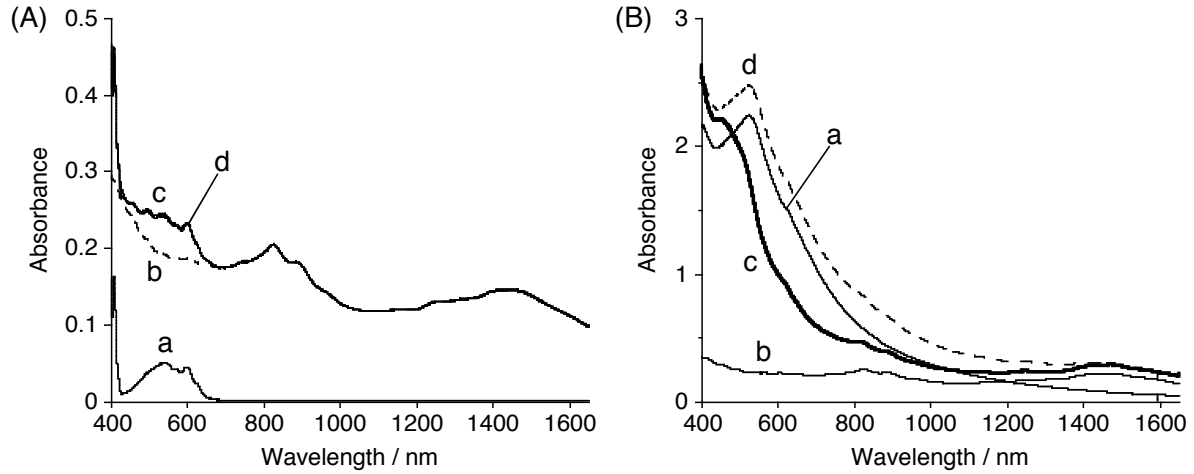

Figure 3. (A) UV–vis–NIR absorption spectra of (a) C_{60} (0.56 mM, 0.40 g L^{-1}), (b) f-SWNT (0.098 g L^{-1}), and (c) a mixture of C_{60} (0.56 mM) and f-SWNT (0.098 g L^{-1}) in ODCB and (d) the sum of the spectra (a) and (b). Path length: 1 mm. (B) UV–vis–NIR absorption spectra of (a) C_{60} (0.070 mM, 0.050 g L^{-1}), (b) f-SWNT (0.012 g L^{-1}), and (c) a mixture of C_{60} (0.070 mM) and f-SWNT (0.012 g L^{-1}) in ODCB–acetonitrile mixture (1:3, v/v) and (d) the sum of spectra (a) and (b). Path length: 1 cm.

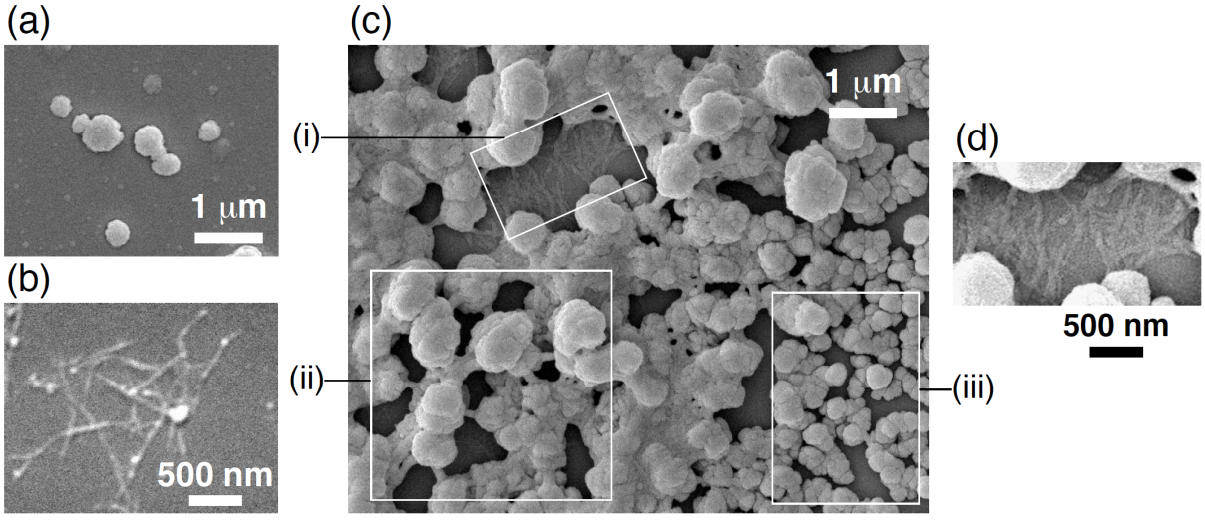

Figure 4. FE-SEM images of clusters of (a) C_{60}, (b) f-SWNT, and (c) composites of f-SWNT and C_{60}. The samples were prepared by casting ODCB–acetonitrile (1:3, v/v) solution of C_{60} (0.14 mM) and/or f-SWNT (0.024 g L^{-1}) on a glass plate. The image (c) is classified into three regions (i, ii, iii). (d) Enlarged, rotated image of area (i) in (c).

ODCB–acetonitrile mixture. The samples for the FE-SEM measurements were prepared by casting the ODCB–acetonitrile solution to a glass plate. The FE-SEM image of $(C_{60})_m$ clusters discloses spherical particles with sizes of 150 – 350 nm (Figure 4a), which is consistent with the average diameter (200 nm) of $(C_{60})_m$ clusters obtained by the DLS measurement (*vide supra*). The FE-SEM image of f-SWNT reveals spaghetti-like structure where fibrils are

entangled (Figure 4b). Obviously, the observed fibrous structure results from the bundles of f-SWNT, since the size of individual f-SWNT (an average diameter of ~ 1 nm) is beyond the instrument's resolution. On the other hand, the FE-SEM image of $(C_{60}$+f-SWNT$)_m$ is classified into three groups (Figure 4c). The first area (i) shows the entangled fibril-like structure (Figure 4d), as seen in the FE-SEM image of f-SWNT. However, the average diameter of the fibrils is larger by 10 – 20 nm than that of f-SWNT in Figure 4b,[27] suggesting the interaction of the bundles of f-SWNT with C_{60} to yield the fibrils with the larger diameter (*vide infra*). The second area (ii) displays network structure in which spherical particles with diameters of 500 – 1000 nm are interconnected each other. The network structure suggests that C_{60} clusters are self-assembled with the bundles of f-SWNT to form larger clusters involving f-SWNT, resulting in formation of the interconnected structure. In the third area (iii), there exist spherical particles with an average diameter of 200 nm, which agrees well with the size of the $(C_{60})_m$ clusters determined by using DLS and FE-SEM. Judging from the size and the shape, the spherical particles are assigned to $(C_{60})_m$. The formation of the $(C_{60})_m$ clusters is reasonable considering the high weight ratio of C_{60} *vs*. f-SWNT (4.1:1) in the mixed solution. Hereafter, the clusters observed in the areas (i), (ii), and (iii) are referred to cluster I, II, and III, respectively.[28]

Electrophoretic Deposition: It is known that clusters of C_{60},[23–25] cup-stacked carbon nanostructures,[29] and SWNTs[30,31] can be deposited electrophoretically onto electrodes by applying dc voltage to the electrode. In a similar manner, the clusters of C_{60}, f-SWNT, and the composites in ODCB–acetonitrile mixture ([C_{60}] = 0.14 mM, [f-SWNT] = 0.024 g L^{-1}) were attached to the fluorine-doped tin oxide (FTO) electrodes with nanostructured SnO_2 modification (denoted as FTO/SnO_2/$(C_{60})_m$, FTO/SnO_2/(f-SWNT)$_m$, and FTO/SnO_2/(C_{60}+ f-SWNT)$_m$), respectively. Under application of a high dc electric field (200 V for 120 s), the clusters of C_{60}, f-SWNT, and the composites, which are negatively charged in the mixed solvent, are driven toward the positively charged electrode (*i.e.*, FTO/SnO_2). With increasing time of deposition, the FTO/SnO_2 electrode turns brown for $(C_{60})_m$ and (C_{60}+f-SWNT)$_m$ or black for (f-SWNT)$_m$ in color with simultaneous discoloration of the cluster solution. All of the electrophoretically deposited films are sufficiently robust for the photoelectrochemical measurements. The change in absorbance of the electrophoretically deposited electrodes is monitored at 400 nm with increasing time of deposition (Figure 5A). The time to reach a maximum absorbance becomes long in the order of (f-SWNT)$_m$ < (C_{60}+f-SWNT)$_m$ ~ $(C_{60})_m$, showing the faster deposition of (f-SWNT)$_m$ than that of $(C_{60})_m$. As the author discusses later, the difference in the mobilities of the clusters affects the structures of the deposited composite film of C_{60} and f-SWNT. For the following experiments, the author used electrodes prepared

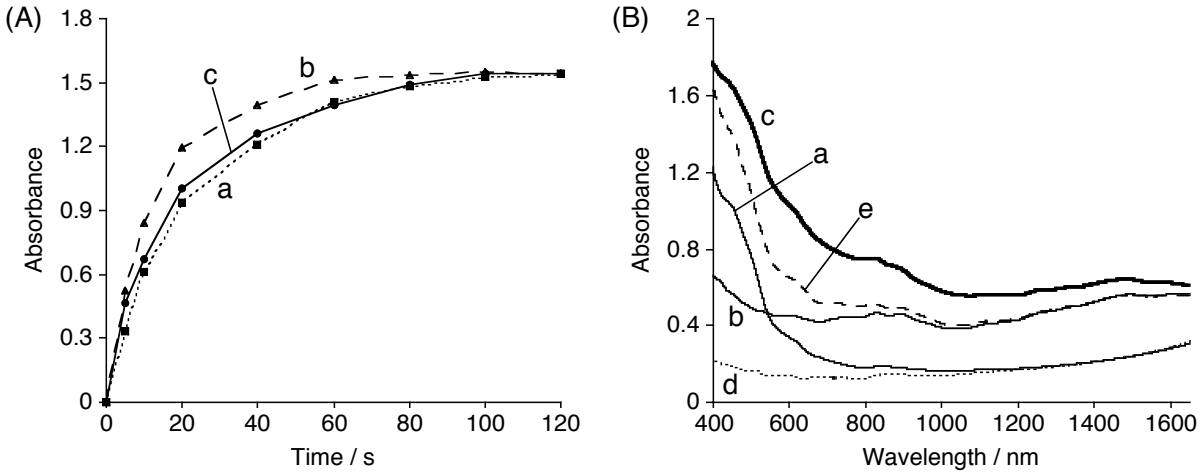

Figure 5. (A) Change in absorbance of (a) FTO/SnO_2/$(C_{60})_m$, (b) FTO/SnO_2/(f-SWNT)$_m$, and (c) FTO/SnO_2/(C_{60}+f-SWNT)$_m$ at different time intervals during electrophoretic deposition process. The absorbance of FTO/SnO_2 electrode was subtracted from each spectrum. The time profiles of (a) and (b) are normalized to that of (c) for comparison. (B) UV–vis–NIR absorption spectra of (a) FTO/SnO_2/$(C_{60})_m$, (b) FTO/SnO_2/(f-SWNT)$_m$, (c) FTO/SnO_2/(C_{60}+f-SWNT)$_m$, and (d) FTO/SnO_2 electrodes. (e) Spectrum of (a) + (b) – (d) is shown for comparison. The films were prepared by electrophoretic deposition with duration time of 120 s, using the corresponding cluster solutions.

by the electrophoretic deposition of C_{60} and/or f-SWNT in ODCB–acetonitrile mixture (1:3, v/v; [C_{60}] = 0.14 mM, [f-SWNT] = 0.024 g L^{-1}) with the duration time of 120 s, unless otherwise noted.

The UV–vis–NIR absorption spectra of the deposited films on nanostructured SnO_2 electrodes are shown in Figure 5B. The absorption features of the deposited films are largely similar to those in the corresponding ODCB–acetonitrile solutions (Figure 3B), showing that the clusters in the mixed solvent are successfully deposited onto the nanostructured SnO_2 electrodes without significant change in the cluster structures. In addition, the broad absorption of these films as well as the high molar absorptivity in the visible and NIR regions makes these films suitable for harvesting the solar energy.

Resonant Raman spectroscopy is a valuable tool to characterize SWNTs, since it provides detailed information on the structure. Low-wavenumber phonon modes, *i.e.*, radial breathing modes (RBMs), are very susceptible to the nanotube diameter and electronic states. Taking into account Kataura plot[32] with diameters of HiPco SWNTs (0.8 – 1.3 nm),[8] one can monitor semiconducting and metallic SWNTs with diameters of 0.8 – 1.0 and 1.0 – 1.3 nm, respectively, by an excitation energy of 1.96 eV (λ_{ex} = 633 nm). The resonant Raman spectra of FTO/SnO_2/$(C_{60})_m$, FTO/SnO_2/(f-SWNT)$_m$, FTO/SnO_2/(C_{60}+f-SWNT)$_m$, and f-SWNT cast on a glass plate from the ODCB solution were measured with a laser excitation energy of 1.96 eV (Figure 6). The Raman spectrum of FTO/SnO_2/$(C_{60})_m$ exhibits several peaks (200 – 300 cm^{-1})

stemming from the vibration of C_{60} (Figure 6b).[33] Intensity of the Raman signals of FTO/SnO_2/$(C_{60})_m$, however, is much smaller than that of the FTO/SnO_2/(f-SWNT)$_m$ (Figure 6c). On the other hand, it is well known that SWNTs show characteristic peaks attributed to tangential mode (G-band) around 1600 cm^{-1} and disorder mode (D-band) around 1350 cm^{-1}.[34] The ratio of the peak intensities (G/D ratio) reflects the relative amount of sp^3 carbon, and is used to determine the degree of functionalization in SWNTs.[34] The G/D ratios of f-SWNT (Figure 6a), FTO/SnO_2/(f-SWNT)$_m$, and FTO/SnO_2/(C_{60}+f-SWNT)$_m$ (Figure 6d) are virtually the same, implying that the electronic structure of f-SWNT is preserved after the electrophoretic deposition of (f-SWNT)$_m$ and (C_{60}+f-SWNT)$_m$ onto FTO/SnO_2 electrodes. In addition, the positions and shapes of the peaks in RBM region are almost the same, indicating that the structure and composition of f-SWNT are also retained after the electrophoretic deposition process.

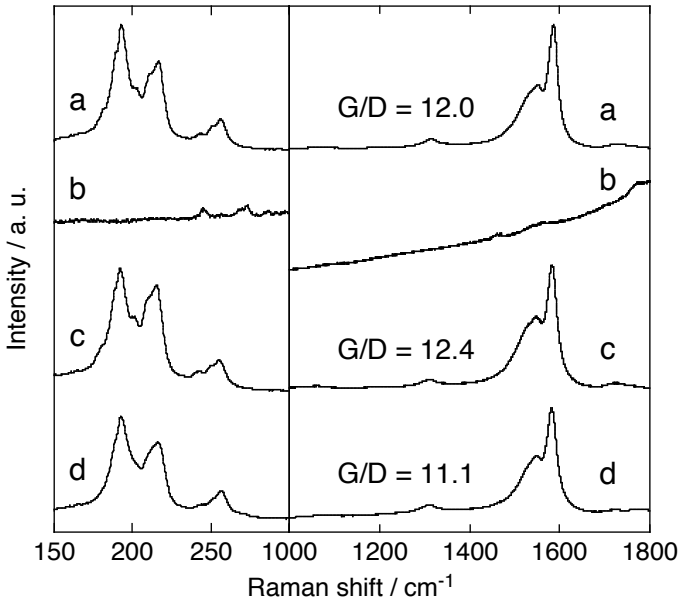

Figure 6. Resonant Raman spectra of (a) f-SWNT cast on a glass plate from the ODCB solution, (b) FTO/SnO_2/$(C_{60})_m$, (c) FTO/SnO_2/(f-SWNT)$_m$, and (d) FTO/SnO_2/(C_{60}+f-SWNT)$_m$ under laser excitation with an excitation energy of 1.96 eV (633 nm). Each spectrum is normalized with respect to its maximum and offset for comparison.

FE-SEM was employed to evaluate the surface morphology of the films prepared by the electrophoretic deposition with the duration time of 120 s as shown in Figure 7. The FE-SEM image of FTO/SnO_2/$(C_{60})_m$ electrode (Figure 7a) shows closely packed clusters with sizes of 100 – 200 nm, which are largely similar to that of $(C_{60})_m$ in the mixed solvent.[23–25] The FTO/SnO_2/(f-SWNT)$_m$ electrode reveals that the bundles of f-SWNT lie horizontally on the electrode surface and are entangled each other (Figure 7b). The spherical particles on the surface of the f-SWNT bundles may be metal particles that are persisting in the sample of f-SWNT even after the purification procedure. The average diameter of the bundles is determined to be 12 nm. It is noteworthy that the surface morphology of FTO/SnO_2/(C_{60}+f-SWNT)$_m$ (Figure 7c) is quite similar to that of FTO/SnO_2/$(C_{60})_m$ (Figure 7a). This observation manifests that the top layer of the (C_{60}+f-SWNT)$_m$ film consists of C_{60} clusters originating from the cluster III in Figure 4c. This result agrees well with the higher mobility of

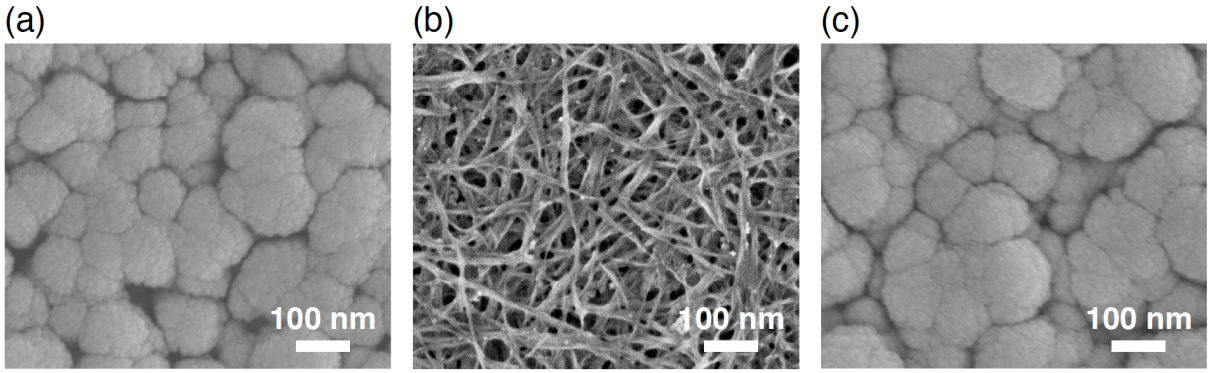

Figure 7. FE-SEM images of (a) FTO/SnO_2/$(C_{60})_m$, (b) FTO/SnO_2/(f-SWNT)$_m$, and (c) FTO/SnO_2/(C_{60}+f-SWNT)$_m$ electrodes. The samples were prepared from corresponding cluster solutions by electrophoretic deposition with duration time of 120 s.

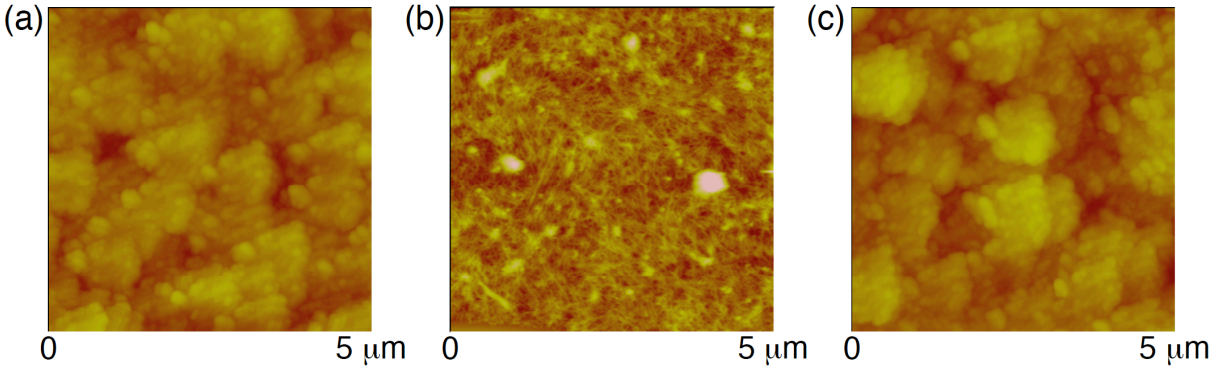

Figure 8. AFM images of (a) FTO/SnO_2/$(C_{60})_m$, (b) FTO/SnO_2/(f-SWNT)$_m$, and (c) FTO/SnO_2/(C_{60}+f-SWNT)$_m$ electrodes (Z range: (a) 800 nm, (b) 200 nm, (c) 800 nm). The samples were same as those used for FE-SEM observation (Figure 7).

(f-SWNT)$_m$ than that of $(C_{60})_m$ during the electrophoretic deposition (Figure 5A). The author also performed AFM measurements of FTO/SnO_2/$(C_{60})_m$, FTO/SnO_2/(f-SWNT)$_m$, and FTO/SnO_2/(C_{60}+f-SWNT)$_m$ electrodes (Figure 8). The AFM images of FTO/SnO_2/$(C_{60})_m$ (Figure 8a) and FTO/SnO_2/(C_{60}+f-SWNT)$_m$ (Figure 8c) exhibit the closely-packed $(C_{60})_m$ clusters with similar diameters of 100 – 200 nm, whereas that of FTO/SnO_2/(f-SWNT)$_m$ (Figure 8b) discloses the entangled, fibrous-shaped (f-SWNT)$_m$ clusters. Thus, the AFM images match well the corresponding FE-SEM images.

To shed light on the inner topography of the (C_{60}+f-SWNT)$_m$ film on the FTO/SnO_2 electrode, the author examined the change of the (C_{60}+f-SWNT)$_m$ films as a function of deposition time. Figure 9 shows the FE-SEM images of FTO/SnO_2/(C_{60}+f-SWNT)$_m$ electrodes obtained from the ODCB–acetonitrile solution (1:3, v/v) of C_{60} (0.14 mM) and f-SWNT (0.024 g L^{-1}) with the deposition time of 10, 20, 40, and 60 s. At the deposition time of 10 s, the FE-SEM image reveals entangled fibrous structures lying horizontally on the electrode surface

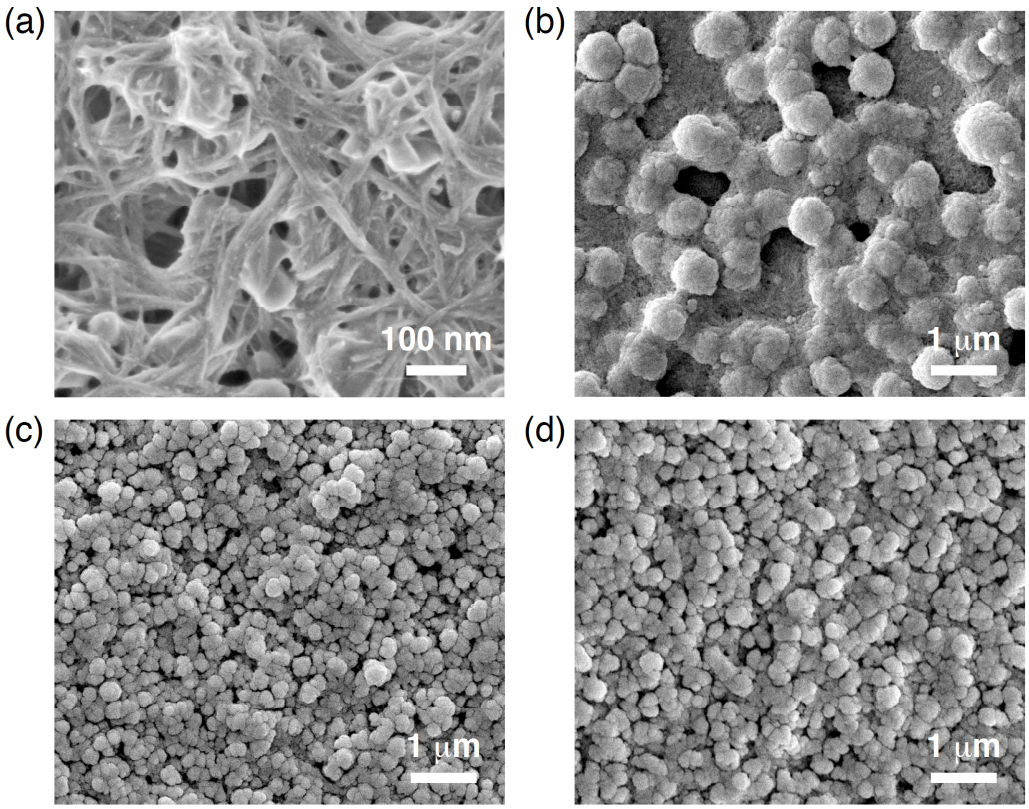

Figure 9. FE-SEM images of FTO/SnO_2/(C_{60}+f-SWNT)$_m$ electrodes obtained with deposition time of (a) 10 s, (b) 20 s, (c) 40 s, and (d) 60 s.

(Figure 9a). The average diameter of the strings are estimated as 18 nm, which is evidently larger than that of the bundles (12 nm) for FTO/ SnO_2/(f-SWNT)$_m$ without C_{60} (Figure 7b). This result is in accordance with the difference in the FE-SEM images of (f-SWNT)$_m$ and cluster I (Figure 4b and d).[27,35] In addition, the FE-SEM image of FTO/SnO_2/(f-SWNT)$_m$ electrode at the deposition time of 10 s exhibits well-defined bundle structures with an average diameter of 12 nm (Figure 10), as seen in the FE-SEM image at the deposition time of 120 s. Thus, the author can conclude that the increase in the diameter of the strings in Figure 9a compared to that in Figure 7b is attributed to C_{60} molecules on the bundles of (f-SWNT)$_m$. In other words, when acetonitrile is injected into the ODCB solution of C_{60} and f-SWNT, some of C_{60} molecules interact with the sidewall of the bundles of f-SWNT by π-π and lyophobic interaction, leading to the arrangement of C_{60} molecules on the sidewall of the bundles of f-SWNT, as depicted in

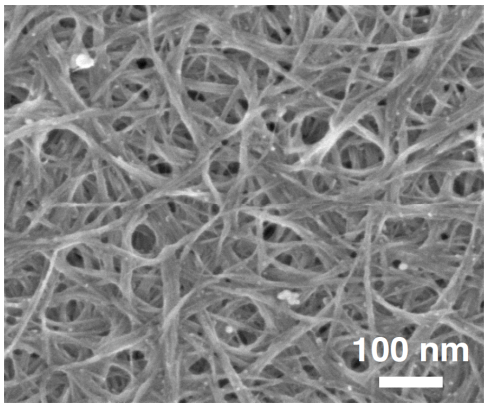

Figure 10. FE-SEM image of FTO/ SnO_2/(f-SWNT)$_m$ electrode prepared with deposition time of 10 s.

Scheme 1. Considering the difference (6 nm) in the average diameters of (f-SWNT)$_m$ and (C_{60}+f-SWNT)$_m$ on the electrodes, the thickness of the C_{60} layer is calculated to be *ca.* 3 nm, corresponding to a three layer of C_{60}.

At the deposition time of 20 s, the FE-SEM image of FTO/SnO_2/(C_{60}+f-SWNT)$_m$ electrode shows the structure composed of connected round-shaped, rugged particles with diameters of 500 – 1000 nm (Figure 9b). Taking into account the similar shape and size of the particles and cluster II, the author assigns the particles as cluster II, where small C_{60} clusters would be further self-assembled with f-SWNT to yield the large spherical clusters comprising of C_{60} and f-SWNT. The FE-SEM images of FTO/SnO_2/(C_{60}+f-SWNT)$_m$ electrodes at the deposition time of 40 and 60 s (Figure 9c and d) exhibit similar closely-packed particles with diameters of 150 – 300 nm, which are almost identical to the FE-SEM image at the deposition time of 120 s (Figure 7c). These results corroborate that clusters I, II, and III are sequentially deposited onto the FTO/SnO_2 electrode, depending on the difference in the mobilities under the application of dc voltage to the cluster solution, yielding the hierarchical film with the gradient composition along the direction of the film thickness.

Photoelectrochemical Properties: Photoelectrochemical measurements were performed in deaerated acetonitrile containing 0.5 M LiI and 0.01 M I_2 with FTO/SnO_2/(C_{60}+f-SWNT)$_m$ as a working electrode, a platinum wire as a counter electrode, and I^-/I_3^- reference electrode. The FTO/SnO_2/(C_{60}+f-SWNT)$_m$ electrode was prepared from the cluster solution of (C_{60}+f-SWNT)$_m$ ([C_{60}] = 0.14 mM, [f-SWNT] = 0.024 g L^{-1}) in ODCB–acetonitrile (1:3, v/v). Figure 11a displays photocurrent response of the FTO/SnO_2/(C_{60}+f-SWNT)$_m$ electrode illuminated at an excitation wavelength of 400 nm (input power: 1.81 μW cm^{-2}) at +0.05 V *vs*. SCE. The photocurrent responses are prompt, steady, and reproducible during the repeated on/off cycles of the visible light illumination. Blank experiments of FTO/SnO_2 electrode without the composite film exhibited much smaller photocurrent responses under the same conditions. These results confirm the role of the composite film toward harvesting light energy and generating electron flow from the electrolyte to the FTO/SnO_2 electrode through the film during the operation of the photoelectrochemical device. Figure 11b shows current–applied potential curve of the FTO/SnO_2/(C_{60}+f-SWNT)$_m$ system under white light illumination (λ > 380 nm; input power: 78.8 mW cm^{-2}). With increasing positive bias up to 0.05 V *vs*. SCE, the photocurrent increases compared to the dark current. Increased charge separation and the facile transportation of charge carriers under positive bias are responsible for the enhanced photocurrent generation. As reported by Kamat and co-workers,[23–25,30,31] FTO/SnO_2/(C_{60})$_m$ and FTO/SnO_2/(f-SWNT)$_m$ systems show similar photoelectrochemical behavior to that of the FTO/SnO_2/(C_{60}+f-SWNT)$_m$ system (*vide infra*).

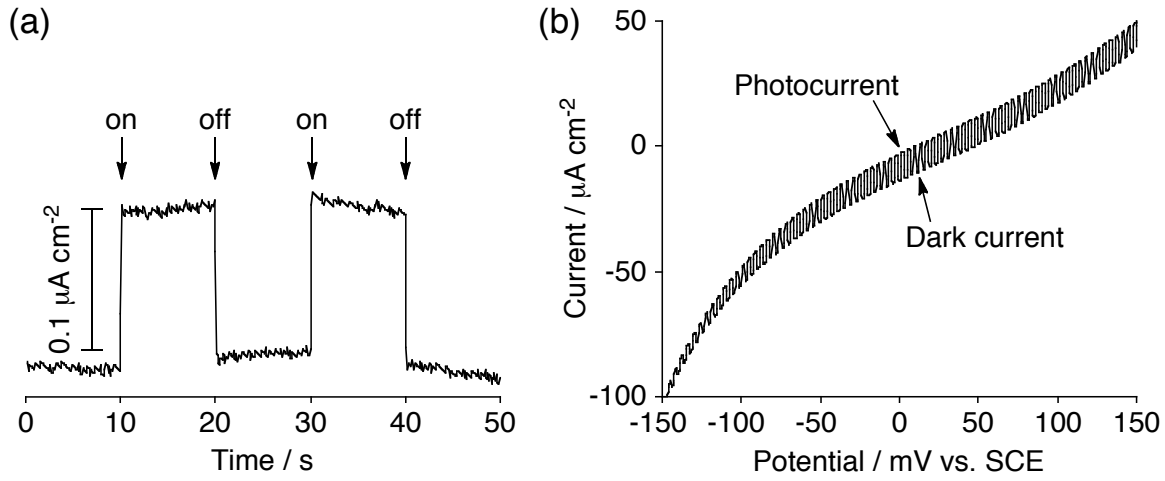

Figure 11. (a) Photocurrent response of FTO/SnO_2/(C_{60}+f-SWNT)$_m$ illuminated at 400 nm (1.81 μW cm^{-2}). Applied potential: +0.05 V *vs.* SCE. (b) Current *vs.* potential curve for FTO/SnO_2/(C_{60}+f-SWNT)$_m$ device under illumination with white light (λ > 380 nm, input power: 78.8 mW cm^{-2}). Electrolyte: 0.5 M LiI and 0.01 M I_2 in acetonitrile.

To evaluate the photoelectrochemical response of the FTO/SnO_2/(C_{60}+f-SWNT)$_m$ system, the author examined the wavelength dependence of the incident photon-to-current efficiency (IPCE) of the film on FTO/SnO_2. The IPCE values are calculated by normalizing the photocurrent densities for incident light energy and intensity and by use of the expression:

$$\text{IPCE (\%)} = 100 \times 1240 \times i/(W_{\text{in}} \times \lambda)$$

where i is the photocurrent density (A cm^{-2}), W_{in} is the incident light intensity (W cm^{-2}), and λ is the excitation wavelength (nm). Figure 12a illustrates the photocurrent action spectrum of the FTO/SnO_2/(C_{60}+f-SWNT)$_m$ system. The maximum IPCE value reaches up to 18% at 400 nm under an applied potential of 0.05 V *vs*. SCE. It should be noted here that the IPCE value of the FTO/SnO_2/(C_{60}+f-SWNT)$_m$ system monotonically decreases with increasing the wavelength to reach almost zero at 730 nm, which does not match the absorption feature of the FTO/SnO_2/(C_{60}+f-SWNT)$_m$ electrode (Figure 5B(c)). Namely, the FTO/SnO_2/(C_{60}+f-SWNT)$_m$ electrode exhibits significant absorbance at 700 – 1600 nm, which mainly results from the absorption of f-SWNT and light scattering. These results suggest that the absorption of visible light (400 – 700 nm) by C_{60} molecules is responsible for the photocurrent generation and the contribution by the excitation of f-SWNT is minor.

The photocurrent action spectrum of the FTO/SnO_2/(C_{60}+f-SWNT)$_m$ system is also compared to those of the FTO/SnO_2/(C_{60})$_m$, FTO/SnO_2/(f-SWNT)$_m$, and FTO/SnO_2 to gain deep insight into the photocurrent generation (Figure 12). The IPCE values of the FTO/SnO_2/

(C_{60}+f-SWNT)$_m$ system (Figure 12a) are 3 – 5 times as large as those of the FTO/SnO_2/(C_{60})$_m$ (Figure 12b) and FTO/SnO_2/(f-SWNT)$_m$ (Figure 12c). In addition, the IPCE values of the FTO/SnO_2/(C_{60}+f-SWNT)$_m$ system are still much larger than those of the FTO/SnO_2/(f-SWNT)$_m$/(C_{60})$_m$ (Figure 12d), where the FTO/SnO_2/(f-SWNT)$_m$ electrode is further modified with (C_{60})$_m$ electrophoretically by using the cluster solution ([C_{60}] = 0.14 mM in ODCB–acetonitrile). Thus, the complex formation of C_{60} and f-SWNT in the mixed solvent by the lyophobic and π-π interaction is essential for the efficient photocurrent generation. It should be emphasized here that the observed maximum IPCE value of 18% in the FTO/SnO_2/(C_{60}+f-SWNT)$_m$ system is the highest among the carbon nanotube-based photoelectrochemical devices (up to 9.3%) in which the carbon nanotubes are deposited onto electrodes electrophoretically,[30,31] electrostatically[36] or covalently.[37]

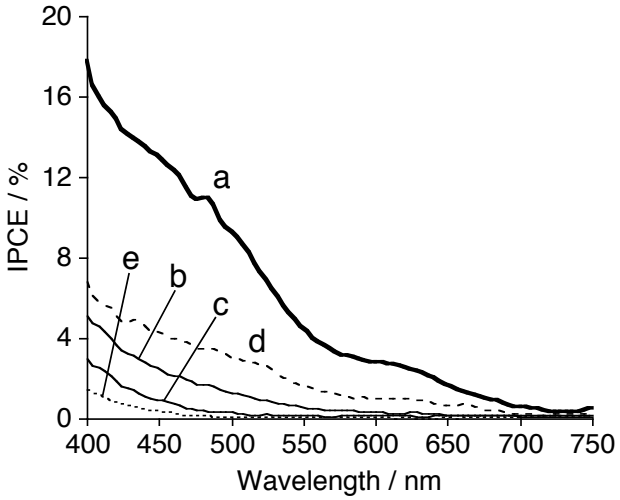

Figure 12. Photocurrent action spectra of (a) FTO/SnO_2/(C_{60}+f-SWNT)$_m$, (b) FTO/SnO_2/(C_{60})$_m$, (c) FTO/SnO_2/(f-SWNT)$_m$, (d) FTO/SnO_2/(f-SWNT)$_m$/(C_{60})$_m$, and (e) FTO/SnO_2 electrodes. The samples were prepared from corresponding cluster solutions by electrophoretic deposition with duration time of 120 s. Applied potential: +0.05 V *vs.* SCE. Electrolyte: 0.5 M LiI and 0.01 M I_2 in acetonitrile.

To examine the relationship between the gradient composition of the composite films along the direction of the film thickness and the photocurrent generation, photocurrent action spectra of the FTO/SnO_2/(C_{60}+f-SWNT)$_m$ system (Figure 13A) were measured by using the FTO/SnO_2/(C_{60}+f-SWNT)$_m$ electrodes prepared with different deposition time (*i.e.*, 10, 20, 40, and 120 s). The UV–vis absorption spectra of the FTO/SnO_2/(C_{60}+f-SWNT)$_m$ electrodes (Figure 13B) are also monitored to compare the corresponding FE-SEM images (Figure 9a, b, c and Figure 7c) and the photocurrent action spectra. All the electrodes exhibit similar structureless absorption and the absorbance gradually increases with increasing the deposition time. The overall photocurrent action spectra of the FTO/SnO_2/(C_{60}+f-SWNT)$_m$ system parallel the broad absorption spectral features. It is noteworthy that, with increasing the deposition time (0 – 40 s), the IPCE values increase and level off at the deposition time of 40 – 120 s. Considering the exclusive deposition of cluster I, the bundles of f-SWNT covered with C_{60} molecules, at the deposition time of 10 s and the corresponding large IPCE value (12.5% at 400 nm), the film of cluster I without clusters II and III has a large impact on the photocurrent generation. The aligned C_{60} molecules on the bundles of f-SWNT are responsible for the

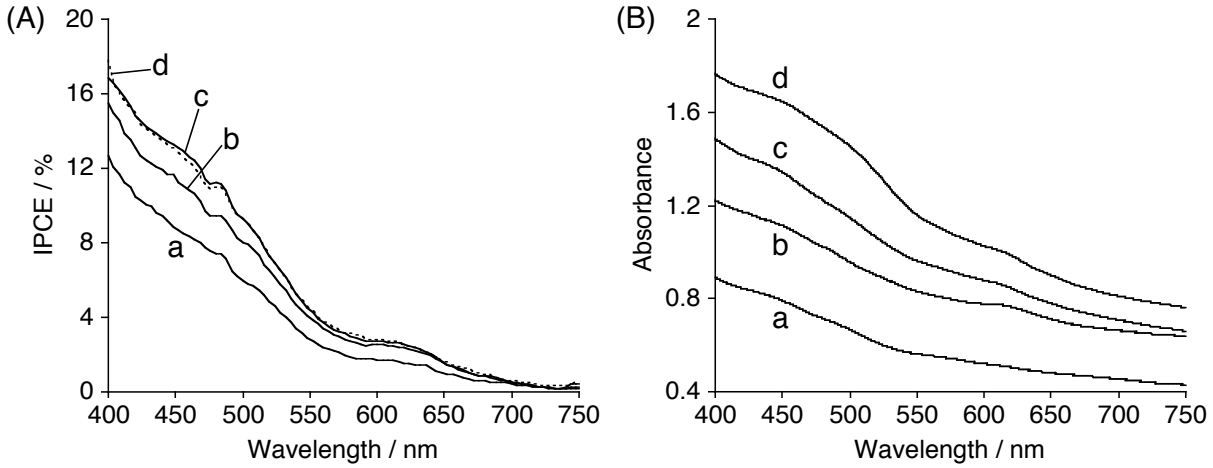

Figure 13. (A) Photocurrent action spectra and (B) UV–vis absorption spectra of FTO/SnO_2/$(C_{60}$+f-SWNT$)_m$ electrodes prepared by electrophoretic method with deposition time of (a) 10, (b) 20, (c) 40, and (d) 120 s. Action spectra were measured under an applied potential of +0.05 V *vs.* SCE. Electrolyte: 0.5 M LiI and 0.01 M I_2 in acetonitrile.

efficient photocurrent generation. The gradual increase in the IPCE value with the deposition time of 20 and 40 s relative to that with the deposition time of 10 s reveals that the cluster II (large-sized C_{60} cluster including f-SWNT) and cluster III (middle-sized C_{60} cluster) also make contribution to the photocurrent generation.

Photocurrent Generation Mechanism: On the basis of the previous studies on similar photochemical systems consisting of C_{60}[23] or f-SWNT[30,31] as well as the film structure and the photoelectrochemical properties of the present system, the author proposes photocurrent generation mechanism as shown in Schemes 2 and 3. As a representative example, (8,6) SWNT, which is the highest distribution of (*n*,*m*) species in the present p-SWNT, is given in the schemes.[31,38] Although the direct injection from the excited states of f-SWNT to the conduction band (CB) of SnO_2 is possible,[31] its contribution in the present system should be minor according to the relatively low IPCE values (up to 3%) of the FTO/SnO_2/(f-SWNT$)_m$ system (Figure 12c).

Scheme 2 illustrates a plausible photocurrent generation pathway, where photoinduced ET between iodide ion (I_3^-/I^- = 0.5 V *vs*. NHE)[23] and the excited states of C_{60} ($^1C_{60}^*/C_{60}^{\bullet-}$ = 1.7 V *vs*. NHE; $^3C_{60}^*/C_{60}^{\bullet-}$ = 1.4 V *vs*. NHE)[23] is the primary step in the photocurrent generation. The reduced C_{60} ($C_{60}/C_{60}^{\bullet-}$ = –0.2 V *vs*. NHE)[23] injects an electron into the CB of SnO_2 (E_{CB} = 0 V *vs*. NHE) through electron hopping between C_{60} molecules. ET from the reduced C_{60} molecules in clusters I, II, and III to the f-SWNT (c_1 = –0.094 V *vs*. NHE) may also occur to transport the electron to the SnO_2 electrode though the network of f-SWNT. The electron

SCHEME 2

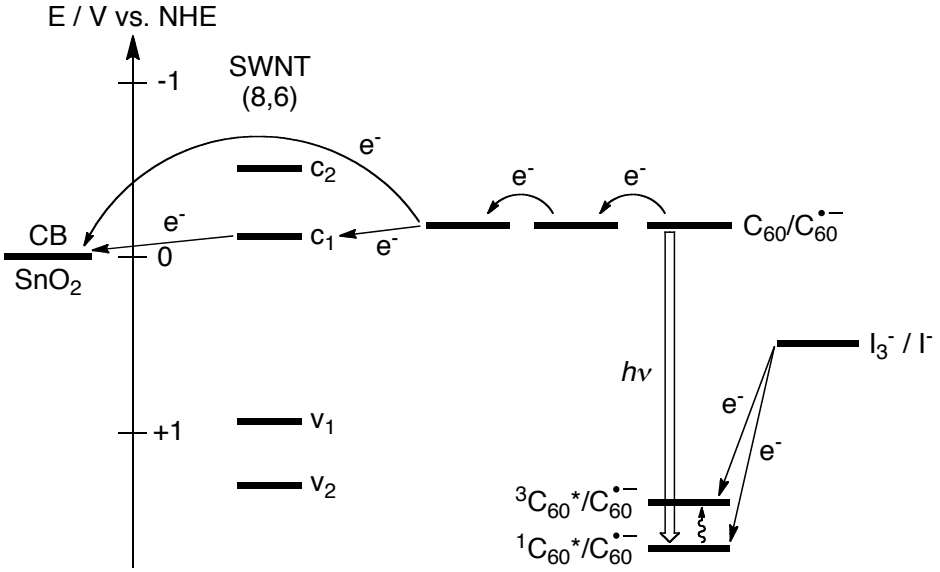

SCHEME 3

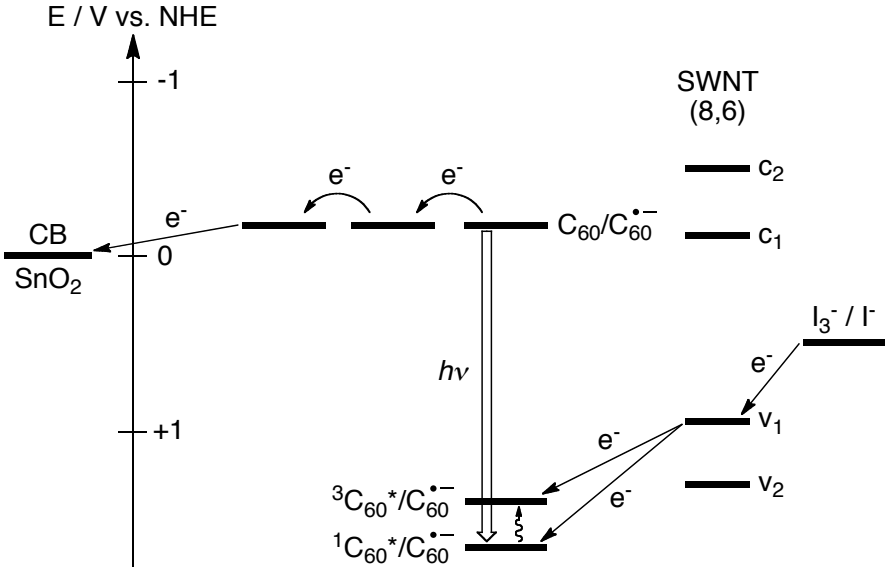

transferred to the SnO_2 electrode is driven to the counter electrode via external circuit to regenerate the redox couple. The highly aligned structure of C_{60} molecules on the f-SWNT sidewalls and the high electron transport capability of f-SWNT may facilitate the electron flow, leading to the efficient photocurrent generation in the present system. In addition to the mechanism in Scheme 2, direct CS between C_{60} and f-SWNT in clusters I and II for the photocurrent generation is energetically possible (Scheme 3). Namely, initial ET takes place from v_1 (or v_2) of f-SWNT (0.96 V *vs*. NHE) to the C_{60} excited states. Then, subsequent ET from the reduced C_{60} to the CB of the SnO_2 electrode and from I^- to v_1 (or v_2) of f-SWNT

occurs, resulting in the photocurrent generation. The author tried to measure the transient absorption spectrum of $(C_{60}$+f-SWNT$)_m$ cluster in the ODCB–acetonitrile mixture, but the attempt was unsuccessful owing to the instability of the clusters under the laser-irradiation conditions. The preliminary transient absorption measurements using the FTO/SnO_2/(C_{60}+ f-SWNT$)_m$ electrode did not exhibit the fingerprint of C_{60} radical anion at 1000 – 1100 nm, indicating no occurrence of the direct CS between C_{60} and f-SWNT. Thus, the photocurrent generation mechanism in Scheme 3 may be ruled out.

Conclusion

The author has successfully developed the novel strategy for the arrangement of C_{60} molecules on the external surface of SWNTs. First, acid treatment cuts pristine SWNTs to yield shortened SWNTs with carboxylic groups at the open ends and defect sites. Then, the shortened SWNTs is functionalized with sterically bulky amine to yield highly soluble, functionalized SWNTs (f-SWNT) in organic solvents. Finally, poor solvent (*i.e.*, acetonitrile) is rapidly injected into a mixture of C_{60} and f-SWNT in good solvent (*o*-dichlorobenzene (ODCB)), resulting in formation of the composite clusters of C_{60} and f-SWNT. The lyophobic interaction between C_{60}–f-SWNT and the mixed solvent as well as the π-π interaction between C_{60} molecules and between C_{60} and f-SWNT was found to be responsible for the desirable arrangement of C_{60} molecules on the external surface of SWNTs in the mixed solvent. The electrophoretic deposition of the composites onto a nanostructured SnO_2 electrode gradually yielded the hierarchical film with gradient composition depending on the difference in the mobilities of C_{60} and f-SWNT during the electrophoretic process. The composite film exhibited an incident photon-to-current efficiency as high as 18% at 400 nm under an applied potential of 0.05 V *vs*. SCE. The photocurrent generation efficiency is the highest value among carbon nanotube-based photoelectrochemical devices in which carbon nanotubes are deposited onto electrodes electrophoretically, electrostatically or covalently. The highly aligned structure of C_{60} molecules on f-SWNT can rationalize the efficient photocurrent generation. Thus, the results obtained here will provide valuable information on the design of carbon nanotube-based molecular devices.

Experimental Section

General Procedure: UV–vis–NIR spectra of solutions and films were measured on a Perkin-Elmer Lambda 900 UV/vis/NIR spectrometer. Resonance Raman spectra were recorded with a Horiba JobinYvon LabRAM HR-800 equipped with a 1.96 eV (633 nm) laser. FE-SEM observation was carried out with a JEOL JSM-6500FE, JSM-7500F, and Hitachi

S-4700. For preparation of the cluster samples, a mixture of ODCB–acetonitrile containing f-SWNT and/or C_{60} was cast on glass plates and the solvent was evaporated. The samples in Figure 4, Figure 7a,c and Figure 9b–d were coated by Pt using JEOL JFC-1600 auto fine coater before the measurements. AFM images of SWNT samples were obtained from a Digital Instruments Nanoscope III in the tapping mode. A solution containing f-SWNT was spin-coated on freshly cleaved mica at a rotation speed of 500 rpm. DLS measurements of the cluster solutions were performed using a Horiba LB550 particle size analyzer. s-SWNT was prepared using HiPco SWNTs (Carbon Nanotechnologies, Inc.) as published elsewhere.[2] 8-Aminopentadecane was synthesized according to the literature.[39] C_{60} (99.98%) was obtained from MTR Ltd. An optically transparent FTO electrode (Asahi Glass Inc.) was washed by sonication in 2-propanol and cleaned in an O_3 atmosphere in advance. A 15% SnO_2 colloidal solution (particle size = 15 nm; Chemat Technology, Inc.) was deposited on the FTO electrode using doctor blade technique.[23g,25e–g] The electrode was annealed at 673 K to yield 1.3 μm thick SnO_2 film (denoted as FTO/SnO_2). All other chemicals were purchased from commercial sources and used without further purification.

Synthesis of f-SWNT: s-SWNT (45 mg) was dispersed in thionyl chloride (10 mL) and stirred vigorously at 70 ^{o}C for 1 day under Ar. The excess thionyl chloride was removed by distillation under reduced pressure. Then, 8-aminopentadecane (5 mL) was added to the remaining black solid in a grove box and the mixture was stirred at 100 ^{o}C for 5 days. Cooled to room temperature, the reaction mixture was diluted by ethanol and filtered by 0.22 μm polycarbonate membrane filter. The resulting black residue was washed with ethanol, acetone, and hexane repeatedly. Reprecipitation from ODCB/methanol and subsequent ODCB/acetone and finally drying at 60 ^{o}C for 9 h gave f-SWNT (41 mg).

Preparation of Cluster Solutions and Films: The cluster solutions of f-SWNT (0.024 g L^{-1}) and/or C_{60} (0.14 mM) were prepared in a 1 cm cuvette by injecting acetonitrile (1.2 mL) into a solution of f-SWNT (0.098 g L^{-1}) and/or C_{60} (0.56 mM) in ODCB (0.4 mL) (ODCB/acetonitrile = 1/3, v/v).[23–25] Two electrodes (*i.e.*, FTO and FTO/SnO_2) were inserted into the cuvette with keeping at a distance of 6.0 mm by a Teflon spacer. A dc voltage (200 V) was applied for 2 min between these two electrodes using a power supply (ATTO, model AE-8750). The deposition of the film could be visibly confirmed as the suspension became colorless with the simultaneous colorization of the FTO/SnO_2 electrode. After the deposition, the deposited film was dried immediately with a hair dryer.

Photoelectrochemical Measurements: All electrochemical measurements were carried out in a standard three-electrode system using an ALS 630A electrochemical analyzer.[23g,25e–g] The deposited film as a working electrode was immersed into the electrolyte solution containing 0.5 M LiI and 0.01 M I_2 in acetonitrile. A Pt wire covered with a glass Luggin

capillary, whose tip was located near the working electrode, was used as a quasi-reference electrode, whereas a Pt coil was employed as a counter electrode. The potential measured was converted to the saturated calomel electrode (SCE) scale by adding +0.05 V. The stability of the reference electrode potential was confirmed under the experimental conditions. A 500 W xenon lamp (USHIO, XB-50101AAA) was used as a light source. Potential versus current characteristics were measured with controlled-potential scan (1 mV s^{-1}) under 0.5 Hz chopped white light (λ > 380 nm, input power: 78.8 mW cm^{-2}). The monochromatic light through a monochromator (Ritsu, MC-10N) was illuminated on the modified area of the working electrode (0.20 cm^2) from the backside. The light intensity was monitored by an optical power meter (Anritsu, ML9002A) and corrected.

References and Notes

[1] a) S. Niyogi, M. A. Hamon, H. Hu, B. Zhao, P. Bhowmik, R. Sen, M. E. Itkis, R. C. Haddon, *Acc. Chem. Res.* **2002**, *35*, 1105; b) Y.-P. Sun, K. Fu, Y. Lin, W. Huang, *Acc. Chem. Res.* **2002**, *35*, 1096; c) E. Katz, I. Willner, *ChemPhysChem* **2004**, *5*, 1084; d) C. A. Dyke, J. M. Tour, *J. Phys. Chem. A* **2004**, *108*, 11151; e) C. A. Dyke, J. M. Tour, *Chem.-Eur. J.* **2004**, *10*, 812; f) D. M. Guldi, G. M. A. Rahman, F. Zerbetto, M. Prato, *Acc. Chem. Res.* **2005**, *38*, 871; g) D. Tasis, N. Tagmatarchis, A. Blamco, M. Prato, *Chem. Rev.* **2006**, *106*, 1105.

[2] a) J. Chen, M. A. Hamon, H. Hu, Y. Chen, M. A. Rao, P. C. Eklund, R. C. Haddon, *Science* **1998**, *282*, 95; b) Y.-P. Sun, W. Huang, Y. Lin, K. Fu, A. Kitaygorodskiy, L. A. Riddle, Y. J. Yu, D. L. Carroll, *Chem. Mater.* **2001**, *13*, 2864; c) Y. Lian, Y. Maeda, T. Wakahara, T. Akasaka, S. Kazaoui, N. Minami, N. Choi, H. Tokumoto, *J. Phys. Chem. B* **2003**, *107*, 12082; d) M. Alvaro, P. Atienzar, P. de la Cruz, J. L. Delgado, H. Garcia, F. Langa, *Chem. Phys. Lett.* **2004**, *386*, 342; e) H. Jia, Y. Lian, M. O. Ishitsuka, T. Nakahodo, Y. Maeda, T. Tsuchiya, T. Wakahara, T. Akasaka, *Sci. Technol. Adv. Mater.* **2005**, *6*, 571; f) M. A. Herranz, N. Martin, S. Campidelli, M. Prato, G. Brehm, D. M. Guldi, *Angew. Chem. Int. Ed.* **2006**, *45*, 4478.

[3] a) J. L. Bahr, J. Yang, D. V. Kosynkin, M. J. Bronikowski, R. E. Smalley, J. M. Tour, *J. Am. Chem. Soc.* **2001**, *123*, 6536; b) J. L. Bahr, J. M. Tour, *Chem. Mater.* **2001**, *13*, 3823; c) J. L. Bahr, J. M. Tour, *J. Mater. Chem.* **2002**, *12*, 1952; d) M. S. Strano, C. A. Dyke, M. L. Usrey, P. W. Barone, M. J. Allen, H. Shan, C. Kittrell, R. H. Hauge, J. M. Tour, R. E. Smalley, *Science* **2003**, *301*, 1519; e) J. J. Stephenson, J. L. Hudson, S. Azad, J. M. Tour, *Chem. Mater.* **2006**, *18*, 374.

[4] a) V. Georgakilas, K. Kordatos, M. Prato, D. M. Guldi, M. Holzinger, A. Hirsch, *J. Am.*

Chem. Soc. **2002**, *124*, 760; b) V. Georgakilas, D. Voulgaris, E. Vazquez, M. Prato, D. M. Guldi, A. Kukovecz, H. Kuzmany, *J. Am. Chem. Soc.* **2002**, *124*, 14318; c) D. M. Guldi, M. Marcaccio, D. Paolucci, F. Paolucci, N. Tagmatarchis, D. Tasis, E. Vazquez, M. Prato, *Angew. Chem. Int. Ed.* **2003**, *42*, 4206; d) M. Melle-Franco, M. Marcaccio, D. Paolucci, F. Paolucci, V. Georgakilas, D. M. Guldi, M. Prato, F. Zerbetto, *J. Am. Chem. Soc.* **2004**, *126*, 1646; e) N. Tagmatarchis, M. Prato, *J. Mater. Chem.* **2004**, *14*, 437.

[5] a) K. S. Coleman, S. R. Bailey, S. Fogden, M. L. H. Green, *J. Am. Chem. Soc.* **2003**, *125*, 8722; b) K. A. Worsley, K. R. Moonoosawmy, P. Kruse, *Nano Lett.* **2004**, *4*, 1541; c) T. Umeyama, N. Tezuka, M. Fujita, Y. Matano, N. Takeda, K. Murakoshi, K. Yoshida, S. Isoda, H. Imahori, *J. Phys. Chem. C* **2007**, *111*, 9734.

[6] a) J. L. Delgado, P. Cruz, F. Langa, A. Urbina, J. Casado, J. T. L. Navarrete, *Chem. Commun.* **2004**, 1734; b) M. Alvaro, P. Atienzar, P. de la Cruz, J. L. Delgado, H. Garcia, F. Langa, *J. Phys. Chem. B* **2004**, *108*, 12691; c) M. Alvaro, P. Atienzar, P. de la Cruz, J. L. Delgado, V. Troiani, H. Garcia, F. Langa, A. Palkar, L. Echegoyen, *J. Am. Chem. Soc.* **2006**, *128*, 6626.

[7] a) Y. Wang, Z. Iqbal, S. Mitra, *Carbon* **2005**, *43*, 1015; b) K. Kubota, M. Sano, T. Masuko, *Jpn. J. Appl. Phys.* **2005**, *44*, 465; c) Y. Wang, Z. Iqbal, S. Mitra, *J. Am. Chem. Soc.* **2006**, *128*, 95; d) J. Li, H. Grennberg, *Chem.-Eur. J.* **2006**, *12*, 3869; e) Y. Wang, Z. Iqbal, S. Mitra, *Carbon* **2006**, *44*, 2804.

[8] a) J. Liu, A. G. Rinzler, H. Dai, J. H. Hafner, R. K. Bradley, P. J. Boul, A. Lu, T. Iverson, K. Shelimov, C. B. Huffman, F. Rodriguez-Macias, Y.-S. Shon, T. R. Lee, D. T. Colbert, R. E. Smalley, *Science* **1998**, *280*, 1253; b) V. C. Moore, M. S. Strano, E. H. Haroz, R. H. Hauge, R. E. Smalley, J. Schmidt, Y. Talmon, *Nano Lett.* **2003**, *3*, 1379; c) M. F. Islam, E. Rojas, D. M. Bergey, A. T. Johnson, A. G. Yodh, *Nano Lett.* **2003**, *3*, 269; d) M. J. O'Connell, S. M. Bachilo, C. B. Huffman, V. C. Moore, M. S. Strano, E. H. Haroz, K. L. Rialon, P. J. Boul, W. H. Noo, C. Kittrell, J. Ma, R. H. Hauge, R. B. Weisman, R. E. Smalley, *Science* **2002**, *297*, 593; e) S. M. Bachilo, M. S. Strano, C. Kittrell, R. H. Hauge, R. E. Smalley, R. B. Weisman, *Science* **2002**, *298*, 2361.

[9] a) N. Nakashima, Y. Tomonari, H. Murakami, *Chem. Lett.* **2002**, *31*, 638; b) D. M. Guldi, G. M. A. Rahaman, N. Jux, N. Tagmatarchis, M. Prato, *Angew. Chem. Int. Ed.* **2004**, *43*, 5526; c) T. Ogoshi, Y. Takashima, H. Yamaguchi, A. Harada, *J. Am. Chem. Soc.* **2007**, *129*, 4878.

[10] a) M. J. O'Connell, P. Boul, L. M. Ericson, C. Huffman, Y. Wang, E. Haroz, C. Kuper, J. Tour, K. D. Ausman, R. E. Smalley, *Chem. Phys. Lett.* **2001**, *342*, 265; b) M. Zheng, A. Jagota, E. D. Semke, B. A. Diner, R. S. Mclean, S. R. Lustig, R. E. Richardson, N. G. Tassi, *Nature Mater.* **2003**, *2*, 338; c) A. Star, D. W. Steuerman, J. R. Heath, J. F. Stoddart,

Angew. Chem. Int. Ed. **2002**, *41*, 2508; d) M. Numata, M. Asai, K. Kaneko, A.-H. Bae, T. Hasegawa, K. Sakurai, S. Shinkai, *J. Am. Chem. Soc.* **2005**, *127*, 5875.

[11] a) R. J. Chen, Y. Zhang, D. Wang, H. Dai, *J. Am. Chem. Soc.* **2001**, *123*, 3838; b) F. J. Gomez, R. J. Chen, D. Wang, R. M. Waymouth, H. Dai, *Chem. Commun.* **2003**, 190; c) D. M. Guldi, E. Menna, M. Maggini, M. Marcaccio, D. Paolucci, F. Paolucci, S. Campidelli, M. Prato, G. M. A. Rahman, S. Schergna, *Chem.-Eur. J.* **2006**, *12*, 3975; d) R. Chitta, A. S. D. Sandanayaka, A. L. Schumacher, L. D'Souza, Y. Araki, O. Ito, F. D'Souza, *J. Phys. Chem. C* **2007**, *111*, 6947.

[12] a) H. Murakami, T. Nomura, N. Nakashima, *Chem. Phys. Lett.* **2003**, *378*, 481; b) H. Li, B. Zhou, Y. Lin, L. Gu, W. Wang, K. A. S. Fernando, S. Kumar, L. F. Allard, Y.-P. Sun, *J. Am. Chem. Soc.* **2004**, *126*, 1014; c) T. Hasobe, S. Fukuzumi, P. V. Kamat, *J. Am. Chem. Soc.* **2005**, *127*, 11884; d) F. Cheng, A. Adronov, *Chem.-Eur. J.* **2006**, *12*, 5053; e) F. Y. Chen, S. Zhang, A. Adronov, L. Echegoyen, F. Diederich, *Chem.-Eur. J.* **2006**, *12*, 6062; f) F. Langa, M. J. Gomez-Escalonilla, P. de la Cruz, *J. Porphyrins Phthalocyanines* **2007**, *11*, 348.

[13] a) S. A. Curran, P. M. Ajayan, W. J. Blau, D. L. Carroll, J. N. Coleman, A. B. Dalton, A. P. Davey, A. Drury, B. McCarthy, S. Maier, A. Strevens, *Adv. Mater.* **1998**, *10*, 1091; b) D. W. Steuerman, A. Star, R. Narizzano, H. Choi, R. S. Ries, C. Nicolini, J. F. Stoddart, J. R. Heath, *J. Phys. Chem. B* **2002**, *106*, 3124; c) J. Chen, H. Liu, W. A. Weimer, M. D. Halls, D. H. Ealdeck, G. C. Walker, *J. Am. Chem. Soc.* **2002**, *124*, 9034; d) A. Star, Y. Liu, K. Grant, L. Ridvan, J. F. Stoddart, D. W. Steuerman, M. R. Diehl, A. Boukai, J. R. Heath, *Macromolecules* **2003**, *36*, 553; e) A. Ikeda, K. Nobusawa, T. Hamano, J.-i. Kikuchi, *Org. Lett.* **2006**, *8*, 5489; f) T. Umeyama, N. Kadota, N. Tezuka, Y. Matano, H. Imahori, *Chem. Phys. Lett.* **2007**, *444*, 263.

[14] a) H. Ago, K. Petritsch, M. S. P. Shaffer, A. H. Windle, R. H. Friend, *Adv. Mater.* **1999**, *11*, 1281; b) A. Star, J. F. Stoddart, D. Steuerman, M. Diehl, A. Boukai, E. W. Wong, X. Yang, S.-W. Chung, H. Choi, J. R. Heath, *Angew. Chem. Int. Ed.* **2001**, *40*, 1721; c) S. Bhattacharyya, E. Kymakis, G. A. J. Amaratunga, *Chem. Mater.* **2004**, *16*, 4819; d) T. Hasobe, S. Fukuzumi, P. V. Kamat, *J. Phys. Chem. B* **2006**, *110*, 25477.

[15] a) M. S. Dresselhaus, G. Dresselhaus, P. C. Eklund, *Science of Fullerenes and Carbon Nanotubes*, Academic Press, San Diego, 1996; b) *Fullerenes*, K. M. Kadish, R. S. Ruoff, Eds., Wiley, New York, 2000; c) S. Reich, C. Thomsen, J. Maultzsch, *Carbon Nanotubes*, Wiley-VCH, Weinheim, 2004; d) *Applied Physics of Carbon Nanotubes*, S. V. Rotkin, S. Subramoney, Eds., Springer, Berlin, 2005; e) *Organic Photovoltaics*, C. Brabec, V. Dyakonov, J. Parisi, N. S. Sariciftci, Eds., Springer, Berlin, 2003.

[16] a) D. M. Guldi, *J. Phys. Chem. B* **2005**, *109*, 11432; b) P. V. Kamat, *J. Phys. Chem. C*

2007, *111*, 2834.

[17] a) H. Imahori, Y. Sakata, *Adv. Mater.* **1997**, *9*, 537; b) H. Imahori, Y. Sakata, *Eur. J. Org. Chem.* **1999**, 2445; c) H. Imahori, *Org. Biomol. Chem.* **2004**, *2*, 1425; d) H. Imahori, *J. Phys. Chem. B* **2004**, *108*, 6130; e) H. Imahori, S. Fukuzumi, *Adv. Funct. Mater.* **2004**, *14*, 525; f) H. Imahori, *Bull. Chem. Soc. Jpn.* **2007**, *80*, 621.

[18] a) B. W. Smith, M. Monthioux, D. E. Luzzi, *Nature* **1998**, *396*, 323; b) H. Kataura, Y. Maniwa, M. Abe, A. Fujiwara, T. Kodama, K. Kikuchi, H. Imahori, Y. Misaki, S. Suzuki, Y. Achiba, *Appl. Phys. A* **2002**, *74*, 349; c) D. A. Britz, A. N. Khlobystov, J. Wang, A. S. O'Neil, M. Poliakoff, A. Ardavan, G. A. D. Briggs, *Chem. Commun.* **2004**, 176; d) A. N. Khlobystov, D. A. Britz, G. A. D. Briggs, *Acc. Chem. Res.* **2005**, *38*, 901.

[19] There are a few reports on C_{60}–SWNT composite system other than bucky-peapods. a) Y. Takaguchi, M. Tamura, Y. Sako, Y. Yanagimoto, S. Tsuboi, T. Uchida, K. Shimamura, S. Kimura, T. Wakahara, Y. Maeda, T. Akasaka, *Chem. Lett.* **2005**, *34*, 1608; b) D. M. Guldi, E. Menna, M. Maggini, M. Marcaccio, D. Paolucci, F. Paolucci, S. Campidelli, M. Prato, G. M. A. Rahman, S. Schergna, *Chem.-Eur. J.* **2006**, *12*, 3975; c) A. G. Nasibulin, P. V. Pikhitsa, H. Jiang, D. P. Brown, A. V. Krasheninnikov, A. S. Anisimov, P. Queipo, A. Moisala, D. Gonzalez, G. Lientschnig, A. Hassanien, S. D. Shandakov, G. Lolli, D. E. Resasco, M. Choi, D. Tománek, E. I. Kauppinen, *Nature Nanotech.* **2007**, *2*, 156; d) J. L. Delgado, P. Cruz, A. Urbina, J. T. L. Navarrete, J. Casado, F. Langa, *Carbon* **2007**, *45*, 2250.

[20] a) A. D. Pasquier, H. E. Unalan, A. Kanwal. S. Miller, M. Chhowalla, *Appl. Phys. Lett.* **2005**, *87*, 203511; b) B. Pradhan, S. K. Batabyal, A. J. Pal, *Appl. Phys. Lett.* **2006**, *88*, 093106; c) S. Chaudhary, H. Lu, A. M. Muller, C. J. Bardeen, M. Ozkan, *Nano Lett.* **2007**, *7*, 1973.

[21] C. Li, Y. Chen, Y. Wang, Z. Iqbal, M. Chhowalla, S. Mitra, *J. Mater. Chem.* **2007**, *17*, 2406.

[22] a) W. Ma, C. Yang, X. Gong, K. Lee, A. J. Heeger, *Adv. Funct. Mater.* **2005**, *15*, 1617; b) G. Li, V. Shrotriya, J. Huang, Y. Yao, T. Moriarty, K. Emery, Y. Yang, *Nature Mater.* **2005**, *4*, 864; c) Y. Kim, S. Cook, S. M. Tuladhar, S. A. Choulis, J. Nelson, J. R. Durrant, D. D. C. Bradley, M. Giles, I. Mcculloch, C.-S. Ha, M. Ree, *Nature Mater.* **2006**, *5*, 197; d) H. Hoppe, N. S. Sariciftci, *J. Mater. Chem.* **2006**, *16*, 45.

[23] The clusterization of fullerene single components by lyophobic interaction has been reported. a) Y.-P. Sun, C. E. Bunker, *Nature* **1993**, *365*, 398; b) Y. M. Wang, P. V. Kamat, L. K. Patterson, *J. Phys. Chem.* **1993**, *97*, 8793; c) Y.-P. Sun, B. Ma, C. E. Bunker, B. Liu, *J. Am. Chem. Soc.* **1995**, *117*, 12705; d) S. Nath, H. Pal, D. K. Palit, A. V. Sapre, J. P. Mittal, *J. Phys. Chem. B* **1998**, *102*, 10158; e) P. V. Kamat, S. Barazzouk, K. G.

Thomas, S. Hotchandani, *J. Phys. Chem. B* **2000**, *104*, 4014; f) S. Barazzouk, S. Hotchandani, P. V. Kamat, *Adv. Mater.* **2001**, *13*, 1614; g) H. Hotta, S. Kang, T. Umeyama, Y. Matano, K. Yoshida, S. Isoda, H. Imahori, *J. Phys. Chem. B* **2005**, *109*, 5700; h) K. G. Thomas, M. V. George, P. V. Kamat, *Helv. Chim. Acta* **2005**, *88*, 1291.

[24] H. Imahori, *J. Mater. Chem.* **2007**, *17*, 31.

[25] a) H. Imahori, T. Hasobe, H. Yamada, P. V. Kamat, S. Barazzouk, M. Fujitsuka, O. Ito, S. Fukuzumi, *Chem. Lett.* **2001**, 784; b) T. Hasobe, Y. Kashiwagi, M. A. Absalom, J. Sly, K. Hosomizu, M. J. Crossley, H. Imahori, P. V. Kamat, S. Fukuzumi, *Adv. Mater.* **2004**, *16*, 975; c) T. Hasobe, P. V. Kamat, V. Troiani, N. Solladie, T. K. Ahn, S. K. Kim, D. Kim, A. Kongkanand, S. Kuwabata, S. Fukuzumi, *J. Phys. Chem. B* **2005**, *109*, 19; d) T. Hasobe, H. Imahori, P. V. Kamat, S. Fukuzumi, *J. Am. Chem. Soc.* **2003**, *125*, 14962; e) S. Kang, T. Umeyama, M. Ueda, Y. Matano, H. Hotta, K. Yoshida, S. Isoda, M. Shiro, H. Imahori, *Adv. Mater.* **2006**, *18*, 2549; f) A. Kira, M. Tanaka, T. Umeyama, Y. Matano, G. Li, S. Ye, M. Isosomppi, N. V. Tkachenko, H. Lemmetyinen, H. Imahori, *J. Phys. Chem. C* **2007**, *111*, 13618; g) H. Imahori, M. Ueda, S. Kang, H. Hayashi, S. Hayashi, H. Kaji, S. Seki, A. Saeki, S. Tagawa, T. Umeyama, Y. Matano, K. Yoshida, S. Isoda, M. Shiro, N. V. Tkachenko, H. Lemmetyinen, *Chem.-Eur. J.* **2007**, *13*, 10182.

[26] To avoid the precipitation of $(C_{60}$+f-SWNT$)_m$, the absorption spectrum of the mixture of C_{60} and f-SWNT in the mixed solvent was measured using a 1 cm optical cuvette. The same volume of ODCB/acetonitrile (1:3, v/v) was further added to the solution before the measurement.

[27] Since the author could obtain the only blurred FE-SEM images of the fibrils in Figures 4b and d, the average diameters of the fibrils may include an experimental error to some extent.

[28] The DLS measurement of $(C_{60}$+f-SWNT$)_m$ in ODCB–acetonitrile showed the two particles with average diameters of 200 and 2000 nm. The small particle can be assigned to $(C_{60})_m$ (cluster III), whereas the large particle may originate from clusters I and II. The size and the distribution of large particle are not accurate because of the fibrous structure of cluster I and the network structure of cluster II.

[29] T. Hasobe, S. Fukuzumi, P. V. Kamat, *Angew. Chem. Int. Ed.* **2006**, *45*, 755.

[30] a) P. V. Kamat, K. G. Thomas, S. Barazzouk, G. Girishkumar, K. Vinodgopal, D. Meisel, *J. Am. Chem. Soc.* **2004**, *126*, 10757; b) S. Barazzouk, S. Hotchandani, K. Vinodgopal, P. V. Kamat, *J. Phys. Chem. B* **2004**, *108*, 17015; c) F. Itoh, I. Suzuki, K. Miyairi, *Jpn. J. Appl. Phys.* **2005**, *44*, 636.

[31] T. Umeyama, M. Fujita, N. Tezuka, N. Kadota, Y. Matano, K. Yoshida, S. Isoda, H. Imahori, *J. Phys. Chem. C* **2007**, *111*, 11484.

[32] H. Kataura, Y. Kumazawa, Y. Maniwa, I. Umezu, S. Suzuki, Y. Ohtsuka, Y. Achiba, *Synth. Metals* **1999**, *103*, 2555.

[33] A. M. Rao, P. C. Eklund, J.-L. Hodeau, L. Marques, M. Nunez-Regueiro, *Phys. Rev. B* **1997**, *55*, 4766.

[34] M. S. Dresselhaus, G. Dresselhaus, R. Saito, A. Jorio, *Phys. Rep.* **2005**, *409*, 47.

[35] The difference (10 – 20 nm) in the average diameters of the bundles of $(f\text{-SWNT})_m$ and cluster I in Figure 4b and Figure 4d is slightly larger than that (6 nm) in Figure 7b and Figure 9a. This may result from the inaccuracy in the former case[27] as well as the difference in the sample preparation.

[36] G. M. A. Rahaman, D. M. Guldi, R. Cagnoli, A. Mucci, L. Schenetti, L. Vaccari, M. Prato, *J. Am. Chem. Soc.* **2005**, *127*, 10551.

[37] a) F. Patolsky, Y. Weizmann, I. Willner, *Angew. Chem. Int. Ed.* **2004**, *43*, 2113; b) L. Sheeney-Haj-Khia, B. Basnar, I. Willner, *Angew. Chem. Int. Ed.* **2005**, *44*, 78.

[38] a) K.-i. Okazaki, Y. Nakato, K. Murakoshi, *Phys. Rev. B* **2003**, *68*, 035434; b) A. Jorio, R. Saito, J. H. Hafner, C. M. Lieber, M. Hunter, T. McClure, G. Dresselhaus, M. S. Dresselhaus, *Phys. Rev. Lett.* **2001**, *86*, 1118; c) J. Zhao, J. Han, J. P. Lu, *Phys. Rev. B* **2002**, *65*, 193401.

[39] S. Demmig, H. Langhals, *Chem. Ber.* **1988**, *121*, 225.

Chapter 6

Selective Formation and Efficient Photocurrent Generation of [70]Fullerene–Single-Walled Carbon Nanotube Composites

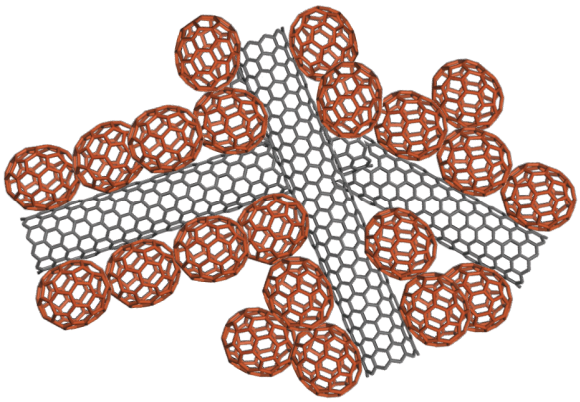

Abstract: The author has successfully constructed nanocarbon composites, where C_{70} molecules are aligned on the sidewall of single-walled carbon nanotubes (SWNTs). Enhanced interaction between the flattened-shaped C_{70} and SWNTs led to formation of the single component cluster in the *o*-dichlorobenzene–acetonitrile mixture, which is in marked contract to the case of C_{60}–SWNT composite with three different structures. Time-resolved microwave conductivity measurements revealed superb electron mobility through the SWNT network formed in the composite. The C_{70}–SWNT photoelectrochemical device exhibited efficient photocurrent generation properties resulting from selective formation of the single composite film consisting of the SWNT network covered with C_{70} molecules in addition to the high electron mobility through the C_{70}–SWNT network. The results obtained here will open up a way to harness the nanocarbon composites for efficient photoelectrochemical devices.

Introduction

Recently, organic solar cells have drawn much attention because of their potential for the production of flexible and large-sized devices at low-costs. The state-of-the art in the field of organic solar cells is represented by bulk heterojunction (BHJ) solar cells based on conjugated polymers and fullerene derivatives.[1] In particular, the BHJ solar cell consisting of poly(3-hexylthiophene) (P3HT) and [6,6]-phenyl-C61-butyric acid methyl ester ([60]PCBM) has achieved a power conversion efficiency (η) of ~ 5%, which is among the highest values reported for polymer-based solar cells.[2] The excellent cell performance results from thermal annealing leading to the high crystalline structure of P3HT and, in turn, the phase segregation of P3HT and PCBM into bicontinuous domains. In contrast, it is still difficult to control nanometer-scale network structures of fullerenes by self-assembly of the fullerenes. Although the introduction of self-assembling substituents into fullerenes can realize such network structures, the photocurrent generation in BHJ solar cells and photoelectrochemical devices remains poor owing to the reduction in fullerene density in the film and incomplete control of the network structures.[3] Nevertheless, the formation of fullerene-based network is more desirable for higher fullerenes (*i.e.*, C_{70}) and their derivatives ([70]PCBM) that have recently achieved one of the highest η values when combined with novel low-band gap polymers.[4]

Here the author reports the first selective formation of higher fullerene (*i.e.*, C_{70})–single-walled carbon nanotubes (SWNTs) composite for photoelectrochemical devices (Scheme 1).[5–7] SWNTs were chosen as a nanoscaffold for organizing C_{70} molecules on the sidewall with a hope that hetero-interaction between C_{70} and SWNTs is more favorable than homo-interactions between C_{70} molecules as well as SWNTs. In such a case, the author can expect selective formation of the C_{70}–SWNT composite and resultant efficient electron transportation through the one-dimensional (1-D) arrays of C_{70} molecules that would be applicable to photoelectrochemical devices. The author also anticipated that electron transfer (ET) from C_{70} radical anion ($C_{70}^{\bullet -}$) into SWNTs would also facilitate electron transportation through the 1-D structure of SWNT, resulting in enhanced current flow in the devices.[8]

SCHEME 1

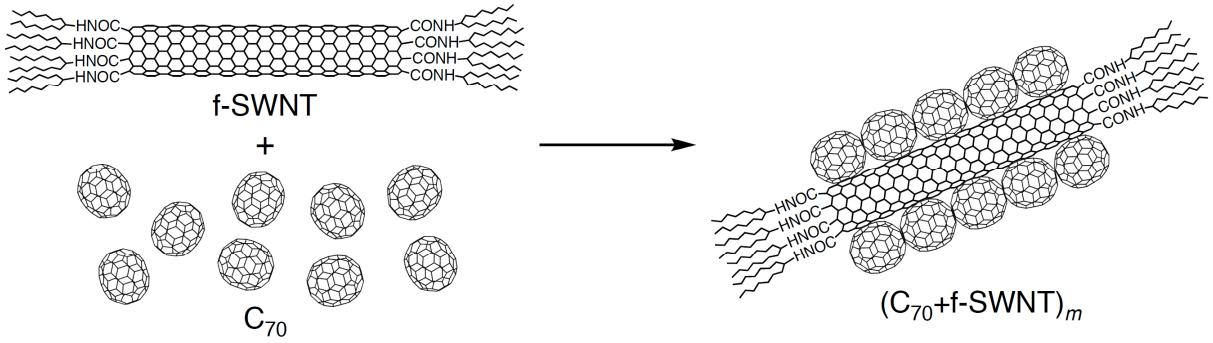

To form the C_{70}–SWNT composite and deposit it on a semiconducting electrode (*i.e.*, SnO_2) for photoelectrochemical devices, the author applied rapid injection and electrophoretic deposition methods to C_{70} and the chemically functionalized SWNTs (f-SWNT).[5,9] Namely, a poor solvent (*i.e.*, acetonitrile) is rapidly injected into a mixture of C_{70} and f-SWNT, which are dissolved in a good solvent (*i.e.*, *o*-dichlorobenzene (ODCB)). The f-SWNT with sterically hindered alkyl substituents exhibits excellent solubility in ODCB, allowing the sidewall to interact well with C_{70} in ODCB–acetonitrile. Then, high voltage is applied to the cluster solution to deposit the clusters onto a SnO_2 electrode for photoelectrochemical measurements.

Results and Discussion

Preparation of C_{70}–SWNT Composite: To examine the composite cluster formation of C_{70} and f-SWNT, the author first measured the UV–vis–near IR (NIR) absorption spectra in ODCB–acetonitrile (1:4, v/v) (Figure 1A). The absorption spectrum of the mixture exhibits the broad absorption in visible to NIR region with maximum at 547 nm (Figure 1A(c)), which is different from the sum of the absorption spectra of C_{70} and f-SWNT in (Figure 1A(d)). The observed discordance obviously manifests the composite cluster formation of C_{70} and f-SWNT (denoted as $(C_{70}$+f-SWNT$)_m$) in ODCB–acetonitrile.

Consistently, the field emission scanning electron microscopy (FE-SEM) image of spin-coated $(C_{70}$+f-SWNT$)_m$ reveals an exclusive network structure in which cuboid particles of C_{70} (200 nm) are fused to SWNTs (Figure 2a). This is in marked contrast with the unselective formation of three different clusters in the composite clusters of C_{60} and f-SWNT

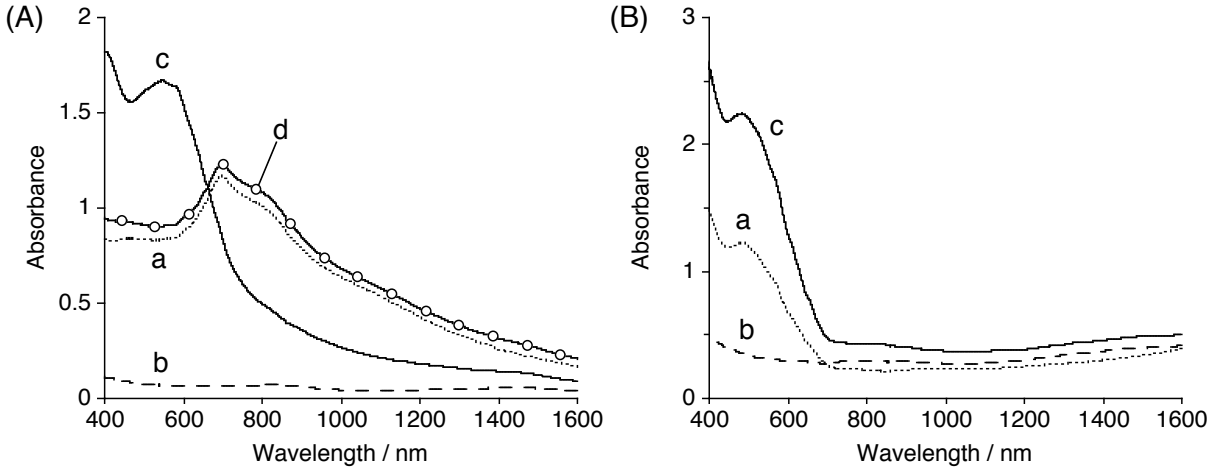

Figure 1. (A) UV–vis–NIR absorption spectra of (a) C_{70}, (b) f-SWNT, (c) a mixture of C_{70} and f-SWNT measured in ODCB–acetonitrile mixture (1:4, v/v; $[C_{70}]$ = 0.14 mM, [f-SWNT] = 0.012 g L^{-1}; path length 3 mm), and (d) sum of spectra (a) and (b). (B) UV–vis–NIR absorption spectra of (a) FTO/SnO_2/$(C_{70})_m$, (b) FTO/SnO_2/(f-SWNT)$_m$, and (c) FTO/SnO_2/$(C_{70}$+f-SWNT$)_m$.

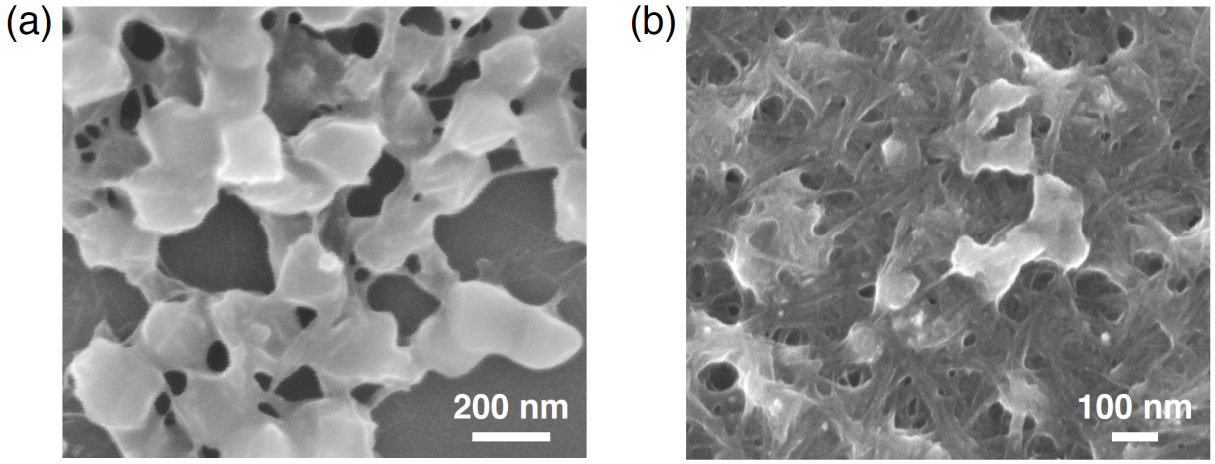

Figure 2. (a) FE-SEM image of $(C_{70}$+f-SWNT$)_m$. The sample was prepared by spin-coating the cluster solution ([C_{70}] = 0.14 mM, [f-SWNT] = 0.012 g L^{-1}) from the ODCB–acetonitrile mixture (1:4, v/v) on Si wafer. (b) FE-SEM image of FTO/SnO_2/$(C_{70}$+f-SWNT$)_m$.

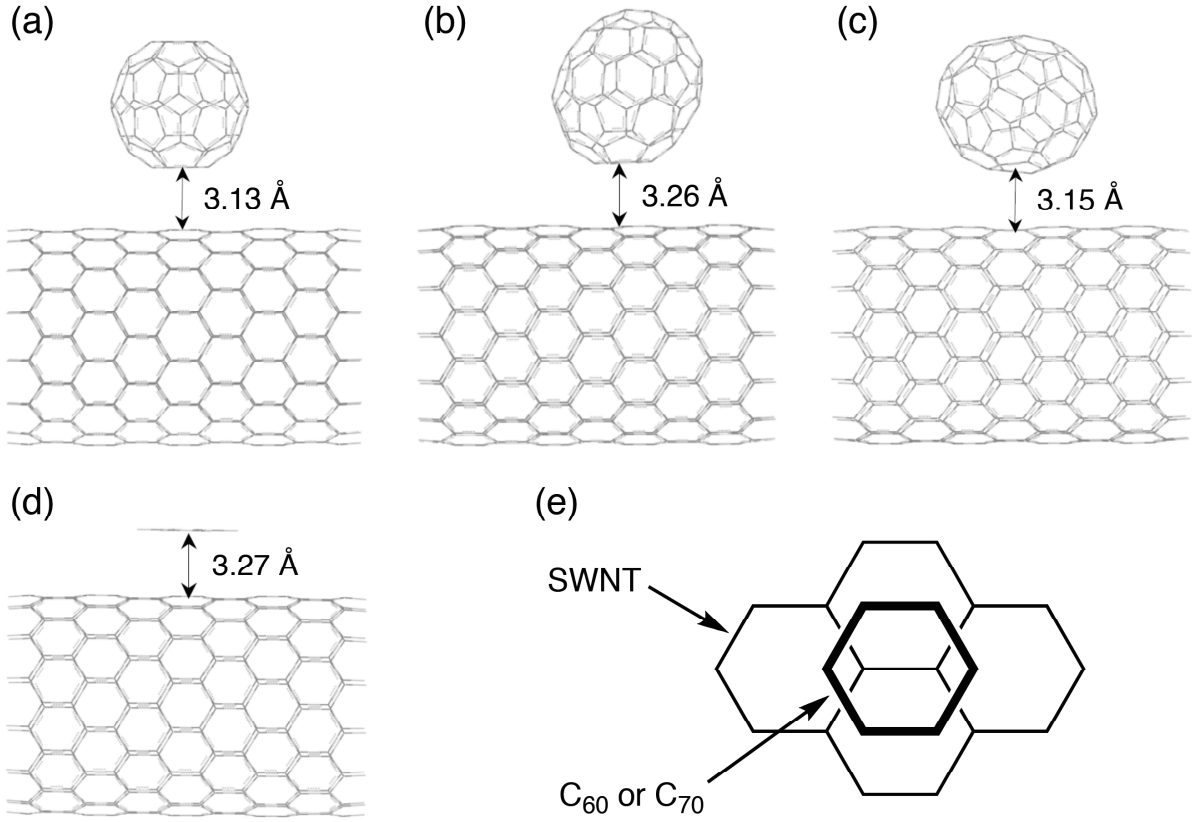

Figure 3. Molecular models of the complexes between (a) SWNT (14,0) and C_{60}, (b) SWNT (14,0) and C_{70} with end-on structure, (c) SWNT (14,0) and C_{70} with side-on structure, and (d) SWNT (14,0) and C_6H_6. All models are depicted with complete geometry optimization under AMBER force field using the Gaussian 03 program package. (e) Schematic representation of the mutual positions between the SWNT (plain line) and the fullerenes or C_6H_6 (bold line) in model (a) – (d).

(denoted as $(C_{60}$+f-SWNT$)_m$), as disclosed in the previous study.[5] Ellipsoidal shape and large size of C_{70} relative to C_{60} may contribute to the enhanced interaction with the sidewall of f-SWNT, leading to the exclusive formation of the composite cluster. Preliminary density functional theory calculations reveal that the binding energies between C_{70} and SWNT systems are larger by ~ 3 kcal mol^{-1} than those between C_{60} and SWNTs, when C_{70} molecule is stacked on the sidewall of SWNTs with its long axis parallel to the tube axis (side-on structure, Figure 3 and Table 1). In contrast, almost the same energies as for C_{60} were calculated with an alignment where the long axis of C_{70} is oriented perpendicular to the tube axis (end-on structure). These results, at least partially, rationalize more favorable formation of the composite cluster of SWNTs with C_{70} than with C_{60}, as well as the feasible side-on structure in the $(C_{70}$+f-SWNT$)_m$.

Electrophoretic Deposition: Upon subjecting the resulting cluster suspension to a high electric (dc) field (200 V, 2 min), the clusters of C_{70} and/or f-SWNT were deposited onto the fluorine-doped tin oxide (FTO) electrodes with nanostructured SnO_2 modification (denoted as FTO/SnO_2/$(C_{70})_m$, FTO/SnO_2/(f-SWNT$)_m$, and FTO/SnO_2/$(C_{70}$+f-SWNT$)_m$). It is noteworthy that the absorption spectrum of the FTO/SnO_2/$(C_{70}$+f-SWNT$)_m$ electrode (Figure 1B(c)) differs from that of $(C_{70}$+f-SWNT$)_m$ in ODCB–acetonitrile (Figure 1A(c)). Furthermore, the FE-SEM image of FTO/SnO_2/$(C_{70}$+f-SWNT$)_m$ electrode reveals coalescent fibrous network (Figure 2b), in which SWNTs are covered tightly by C_{70} layers. Note that the C_{70} particles observed in the spin-coated sample (Figure 2a) are not seen, whereas some granulous structures are present in places. Such rearrangements of C_{70} molecules may be caused by the solvent annealing effect during the drying process due to the much faster vaporization of acetonitrile (boiling point (bp) = 82 ^{o}C) than ODCB (bp = 180 ^{o}C). Similar rearrangement was also seen in the FTO/SnO_2/$(C_{70})_m$ electrode, whereas it was not apparent for the $(C_{60})_m$ and $(C_{60}$+f-SWNT$)_m$.[5]

TABLE 1: Binding Energies (kcal mol^{-1}) between SWNTs and Fullerenes [a]

	C_{60}	C_{70} (end-on) [b]	C_{70} (side-on) [c]	C_6H_6
SWNT (14,0)	16.9	17.0	19.6	9.7
SWNT (8,6)	15.9	16.7	19.0	8.8

[a] Geometry optimizations were carried out by AMBER force field using the Gaussian 03 program package, as illustrated in Figure 3. Binding energies were calculated by the B3LYP-D method with the cc-pVDZ basis set using the GAMESS program package. SWNT (14,0) and SWNT (8,6) were modeled as $C_{224}H_{28}$. [b] Long axis of C_{70} molecule is oriented perpendicular to the tube axis of SWNTs (see Figure 3(b)). [c] Long axis of C_{70} molecule is oriented parallel to the tube axis of SWNTs (see Figure 3(c)).

Charge Carrier Mobility: To evaluate the charge carrier mobility (μ) of the deposited films, the author measured the flash-photolysis time-resolved microwave conductivity (TRMC).[10] Upon exposure to a laser pulse with an excitation wavelength of 355 nm, all samples reveal a rise of the transient conductivity $<\phi\Sigma\mu>$, in which ϕ is the quantum efficiency of charge separation (CS) and $\Sigma\mu$ is the sum of the mobility of all the transient-charge carriers (Figure 4 and Table 2). The major charge carriers are found to stem from electrons for all films. The $\Sigma\mu$ value (3.2 cm^2 V^{-1} s^{-1}) of the FTO/SnO_2/(f-SWNT)$_m$ electrode is the highest, demonstrating the potentially superior electron-transporting property of f-SWNT. Notably, nearly 30% increase in the $\Sigma\mu$ value is discernible when C_{70} is clusterized with f-SWNT, accompanying a 13% increase in the ϕ value relative to those of FTO/SnO_2/(C_{70})$_m$. The rise profile of the transient conductivity for the FTO/SnO_2/(C_{70}+f-SWNT)$_m$ (Figure 4c) is close to that for the FTO/SnO_2/(C_{70})$_m$ (Figure 4a), both reaching the conductivity maxima within 0.4 μs, while that for the FTO/SnO_2/(f-SWNT)$_m$ (Figure 4b) reveals a slower rise component. Similarity in the photoresponse behavior of the TRMC signals for the FTO/SnO_2/(C_{70}+f-SWNT)$_m$ and FTO/SnO_2/(C_{70})$_m$ implies that the large majority of the photocarriers in the C_{70}–f-SWNT composites is generated by excitation of C_{70}. On the other hand, decay kinetics of the conductivity transients for the FTO/SnO_2/(C_{70}+f-SWNT)$_m$ exhibits a pseudo-first to second order profile (time constant = 4.2×10^5 s^{-1} and 1.4×10^6 s^{-1} for pseudo-first and second order decay, respectively), which is different from those of the FTO/SnO_2/(C_{70})$_m$ and FTO/SnO_2/(f-SWNT)$_m$. The second order decay profile was observed only for the FTO/SnO_2/(C_{70}+f-SWNT)$_m$. All of these features can be interpreted by the occurrence of ET from $C_{70}^{\bullet-}$ to f-SWNT, followed by bulk recombination of charge carriers during electron transportation through f-SWNT, in addition to electron hopping on C_{70} arrays due to the alignment of C_{70} on the sidewalls of f-SWNT in the FTO/SnO_2/(C_{70}+f-SWNT)$_m$. The small $\Sigma\mu$ value (1.2 cm^2 V^{-1} s^{-1}) of the FTO/SnO_2/(C_{60}+f-SWNT)$_m$ relative to that of the FTO/SnO_2/(C_{70}+f-SWNT)$_m$ may

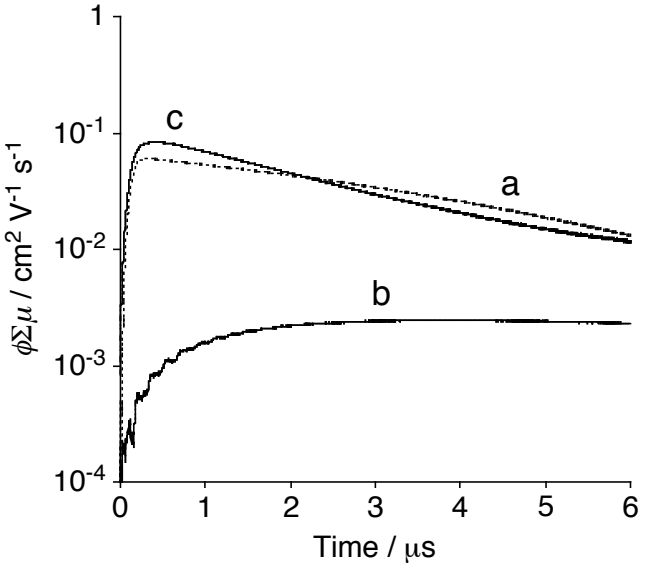

Figure 4. Flash-photolysis TRMC transients for (a) FTO/SnO_2/(C_{70})$_m$, (b) FTO/SnO_2/(f-SWNT)$_m$, and (c) FTO/SnO_2/(C_{70}+f-SWNT)$_m$ electrodes. The transient were recorded at an excitation wavelength of 355 nm with a photon density of 3.3×10^{15} cm^{-2}. All samples are fixed on quartz substrates with poly(methyl methacrylate) matrices.

result from the presence of the three different clusters, which would lower the electron mobility of the C_{60}–f-SWNT composite. It is experimentally revealed here that the transportation of electron by f-SWNT contributes to the higher value of electron mobility in the C_{70}–f-SWNT composites than that in C_{70} cluster. To the best of the author's knowledge, this is the first example determining the electron mobilities of SWNTs as well as fullerene–SWNT composites by using TRMC technique.

Photoelectrochemical Properties: Figure 5A depicts the photocurrent action spectra of the FTO/SnO_2/$(C_{70})_m$, FTO/SnO_2/$(f\text{-SWNT})_m$, and FTO/SnO_2/$(C_{70}+f\text{-SWNT})_m$ devices. The action spectra largely resemble the absorption spectra of the deposited electrodes (Figure 1B). The incident photon-to-current efficiency (IPCE) value (26%) of the FTO/SnO_2/$(C_{70}+f\text{-SWNT})_m$ device (Figure 5A(c)) at 400 nm is 2.6 times larger than that (10%) of the FTO/SnO_2/$(C_{70})_m$ device[11] (Figure 5A(a)) and 10 times larger than that (2.6%) of the FTO/SnO_2/$(f\text{-SWNT})_m$ device (Figure 5A(b)) (Table 2). The IPCE value (26%) of the FTO/SnO_2/$(C_{70}+f\text{-SWNT})_m$ device is the highest one ever reported for analogous SWNT-based photoelectrochemical devices[12] in which the SWNTs are deposited electrophoretically, electrostatically, covalently, or physisorptionally onto semiconducting electrodes.

Photocurrent generation (Figure 5B) is initiated by photoinduced ET from iodide ion (I_3^-/I^- = 0.5 V *vs.* NHE)[5] in the electrolyte to the C_{70} excited states ($^1C_{70}^*/C_{70}^{\bullet-} \approx 1.7$ V *vs.* NHE; $^3C_{70}^*/C_{70}^{\bullet-} \approx 1.3$ V *vs.* NHE),[13,14] and $C_{70}^{\bullet-}$ ($C_{70}/C_{70}^{\bullet-} \approx -0.2$ V *vs.* NHE)[14] injects electrons into the conduction band (CB) of f-SWNT (c_1 = –0.1 V *vs.* NHE).[15] The excellent electron mobility of f-SWNT bundles, as revealed by the TRMC measurements, facilitates the electron flow toward the SnO_2 electrode (E_{CB} = 0 V *vs.* NHE).[9,15] Additionally, $C_{70}^{\bullet-}$ injects

TABLE 2: Microwave Conductivity, Quantum Efficiency of CS, Electron Mobility, and IPCE Value

	$\phi\Sigma\mu^{a,b}$ / $cm^2\ V^{-1}\ s^{-1}$	$\phi^{a,c}$ / %	$\Sigma\mu^a$ / $cm^2\ V^{-1}\ s^{-1}$	IPCE[d] / %
$(C_{70}+f\text{-SWNT})_m$	0.084	3.5	2.4	26
$(C_{70})_m$	0.061	3.1	1.9	10
$(f\text{-SWNT})_m$	0.0024	0.075	3.2	2.6
$(C_{60}+f\text{-SWNT})_m$	0.0056	0.50	1.2	18[e]

[a] ϕ = quantum efficiency of CS; $\Sigma\mu$ = sum of mobility of all the transient-charge carriers. [b] Maximum value of the transient conductivity upon photoirradiation at 355 nm (photon density: 3.3×10^{15} cm^{-2}). [c] Determined by conventional DC-current integration technique with a photoexcitation at 355 nm. [d] At 400 nm. [e] Taken from ref 5.

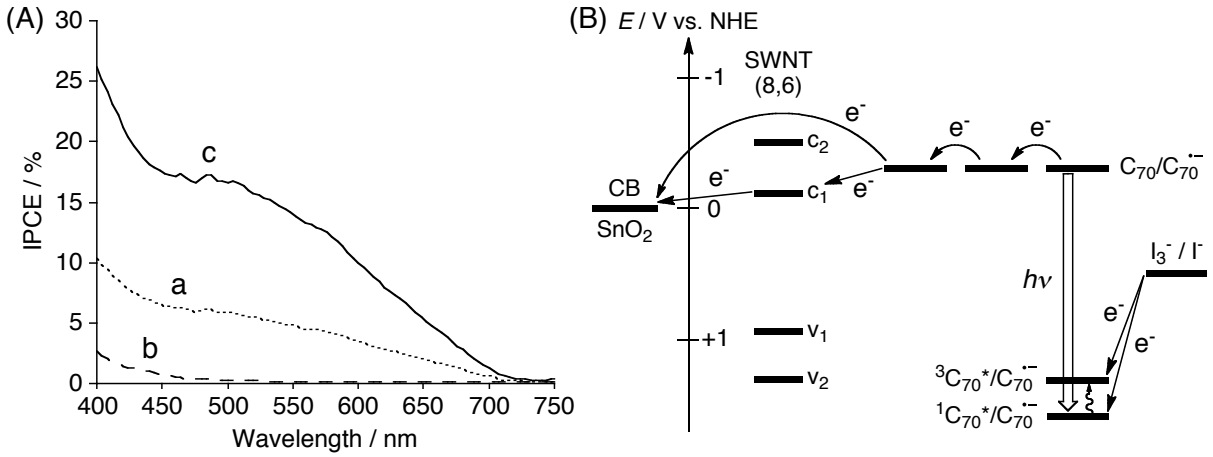

Figure 5. (A) Photocurrent action spectra of (a) FTO/SnO_2/$(C_{70})_m$, (b) FTO/SnO_2/(f-SWNT)$_m$, and (c) FTO/SnO_2/(C_{70}+f-SWNT)$_m$ devices. Applied potential: +0.05 V *vs.* SCE. Electrolyte: 0.5 M LiI and 0.01 M I_2 in acetonitrile. (B) Photocurrent generation diagram for the FTO/SnO_2/(C_{70}+ f-SWNT)$_m$ device. As a representative example, (8,6) SWNT, which is regarded as single (*n*,*m*) chirality species with the highest distribution in f-SWNT prepared from commercially available HiPco SWNTs, is used in the scheme.

electrons into the CB of the SnO_2 by electron hopping through the C_{70} arrays on the SWNT sidewalls. It should be noted here that the time-resolved transient absorption measurements using the FTO/ SnO_2/(C_{70}+f-SWNT)$_m$ electrode did not exhibit the fingerprint of $C_{70}^{\bullet-}$ at 880 and 1370 nm or $C_{70}^{\bullet+}$ at 930 nm (Figure 6).[16] This rules out the possibility of direct CS between C_{70} and f-SWNT as an initial step for photocurrent generation.

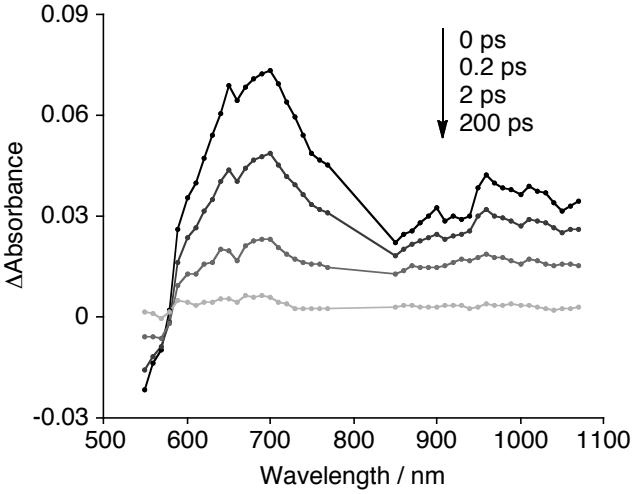

Figure 6. Sub-picosecond to sub-nanosecond time-resolved absorption spectra of FTO/SnO_2/ (C_{70}+f-SWNT)$_m$ electrode after laser excitation at 410 nm at 298 K.

Here, the emphasis should be placed on the fact that maximum IPCE value (26%) of the FTO/SnO_2/(C_{70}+f-SWNT)$_m$ device is higher than that (18%) of the FTO/SnO_2/(C_{60}+f-SWNT)$_m$ device,[5] despite of the similar light-harvesting efficiency, reduction potentials ($C_{60}/C_{60}^{\bullet-} \approx -0.2$ V *vs.* NHE),[5,9] and excited state behavior of C_{60} and C_{70}.[17] The efficient photocurrent generation may result from higher electron mobility (2.4 $cm^2\ V^{-1}\ s^{-1}$) of the (C_{70}+f-SWNT)$_m$ in comparison with that (1.2 $cm^2\ V^{-1}\ s^{-1}$) of the (C_{60}+f-SWNT)$_m$. The higher electron mobility of (C_{70}+f-SWNT)$_m$ may also originate from the single network structure on the FTO/SnO_2/(C_{70}+f-SWNT)$_m$ electrode compared with the unselective cluster formation of (C_{60}+f-SWNT)$_m$.

Conclusion

In summary, the author has successfully constructed nanocarbon composites, where C_{70} molecules are aligned on the sidewall of SWNTs for the first time. The C_{70}–SWNT photoelectrochemical device exhibited the highest IPCE value (26%) ever reported for analogous SWNT-based photoelectrochemical devices. The highest IPCE value results from selective formation of the composite film consisting of the SWNT network covered with C_{70} molecules, which is in marked contrast with the unselective formation of three different clusters in the C_{60}–f-SWNT composites. Thus, these results will provide basic clue for the design of nanocarbon composite-based molecular devices including organic photovoltaics.

Experimental Section

General Procedure: NIR spectra of solutions and films were measured on a Perkin-Elmer Lambda 900 UV/vis/NIR spectrometer. FE-SEM observation was carried out with a JEOL JSM-6705F. f-SWNT was prepared according to the previous report.[5] C_{70} (99.5%) was obtained from MTR Ltd. An optically transparent FTO electrode (Asahi Glass Inc.) was washed by sonication in 2-propanol and cleaned in an O_3 atmosphere in advance. A 15% SnO_2 colloidal solution (particle size = 15 nm; Chemat Technology, Inc.) was deposited on the FTO electrode using the doctor blade technique.[5] The electrode was annealed at 673 K to yield 1.3 μm thick SnO_2 film (denoted as FTO/SnO_2). All other chemicals were purchased from commercial sources and used without further purification.

Preparation of Cluster Solutions and Films: The cluster solutions of f-SWNT (0.012 g L^{-1}) and/or C_{70} (0.14 mM) were prepared in a 1 cm cuvette by injecting 1.6 mL of acetonitrile into a solution of f-SWNT (0.062 g L^{-1}) and/or C_{70} (0.68 mM) in 0.4 mL of ODCB (ODCB/acetonitrile = 1/4, v/v). Then, two electrodes (*i.e.*, FTO and FTO/SnO_2) were inserted into the cuvette with keeping at a distance of 0.6 cm by a Teflon spacer. A dc voltage (200 V) was applied for 120 s between these two electrodes using a power supply (ATTO, model AE-8750). The deposition of the film could be visibly confirmed as the suspension became colorless with simultaneous colorization of the FTO/SnO_2 electrode. After the deposition, the deposited film was dried immediately with a hair dryer.

Theoretical Calculation: Computational calculations of the binding energies for complexes of fullerenes (*i.e.*, C_{60} or C_{70}) and SWNTs were performed using B3LYP-D functional and cc-pVDZ basis set implemented in the GAMESS program package,[18] following the complete geometry optimization under AMBER force field using the Gaussian 03 program package.[19] As a representative example, SWNT with a chiral index of (14,0) or (8,6) was incorporated and modeled as $C_{224}H_{28}$.

Photoelectrochemical Measurements: All electrochemical measurements were carried out in a standard three-electrode system using an ALS 630A electrochemical analyzer. The deposited film as a working electrode was immersed into an electrolyte solution containing 0.5 M LiI and 0.01 M I_2 in acetonitrile. A Pt wire covered with a glass Luggin capillary, whose tip was located near the working electrode, was used as a quasi-reference electrode. A Pt coil was employed as a counter electrode. The potential measured was converted to the saturated calomel electrode (SCE) scale by adding +0.05 V. The stability of the reference electrode potential was confirmed under the experimental conditions. A 500 W xenon lamp (USHIO, XB-50101AAA) was used as a light source. Monochromatic light through a monochromator (Ritsu, MC-10N) was illuminated on the modified area of the working electrode (0.20 cm^2) from the backside. The light intensity was monitored by an optical power meter (Anritsu, ML9002A) and corrected.

Time-resolved Microwave Conductivity Measurements: Nanosecond laser pulses from a Nd:YAG laser (Spectra Physics, INDY-HG; third harmonic generation (THG), 355 nm) with full width at half maximum (FWHM) of 3 – 5 ns were used as excitation sources. The photon density of the laser was set at 1.6×10^{15} – 3.6×10^{16} photons cm^{-2}. For TRMC measurements, a microwave frequency of 9.1 GHz and a power of 3 mW were employed so that the motion of charge carriers could not be disturbed by the low electric field of the microwaves. The TRMC signal, picked up by a diode (rise time < 1 ns), was monitored by a digital oscilloscope (Tektronix, TDS3032B; rise time ~ 1.2 ns). All the experiments were carried out at room temperature. The transient photoconductivity ($\Delta\sigma$) of the samples is related to the reflected microwave power ($\Delta P_r/P_r$) and the sum of the mobility of charge carriers via Equation (1) and (2):

$$\langle \Delta\sigma \rangle = \frac{1}{A}\frac{\Delta P_r}{P_r} \qquad (1)$$

$$\Delta\sigma = e\sum \mu\phi N \qquad (2)$$

where A is the sensitivity factor, e is the elementary charge of electron, ϕ is the photo-carrier generation yield (quantum efficiency), N is the number of absorbed photons per unit volume, and $\Sigma\mu$ is the sum of mobility for the negative and positive carriers. The number of photons absorbed by the sample was estimated based on the power loss of incident laser pulses averaged over 200 shots. The ϕ values were determined by the conventional DC current integration technique. The electrophoretically deposited films were overcoated by Au semitransparent electrodes at 20 mm^2, vacuum evaporated to a thickness of 25 nm, and excited by laser pulses at 355 nm with a pulse duration of 3 – 5 ns and a photon density of 3.0×10^{15} photons cm^{-2}. Current transients were monitored by a digital oscilloscope (Tektronix, TDS430A) through 300 kΩ terminate resistances, and the charges were also accumulated by an

electrometer of Keithley Instruments 6514. Other details of the apparatus set are described elsewhere.[10]

Transient Absorption Measurements: Sub-picosecond to nanosecond time-resolved absorption spectra were collected using a pump-probe technique as described elsewhere.[20] The femtosecond pulses of the Ti:sapphire generator were amplified by using a multipass amplifier (CDP-Avesta) pumped by a second harmonic of the Nd:YAG Q-switched laser (Solar TII, model LF114). The amplified pulses were used to generate a second harmonic (410 nm) for sample excitation (pump beam) and a white continuum for time-resolved spectrum detection (probe beam). An average of 100 pulses at 10 Hz repetition rate was used to improve the signal-to-noise ratio. The transient spectra were recorded by a charge-coupled device (CCD) detector (Princeton Instruments, PI 1100 × 330) coupled with a monochromator in the visible and near-infrared ranges. The wavelength range for a single measurement was 227 nm and typically two regions were studied, 550 – 770 and 850 – 1070 nm. The typical response time of the instrument was 150 fs (FWHM). A global multi-exponential fitting procedure was applied to process the data. The procedure takes into account the instrument time response function and the group velocity dispersion of the white continuum, and allows one to calculate the decay time constants and dispersion-compensated transient absorption spectra. The excitation energy was adjusted to the highest value at which the photodegradation of the samples during measurements is negligible. All measurements were carried out at room temperature in air.

References and Notes

[1] a) S. Günes, H. Neugebauer, N. S. Sariciftci, *Chem. Rev.* **2007**, *107*, 1324; b) B. C. Thompson, J. M. J. Fréchet, *Angew. Chem. Int. Ed.* **2008**, *47*, 58.

[2] a) W. Ma, C. Yang, X. Gong, K. Lee, A. J. Heeger, *Adv. Funct. Mater.* **2005**, *15*, 1617; b) Y. Kim, S. Cook, S. M. Tuladhar, S. A. Choulis, J. Nelson, J. M. Durrant, D. D. C. Bradley, M. Giles, I. Mcculloch, C.-S. Ha, M. Ree, *Nature Mater.* **2006**, *5*, 197.

[3] a) A. Kira, M. Tanaka, T. Umeyama, Y. Matano, N. Yoshimoto, Y. Zhang, S. Ye, H. Lehtivuori, N. V. Tkachenko, H. Lemmetyinen, H. Imahori, *J. Phys. Chem. C* **2007**, *111*, 13618; b) W.-S. Li, Y. Yamamoto, T. Fukushima, A. Saeki, S. Seki, S. Tagawa, H. Masunaga, S. Sasaki, M. Takata, T. Aida, *J. Am. Chem. Soc.* **2008**, *130*, 8886; c) A. Kira, T. Umeyama, Y. Matano, K. Yoshida, S. Isoda, J. K. Park, D. Kim, H. Imahori, *J. Am. Chem. Soc.* **2009**, *131*, 3198.

[4] a) J. Peet, J. Y. Kim, N. E. Coates, W. L. Ma, D. Moses, A. J. Heeger, G. C. Bazan, *Nature Mater.* **2007**, *6*, 497; b) C.-P. Chen, S.-H. Chan, T.-C. Chao, C. Ting, B.-T. Ko, *J.*

Am. Chem. Soc. **2008**, *130*, 12828; c) J. Hou, H.-Y. Chen, S. Zhang, G. Li, Y. Yang, *J. Am. Chem. Soc.* **2008**, *130*, 16144; d) Y. Liang, D. Feng, Y. Wu, S.-T. Tsai, G. Li, C. Ray, L. Yu, *J. Am. Chem. Soc.* **2009**, *131*, 7792; e) S. H. Park, A. Roy, S. Beaupre, S. Cho, N. Coates, J. S. Moon, D. Moses, M. Leclerc, K. Lee, A. J. Heeger, *Nat. Photonics* **2009**, *3*, 297.

[5] Although the author has already modified the sidewall of SWNTs with C_{60} molecules, the modification was found to be unselective, leading to the formation of three different clusters. a) T. Umeyama, N. Tezuka, M. Fujita, S. Hayashi, N. Kadota, Y. Matano, H. Imahori, *Chem.-Eur. J.* **2008**, *14*, 4875; b) T. Umeyama, H. Imahori, *Energy Environ. Sci.* **2008**, *1*, 120.

[6] The outside of SWNTs has been modified with C_{60} and C_{60} derivatives. a) Y. Takaguchi, M. Tamura, Y. Sako, Y. Yanagimoto, S. Tsuboi, T. Uchida, K. Shimamura, S. Kimura, T. Wakahara, Y. Maeda, T. Akasaka, *Chem. Lett.* **2005**, *34*, 1608; b) D. M. Guldi, E. Menna, M. Maggini, M. Marcaccio, D. Paolucci, F. Paolucci, S. Campidelli, M. Prato, G. M. A. Rahman, S. Schergna, *Chem.-Eur. J.* **2006**, *12*, 3975; c) F. D'Souza, R. Chitta, A. S. D. Sandanayaka, N. K. Subbaiyan, L. D'Souza, Y. Araki, O. Ito, *J. Am. Chem. Soc.* **2007**, *129*, 15865.

[7] Although BHJ solar cells consisting of polythiophene–C_{60}–carbon nanotube ternary composites have been reported, the composite structures and photocurrent generation mechanism have not been elucidated. a) G. Kalita, S. Adhikari, H. Ram Aryal, M. Umeno, R. Afre, T. Soga, M. Sharon, *Appl. Phys. Lett.* **2008**, *92*, 063508; b) C. Li, Y. Chen, Y. Wang, Z. Iqbal, M. Chhowalla, S. Mitra, *J. Mater. Chem.* **2007**, *17*, 2406.

[8] Electron injection from C_{60} radical anion to SWNT in C_{60}–SWNT composites has not been corroborated experimentally.[5]

[9] P. V. Kamat, S. Barazzouk, K. G. Thomas, S. Hotchandani, *J. Phys. Chem. B* **2000**, *104*, 4014.

[10] a) F. C. Grozema, L. D. A. Siebbeles, J. M. Warman, S. Seki, S. Tagawa, U. Scherf, *Adv. Mater.* **2002**, *14*, 228; b) A. Saeki, S. Seki, Y. Koizumi, T. Sunagawa, K. Ushida, S. Tagawa, *J. Phys. Chem. B* **2005**, *109*, 10015; c) A. Acharya, S. Seki, Y. Koizumi, A. Saeki, S. Tagawa, *J. Phys. Chem. B* **2005**, *109*, 20174; d) A. Saeki, S. Seki, T. Sunagawa, K. Ushida, S. Tagawa, *Philos. Mag.* **2006**, *86*, 1261; e) T. Amaya, S. Seki, T. Moriuchi, K. Nakamoto, T. Nakata, H. Sakane, A. Saeki, S. Tagawa, T. Hirao, *J. Am. Chem. Soc.* **2009**, *131*, 408.

[11] The IPCE value of C_{70} clusters was reported to be low (< 1%) when deposited on a nanostructured SnO_2 electrode from a toluene–acetonitrile mixture, where the pristine structure of C_{70} clusters is preserved. Accordingly, the rather high IPCE value (10%) in

this work probably originates from the structural alteration of $(C_{70})_m$ on the electrode during the drying process as well as the difference in the cluster states arising from the ODCB–acetonitrile and toluene–acetonitrile mixtures. T. Hasobe, H. Imahori, P. V. Kamat, T. K. Ahn, S. K. Kim, D. Kim, A. Fujimoto, T. Hirakawa, S. Fukuzumi, *J. Am. Chem. Soc.* **2005**, *127*, 1216.

[12] a) G. M. A. Rahman, D. M. Guldi, R. Cagnoli, A. Mucci, L. Schenetti, L. Vaccari, M. Prato, *J. Am. Chem. Soc.* **2005**, *127*, 10051; b) L. Sheeney-Haj-Ichia, B. Basnar, I. Willner, *Angew. Chem. Int. Ed.* **2005**, *44*, 78; c) S. Campidelli, B. Ballesteros, A. Filoramo, D. D. Diaz, G. D. L. Torre, T. Torres, G. M. A. Rahman, C. Ehli, D. Kiessling, F. Werner, V. Sgobba, D. M. Guldi, C. Cioffi, M. Prato, J.-P. Bourgoin, *J. Am. Chem. Soc.* **2008**, *130*, 11503.

[13] J. W. Arbogast, C. S. Foote, *J. Am. Chem. Soc.* **1991**, *113*, 8886.

[14] P.-M. Allemand, A. Koch, F. Wudl, Y. Rubin, F. Diederich, M. M. Alvarez, S. J. Anz, R. L. Whetten, *J. Am. Chem. Soc.* **1991**, *113*, 1050.

[15] T. Umeyama, M. Fujita, N. Tezuka, N. Kadota, Y. Matano, K. Yoshida, S. Isoda, H. Imahori, *J. Phys. Chem. C* **2007**, *111*, 11484.

[16] a) D. R. Lawson, D. L. Feldheim, C. A. Foss, P. K. Dorhout, M. Elliott, C. R. Martin, B. Parkinson, *J. Phys. Chem.* **1992**, *96*, 7175; b) D. M. Guldi, H. Hungerbühler, M. Wilhelm, K.-D. Asmus, *J. Chem. Soc., Faraday Trans.* **1994**, *90*, 1391.

[17] The lifetimes of C_{70} singlet (660 ps) and triplet (130 μs) states are rather comparable to those of the C_{60} singlet (1200 ps) and triplet (40 μs) states. Given the high intersystem crossing yield of C_{60} (96%) and C_{70} (90%), intermolecular ET process from I^- in the electrolyte to the fullerene excited states would not affect the difference in the IPCE values. M. Lee, O.-K. Song, J.-C. Seo, D. Kim, Y. D. Suh, S. M. Jin, S. K. Kim, *Chem. Phys. Lett.* **1992**, *196*, 325.

[18] M. W. Schmidt, K. K. Baldridge, J. A. Boatz, S. T. Elbert, M. S. Gordon, J. H. Jensen, S. Koseki, N. Matsunaga, K. A. Nguyen, S. Su, T. L. Windus, M. Dupuis, J. A. Montgomery, Jr., *J. Comput. Chem.* **1993**, *14*, 1347.

[19] M. J. Frisch, G. W. Trucks, H. B. Schlegel, G. E. Scuseria, M. A. Robb, J. R. Cheeseman, J. A. Montgomery, Jr., T. Vreven, K. N. Kudin, J. C. Burant, J. M. Millam, S. S. Iyengar, J. Tomasi, V. Barone, B. Mennucci, M. Cossi, G. Scalmani, N. Rega, G. A. Petersson, H. Nakatsuji, M. Hada, M. Ehara, K. Toyota, R. Fukuda, J. Hasegawa, M. Ishida, T. Nakajima, Y. Honda, O. Kitao, H. Nakai, M. Klene, X. Li, J. E. Knox, H. P. Hratchian, J. B. Cross, V. Bakken, C. Adamo, J. Jaramillo, R. Gomperts, R. E. Stratmann, O. Yazyev, A. J. Austin, R. Cammi, C. Pomelli, J. W. Ochterski, P. Y. Ayala, K. Morokuma, G. A. Voth, P. Salvador, J. J. Dannenberg, V. G. Zakrzewski, S. Dapprich, A. D. Daniels, M. C.

Strain, O. Farkas, D. K. Malick, A. D. Rabuck, K. Raghavachari, J. B. Foresman, J. V. Ortiz, Q. Cui, A. G. Baboul, S. Clifford, J. Cioslowski, B. B. Stefanov, G. Liu, A. Liashenko, P. Piskorz, I. Komaromi, R. L. Martin, D. J. Fox, T. Keith, M. A. Al-Laham, C. Y. Peng, A. Nanayakkara, M. Challacombe, P. M. W. Gill, B. Johnson, W. Chen, M. W. Wong, C. Gonzalez, J. A. Pople, *Gaussian 03*, revision C.02; Gaussian, Inc.: Wallingford, CT, 2004.

[20] N. V. Tkachenko, L. Rantala, A. Y. Tauber, J. Helaja, P. H. Hynninen, H. Lemmetyinen, *J. Am. Chem. Soc.* **1999**, *121*, 9378.

Chapter 7

Comparison of Cluster Formation, Film Structure, Microwave Conductivity, and Photoelectrochemical Properties of Composites Consisting of Single-Walled Carbon Nanotubes with C_{60}, C_{70}, and C_{84}

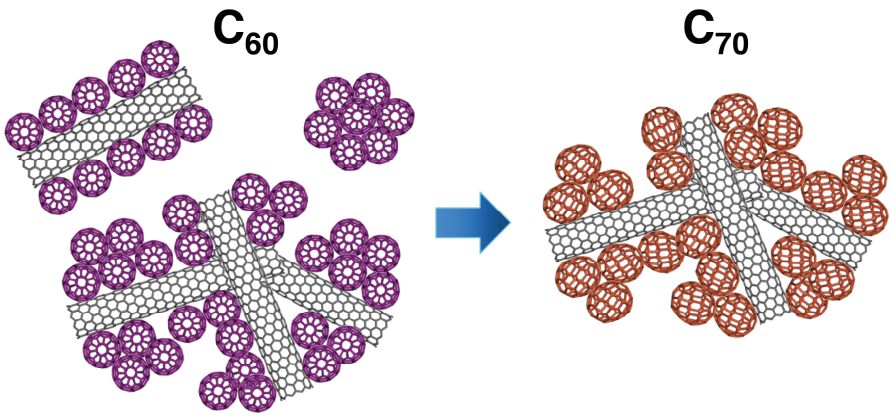

Abstract: The cluster formation, electrophoretically deposited film structures, microwave conductivity, and photoelectrochemical properties of the composites consisting of single-walled carbon nanotubes (SWNTs) with C_{60}, C_{70}, or C_{84} have been systematically compared. In *o*-dichlorobenzene (ODCB)–acetonitrile mixture, the higher fullerenes (*i.e.*, C_{70} and C_{84}) were found to form single composite clusters exclusively with highly soluble SWNTs bearing bulky swallow-tailed substituents (f-SWNT). These are in marked contrast with the unselective formation of three different clusters in the C_{60}–f-SWNT composites. The microwave conductivity measurements revealed the occurrence of electron transfer from C_{70} to f-SWNT, followed by electron transportation through f-SWNT, in addition to electron hopping through C_{70} molecule arrays due to the alignment of C_{70} on the sidewalls of f-SWNT in the C_{70}–f-SWNT film. The C_{70}–f-SWNT photoelectrochemical device exhibited higher incident photon-to-current efficiency (IPCE) value (26% at 400 nm) than the C_{60}–f-SWNT device (18%). The higher IPCE value results from selective formation of the single composite film, in which the SWNT network is covered with C_{70} molecules, and the high electron mobility (2.4 $cm^2\ V^{-1}\ s^{-1}$) through the C_{70}–SWNT network. In contrast, the C_{84}–f-SWNT photoelectrochemical device revealed poor photocurrent generation (4.8%) owing to the inefficient electron injection from C_{84} radical anion ($C_{84}/C_{84}^{\bullet -} \approx 0.0$ V *vs.* NHE) to the SnO_2 electrode ($E_{CB} = 0$ V *vs.* NHE) directly or indirectly despite of the exclusive formation of single composite clusters.

Introduction

Carbon nanotubes are mechanically strong, high modulus graphitic fibers with a diameter of 1 – 40 nanometers and a length of micrometers.[1] In particular, single-walled nanotubes (SWNTs) are an important class of carbon nanotubes because they exhibit unique electric properties that are not shared by multi-walled carbon nanotubes.[2] SWNTs are highly promising for miniaturizing electronics beyond the scale currently used in electronics.[2] Specifically, one-dimensional (1-D), nanowire-like structure of SWNTs provides the potential to construct ideal nanohighways for charge carrier on electrodes. Thus, SWNTs have been attempted for the use of electron- or hole-transporting materials in photovoltaic and photoelectrochemical devices.[3–9] Most widely studied SWNT-based photovoltaic devices involve a photoactive layer of bulk heterojunction structures, in which SWNTs are blended with electron-donating π-conjugated polymers such as poly(*p*-phenylenevinylene) and polythiophene.[4] In such cases SWNTs are expected to act as electron-transporting pathways as well as electron acceptors. In addition, individual SWNTs provide large surface area at the polymer–SWNT interface, which would be favorable for efficient dissociation of excitons. Kamat *et al.* also reported photoelectrochemical devices in which supramolecular complexes of SWNTs and protonated porphyrin were electrophoretically deposited onto a nanostructured SnO_2 electrode.[5b] It was suggested that the excited porphyrins injected electrons into SWNTs under illumination and the resulting electrons were further injected into a conduction band (CB) of the SnO_2 electrode through 1-D SWNTs. The dual role of SWNTs, *i.e.*, promoting photoinduced charge separation (CS) and facilitating charge transport, resulted in an incident photon-to-current efficiency (IPCE) up to 13%. More recently, Torres and co-workers integrated a covalently bonded SWNT–phthalocyanine complex into photoactive electrodes.[9a] The indium-tin oxide (ITO) electrode functionalized with the complex exhibited a maximum IPCE value of 17.3%. Electron transfer (ET) from the phthalocyanine excited singlet state to SWNTs and successive electron transport through SWNTs were responsible for the enhanced photocurrent generation. In such a situation, however, the photocurrent generation efficiency of SWNT-based photoelectrochemical devices is still lower than that of analogous fullerene-based photoelectrochemical devices.[3] The poor device performance may at least partially result from the unfavorable bundle formation of SWNTs as well as the significant ratio of metallic SWNTs that leads to energy-wasting quenching of the excited states and the difficulty for forming interpenetrating networks with donors owing to the poor solubility.

Fullerenes have been recognized as promising building blocks for various molecular architectures including optoelectronic and photovoltaic devices, due to their fascinating electrical and photophysical properties.[10] Fullerenes and their derivatives have been ubiquitously employed as the electron-accepting component in bulk heterojunction solar

cells,[11] other photoelectrochemical devices,[12] and artificial photosynthetic models.[13,14] As Imahori *et al.* have demonstrated,[14] this can be rationalized by small reorganization energies of fullerenes in ET, which allows one to achieve fast CS and electron transportation as well as slow charge recombination (CR), as compared with conventional acceptors. Another important aspect for efficient photocurrent generation is to create electron- and hole-transporting pathways in the blend films of donor and fullerene. With this regards, supramolecular complexes of porphyrins and fullerenes have been integrated into photoelectrochemical devices.[15–19] It has been elucidated that the photocurrent generation efficiency could be increased remarkably by the bottom-up organization of porphyrins and fullerenes using diverse nanoscaffolds including dendrimers,[15] polymers,[16] and nanoparticles,[17] or using various intermolecular interactions.[18,19] The suitable arrangement of donor and/or acceptor molecules to achieve efficient hole- and electron-transportation in the blend films is essential for attaining efficient photocurrent generation.

Under these situations, the author initiated studies on the integration of SWNTs with fullerene (*i.e.*, C_{60}) for photoelectrochemical devices.[20] The author envisaged that 1-D SWNTs would act as a nanoscaffold to arrange C_{60} molecules on the sidewalls due to π-π interaction between SWNTs and C_{60}.[21] Furthermore, chemically shortened SWNTs modified with sterically hindered substituents would facilitate such complexation as a result of sufficient debundling of SWNTs in solution.[22] With these in mind, the author developed a novel methodology for the self-organization of C_{60} molecules on the sidewall of SWNTs, as illustrated in Scheme 1.[20] First, acid treatment cuts pristine SWNTs (denoted as p-SWNT) to yield shortened SWNTs (denoted as s-SWNT) with carboxylic groups at the open ends and defect sites (Scheme 1, step 1).[23] Then, s-SWNT is functionalized with sterically hindered swallow-tailed secondary amine to yield soluble, functionalized SWNTs (denoted as f-SWNT) in organic solvents (step 2). Finally, poor solvent (*i.e.*, acetonitrile) is rapidly injected into a mixture of C_{60} and f-SWNT dissolved in good solvent (*o*-dichlorobenzene (ODCB)), resulting in formation of the composite clusters of C_{60} and f-SWNT (denoted as $(C_{60}$+f-SWNT$)_m$, step 3). The SnO_2 electrode modified electrophoretically with the $(C_{60}$+f-SWNT$)_m$ exhibited an IPCE value as high as 18% at 400 nm under an applied potential of 0.05 V *vs.* SCE. The IPCE value is comparable to the highest one ever reported for analogous SWNT-based photoelectrochemical devices in which SWNTs are deposited electrophoretically,[5,6] electrostatically,[7] covalently,[8] or physisorptionally[9] onto semiconducting electrodes. However, there is still much room for improvement in the photocurrent generation efficiency. Drawback of the $(C_{60}$+f-SWNT$)_m$ composite is the unselective formation of three different composite clusters: i) f-SWNT bundles covered with layers of C_{60} molecules (denoted as cluster I), ii) round, large C_{60} clusters with a size of 500 – 1000 nm containing f-SWNT bundles (denoted as cluster II),

and iii) typical, round C_{60} clusters with a size of 150 – 250 nm (denoted as cluster III). The electrophoretic deposition of the composites onto a nanostructured SnO_2 electrode yielded the hierarchical film with gradient composition of clusters I, II, and III sequentially from the bottom to the top as a consequence of the difference in the mobilities during the electrophoretic process. The exclusive deposition of cluster I with a short deposition time led to the large IPCE value of 12.5%. Therefore, selective cluster formation like cluster I and subsequent electrophoretic deposition would be a challenge for improvement of the photocurrent generation efficiency as well as elucidation of the interaction between fullerenes and SWNTs. Considering the different shapes and sizes of higher fullerenes (*i.e.*, rugby ball-shaped C_{70} and rather spherical-shaped C_{84}) in comparison with C_{60}, a combination of f-SWNT with higher fullerenes will affect the cluster formation, deposited film structures, and electron-transporting and photoelectrochemical properties greatly.[24] Although there are a number of reports on C_{60}–SWNT composites,[25–27] comparison of the composite structures and the photoelectrochemical properties of various fullerene–SWNT composites in which the outside of SWNTs interacts with fullerenes has yet to be examined systematically.

SCHEME 1

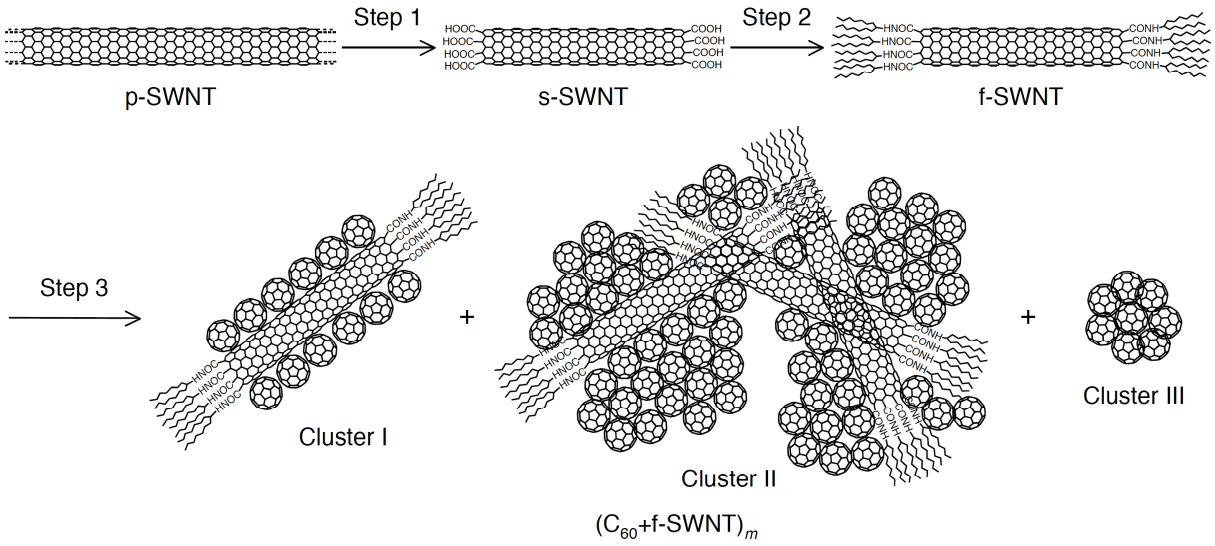

Here the author reports the first systematic studies on the cluster formation, electrophoretically deposited film structures, and carrier-transporting and photoelectrochemical properties of the composites consisting of f-SWNT with C_{60}, C_{70}, or C_{84}. The properties of the C_{70}–f-SWNT and C_{84}–f-SWNT composites were compared with those of the C_{60}–f-SWNT composites, some of which have been reported previously.[20,24] The author also carried out the time-resolved microwave conductivity measurements on all the deposited films including the C_{60}–f-SWNT, C_{70}–f-SWNT, and C_{84}–f-SWNT composites to shed light on the photocurrent

generation mechanism. The electron mobility within the composite was found to be a striking factor toward efficient photocurrent generation.

Results and Discussion

Spectroscopic Characterization on the Composite Clusters: To investigate the effects of higher fullerenes (*i.e.*, C_{70}, C_{84}) on the cluster formation of the fullerene–f-SWNT composites, the author first measured the UV–vis–near NIR (NIR) absorption spectra in ODCB and ODCB–acetonitrile mixture (1:4, v/v). Figure 1A(a) displays absorption spectrum of C_{70} in ODCB. The absorption feature with maximum at 471 nm and shoulders around 550 – 680 nm agrees well with the characteristics of the monomeric C_{70} absorption.[28] In the ODCB–acetonitrile solution, the intense peak at 471 nm observed in ODCB disappears and a new broad band around 695 nm emerges with an absorption tail extending to NIR (Figure 1B(a)). This drastic change in the absorption spectra of C_{70} is attributed to the formation of C_{70} clusters (denoted as $(C_{70})_m$) by lyophobic interaction in the mixed solvent in addition to π-π interaction between C_{70}.[29] Similar absorption behavior was noted for $(C_{60})_m$ cluster.[20] The UV–vis–NIR absorption spectrum of f-SWNT in ODCB–acetonitrile (Figure 1B(b) and inset) is virtually similar to that in ODCB (Figure 1A(b) and inset), exhibiting the characteristic peaks associated with the transitions between symmetric van Hove singularities in the density of states for SWNTs.[30] This implies that the formation of f-SWNT clusters (denoted as $(\text{f-SWNT})_m$) is

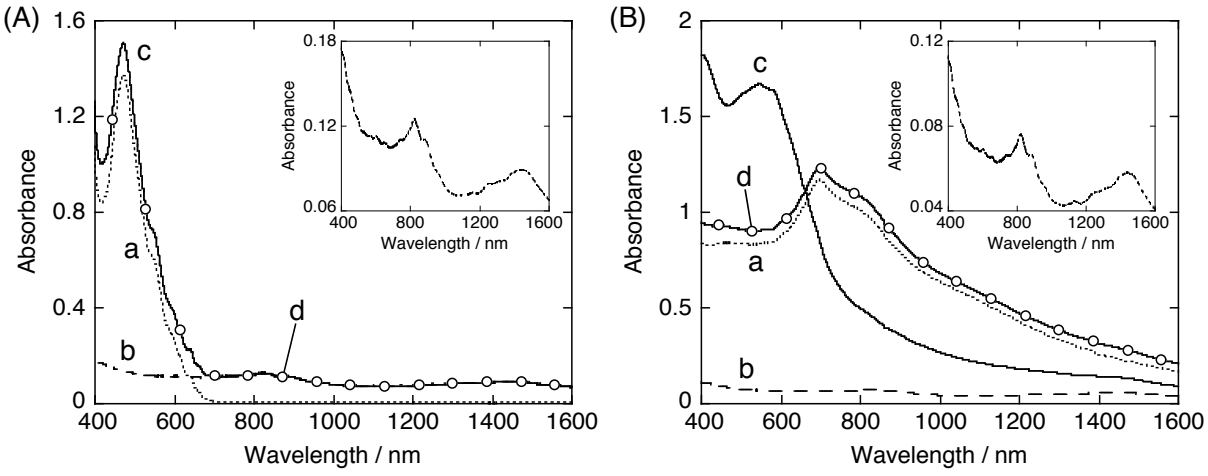

Figure 1. (A) UV–vis–NIR absorption spectra of (a) C_{70}, (b) f-SWNT, (c) a mixture of C_{70} and f-SWNT measured in ODCB ([C_{70}] = 0.68 mM, [f-SWNT] = 0.062 g L^{-1}; path length 1 mm), and (d) sum of spectra (a) and (b). Inset shows enlarged spectrum of (b). (B) UV–vis–NIR absorption spectra of (a) C_{70}, (b) f-SWNT, (c) a mixture of C_{70} and f-SWNT measured in ODCB–acetonitrile mixture (1:4, v/v; [C_{70}] = 0.14 mM, [f-SWNT] = 0.012 g L^{-1}; path length 3 mm), and (d) sum of spectra (a) and (b). Inset shows enlarged spectrum of (b).

suppressed owing to the large steric hindrance of the swallow-tailed substituents around f-SWNT.[20] However, slight vibration of the solution caused precipitation of black solids, showing the instability of $(\text{f-SWNT})_m$ in the mixed solvent.

The absorption spectrum of the mixture of C_{70} and f-SWNT in ODCB (Figure 1A(c)) matches the sum of the absorption spectra of C_{70} and f-SWNT (Figure 1A(d)), implying negligible interaction between C_{70} and f-SWNT in ODCB. In contrast, the absorption spectrum of the mixture in ODCB–acetonitrile exhibits the broad absorption in visible to NIR region with maximum at ~ 547 nm (Figure 1B(c)), which is different from the sum of the absorption spectra of C_{70} and f-SWNT in the mixed solvent (Figure 1B(d)). The observed discordance obviously manifests the formation of the composite clusters of C_{70} and f-SWNT (denoted as $(C_{70}\text{+f-SWNT})_m$) in the ODCB–acetonitrile mixture. Similar formation of $(C_{60}\text{+f-SWNT})_m$ clusters has been seen in ODCB–acetonitrile mixed solvent.[20]

Figure 2A(a) depicts the absorption spectrum of C_{84} in ODCB. The spectrum with virtually no significant structures is essentially the same as the previously reported one for commercially available C_{84}, which consists of several structural isomers.[31,32] Flattened-shaped D_2 and spherical D_{2d} isomers[33] are likely the most abundant components of > 70%, as it is well known that the standard Huffman-Krätschmer soot provides these two isomers as major constituents of 50% for D_2 and 25% for D_{2d}.[34] The absorption spectrum of C_{84} in ODCB–acetonitrile mixture (Figure 2B(a)) yields structureless absorption similar to that in ODCB. However, molar absorptivity (ε) of C_{84} in ODCB–acetonitrile mixture is much higher

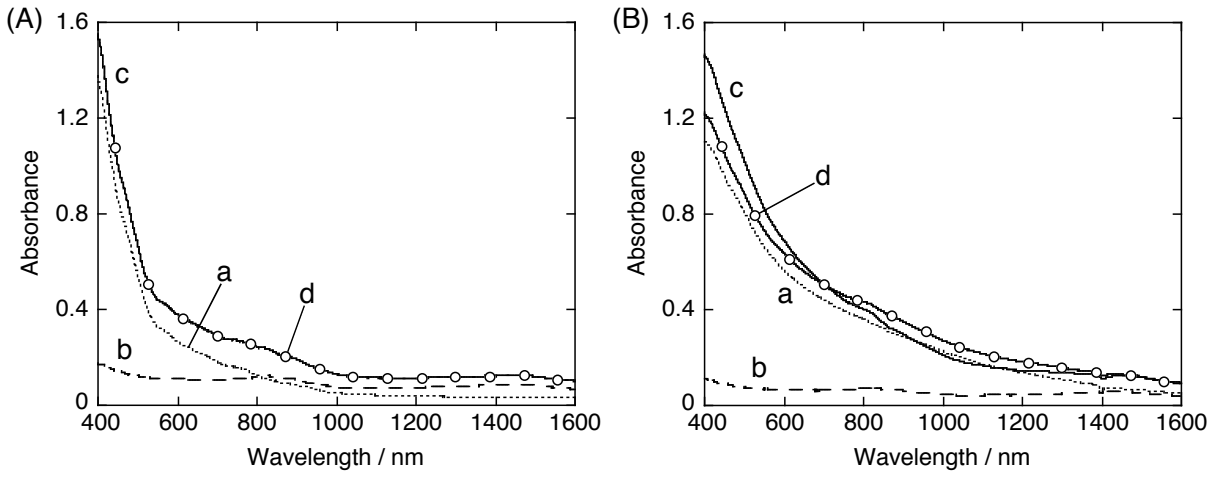

Figure 2. (A) UV–vis–NIR absorption spectra of (a) C_{84}, (b) f-SWNT, (c) a mixture of C_{84} and f-SWNT measured in ODCB ([C_{84}] = 0.68 mM, [f-SWNT] = 0.062 g L^{-1}; path length 1 mm), and (d) sum of spectra (a) and (b). (B) UV–vis–NIR absorption spectra of (a) C_{84}, (b) f-SWNT, (c) a mixture of C_{84} and f-SWNT measured in ODCB–acetonitrile mixture (1:4, v/v; [C_{84}] = 0.14 mM, [f-SWNT] = 0.012 g L^{-1}; path length 3 mm), and (d) sum of spectra (a) and (b).

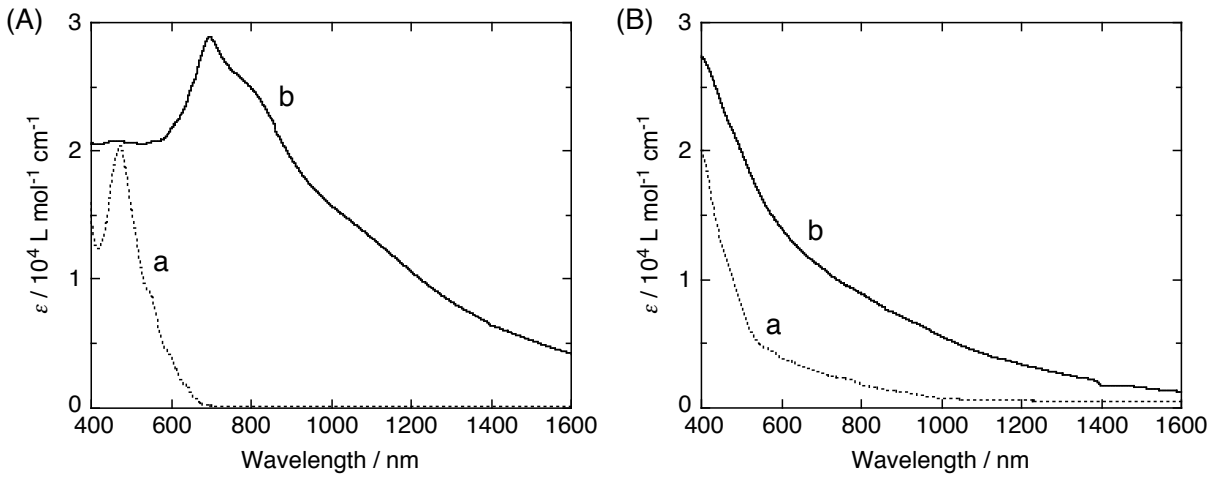

Figure 3. (A) UV–vis–NIR absorption spectra of C_{70} in (a) ODCB (0.68 mM) and (b) ODCB–acetonitrile mixture (1:4, v/v; 0.14 mM). (B) UV–vis–NIR absorption spectra of C_{84} in (a) ODCB (0.68 mM) and (b) ODCB–acetonitrile mixture (1:4, v/v; 0.14 mM).

than that in ODCB (Figure 3B), as seen for $(C_{70})_m$ (Figure 3A), suggesting the formation of C_{84} clusters (denoted as $(C_{84})_m$) in the mixed solvent (*vide infra*).[35]

The absorption spectrum of the mixture of C_{84} and f-SWNT in ODCB (Figure 2A(c)) coincides with the sum of the absorption spectra of C_{84} and f-SWNT (Figure 2A(d)), as in the cases of C_{60} and C_{70}. Thus, there is no significant interaction between C_{84} and f-SWNT in ODCB. In contrast, the absorption spectrum of the mixture of C_{84} and f-SWNT in ODCB–acetonitrile mixture (Figure 2B(c)) differs slightly from the sum of the absorption of $(C_{84})_m$ and $(\text{f-SWNT})_m$ in the mixed solvent (Figure 2B(d)). This also indicates the formation of the composite cluster of C_{84} and f-SWNT (denoted as $(C_{84}+\text{f-SWNT})_m$).

Microscopic Observations of the Composite Clusters: Field emission scanning electron microscopy (FE-SEM) measurements were conducted to evaluate the structures of the composite clusters prepared in the ODCB–acetonitrile mixture (Figure 4). The samples for the FE-SEM measurements were prepared by spin-coating the cluster solutions to silicon wafer. The rotation speed was set to 1200 rpm, at which the shapes of the clusters were preserved during the spin-coating process due to the prompt evaporation of solvents (*vide infra*). In parallel, dynamic light scattering (DLS) measurements were also performed to complement the results of the FE-SEM measurements (Figure 5). The FE-SEM image of $(C_{70})_m$ discloses cuboid particles with a size of 250 – 350 nm (Figure 4a).[29f,g] DLS measurement of $(C_{70})_m$ reveals a relatively narrow size distribution of $(C_{70})_m$ with an average diameter (D_{av}) of 330 nm (Figure 5a), which is consistent with the observed size of $(C_{70})_m$ in Figure 4a. The FE-SEM image of $(C_{60})_m$ manifested spherical particles with a size of 150 – 350 nm, whereas the DLS

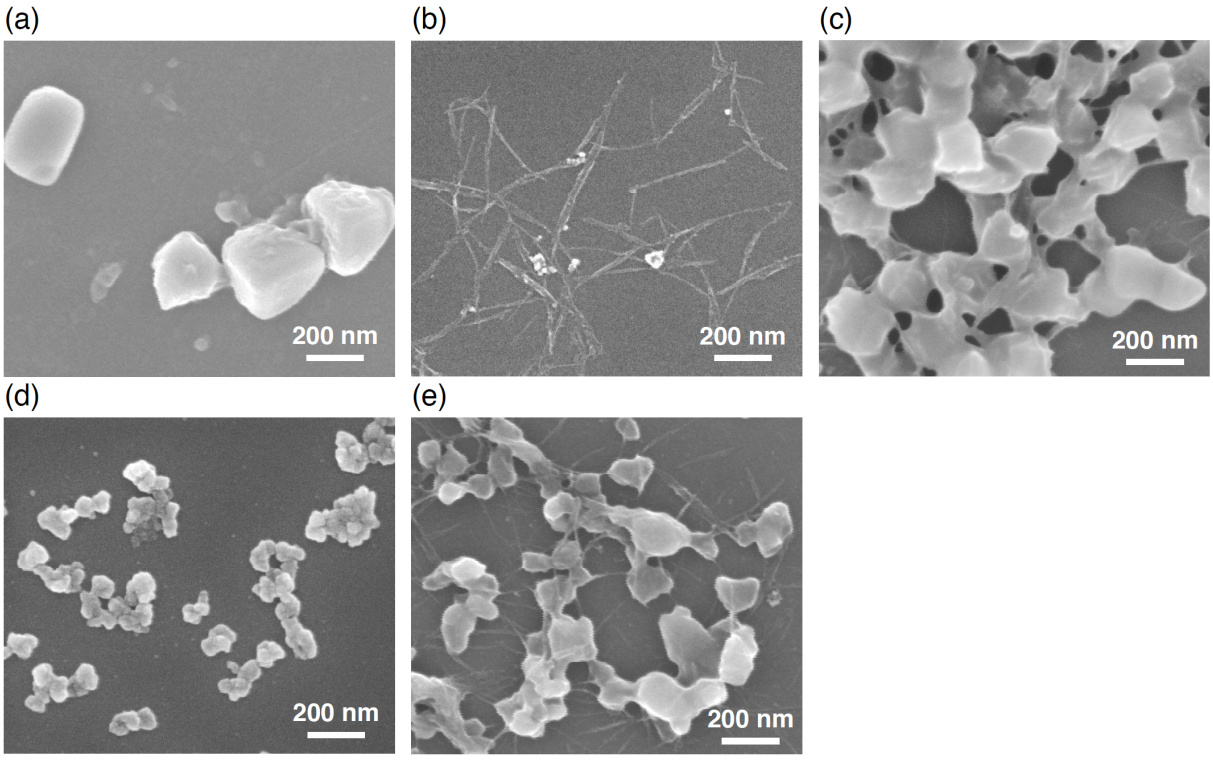

Figure 4. FE-SEM images of (a) $(C_{70})_m$, (b) $(f\text{-SWNT})_m$, (c) $(C_{70}+f\text{-SWNT})_m$, (d) $(C_{84})_m$, and (e) $(C_{84}+f\text{-SWNT})_m$. The samples were prepared by spin-coating the corresponding cluster solutions ($[C_{70}] = [C_{84}] = 0.14$ mM, [f-SWNT] = 0.012 g L^{-1}) from the ODCB–acetonitrile mixture (1:4, v/v) on Si wafer.

measurements exhibited comparable particles with an average diameter of 200 nm.[20] Thus, the shapes of $(C_{60})_m$ and $(C_{70})_m$ are different and the size of $(C_{60})_m$ is slightly smaller than that of $(C_{70})_m$. Figure 4b displays the spaghetti-like structures of $(f\text{-SWNT})_m$ in which the fibrils are entangled. Obviously, the observed fibrous structures result from the bundles of f-SWNT, as the size of individual isolated f-SWNT (~ 1 nm) is beyond the instrument's resolution. Small grains with a size less than 100 nm may be residual metal impurities that are present in the f-SWNT sample even after the purification procedure.

The FE-SEM image of $(C_{70}+f\text{-SWNT})_m$ reveals a sole network structure in which cuboid particles with a size of 150 – 200 nm are fused to be interconnected each other (Figure 4c). This is in marked contrast with the previous result where $(C_{60}+f\text{-SWNT})_m$ consists of three different clusters I – III (Scheme 1).[20] The network structure of $(C_{70}+f\text{-SWNT})_m$ shows that the C_{70} clusters are assembled with the bundles of f-SWNT to form such single, larger nanostructures. This is in agreement with the results of the spectroscopic measurements in which the absorption feature of $(C_{70}+f\text{-SWNT})_m$ differs from those of $(C_{70})_m$ and $(f\text{-SWNT})_m$ (*vide supra*). Exclusive formation of the network structure is further corroborated by the results of the DLS measurements. Namely, The $(C_{70}+f\text{-SWNT})_m$ solution (Figure 5c) exhibits

a sole monomodal cluster, which is different from those of $(C_{70})_m$ and $(f\text{-SWNT})_m$ solutions (Figure 5a and b). Ellipsoidal shape and large size of C_{70} relative to C_{60} may contribute to the enhanced interaction with the sidewall of f-SWNT, leading to the exclusive formation of the composite cluster. Importantly, density functional theory (DFT) calculations showed that the binding energies between C_{70} and SWNTs are larger by ~ 3 kcal mol^{-1} than those between C_{60} and SWNTs when C_{70} molecule is stacked on the sidewall of SWNTs with its long axis parallel to the tube axis, at least partly rationalizing the tendency of C_{70} to form the single composite cluster with f-SWNT.[24]

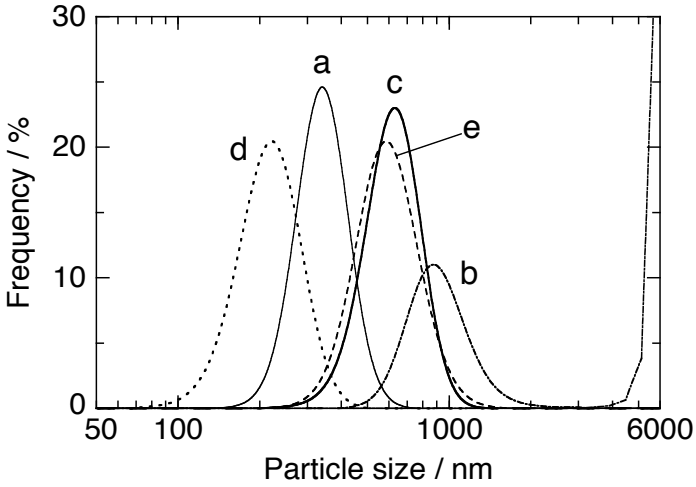

Figure 5. Particle size distribution of (a) $(C_{70})_m$, (b) $(f\text{-SWNT})_m$, (c) $(C_{70}+f\text{-SWNT})_m$, (d) $(C_{84})_m$, and (e) $(C_{84}+f\text{-SWNT})_m$ measured in ODCB–acetonitrile mixture (1:4, v/v). Concentration: $[C_{70}] = [C_{84}] = 0.14$ mM, [f-SWNT] = 0.012 g L^{-1}.

The FE-SEM image of $(C_{84})_m$ sample depicts aggregates of rather spherical small particles with an average size of 75 nm (Figure 4d). Considering that the DLS measurement exhibits a monomodal cluster with D_{av} = 210 nm (Figure 5d), $(C_{84})_m$ likely exists as aggregates of the several small particles. Nevertheless, Figure 4e illustrates a single network structure of $(C_{84}+f\text{-SWNT})_m$ in which particles with a size of 100 – 200 nm are merged each other. Taking into accounts the similar network images of $(C_{70}+f\text{-SWNT})_m$ and $(C_{84}+f\text{-SWNT})_m$, C_{84} clusters are also assembled with the bundles of f-SWNT to form the sole network structure. The DLS measurement also reveals a single monomodal distribution for the $(C_{84}+f\text{-SWNT})_m$ solution (Figure 5e), which differs from those of $(C_{84})_m$ and $(f\text{-SWNT})_m$ solutions (Figure 5d and b). Although $(C_{84})_m$ consists of an isomeric mixture of C_{84} including flattened-shaped D_2 and spherical D_{2d} major isomers,[34] the flattened D_2 isomer compared to that of C_{60} may cause the enhancement in the interaction with f-SWNT, which results in exclusive formation of the single composite cluster as in the case of C_{70}.

Electrophoretic Deposition: For the photoelectrochemical and microwave conductivity measurements, the clusters of f-SWNT and/or fullerenes (C_{60}, C_{70}, C_{84}) were deposited by the electrophoretic method[20] onto the fluorine-doped tin oxide (FTO) electrodes modified with nanostructured SnO_2 (denoted as $FTO/SnO_2/(C_n)_m$ (n = 60, 70, 84), $FTO/SnO_2/(f\text{-SWNT})_m$, $FTO/SnO_2/(C_n+f\text{-SWNT})_m$ (n = 60, 70, 84)). Under an application of the high dc electric field

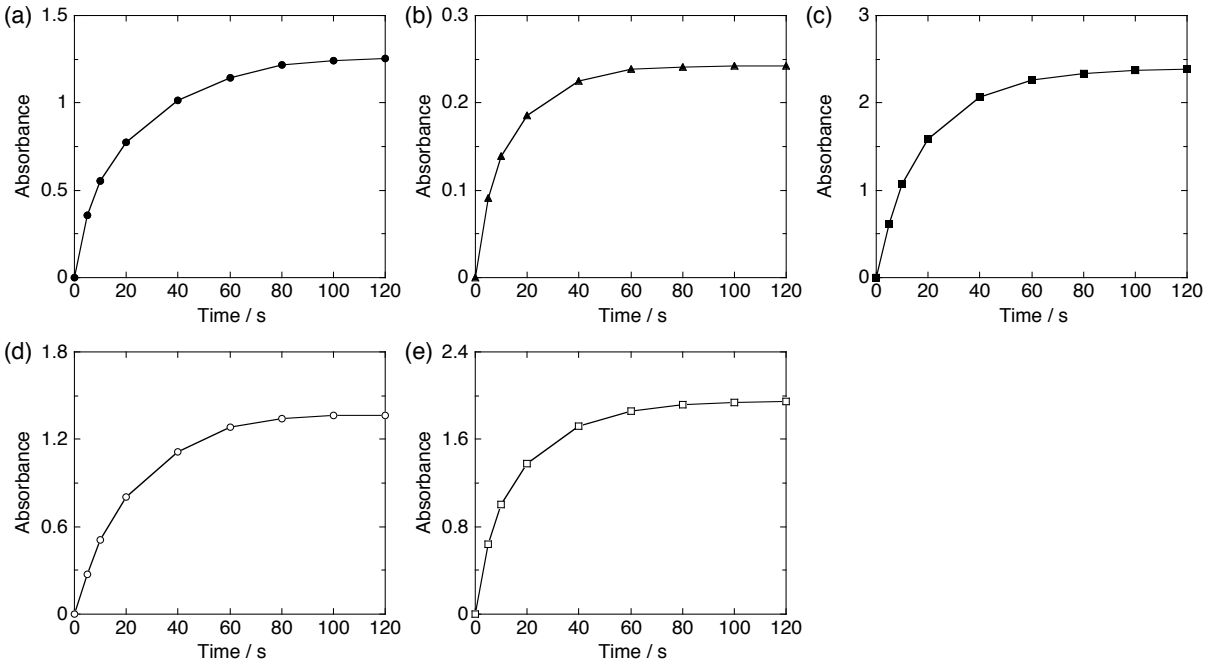

Figure 6. Change in absorption of (a) FTO/SnO_2/$(C_{70})_m$, (b) FTO/SnO_2/(f-SWNT)$_m$, (c) FTO/SnO_2/(C_{70}+f-SWNT)$_m$, (d) FTO/SnO_2/$(C_{84})_m$, and (e) FTO/SnO_2/(C_{84}+f-SWNT)$_m$ electrodes at different time intervals during electrophoretic deposition. Absorbance at 400 nm was monitored. Absorbance of the FTO/SnO_2 electrode was subtracted from each spectrum.

of 200 V for 120 s, the clusters, all of which are negatively charged in the mixed solvent, are driven toward the positively charged electrode (*i.e.*, FTO/SnO_2). The film formation was probed by monitoring the changes in absorbance of the electrophoretically deposited electrodes at 400 nm as a function of deposition time (Figure 6). For all of the electrodes, absorbance was increased by increasing the deposition time to reach a plateau within 120 s, thereby the completion of the film formation. For the following measurements, the author used electrodes prepared with a deposition time of 120 s.

Absorption Spectroscopies of the Deposited Films: The UV–vis–NIR absorption spectra of the deposited films on nanostructured SnO_2 electrodes are shown in Figure 7. Both of the FTO/SnO_2/$(C_{70})_m$ and FTO/SnO_2/(C_{70}+f-SWNT)$_m$ electrodes exhibit a broad absorption feature in the visible region with a maximum at 480 nm (Figure 7A(a) and (c)). It is noteworthy that the absorption spectra of the FTO/SnO_2/$(C_{70})_m$ and FTO/SnO_2/(C_{70}+f-SWNT)$_m$ electrodes differ from those of $(C_{70})_m$ and (C_{70}+f-SWNT)$_m$ in the ODCB–acetonitrile mixture, respectively (Figure 1B(a) and (c)). Namely, broad absorption maxima at 695 nm and 550 nm observed in the cluster solutions, respectively, are shifted to 480 nm after the electrophoretic deposition, which is close to the characteristic peak at 470 nm due to monomeric C_{70} in ODCB (Figure 1A(a)). This suggests that the $(C_{70})_m$ and (C_{70}+f-SWNT)$_m$ cause structural alteration

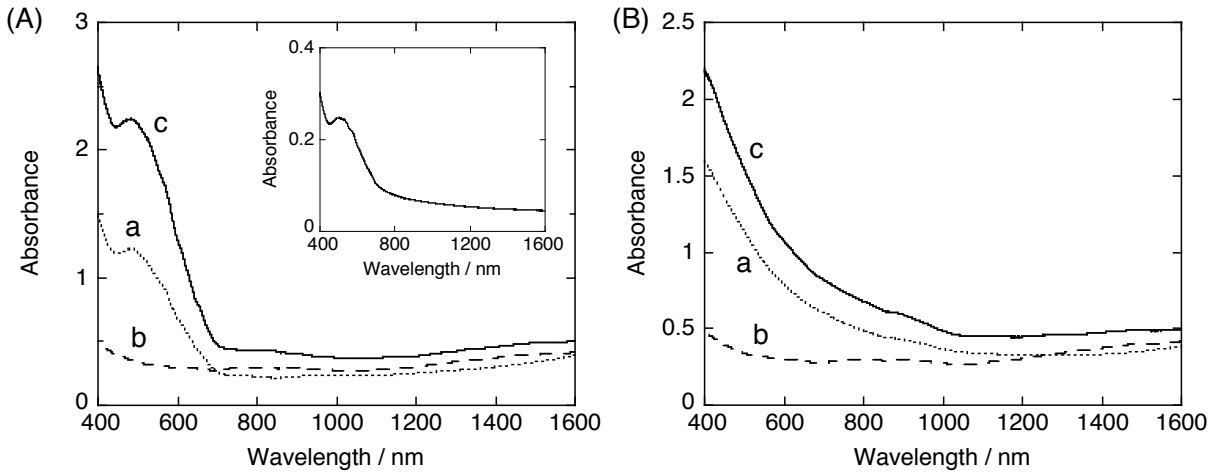

Figure 7. (A) UV–vis–NIR absorption spectra of (a) FTO/SnO_2/$(C_{70})_m$, (b) FTO/SnO_2/(f-SWNT)$_m$, and (c) FTO/SnO_2/(C_{70}+f-SWNT)$_m$ electrodes. Inset shows absorption spectrum of spin-coated film of C_{70} on a slide glass fabricated from ODCB solution. (B) UV–vis–NIR absorption spectra of (a) FTO/SnO_2/$(C_{84})_m$, (b) FTO/SnO_2/(f-SWNT)$_m$, and (c) FTO/SnO_2/(C_{84}+f-SWNT)$_m$ electrodes.

during the electrophoretic deposition (*vide infra*). Although the similarity in the shape of the absorption spectra corresponds to analogous microscopic environments surrounding C_{70} molecules on the two electrodes, more intense absorption of the FTO/SnO_2/(C_{70}+f-SWNT)$_m$ compared to that of the FTO/SnO_2/$(C_{70})_m$ at 400 – 700 nm implies somewhat different environment around C_{70} molecules, which probably arises from the incorporation of f-SWNT. On the other hand, the absorption changes of the FTO/SnO_2/$(C_{60})_m$ and FTO/SnO_2/(C_{60}+ f-SWNT)$_m$ electrodes in comparison with the $(C_{60})_m$ and (C_{60}+f-SWNT)$_m$ clusters in ODCB–acetonitrile mixture were not evident.[20]

In the cases of the FTO/SnO_2/$(C_{84})_m$, FTO/SnO_2/(f-SWNT)$_m$, and FTO/SnO_2/(C_{84}+f-SWNT)$_m$ electrodes, the absorption features of the deposited films (Figure 7B(a) – (c)) are largely identical to those of the corresponding cluster solutions (Figure 2B), suggesting that the deposited clusters on the electrodes retain their cluster structures in the ODCB–acetonitrile mixture. Overall, the broad absorption of the fabricated films in addition to the high molar absorptivity in the visible region makes these films suitable for harvesting the solar energy.

Surface Characterization of the Deposited Films: FE-SEM was employed to evaluate the surface morphology of the electrophoretically deposited films (Figure 8). The FE-SEM image of the FTO/SnO_2/$(C_{70})_m$ electrode (Figure 8a) shows irregular surface with small grains protruding from blurred structureless underlayer. Cuboid C_{70} clusters (~ 300 nm) observed in the spin-coated sample (Figure 4a) are absent on the electrode. Given the fact that the spectral shape of the FTO/SnO_2/$(C_{70})_m$ is close to that of the ODCB solution of C_{70} rather than that of

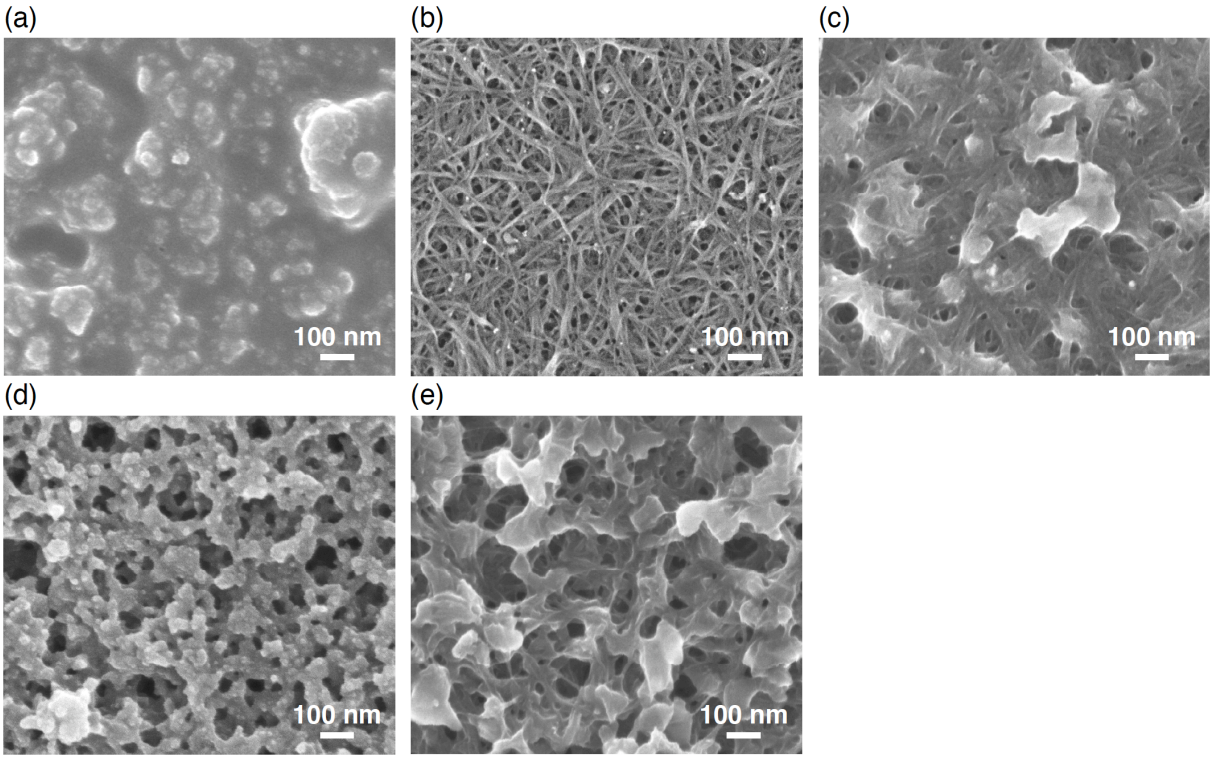

Figure 8. FE-SEM images of (a) FTO/SnO_2/$(C_{70})_m$, (b) FTO/SnO_2/(f-SWNT)$_m$, (c) FTO/SnO_2/(C_{70}+f-SWNT)$_m$, (d) FTO/SnO_2/$(C_{84})_m$, and (e) FTO/SnO_2/(C_{84}+f-SWNT)$_m$ electrodes. Samples (a) and (d) were coated with 5 nm-thick Pt layer prior to the measurements.

the $(C_{70})_m$ cluster in the ODCB–acetonitrile mixture as mentioned above, it is most likely that the $(C_{70})_m$ state is transformed into monomeric C_{70} during the electrophoretic deposition to yield an amorphous-like film with granulous remnants of $(C_{70})_m$.[36] Reversibility between the two states is general in terms of fullerenes, as one can confirm it by adding an excess good solvent to the cluster solution, which leads to regeneration of the monomeric fullerene.[29a,c] As seen in Figure 4a, $(C_{70})_m$ may retain the original cuboid structure on the electrode immediately after the deposition. Then, the electrode is dried with a hair dryer (see experimental section). During the dry process, acetonitrile with a low boiling point of 82 ^oC vaporizes much faster than ODCB with a high boiling point of 180 ^oC. The resultant ODCB-rich environment on the electrode would dissolve $(C_{70})_m$ to regenerate monomeric C_{70}. The absorption spectrum of the C_{70} film on a slide glass spin-coated from the ODCB solution (inset of Figure 7A) reveals virtually the same shape of absorption as that of the FTO/SnO_2/$(C_{70})_m$ electrode (Figure 7A(a)), corroborating the hypothesis.

The FTO/SnO_2/(f-SWNT)$_m$ electrode exhibits the entangled bundles of f-SWNT lying horizontally on the electrode (Figure 8b). On the other hand, the FE-SEM image of the FTO/SnO_2/(C_{70}+f-SWNT)$_m$ electrode reveals coalescent fibrous network (Figure 8c). Note that the interconnected C_{70} particles observed on Si wafer (Figure 4c) are not seen, whereas some

granulous structures are present. This microscopic observation together with the spectroscopic change upon electrophoretic deposition (*vide supra*) obviously manifests the occurrence of melting on the surface of C_{70} cluster moieties in the composite cluster during the drying process, as in the case of the FTO/SnO_2/$(C_{70})_m$. Such regeneration of fullerene monomers from electrophoretically deposited clusters on electrodes was not apparent for the $(C_{60})_m$ and (C_{60}+ f-SWNT)$_m$ clusters.[20] The author emphasizes here, however, that the melting behavior of C_{70} does not lead to unfavorable separation between C_{70} and f-SWNT in the deposited (C_{70}+ f-SWNT)$_m$ cluster, which would deteriorate the electronic interaction between them.

Figures 8d and 8e illustrate interconnected surface morphology of the FTO/SnO_2/$(C_{84})_m$ and FTO/SnO_2/(C_{84}+f-SWNT)$_m$ electrodes. Although the melting trend is also observed to some extent, they largely maintain their original structures as seen in the spin-coated samples from the cluster solutions (Figures 4d and 4e). These results are consistent with little difference in the absorption spectra of the deposited films and the corresponding cluster solutions (*vide supra*). The author notes that the solubility of C_{84} in ODCB (~ 8 mM) is much lower than that of C_{70} (43 mM),[37] which may suppress the melting behavior during the drying process in the case of $(C_{84})_m$ and (C_{84}+f-SWNT)$_m$ clusters. It should be stressed here that the FTO/SnO_2/(C_{70}+f-SWNT)$_m$ and FTO/SnO_2/(C_{84}+f-SWNT)$_m$ electrodes disclose sole network structures in which the fibrous SWNTs are covered with fullerenes, which is in sharp contrast with the hierarchical film structure consisting of three different clusters for the FTO/SnO_2/ (C_{60}+f-SWNT)$_m$ electrode.[20]

Transient Microwave Conductivity Measurements: Flash-photolysis time-resolved microwave conductivity (TRMC) measurements[38] were performed on the deposited films to evaluate charge carrier mobility (μ). For the sample preparation, the deposited films were peeled off from the FTO substrate and fixed on quartz plates with poly(methyl methacrylate) matrices. Upon exposure to a laser pulse with an excitation wavelength of 355 nm, all samples reveal a rise of the transient conductivity $<\phi\Sigma\mu>$, in which ϕ is the quantum efficiency of CS and $\Sigma\mu$ is the sum of mobility of all the transient-charge carriers (Figure 9). It was confirmed that the kinetics of the conductivity transients are independent on the excitation-density in the range of $1.6 \times 10^{15} - 3.6 \times 10^{16}$ cm^{-2} for all samples. The ϕ values of CS were determined by conventional DC-current integration using semitransparent Au electrode as a counter electrode under an excitation at 355 nm. It should be noted that for all films the current transients are observed in negative bias mode giving effective accumulation of the negative charges into the integrator, whereas negligible positive charges are detected with the positive bias mode, thus showing that the major charge carriers stem from electrons. Maximum values of $<\phi\Sigma\mu>$, ϕ, and $\Sigma\mu$ are listed in Table 1.

The $\Sigma\mu$ value (3.2 $cm^2\ V^{-1}\ s^{-1}$) of the FTO/SnO_2/(f-SWNT)$_m$ electrode is the highest one among the samples, demonstrating the superior electron-transporting property of f-SWNT. For a series of the fullerene clusters, the $\Sigma\mu$ value is in the order of FTO/SnO_2/(C_{70})$_m$ (1.9 cm^2

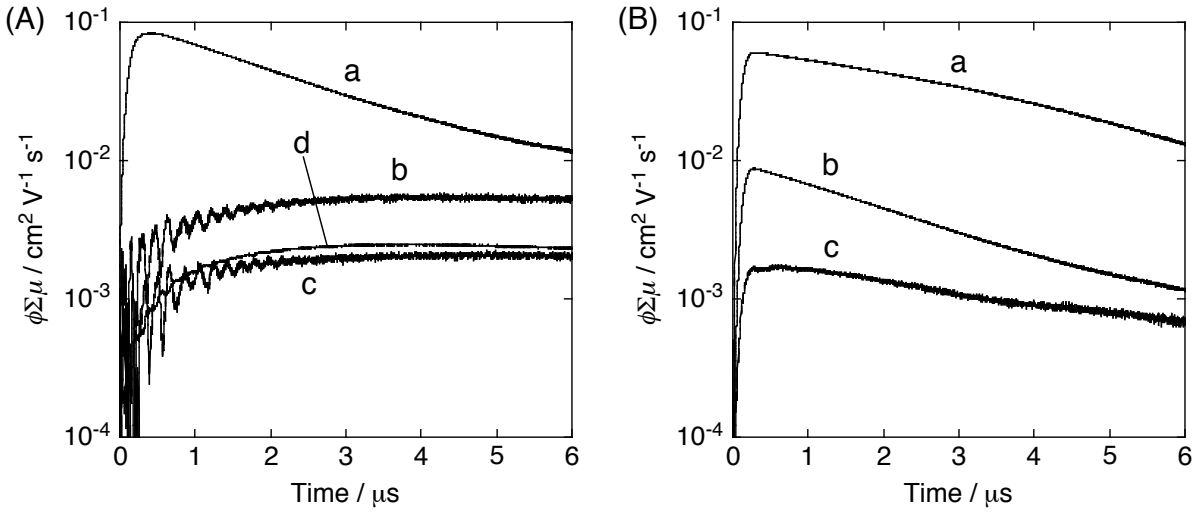

Figure 9. (A) Flash-photolysis TRMC transients for (a) FTO/SnO_2/(C_{70}+f-SWNT)$_m$, (b) FTO/SnO_2/(C_{60}+f-SWNT)$_m$, (c) FTO/SnO_2/(C_{84}+f-SWNT)$_m$, and (d) FTO/SnO_2/(f-SWNT)$_m$ electrodes. (B) Flash-photolysis TRMC transients for (a) FTO/SnO_2/(C_{70})$_m$, (b) FTO/SnO_2/(C_{60})$_m$, and (c) FTO/SnO_2/(C_{84})$_m$ electrodes. The transients were recorded at an excitation wavelength of 355 nm with a photon density of 3.3×10^{15} cm^{-2}. All samples are fixed on quartz substrates with poly(methyl methacrylate) matrices.

TABLE 1: Microwave Conductivity, Quantum Efficiency of CS, Electron Mobility, and Maximal IPCE Value of the Composite Clusters

cluster	$\phi\Sigma\mu$ [a,b] / $cm^2\ V^{-1}\ s^{-1}$	ϕ [a,c] / %	$\Sigma\mu$ [a] / $cm^2\ V^{-1}\ s^{-1}$	maximum IPCE [d] / %
(C_{70})$_m$	0.061	3.1	1.9	10
(C_{60})$_m$	0.0088	1.7	0.52	5.1 [e]
(C_{84})$_m$	0.0018	1.4	0.13	4.1
(C_{70}+f-SWNT)$_m$	0.084	3.5	2.4	26
(C_{60}+f-SWNT)$_m$	0.0056	0.50	1.2	18 [e]
(C_{84}+f-SWNT)$_m$	0.0021	0.12	1.8	4.8
(f-SWNT)$_m$	0.0024	0.075	3.2	2.6

[a] ϕ = quantum efficiency of CS; $\Sigma\mu$ = sum of mobility of all the transient-charge carriers. [b] Maximum value of the transient conductivity upon photoirradiation at 355 nm (photon density: 3.3×10^{15} cm^{-2}). [c] Determined by conventional DC-current integration technique with an photoexcitation at 355 nm. [d] At 400 nm. [e] Taken from ref 20.

V^{-1} s^{-1}) > FTO/SnO_2/$(C_{60})_m$ (0.52 cm^2 V^{-1} s^{-1}) > FTO/SnO_2/$(C_{84})_m$ (0.13 cm^2 V^{-1} s^{-1}). The trend on the electron mobilities is not consistent with the order of the electron mobilities of C_{60} (0.08 cm^2 V^{-1} s^{-1}) > C_{70}, C_{84} (~ 0.002 cm^2 V^{-1} s^{-1}), which were obtained under the operation of field-effect transistor (FET) using the evaporated films.[39] Taking into account the averaged strength of electric field (~ 10^2 V cm^{-1}) in the microwave cavity used in the TRMC system, the perturbation length of the negative charge carriers is estimated as a few nm with the value of observed mobility in $(C_{70})_m$ as ~ 1.9 cm^2 V^{-1} s^{-1}. This implies that the TRMC measurements probe the AC-field induced oscillating motion of the negative charges within a few membered clustering structures of C_{70}. Microscopic differences in the packing structures, thus, mainly contribute to the oscillating motions, whereas long-range (a few tens of μm) translational motion of charge carriers is required under the FET operations. This is the case giving the discrepancy in the mobility values observed by TRMC and FET, and the present results suggest the presence of the nm-scaled passes of highly mobile electrons in C_{70} clusters.

For a series of the composite clusters, the order of the $\Sigma\mu$ values exhibits different tendency: FTO/SnO_2/$(C_{70}$+f-SWNT$)_m$ (2.4 cm^2 V^{-1} s^{-1}) > FTO/SnO_2/$(C_{84}$+f-SWNT$)_m$ (1.8 cm^2 V^{-1} s^{-1}) > FTO/SnO_2/$(C_{60}$+f-SWNT$)_m$ (1.2 cm^2 V^{-1} s^{-1}). Notably, nearly 30% increase in the $\Sigma\mu$ value is discernible when C_{70} is clusterized with f-SWNT, accompanying a 13% increase in the ϕ value. The rise profile of the transient conductivity for the FTO/SnO_2/$(C_{70}$+f-SWNT$)_m$ (Figure 9A(a)) is close to that for the FTO/SnO_2/$(C_{70})_m$ (Figure 9B(a)), both reaching the conductivity maxima within 0.4 μs, while that for the FTO/SnO_2/(f-SWNT$)_m$ (Figure 9A(d)) reveals a slower rise component. Similarity in the photoresponse behavior of the TRMC signals for the FTO/SnO_2/$(C_{70}$+f-SWNT$)_m$ and FTO/SnO_2/$(C_{70})_m$ implies that large majority of the photocarriers in the C_{70}–f-SWNT composites are generated by excitation of C_{70}. On the other hand, decay kinetics of the conductivity transients for the FTO/SnO_2/$(C_{70}$+f-SWNT$)_m$ exhibits a pseudo-first to second order profile (time constant: $k = 4.2 \times 10^5$ s^{-1} and 1.4×10^6 s^{-1} for pseudo-first and second order decay, respectively), which is different from those of the FTO/SnO_2/$(C_{70})_m$ and the FTO/SnO_2/(f-SWNT$)_m$. The second order decay profile was observed only for the FTO/SnO_2/$(C_{70}$+f-SWNT$)_m$. All of these features can be interpreted by the occurrence of ET from C_{70} radical anion to f-SWNT, followed by bulk recombination of charge carriers during electron transportation through f-SWNT, in addition to electron hopping on C_{70} arrays due to the alignment of C_{70} on the sidewalls of f-SWNT in the FTO/SnO_2/ $(C_{70}$+f-SWNT$)_m$. The exclusive formation of network structure on the electrode in which the f-SWNT network is covered with C_{70} molecules contributes to the high electron mobility of the C_{70}–f-SWNT composites.

Transient kinetics of the FTO/SnO_2/$(C_{60}$+f-SWNT$)_m$ (Figure 9A(b)), FTO/SnO_2/$(C_{84}$+ f-SWNT$)_m$ (Figure 9A(c)), and FTO/SnO_2/(f-SWNT$)_m$ (Figure 9A(d)) are similar, exhibiting a

gradual rise of the conductivity over 3 μs. This presents a striking contrast to those of the FTO/SnO_2/$(C_{70})_m$ (Figure 9B(a)), FTO/SnO_2/$(C_{60})_m$ (Figure 9B(b)), and FTO/SnO_2/$(C_{84})_m$ (Figure 9B(c)), giving a prompt rise within 0.5 μs and a fast decay. These results imply that the photogenerated carriers in the FTO/SnO_2/$(C_{60}$+f-SWNT$)_m$ and FTO/SnO_2/$(C_{84}$+f-SWNT$)_m$ arise from the direct excitation of f-SWNT and are localized on f-SWNT. The small $\Sigma\mu$ value of the FTO/SnO_2/$(C_{60}$+f-SWNT$)_m$ relative to that of the FTO/SnO_2/$(C_{84}$+f-SWNT$)_m$ may result from the mixture of the three different clusters, which would mask intrinsic electron mobility of the C_{60}–f-SWNT composite. Rather smaller $\Sigma\mu$ value of the FTO/SnO_2/$(C_{84}$+f-SWNT$)_m$ compared to that of the FTO/SnO_2/(f-SWNT$)_m$ may be attributed to the overestimation of the ϕ value owing to the contribution of the C_{84} excitation, which has no apparent impact on the carrier mobility (*vide infra*).

Photoelectrochemical Measurements: Photoelectrochemical measurements were performed in deaerated acetonitrile containing 0.5 M LiI and 0.01 M I_2 with the modified SnO_2 electrodes as a working electrode, a platinum wire as a counter electrode, and an I^-/I_3^- quasi-reference electrode. Figure 10a displays representative photocurrent response of the FTO/SnO_2/$(C_{70}$+f-SWNT$)_m$ electrode illuminated with white light (λ > 380 nm) at an applied potential of 0.05 V *vs.* SCE. The photocurrent response is prompt, steady, and reproducible during the repeated on/off cycles of the visible light illumination. Blank experiment of the FTO/SnO_2 electrode without deposited films exhibited much smaller photocurrent responses under the same conditions. These results confirm the role of the deposited films toward

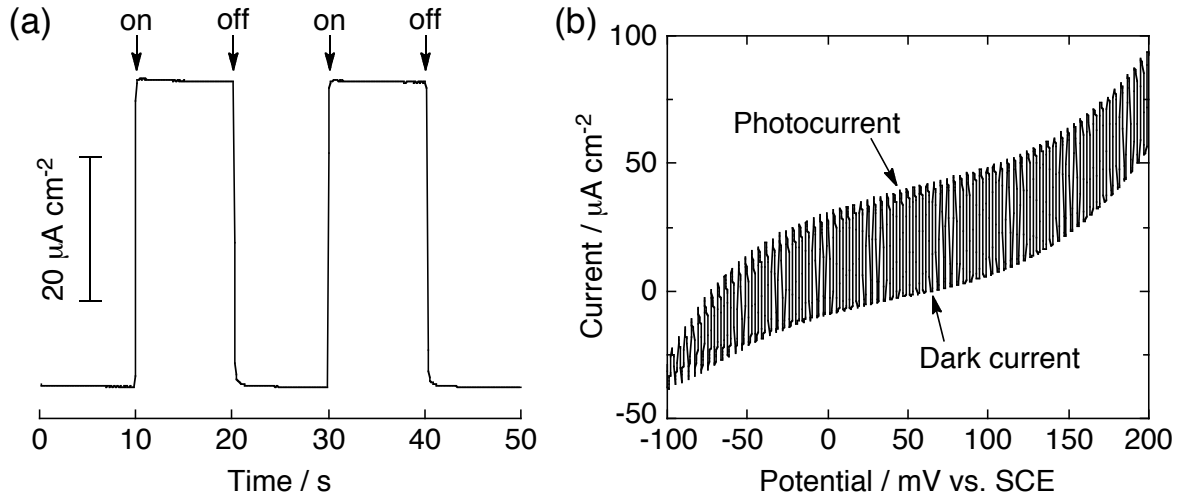

Figure 10. (a) Photocurrent response of the FTO/SnO_2/$(C_{70}$+f-SWNT$)_m$ device under an applied potential of +0.05 V *vs.* SCE. (b) Current *vs.* potential curve for the FTO/SnO_2/$(C_{70}$+f-SWNT$)_m$ device. Illuminated with white light (λ > 380 nm, input power: 37.4 mW cm^{-2}). Electrolyte: 0.5 M LiI and 0.01 M I_2 in acetonitrile.

harvesting light energy and generating electron flow from the electrolyte to the FTO/SnO_2 electrode through the film during the operation of the photoelectrochemical devices. Figure 10b shows current *vs.* potential curve of the FTO/SnO_2/$(C_{70}$+f-SWNT$)_m$ device under the white light illumination (λ > 380 nm). With increasing positive bias up to 0.05 V *vs*. SCE, the photocurrent is increased compared to the dark current. Increased CS and the facile transport of charge carriers under positive bias are responsible for the enhanced photocurrent generation. Analogous photoelectrochemical properties were also observed for the FTO/SnO_2/$(C_{60}$+ f-SWNT$)_m$[20] as well as the FTO/SnO_2/$(C_{84}$+f-SWNT$)_m$ device.

To gain further insights into the photoelectrochemical properties of the deposited films, the author evaluated the wavelength dependent incident photon-to-current efficiency (IPCE) spectra. The IPCE values are calculated by normalizing the photocurrent densities for incident light energy and intensity and by use of the expression:

$$\text{IPCE (\%)} = 100 \times 1240 \times i/(W_{\text{in}} \times \lambda)$$

where i is the photocurrent density (A cm^{-2}), W_{in} is the incident light intensity (W cm^{-2}), and λ is the excitation wavelength (nm).

Figure 11A depicts the photocurrent action spectra of the FTO/SnO_2/$(C_{70})_m$, FTO/SnO_2/ (f-SWNT$)_m$, and FTO/SnO_2/$(C_{70}$+f-SWNT$)_m$ devices. The photocurrent action spectra largely resemble the absorption spectra of the deposited electrodes (Figure 7A). The author can compare the IPCE values at 400 nm where the value is maximal and most of the incident light is virtually absorbed by the films (Table 1). The maximum IPCE value (26%) of the FTO/ SnO_2/$(C_{70}$+f-SWNT$)_m$ device (Figure 11A(c)) is 2.6 times larger than that (10%) of the FTO/ SnO_2/$(C_{70})_m$ device (Figure 11A(a)) and 10 times larger than that (2.6%) of the FTO/SnO_2/ (f-SWNT$)_m$ device (Figure 11A(b)). Note that the maximum IPCE value (26%) is improved remarkably compared with the corresponding value (18%)[20] of the FTO/SnO_2/$(C_{60}$+ f-SWNT$)_m$ device. In addition, the maximum IPCE value of the FTO/SnO_2/$(C_{70}$+f-SWNT$)_m$ device is much larger than the sum (12.6%) of the values of the FTO/SnO_2/$(C_{70})_m$ and FTO/ SnO_2/(f-SWNT$)_m$ devices (Figure 11A(d)), demonstrating that the formation of the composite cluster is responsible for the enhancement of the photocurrent generation. The IPCE value of the FTO/SnO_2/$(C_{70}$+f-SWNT$)_m$ device reaches almost zero at > 700 nm, where the f-SWNT still absorbs light, indicating that the absorption by C_{70} molecules mainly contributes to the photocurrent generation. The maximum IPCE value (26%) of the FTO/SnO_2/$(C_{70}$+f-SWNT$)_m$ device is the highest one ever reported for analogous SWNT-based photoelectrochemical devices in which the SWNTs are deposited electrophoretically,[5,6] electrostatically,[7] covalently,[8] or physisorptionally[9] onto semiconducting electrodes. The low maximum IPCE

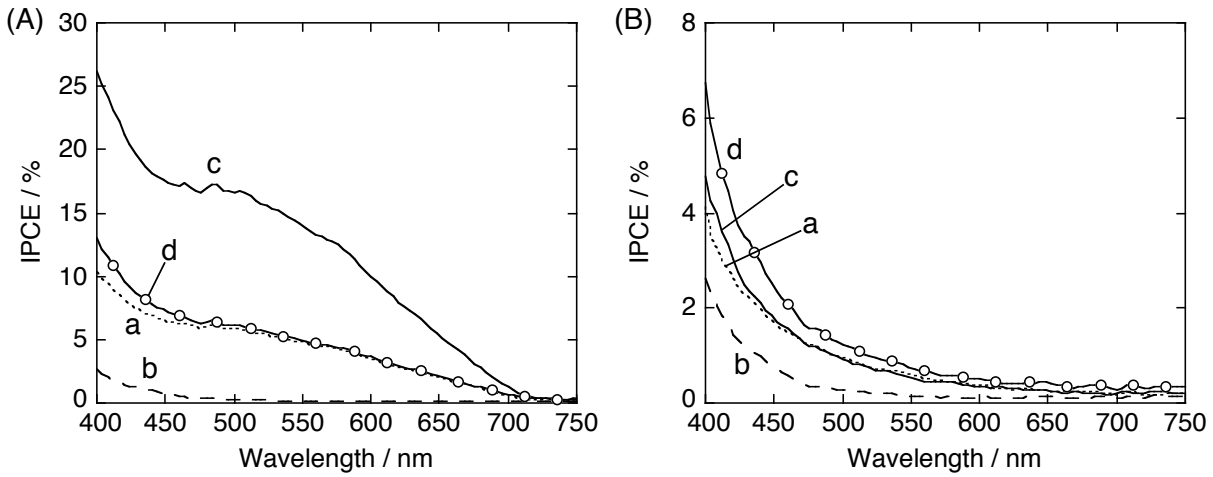

Figure 11. (A) Photocurrent action spectra of (a) FTO/SnO_2/$(C_{70})_m$, (b) FTO/SnO_2/(f-SWNT)$_m$, and (c) FTO/SnO_2/(C_{70}+f-SWNT)$_m$ devices. (d) Sum of the spectra (a) and (b). (B) Photocurrent action spectra of (a) FTO/SnO_2/$(C_{84})_m$, (b) FTO/SnO_2/(f-SWNT)$_m$, and (c) FTO/SnO_2/(C_{84}+ f-SWNT)$_m$ devices. (d) Sum of the spectra (a) and (b). Applied potential: +0.05 V *vs.* SCE. Electrolyte: 0.5 M LiI and 0.01 M I_2 in acetonitrile.

value (2.6%) of the FTO/SnO_2/(f-SWNT)$_m$ device may stem from the relatively low light-harvesting efficiency (67% at 400 nm) and intense self-quenching of the photogenerated excitons in (f-SWNT)$_m$.[6]

Figure 11B illustrates the photocurrent action spectra of the FTO/SnO_2/$(C_{84})_m$, FTO/SnO_2/ (f-SWNT)$_m$, and FTO/SnO_2/(C_{84}+f-SWNT)$_m$ devices. The photocurrent action spectra largely parallel the absorption spectra of the electrodes (Figure 7B). Unlike the trend on the IPCE values of the FTO/SnO_2/$(C_{70})_m$, FTO/SnO_2/(f-SWNT)$_m$, and FTO/SnO_2/(C_{70}+f-SWNT)$_m$ devices, the maximum IPCE value (4.8%) of the FTO/SnO_2/(f-SWNT+C_{84})$_m$ device (Figure 11B(c)) is comparable to that (4.1%) of the FTO/SnO_2/$(C_{84})_m$ device (Figure 11B(a)) and rather lower than the sum (6.7%) of the maximum IPCE values of the FTO/SnO_2/$(C_{84})_m$ and FTO/ SnO_2/(f-SWNT)$_m$ devices (Figure 11B(d)). This implies that the complexation between C_{84} and f-SWNT makes no contribution to the photocurrent generation.

Photocurrent Generation Mechanism: On the basis of the film structures, carrier mobilities, and the photoelectrochemical properties discussed above, as well as the previous studies on similar photoelectrochemical systems consisting of SWNTs[5,6] and the previous study on the C_{60}–f-SWNT composite,[20] a photocurrent generation mechanism for the FTO/ SnO_2/(C_{70}+f-SWNT)$_m$ device is schematically illustrated in Scheme 2. As a representative example, (8,6) SWNT, which is regarded as single (*n*,*m*) chirality species with the highest distribution in f-SWNT prepared from commercially available HiPco,[40] is used in the scheme.

Although direct electron injection from the excited states of f-SWNT to the CB of the SnO_2 electrode is possible,[6] its contribution in the present system should be minor considering the poor photocurrent generation of the FTO/SnO_2/(f-SWNT)$_m$ device (Figure 11).

SCHEME 2

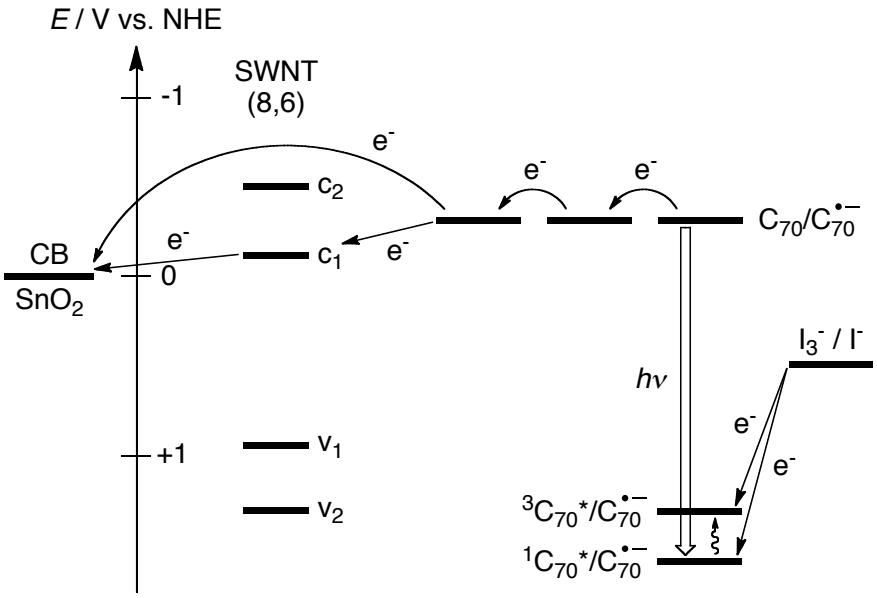

Photocurrent generation is initiated by photoinduced ET from iodide ion (I_3^-/I^- = 0.5 V *vs.* NHE)[5] in the electrolyte to the excited states of C_{70} ($^1C_{70}^*/C_{70}^{\bullet-}$ ≈ 1.7 V *vs.* NHE; $^3C_{70}^*/C_{70}^{\bullet-}$ ≈ 1.3 V *vs.* NHE),[41,42] as in the case of analogous photoelectrochemical devices with the SnO_2 electrodes electrophoretically modified with fullerene clusters.[43,44] The reduced C_{70} ($C_{70}/C_{70}^{\bullet-}$ ≈ –0.2 V *vs.* NHE)[42] injects electrons into the CB of f-SWNT (c_1 = –0.1 V *vs.* NHE).[6] Occurrence of ET from $C_{70}^{\bullet-}$ to f-SWNT is energetically favorable and supported by the results of the TRMC measurements (*vide supra*). Close contact between the sidewalls of f-SWNT and C_{70} molecules disclosed by the FE-SEM observation (Figure 8c) enables the ET from $C_{70}^{\bullet-}$ to f-SWNT. The excellent electron mobility of f-SWNT bundles, as revealed by the TRMC measurements, facilitates the electron flow toward the SnO_2 electrode (E_{CB} = 0 V *vs.* NHE).[5] The electrons injected into the CB of the SnO_2 electrode are driven to the counter electrode via external circuit to regenerate the redox couple. Additionally, the reduced C_{70} injects electrons into the CB of the SnO_2 through electron hopping of C_{70} molecules aligned on the sidewalls of the sole f-SWNT network. It should be noted here that the maximum IPCE value (18%) of the FTO/SnO_2/(C_{60}+f-SWNT)$_m$ device is lower than that (26%) of the FTO/SnO_2/(C_{70}+f-SWNT)$_m$ device, despite of the similar light-harvesting efficiencies, reduction potentials ($C_{60}/C_{60}^{\bullet-}$ ≈ –0.2 V *vs.* NHE),[42,43] and excited state behaviors of C_{60} and C_{70}.[45] The lower IPCE value may result from the low electron mobility (1.2 $cm^2\ V^{-1}\ s^{-1}$) of the FTO/SnO_2/(C_{60}+f-SWNT)$_m$

electrode in comparison with that (2.4 cm^2 V^{-1} s^{-1}) of the FTO/SnO_2/$(C_{70}$+f-SWNT$)_m$ electrode. The low electron mobility may also originate from the hierarchical layer structure of the three different clusters on the FTO/SnO_2/$(C_{60}$+f-SWNT$)_m$ electrode compared with the single network structure of the composite clusters on the FTO/SnO_2/$(C_{70}$+f-SWNT$)_m$ electrode (*vide supra*).

For the FTO/SnO_2/$(C_{84}$+f-SWNT$)_m$ device, the author can depict similar photocurrent generation mechanism as shown in Scheme 3. Taking into account the reduction potential for the excited state of C_{84} ($^1C_{84}$*/$C_{84}^{\bullet-}$ ≈ 1.2 V *vs.* NHE),[32b,46,47] intermolecular ET from I^- in the electrolyte to the C_{84} excited states is a feasible step, as in the cases of the FTO/SnO_2/$(C_{60}$+f-SWNT$)_m$[20] and the FTO/SnO_2/$(C_{70}$+f-SWNT$)_m$ devices. However, the ET efficiency may be low given the short lifetime (35 ps) of the C_{84} excited singlet state and the poor intersystem crossing yield (< 0.01).[32b] Moreover, the reduction potential of C_{84} ($C_{84}/C_{84}^{\bullet-}$ ≈ 0.0 V *vs.* NHE)[47] is comparable to the CB of the SnO_2 electrode and lower by ~ 0.1 V than the c_1 of f-SWNT. Both direct electron injection from the reduced C_{84} to the CB of the SnO_2 electrode and stepwise electron injection through the f-SWNT are not efficient, thereby leading to the poor IPCE value in the FTO/SnO_2/$(C_{84}$+f-SWNT$)_m$ device. This is in good agreement with the results of the TRMC measurements revealing no apparent shift of electrons from C_{84} to f-SWNT in the FTO/SnO_2/$(C_{84}$+f-SWNT$)_m$ electrode (*vide supra*). Overall, it is difficult to utilize the high electron-transporting property of f-SWNT in the FTO/SnO_2/$(C_{84}$+f-SWNT$)_m$ device, despite of the sole network structure of the composite clusters on the electrode (Figure 8e) similar to the FTO/SnO_2/$(C_{70}$+f-SWNT$)_m$ device.

SCHEME 3

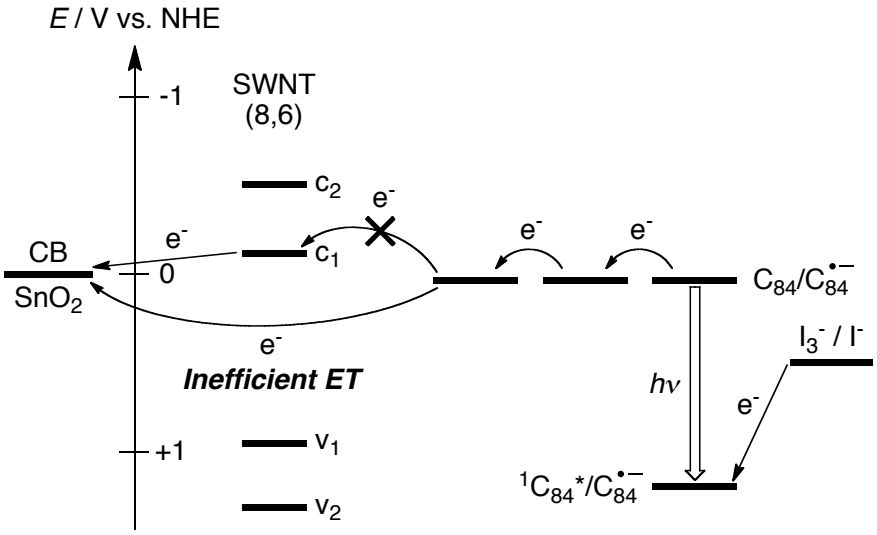

Conclusion

The author has successfully compared the cluster formation, electrophoretically deposited film structure, charge carrier mobility, and photoelectrochemical properties of the composites consisting of SWNTs with C_{60}, C_{70}, or C_{84} for the first time. In particular, the C_{70}–SWNT photoelectrochemical device exhibited the highest IPCE value (26%) ever reported for analogous SWNT-based photoelectrochemical devices including the C_{60}–SWNT device (18%). The highest IPCE value results from selective formation of the single composite film consisting of the SWNT network covered with C_{70} molecules in addition to the high electron mobility (2.4 $cm^2\ V^{-1}\ s^{-1}$) through the C_{70}–SWNT network. This is in marked contrast with the unselective formation of three different clusters in the C_{60}–f-SWNT composites. On the other hand, the C_{84}–f-SWNT photoelectrochemical device revealed the low IPCE value (4.8%) owing to the inefficient electron injection from C_{84} radical anion ($C_{84}/C_{84}^{\bullet-} \approx 0.0$ V *vs.* NHE) to the SnO_2 electrode ($E_{CB} = 0$ V *vs.* NHE) directly or indirectly despite of the exclusive formation of the single composite clusters. Thus, these results will provide basic clue for the design of nano-carbon composite-based molecular devices including organic photovoltaics.

Experimental Section

General Procedure: UV–vis–NIR spectra of solutions and films were measured on a Perkin-Elmer Lambda 900 UV/vis/NIR spectrometer. FE-SEM observation was carried out with a JEOL JSM-6705F. For preparation of the cluster samples, a mixture of ODCB–acetonitrile containing f-SWNT and/or fullerene was spin-coated on Si wafer (polished wafer; SUMCO TECHXIV) at a rotation speed of 1200 rpm. Electrophoretically deposited films that were comprised of fullerene solely were coated with 5 nm thick Pt layer using a JEOL JFC-1600 auto fine coater prior to the measurements, whereas all other samples were used without Pt deposition. DLS measurements of the cluster solutions were performed using a Horiba LB550 particle size analyzer. X-ray diffraction (XRD) analyses were conducted on a Rigaku A2 diffractometer using Cu K_α radiation. Highly soluble f-SWNT was prepared by purification and oxidation of p-SWNT (HiPco SWNTs, Carbon Nanotechnologies, Inc., batch P0313) and subsequent reaction of s-SWNT with thionyl chloride and 8-aminopentadecane as described earlier.[20] C_{60} (99.98%), C_{70} (99.5%), and C_{84} (99%) were obtained from MTR Ltd. and SES Research and used as-received. An optically transparent FTO electrode (Asahi Glass) was washed by sonication in 2-propanol and cleaned in an O_3 atmosphere in advance. A 15% SnO_2 colloidal solution (particle size = 15 nm; Chemat Technology, Inc.) was deposited on the FTO electrode using doctor blade technique.[20,24] The electrode was annealed at 673 K to

yield 0.5 μm thick SnO_2 film (denoted as FTO/SnO_2). All other chemicals were purchased from commercial sources and used without further purification.

Solubility Evaluation of C_{84}: Solubility of C_{84} in ODCB was estimated by using pre-determined molar absorptivity and the absorbance of the saturated solution.[37] Saturated solution was prepared by suspending excess C_{84} (*ca.* 7 mg) in 0.5 mL of ODCB by vigorous bath-sonication for 1 h then removing undissolved sediment by Cosmonice Filter S (Nacalai Tesque, pore size: 0.45 μm) syringe-driven filter unit. For accurate measurement of the absorption spectrum, the saturated solution was diluted 5 times with neat ODCB.

Preparation of Cluster Solutions and Films: The cluster solutions of f-SWNT (0.012 g L^{-1}) and/or higher fullerene (0.14 mM) were prepared in a 1 cm cuvette by injecting 1.6 mL of acetonitrile into a solution of f-SWNT (0.062 g L^{-1}) and/or higher fullerene (0.68 mM) in 0.4 mL of ODCB (ODCB:acetonitrile = 1:4, v/v).[20,24] Then, two electrodes (*i.e.*, FTO and FTO/SnO_2) were inserted into the cuvette with keeping at a distance of 0.6 cm by a Teflon spacer. A dc voltage (200 V) was applied for 120 s between these two electrodes using a power supply (ATTO, model AE-8750). The deposition of the film could be visibly confirmed as the suspension became colorless with simultaneous colorization of the FTO/SnO_2 electrode. After the deposition, the deposited film was dried immediately with a hair dryer. Likewise, the $(C_{60}$+f-SWNT$)_m$ and $(C_{60})_m$ clusters were also prepared for the microwave conductivity measurements.

Photoelectrochemical Measurements: All electrochemical measurements were carried out in a standard three-electrode system using an ALS 630A electrochemical analyzer.[20,24] The deposited film as a working electrode was immersed into an electrolyte solution containing 0.5 M LiI and 0.01 M I_2 in acetonitrile. A Pt wire covered with a glass Luggin capillary, whose tip was located near the working electrode, was used as a quasi-reference electrode. A Pt coil was employed as a counter electrode. The potential measured was converted to the saturated calomel electrode (SCE) scale by adding +0.05 V. A 500 W xenon lamp (USHIO, XB-50101AAA) was used as a light source. Potential *vs*. current characteristics were measured with controlled-potential scan (1 mV s^{-1}) under 0.5 Hz chopped white light ($\lambda > 380$ nm, input power: 37.4 mW cm^{-2}). The monochromatic light through a monochromator (Ritsu, MC-10N) was illuminated on the modified area of the working electrode (0.20 cm^2) from the backside. The light intensity was monitored by an optical power meter (Anritsu, ML9002A) and corrected.

Time-resolved Microwave Conductivity Measurements: The instruments setup as descrived in the previous study[24,38] was used for the TRMC measurements. Namely, nanosecond laser pulses at 355 nm (full width at half maximum (FWHM): 3 – 5 ns) with photon density of $1.6 \times 10^{15} - 3.6 \times 10^{16}$ cm^{-2} were used as an excitation source. A microwave

frequency of 8.6 – 9.4 GHz and a power of 2.1 – 4.6 mW were employed. All the experiments were carried out at room temperature. Other experimental details are described elsewhere.[38]

References and Notes

[1] a) M. S. Dresselhaus, G. Dresselhaus, P. C. Eklund, *Science of Fullerenes and Carbon Nanotubes*, Academic Press, San Diego, 1996; b) S. Reich, C. Thomsen, J. Maultzsch, *Carbon Nanotubes*, Wiley-VCH, Weinheim, 2004; c) *Applied Physics of Carbon Nanotubes*, S. V. Rotkin, S. Subramoney, Eds., Springer, Berlin, 2005.

[2] a) R. H. Baughman, A. A. Zakhidov, W. A. de Heer, *Science* **2002**, *297*, 787; b) H. J. Dai, *Acc. Chem. Res.* **2002**, *35*, 1035; c) M. Ouyang, J. L. Huang, C. M. Lieber, *Acc. Chem. Res.* **2002**, *35*, 1018; d) P. Avouris, Z. H. Chen, V. Perebeinos, *Nature Nanotech.* **2007**, *2*, 605.

[3] a) E. Katz, I. Willner, *ChemPhysChem* **2004**, *5*, 1084; b) D. M. Guldi, G. M. A. Rahman, F. Zerbetto, M. Prato, *Acc. Chem. Res.* **2005**, *38*, 871; c) P. V. Kamat, *J. Phys. Chem. C* **2007**, *111*, 2834; d) P. Avouris, M. Freitag, V. Perebeinos, *Nat. Photonics* **2008**, *2*, 341; e) T. Umeyama, H. Imahori, *Energy Environ. Sci.* **2008**, *1*, 120; f) V. Sgobba, D. M. Guldi, *Chem. Soc. Rev.* **2009**, *38*, 165.

[4] a) H. Ago, K. Petritsch, M. S. P. Shaffer, A. H. Windle, R. H. Friend, *Adv. Mater.* **1999**, *11*, 1281; b) A. Star, J. F. Stoddart, D. Steuerman, M. Diehl, A. Boukai, E. W. Wong, X. Yang, S.-W. Chung, H. Choi, J. R. Heath, *Angew. Chem. Int. Ed.* **2001**, *40*, 1721; c) E. Kymakis, G. A. J. Amaratunga, *Appl. Phys. Lett.* **2002**, *80*, 112; d) E. Kymakis, I. Alexandrou, G. A. J. Amaratunga, *J. Appl. Phys.* **2003**, *93*, 1764.

[5] a) S. Barazzouk, S. Hotchandani, K. Vinodgopal, P. V. Kamat, *J. Phys. Chem. B* **2004**, *108*, 17015; b) T. Hasobe, S. Fukuzumi, P. V. Kamat, *J. Phys. Chem. B* **2006**, *110*, 25477.

[6] T. Umeyama, M. Fujita, N. Tezuka, N. Kadota, Y. Matano, K. Yoshida, S. Isoda, H. Imahori, *J. Phys. Chem. C* **2007**, *111*, 11484.

[7] a) D. M. Guldi, G. M. A. Rahman, M. Prato, N. Jux, S. Qin, W. Ford, *Angew. Chem. Int. Ed.* **2005**, *44*, 2015; b) G. M. A. Rahman, D. M. Guldi, R. Cagnoli, A. Mucci, L. Schenetti, L. Vaccari, M. Prato, *J. Am. Chem. Soc.* **2005**, *127*, 10051; c) G. M. A. Rahman, A. Troeger, V. Sgobba, D. M. Guldi, N. Jux, D. Balbino, M. N. Tchoul, W. T. Ford, A. Mateo-Alonso, M. Prato, *Chem.-Eur. J.* **2008**, *14*, 8837.

[8] L. Sheeney-Haj-Ichia, B. Basnar, I. Willner, *Angew. Chem. Int. Ed.* **2005**, *44*, 78.

[9] a) S. Campidelli, B. Ballesteros, A. Filoramo, D. D. Diaz, G. D. L. Torre, T. Torres, G. M A. Rahman, C. Ehli, D. Kiessling, F. Werner, V. Sgobba, D. M. Guldi, C. Cioffi, M. Prato, J.-P. Bourgoin, *J. Am. Chem. Soc.* **2008**, *130*, 11503; b) T. Arai, S. Nobukuni, A. S. D.

Sandanayaka, O. Ito, *J. Phys. Chem. C* **2009**, *113*, 14493.

[10] a) *Fullerenes*, K. M. Kadish, R. S. Ruoff, Eds., Wiley Interscience, New York, 2000; b) *Fullerenes*, F. Langa, J.-F. Nierengarten, Eds., RSC Publishing, Cambridge, 2007.

[11] a) S. Günes, H. Neugebauer, N. S. Sariciftci, *Chem. Rev.* **2007**, *107*, 1324; b) B. C. Thompson, J. M. J. Fréchet, *Angew. Chem., Int. Ed.* **2008**, *47*, 58.

[12] a) H. Imahori, S. Fukuzumi, *Adv. Funct. Mater.* **2004**, *14*, 525; b) D. M. Guldi, *J. Phys. Chem. B* **2005**, *109*, 11432; c) H. Imahori, *J. Mater. Chem.* **2007**, *17*, 31; d) H. Imahori, T. Umeyama, *J. Phys. Chem. C* **2009**, *113*, 9029.

[13] a) N. Martín, L. Sánchez, B. IIIescas, I. Pérez, *Chem. Rev.* **1998**, *98*, 2527; b) F. Diederich, M. Gómez-López, *Chem. Soc. Rev.* **1999**, *28*, 263; c) D. Gust, T. A. Moore, A. L. Moore, *Acc. Chem. Res.* **2001**, *34*, 40; d) D. M. Guldi, *Chem. Soc. Rev.* **2002**, *31*, 22; e) N. Armaroli, *Photochem. Photobiol. Sci.* **2003**, *2*, 73; f) J.-F. Nierengarten, *New J. Chem.* **2004**, *28*, 1177; g) M. E. El-Khouly, O. Ito, P. M. Smith, F. D'Souza, *J. Photochem. Photobiol. C* **2004**, *5*, 79; h) S. Fukuzumi, T. Kojima, *J. Mater. Chem*. **2008**, *18*, 1427.

[14] a) H. Imahori, Y. Sakata, *Adv. Mater.* **1997**, *9*, 537; b) H. Imahori, Y. Sakata, *Eur. J. Org. Chem.* **1999**, 2445; c) H. Imahori, Y. Mori, Y. Matano, *J. Photochem. Photobiol. C* **2003**, *4*, 51; d) H. Imahori, *Org. Biomol. Chem.* **2004**, *2*, 1425; e) H. Imahori, *Bull. Chem. Soc. Jpn.* **2007**, *80*, 621.

[15] a) T. Hasobe, Y. Kashiwagi, M. A. Absalom, J. Sly, K. Hosomizu, M. J. Crossley, H. Imahori, P. V. Kamat, S. Fukuzumi, *Adv. Mater.* **2004**, *16*, 975; b) T. Hasobe, P. V. Kamat, M. A. Absalom, Y. Kashiwagi, J. Sly, M. J. Crossley, K. Hosomizu, H. Imahori, S. Fukuzumi, *J. Phys. Chem. B* **2004**, *108*, 12865.

[16] a) T. Hasobe, P. V. Kamat, V. Troiani, N. Solladie, T. K. Ahn, S. K. Kim, D. Kim, A. Kongkanand, S. Kuwabata, S. Fukuzumi, *J. Phys. Chem. B* **2005**, *109*, 19; b) T. Umeyama, T. Takamatsu, N. Tezuka, Y. Matano, Y. Araki, T. Wada, O. Yoshikawa, T. Sagawa, S. Yoshikawa, H. Imahori, *J. Phys. Chem. C* **2009**, *113*, 10819.

[17] a) T. Hasobe, H. Imahori, P. V. Kamat, S. Fukuzumi, *J. Am. Chem. Soc.* **2003**, *125*, 14962; b) T. Hasobe, H. Imahori, P. V. Kamat, T. K. Ahn, S. K. Kim, D. Kim, A. Fujimoto, T. Hirakawa, S. Fukuzumi, *J. Am. Chem. Soc.* **2005**, *127*, 1216.

[18] a) S. Kang, T. Umeyama, M. Ueda, Y. Matano, H. Hotta, K. Yoshida, S. Isoda, M. Shiro, H. Imahori, *Adv. Mater.* **2006**, *18*, 2549; b) H. Imahori, M. Ueda, S. Kang, H. Hayashi, S. Hayashi, H. Kaji, S. Seki, A. Saeki, S. Tagawa, T. Umeyama, Y. Matano, K. Yoshida, S. Isoda, M. Shiro, N. V. Tkachenko, H. Lemmetyinen, *Chem.-Eur. J.* **2007**, *13*, 10182.

[19] a) A. Kira, M. Tanaka, T. Umeyama, Y. Matano, N. Yoshimoto, Y. Zhang, S. Ye, H. Lehtivuori, N. V. Tkachenko, H. Lemmetyinen, H. Imahori, *J. Phys. Chem. C* **2007**, *111*, 13618; b) A. Kira, T. Umeyama, Y. Matano, K. Yoshida, S. Isoda, J.-K. Park, D. Kim, H.

Imahori, *J. Am. Chem. Soc.* **2009**, *131*, 3198.

[20] T. Umeyama, N. Tezuka, M. Fujita, S. Hayashi, N. Kadota, Y. Matano, H. Imahori, *Chem.-Eur. J.* **2008**, *14*, 4875.

[21] a) C. Li, Y. Chen, Y. Wang, Z. Iqbal, M. Chhowalla, S. Mitra, *J. Mater. Chem.* **2007**, *17*, 2406; b) C. Li, S. Mitra, *Appl. Phys. Lett.* **2007**, *91*, 253112.

[22] a) A. Hirsch, *Angew. Chem. Int. Ed.* **2002**, *41*, 1853; b) Y.-P. Sun, K. Fu, Y. Lin, W. Huang, *Acc. Chem. Res.* **2002**, *35*, 1096; c) C. A. Dyke, J. M. Tour, *J. Phys. Chem. A* **2004**, *108*, 11151; d) D. Tasis, N. Tagmatarchis, A. Bianco, M. Prato, *Chem. Rev.* **2006**, *106*, 1105.

[23] a) J. Liu, A. G. Rinzler, H. Dai, J. H. Hafner, R. K. Bradley, P. J. Boul, A. Lu, T. Iverson, K. Shelimov, C. B. Huffman, F. Rodriguez-Macias, Y.-S. Shon, T. R. Lee, D. T. Colbert, R. E. Smalley, *Science* **1998**, *280*, 1253; b) J. Chen, M. A. Hamon, H. Hu, Y. Chen, M. A. Rao, P. C. Eklund, R. C. Haddon, *Science* **1998**, *282*, 95.

[24] T. Umeyama, N. Tezuka, S. Seki, Y. Matano, M. Nishi, K. Hirao, H. Lehtivuori, N. V. Tkachenko, H. Lemmetyinen, Y. Nakao, S. Sakaki, H. Imahori, *Adv. Mater.* **2010**, *22*, 1767.

[25] There are a number of examples of fullerene-encapsulated SWNTs (bucky-peapods). a) B. W. Smith, M. Monthioux, D. E. Luzzi, *Nature* **1998**, *396*, 323; b) K. Hirahara, K. Suenaga, S. Bandow, H. Kato, T. Okazaki, H. Shinohara, S. Iijima, *Phys. Rev. Lett.* **2000**, *85*, 5384; c) H. Kataura, Y. Maniwa, M. Abe, A. Fujiwara, T. Kodama, K. Kikuchi, H. Imahori, Y. Misaki, S. Suzuki, Y. Achiba, *Appl. Phys. A* **2002**, *74*, 349; d) F. Simon, H. Kuzmany, B. Nafradi, T. Feher, L. Forro, F. Fulop, A. Janossy, L. Korecz, A. Rockenbauer, F. Hauke, A. Hirsch, *Phys. Rev. Lett.* **2006**, *97*, 136801.

[26] a) Y. Takaguchi, M. Tamura, Y. Sako, Y. Yanagimoto, S. Tsuboi, T. Uchida, K. Shimamura, S. Kimura, T. Wakahara, Y. Maeda, T. Akasaka, *Chem. Lett.* **2005**, *34*, 1608; b) D. M. Guldi, E. Menna, M. Maggini, M. Marcaccio, D. Paolucci, F. Paolucci, S. Campidelli, M. Prato, G. M. A. Rahman, S. Schergna, *Chem.-Eur. J.* **2006**, *12*, 3975; c) J. L. Delgado, P. Cruz, A. Urbina, J. T. L. Navarrete, J. Casado, F. Langa, *Carbon* **2007**, *45*, 2250; d) F. D'Souza, R. Chitta, A. S. D. Sandanayaka, N. K. Subbaiyan, L. D'Souza, Y. Araki, O. Ito, *J. Am. Chem. Soc.* **2007**, *129*, 15865.

[27] a) S. Chaudhary, H. Lu, A. M. Müller, C. J. Bardeen, M. Ozkan, *Nano Lett.* **2007**, *7*, 1973; b) S. Berson, R. de Bettignies, S. Bailly, S. Guillerez, B. Jousselme, *Adv. Funct. Mater.* **2007**, *17*, 3363; c) L. Liu, W. E. Stanchina, G. Li, *Appl. Phys. Lett.* **2009**, *94*, 233309.

[28] H. Ajie, M. M. Alvarez, S. J. Anz, R. D. Beck, F. Diederich, K. Fostiropoulos, D. R. Huffman, W. Krätschmer, Y. Rubin, K. E. Schriver, D. Sensharma, R. L. Whetten, *J. Phys. Chem.* **1990**, *94*, 8630.

[29] a) Y.-P. Sun, C. E. Bunker, *Nature* **1993**, *365*, 398; b) Y.-M. Wang, P. V. Kamat, L. K. Patterson, *J. Phys. Chem.* **1993**, *97*, 8793; c) Y.-P. Sun, C. E. Bunker, *Chem. Mater.* **1994**, *6*, 578; d) H. N. Ghosh, A. V. Sapre, J. P. Mittal, *J. Phys. Chem.* **1996**, *100*, 9439; e) R. G. Alargova, S. Deguchi, K. Tsujii, *J. Am. Chem. Soc.* **2001**, *123*, 10460; f) S. Nath, H. Pal, A. V. Sapre, *Chem. Phys. Lett.* **2002**, *360*, 422; g) K. Datta, A. K. Mukherjee, *J. Chem. Phys.* **2006**, *124*, 144509.

[30] a) M. J. O'Connell, S. M. Bachilo, C. B. Huffman, V. C. Moore, M. S. Strano, E. H. Haroz, K. L. Rialon, P. J. Boul, W. H. Noon, C. Kittrell, J. Ma, R. H. Hauge, R. B. Weisman, R. E. Smalley, *Science* **2002**, *297*, 593; b) S. M. Bachilo. M. S. Strano, C. Kittrell, R. H. Hauge, R. E. Smalley, R. B. Weisman, *Science* **2002**, *298*, 2361.

[31] a) F. Diederich, R. Ettl, Y. Rubin, R. L. Whetten, R. Beck, M. Alvarez, S. Anz, D. Sensharma, F. Wudl, K. C. Khemani, A. Koch, *Science* **1991**, *252*, 548; b) K. Kikuchi, N. Nakahara, M. Honda, S. Suzuki, K. Saito, H. Shiromaru, K. Yamauchi, I. Ikemoto, T. Kuramochi, S. Hino, Y. Achiba, *Chem. Lett.* **1991**, 1607.

[32] a) G. Sauvé, P. V. Kamat, R. S. Ruoff, *J. Phys. Chem.* **1995**, *99*, 2162; b) H. S. Cho, T. K. Ahn, S. I. Yang, S. M. Jin, D. Kim, S. K. Kim, H. D. Kim, *Chem. Phys. Lett.* **2003**, *375*, 292.

[33] D. E. Manolopoulos, P. W. Fowler, *J. Chem. Phys.* **1992**, *96*, 7603.

[34] a) K. Kikuchi, N. Nakahara, T. Wakabayashi, S. Suzuki, H. Shiromaru, Y. Miyake, K. Saito, I. Ikemoto, M. Kainosho, Y. Achiba, *Nature* **1992**, *357*, 142; b) D. E. Manolopoulos, P. W. Fowler, R. Taylor, H. W. Kroto, D. R. M. Walton, *J. Chem. Soc., Faraday Trans.* **1992**, *88*, 3117; c) T. J. S. Dennis, T. Kai, T. Tomiyama, H. Shinohara, *J. Chem. Soc., Chem. Commun.* **1998**, 619; d) T. J. S. Dennis, T. Kai, K. Asato, T. Tomiyama, H. Shinohara, T. Yoshida, Y. Kobayashi, H. Ishiwatari, Y. Miyake, K. Kikuchi, Y. Achiba, *J. Phys. Chem. A* **1999**, *103*, 8747.

[35] Kim *et al.* reported the formation of C_{84} aggregated clusters in a concentrated toluene solution.[32b]

[36] The X-ray diffraction analyses on the deposited cluster films indicated that inner structures of the clusters are rather amorphous or any existing crystallites in the clusters are too small to be detected.

[37] N. Sivaraman, R. Dhamodaran, I. Kaliappan, T. G. Srinivasan, P. R. V. Rao, C. K. Mathews, *Fullerene Sci. Technol.* **1994**, *2*, 233.

[38] a) F. C. Grozema, L. D. A. Siebbeles, J. M. Warman, S. Seki, S. Tagawa, U. Scherf, *Adv. Mater.* **2002**, *14*, 228; b) A. Saeki, S. Seki, Y. Koizumi, T. Sunagawa, K. Ushida, S. Tagawa, *J. Phys. Chem. B* **2005**, *109*, 10015; c) T. Amaya, S. Seki, T. Moriuchi, K. Nakamoto, T. Nakata, H. Sakane, A. Saeki, S. Tagawa, T. Hirao, *J. Am. Chem. Soc.* **2009**,

131, 408.

[39] a) R. C. Haddon, A. S. Perel, R. C. Morris, T. T. M. Palstra, A. F. Hebard, R. M. Fleming, *Appl. Phys. Lett.* **1995**, *67*, 121; b) R. C. Haddon, *J. Am. Chem. Soc.* **1996**, *118*, 3041; c) K. Shibata, Y. Kubozono, T. Kanbara, T. Hosokawa, A. Fujiwara, Y. Ito, H. Shinohara, *Appl. Phys. Lett.* **2004**, *84*, 2572.

[40] HiPco SWNTs is a mixture of semiconducting (~ 70%) and metallic (~ 30%) carbon nanotubes.[30] The metallic SWNTs may quench the excited states of f-SWNT as well as the fullerenes via energy transfer, lowering the photocurrent generation efficiency. The semiconducting SWNTs exhibit different CB and valence band (VB) that can be estimated by Murakoshi's equation. Most of the semiconducting SWNTs including SWNT (8,6) satisfy the requirement for exothermic ET from fullerene (C_{60} and C_{70}) radical anion to the CB of the semiconducting SWNTs, thereby contributing to the photocurrent generation. K.-i. Okazaki, Y. Nakato, K. Murakoshi, *Phys. Rev. B* **2003**, *68*, 035434.

[41] a) J. W. Arbogast, C. S. Foote, *J. Am. Chem. Soc.* **1991**, *113*, 8886; b) M. R. Wasielewski, M. P. O'Neil, K. R. Lykke, M. J. Pellin, D. M. Gruen, *J. Am. Chem. Soc.* **1991**, *113*, 2774.

[42] P.-M. Allemand, A. Koch, F. Wudl, Y. Rubin, F. Diederich, M. M. Alvarez, S. J. Anz, R. L. Whetten, *J. Am. Chem. Soc.* **1991**, *113*, 1050.

[43] P. V. Kamat, S. Barazzouk, K. G. Thomas, S. Hotchandani, *J. Phys. Chem. B* **2000**, *104*, 4014.

[44] According to the results of the time-resolved transient absorption measurements of FTO/SnO_2/(C_{60}+f-SWNT)$_m$ and FTO/SnO_2/(C_{70}+f-SWNT)$_m$ electrodes, photocurrent generation involving direct CS between fullerenes and f-SWNT is unlikely to occur.[20,24]

[45] M. Lee, O.-K. Song, J.-C. Seo, D. Kim, Y. D. Suh, S. M. Jin, S. K. Kim, *Chem. Phys. Lett.* **1992**, *196*, 325.

[46] Since C_{84} has an extremely low quantum yield of intersystem crossing (< 0.01),[32b] the author only considered the singlet excited state for the photocurrent generation.

[47] a) M. S. Meier, T. F. Guarr, J. P. Selegue, V. K. Vance, *J. Chem. Soc., Chem. Commun.* **1993**, 63; b) P. Boulas, M. T. Jones, K. M. Kadish, R. S. Ruoff, D. C. Lorents, D. S. Tse, *J. Am. Chem. Soc.* **1994**, *116*, 9393.

Chapter 8

Carbon Nanotube Wiring of Donor–Acceptor Nanograins by Self-Assembly and Efficient Charge Transport

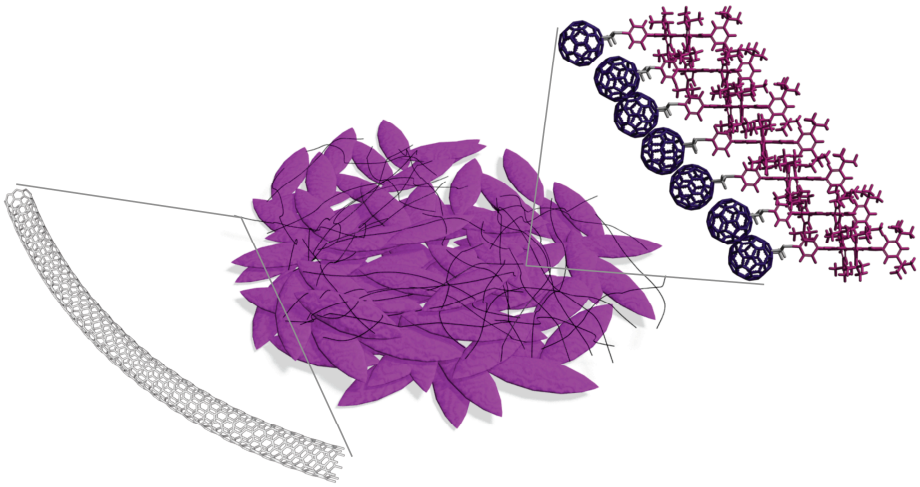

Abstract: Organic electronic materials have drawn much attention due to their potential applications in organic photovoltaics and transistors. So far, efficient charge transport within as well as between grains of organic thin films has been limited by rather poor interactions at nanostructures and nanograin boundaries. Here, the author has successfully developed an unprecedented self-assembly method to build up well-ordered donor–acceptor nanograins and their efficient molecular wiring that can be detected as photocurrent. The semiflexible methylene linkage of porphyrin (donor)–C_{60} (acceptor) successfully allowed the author to form impressive ellipsoid-shaped nanograins in a good–poor solvent mixture. The porphyrin–C_{60} linked molecules in the nanograins were found to yield highly ordered donor–acceptor arrays, making it possible to achieve efficient intra charge transport within the nanograins. More importantly, functionalized single-walled carbon nanotube wiring between the nanograins also rendered the inter charge transport extremely efficient, leading to the highest incident photon-to-current efficiency (22%) ever reported for analogous photoelectrochemical devices utilizing donor–acceptor linked dyads. Such ternary self-assembly of donor–acceptor linked molecules with molecular wires will be a highly promising method to achieve excellent device performances in organic photovoltaics and transistors.

Introduction

Organic π-conjugated compounds have drawn much attention due to their potential applications in organic thin-film optoelectronics.[1] Over the last 20 years, tremendous progress has been achieved in the design and fabrication of the compounds. In this regard, charge-transporting properties of organic thin films have found to be crucial in the device performances. Especially, it is well known that charge transport is limited by grain boundaries in the films as well as molecular arrangements within the grains. Therefore, a new method enhancing electrical communication between the grains as well as modulating the arrangements within the grains is necessary to improve device performances.

Here the author has explored a novel self-assembly strategy to build up well-ordered donor–acceptor (D–A) nanograins and their efficient molecular wiring that can be detected as photocurrent (Scheme 1). A covalent linkage between porphyrin as a donor and C_{60} as an acceptor was chosen because this combination is known to yield a long-lived charge-separated state efficiently.[2] The author expected that π-π interactions between porphyrin as well as C_{60} molecules rather than between porphyrin and C_{60} molecules would prevail to form nanograins, where D and A molecules are arranged separately for efficient photocurrent generation.[2a,3] Utilization of a semiflexible, short methylene spacer between the porphyrin and C_{60} moieties would be suitable to strengthen the desirable interactions. Rapid injection of a poor solvent into a good solvent containing the D–A linked dyads was used to accelerate the formation of D–A nanograins in the mixed solvent.[2b] More importantly, an addition of single-walled carbon nanotubes (SWNTs) as a molecular wire was anticipated to cross-link the D–A nanograins in the mixed solvent, enhancing the electric communication between the grains. Electrophoretic deposition[2b] of the ternary component aggregates onto a nanostructured SnO_2 electrode allowed the author to fabricate a desirable D–A–SWNT composite film on the electrode (Scheme 1). To the best of the author's knowledge, the

SCHEME 1

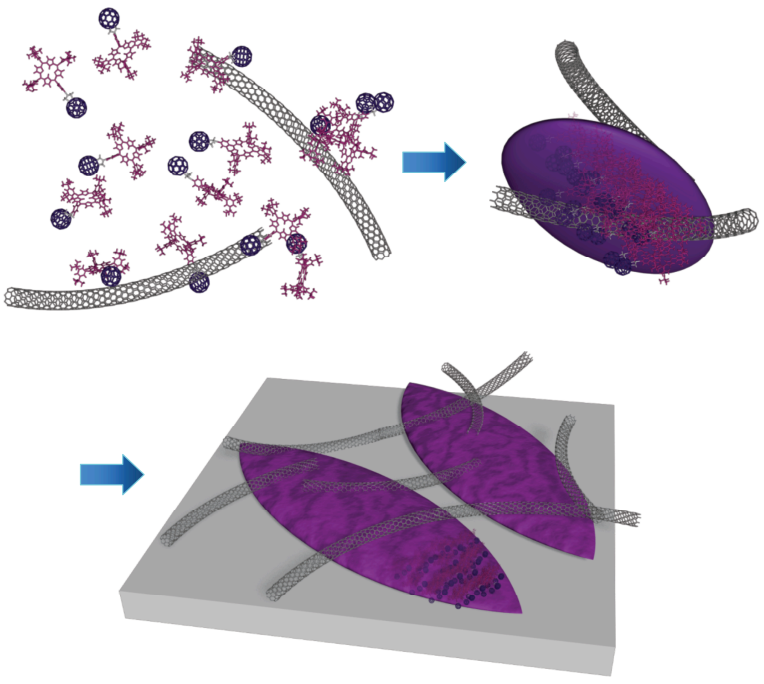

"wiring effect" of SWNTs between photoactive nanograins has never been investigated so far. In addition, this is the first example of the ternary component system consisting of porphyrin, fullerene, and SWNTs, although the binary systems have been frequently utilized for photo- and electronic devices.[4–6]

Results and Discussion

Basic Characterization of Novel Porphrin–C_{60} Dyad: Novel porphyrin–C_{60} linked dyad (H_2P-C_{60}), porphyrin and C_{60} reference compounds (H_2P-ref and C_{60}-ref),[7,8] and highly soluble SWNTs (f-SWNT)[5a] were synthesized according to reported procedures (Figure 1, see experimental section). Basic photophysical and electrochemical properties of the compounds are provided in Table 1. Steady-state fluorescence measurements in *o*-dichlorobenzene (ODCB) indicate efficient photoinduced electron transfer (ET) from the porphyrin excited singlet state to the C_{60} in H_2P-C_{60}. Namely, emission from the porphyrin moiety was strongly quenched compared to that from H_2P-ref (Figure 2A). The occurrence of the photoinduced ET was further confirmed by the femtosecond time-resolved transient absorption measurements with a laser excitation of H_2P-C_{60} at 420 nm, where three components (0.8 ps, 48 ps, and 1.3 ns) are reasonably derived from the global analysis of the transient spectra (Figure 2B). The long-lived component (1.3 ns) can be assigned as a charge-separated state exhibiting characteristic absorption of the freebase porphyrin radical cation (600 – 700 nm) and monofunctionalized C_{60} radical anion (1000 nm).[9] The short-lived (0.8 ps) and moderate-lived (48 ps) components can be attributed to the porphyrin singlet excited state and an intramolecular exciplex that relaxes to the charge-separated state, respectively.[10]

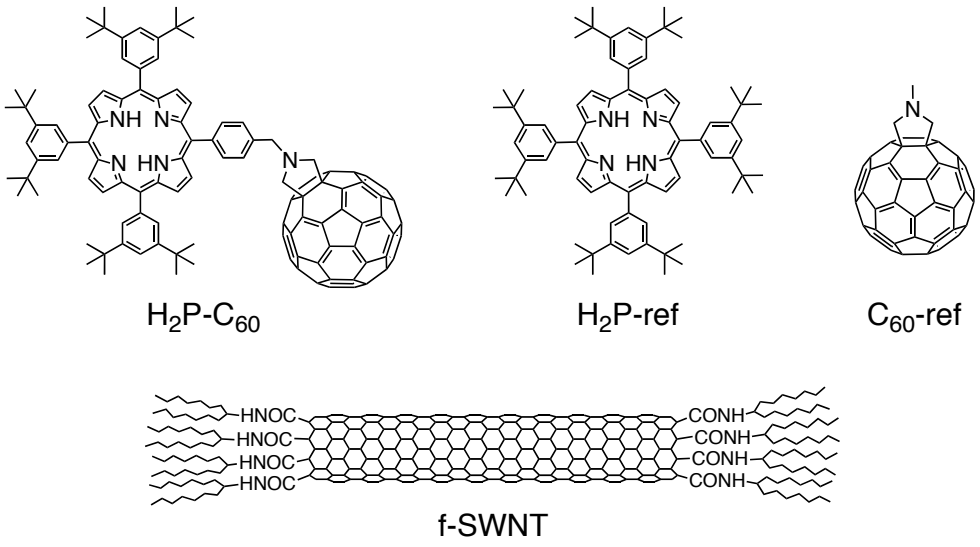

Figure 1. Structures of H_2P-C_{60}, H_2P-ref, C_{60}-ref, and f-SWNT.

TABLE 1: One-Electron Oxidation Potentials ($E°_{ox}$), Reduction Potentials ($E°_{red}$), Energy Level of Lowest Singlet Excited State ($\Delta E_{0\text{-}0}$) of Porphyrin Moiety, Free Energy Changes of Photoinduced Charge Separation ($\Delta G°_{CS}$) and Charge Recombination ($\Delta G°_{CR}$), and Rate Constants for Charge Separation (k_{CS}) and Charge Recombination (k_{CR}) in Deaerated Benzonitrile at 298 K

compound	$E°_{ox}$ [a] / V *vs.* NHE	$E°_{red}$ [a] / V *vs.* NHE	$\Delta E_{0\text{-}0}$ / eV	$\Delta G°_{CS}$ [b] / eV	$\Delta G°_{CR}$ [b] / eV	k_{CS} / s^{-1}	k_{CR} / s^{-1}
H_2P-C_{60}	1.18	–0.40	1.90	–0.32	–1.58	2.1×10^{10} [c]	7.7×10^{8}
H_2P-ref	1.20	—	1.90	—	—	—	—
C_{60}-ref	—	–0.40	—	—	—	—	—

[a] Determined from cyclic voltammetry. [b] $\Delta G°_{CR} = e(E°_{red} - E°_{ox}) - \Delta G°_{S}$, $\Delta G°_{CS} = -\Delta G°_{CR} - \Delta E_{0\text{-}0}$, $\Delta G°_{S} = -e^2/(4\pi\varepsilon_0\varepsilon_s R_{cc})$, where e is the elementary charge of electron, ε_0 is the vacuum permittivity, ε_s is the static dielectric constant of benzonitrile (25.2), and R_{cc} is the center-to-center distance between the porphyrin unit and the fullerene unit (for H_2P-C_{60}, 15.1 Å). [c] Formation rate from exciplex.

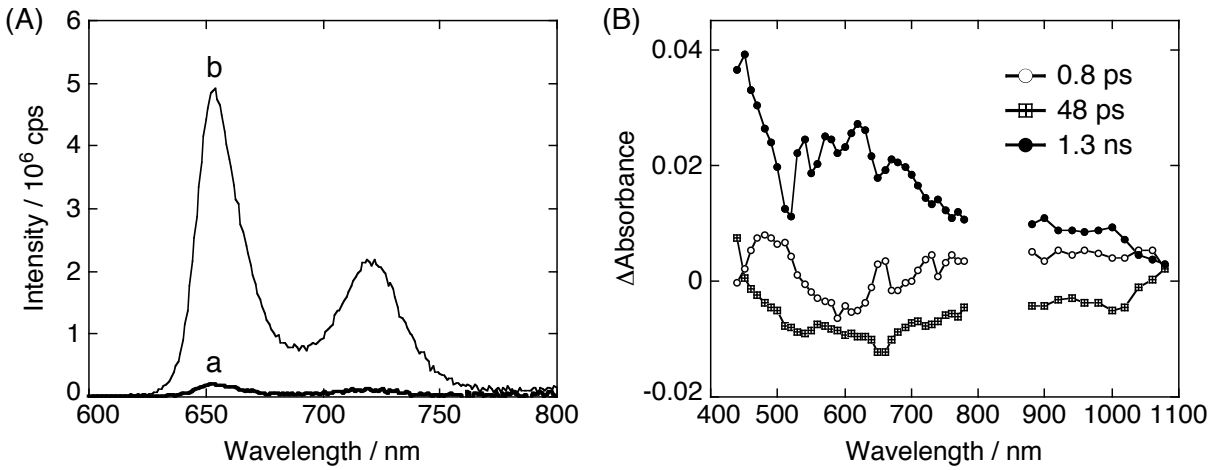

Figure 2. (A) Steady-state fluorescence spectra of (a) H_2P-C_{60} and (b) H_2P-ref in ODCB. The absorbance at the Soret band was adjusted to be 0.1 for the excitation. (B) Transient absorption decay component spectra of H_2P-C_{60} in benzonitrile obtained with global three-component fit of the time-resolved spectra. Excitation wavelength is 420 nm. Fitted time constants are shown in the figure.

Self-Assembling Behavior: At first, self-assembling behavior of H_2P-C_{60} in an ODCB–acetonitrile mixture was investigated for the better understanding of the more complex H_2P-C_{60}–SWNT composite. Absorption spectrum of H_2P-C_{60} in ODCB exhibits characteristic Soret band and Q bands (Figure 3A(a)). In the ODCB–acetonitrile mixture, the Soret and Q

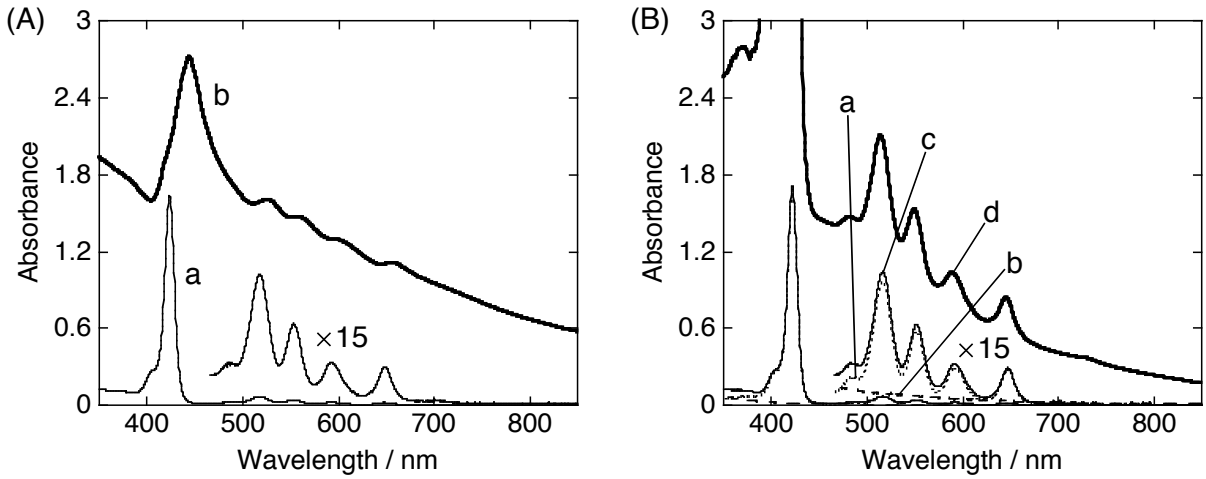

Figure 3. (A) UV–vis–NIR absorption spectra of H_2P-C_{60} in (a) ODCB ([H_2P-C_{60}] = 0.011 mM; path length 3 mm) and (b) ODCB–acetonitrile mixture (2:5, v/v; [H_2P-C_{60}] = 0.16 mM; path length 3 mm). (B) UV–vis–NIR absorption spectra of (a) H_2P-ref, (b) C_{60}-ref, and (c) the mixture of H_2P-ref and C_{60}-ref in ODCB ([H_2P-ref] = [C_{60}-ref] = 0.011 mM; path length 3 mm) and (d) the mixture of H_2P-ref and C_{60}-ref in ODCB–acetonitrile (2:5, v/v; [H_2P-ref] = [C_{60}-ref] = 0.16 mM; path length 3 mm).

bands are broadened and red-shifted relative to those in ODCB (Figure 3A(b)). All of these changes are ascribed to the formation of nanograins of H_2P-C_{60} (denoted as $(H_2P\text{-}C_{60})_m$),[2b] as described later. In contrast, H_2P-ref–C_{60}-ref composite (denoted as $(H_2P\text{-ref}+C_{60}\text{-ref})_m$) does not show the broadening and shift of the Soret and Q bands (Figure 3B). This indicates that H_2P-ref molecules are not co-aggregating with C_{60}-ref efficiently to yield $(H_2P\text{-ref}+C_{60}\text{-ref})_m$ during the self-assembly process.

In accord with the absorption behavior, the field emission scanning electron microscopy (FE-SEM) measurement of $(H_2P\text{-}C_{60})_m$ disclosed unique ellipsoid-shaped nanograins as large as 1.5 – 2.7 μm in long axis and ~ 500 nm in short axis (Figure 4a). In contrast, the FE-SEM image of $(H_2P\text{-ref}+C_{60}\text{-ref})_m$ depicts irregular cubic structures with a small size of 50 – 100 nm (Figure 4b). The well-defined ellipsoid-shaped structure of $(H_2P\text{-}C_{60})_m$ supports that H_2P-C_{60} molecules are well-organized in the nanograins. Consistently, the X-ray diffraction (XRD) measurement of $(H_2P\text{-}C_{60})_m$ revealed a weak diffraction peak at 11.6 °, corresponding to an inter-plane distance of 7.3 Å (Figure 5A). According to the crystallographic study on the single crystal of H_2P-ref,[11] this value is reasonably assigned as the inter-plane distance between the porphyrins in which one of eight *tert*-butyl groups of one porphyrin is fit into a one-sided hollow center of another porphyrin surrounded by the four *tert*-butyl groups. This results in a slipped stacked *J*-aggregate of the porphyrin moieties, consistent with the red shift of the Soret band. Similar *J*-like arrangement of porphyrin moieties has been implied in the rod-like aggregates of ionic porphyrin–C_{60} dyads.[12] A plausible molecular structure of

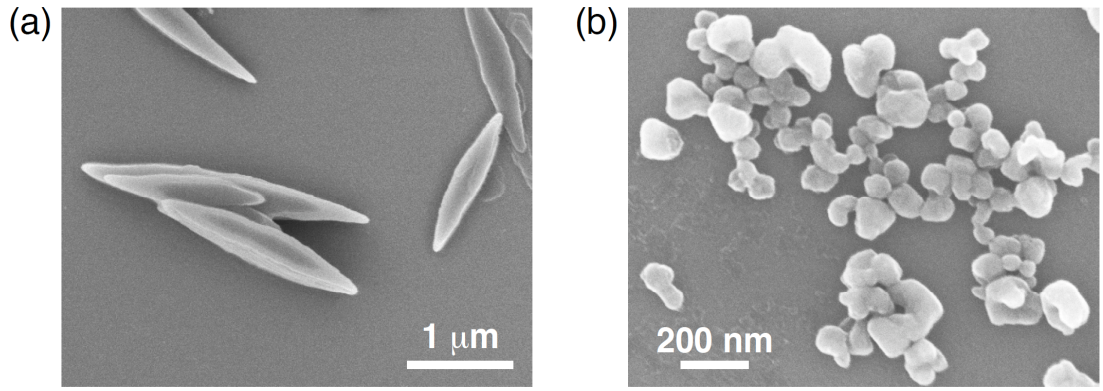

Figure 4. FE-SEM images of (a) $(H_2P\text{-}C_{60})_m$ and (b) $(H_2P\text{-ref}+C_{60}\text{-ref})_m$. The samples were prepared by spin-coating the corresponding grain solutions ([porphyrin] = [C_{60}] = 0.16 mM) from the ODCB–acetonitrile mixture (2:5, v/v) on Si wafer.

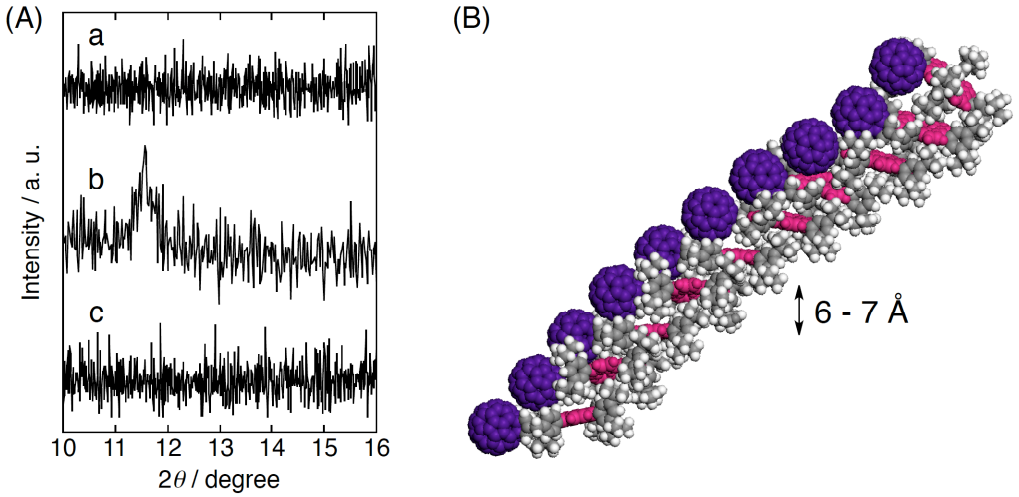

Figure 5. (A) XRD patterns of (a) FTO/SnO_2 substrate and (b) $(H_2P\text{-}C_{60})_m$ and (c) $(H_2P\text{-ref}+C_{60}\text{-ref})_m$ nanograins deposited on FTO/SnO_2 substrate. All curves are normalized and offset for comparison. (B) Molecular modeling of $H_2P\text{-}C_{60}$ arrangement in the nanograins. For clarification, the porphyrin core and C_{60} sphere are colored in pink and purple, respectively.

$(H_2P\text{-}C_{60})_{10}$ optimized by the MM3 force field reveals the formation of slipped stacked porphyrin arrays with inter-plane distance of 6 – 7 Å, where the C_{60} moieties are arranged continuously along the one-dimensional (1-D) porphyrin array (Figure 5B). The steady-state fluorescence of $(H_2P\text{-}C_{60})_m$ shows strong quenching of the porphyrin fluorescence without exhibiting charge transfer emission from the direct contact with the porphyrin and C_{60}.[2] All of these data suggest that the porphyrin moieties are stacked linearly and the C_{60} moieties are closely located around the porphyrin alignment in the ellipsoid-shaped nanoaggregates

Electrophoretic Deposition: Upon subjecting the grain solution to a high electric (dc) field (200V, 120 s), $(H_2P\text{-}C_{60})_m$ and $(H_2P\text{-ref}+C_{60}\text{-ref})_m$ were deposited onto the fluorine-doped

tin oxide (FTO) electrodes with nanostructured SnO_2 modification (denoted as FTO/SnO_2/$(H_2P\text{-}C_{60})_m$ and FTO/SnO_2/$(H_2P\text{-ref}+C_{60}\text{-ref})_m$).[2b] The absorption feature of the FTO/SnO_2/$(H_2P\text{-}C_{60})_m$ electrode is largely similar to that in the corresponding ODCB–acetonitrile solutions (Figure 6a). On the other hand, the FTO/SnO_2/$(H_2P\text{-ref}+C_{60}\text{-ref})_m$ electrode shows structureless absorption feature resembling the C_{60} absorption, supporting that few H_2P-ref molecules are incorporated into the nano-aggregates as a result of the weak π-π interaction between the porphyrin and C_{60} molecules (Figure 6b). The broad absorption of the fabricated films together with the high absorption in the visible region makes these films suitable for harvesting the solar energy.

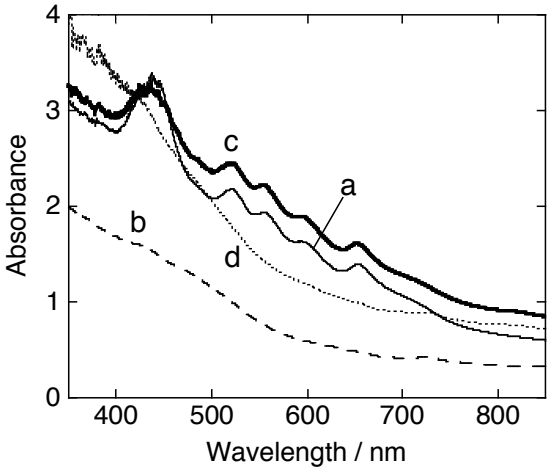

Figure 6. Absorption spectra of (a) FTO/SnO_2/$(H_2P\text{-}C_{60})_m$, (b) FTO/SnO_2/$(H_2P\text{-ref}+C_{60}\text{-ref})_m$, (c) FTO/$SnO_2$/$(H_2P\text{-}C_{60}$+f-SWNT$)_m$, and (d) FTO/$SnO_2$/$(H_2P\text{-ref}+C_{60}\text{-ref}$+f-SWNT$)_m$ electrodes.

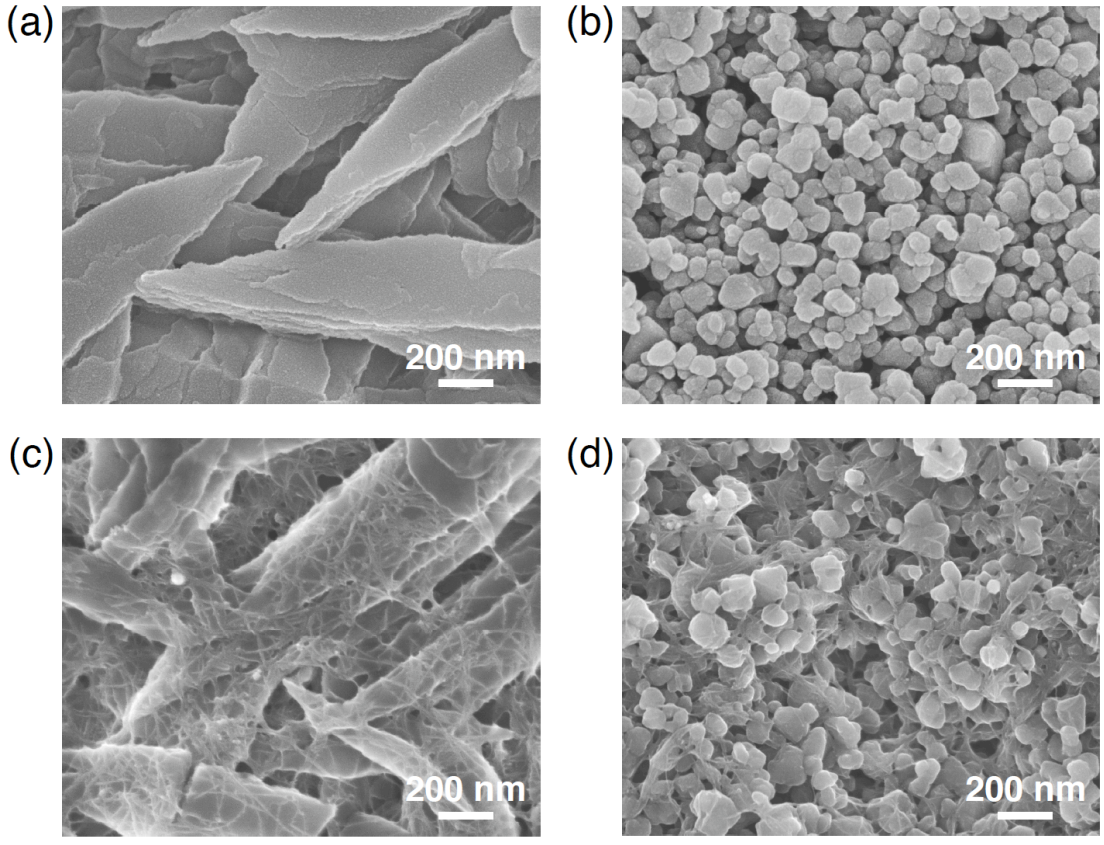

Figure 7. FE-SEM images of (a) FTO/SnO_2/$(H_2P\text{-}C_{60})_m$, (b) FTO/SnO_2/$(H_2P\text{-ref}+C_{60}\text{-ref})_m$, (c) FTO/$SnO_2$/$(H_2P\text{-}C_{60}$+f-SWNT$)_m$, and (d) FTO/$SnO_2$/$(H_2P\text{-ref}+C_{60}\text{-ref}$+f-SWNT$)_m$ electrodes.

The FE-SEM image of the FTO/SnO_2/$(H_2P\text{-}C_{60})_m$ electrode (Figure 7a) displays packing of the ellipsoid-shaped nanograins, which are almost identical to the spin-coated ones observed in Figure 4a. This corroborates that $(H_2P\text{-}C_{60})_m$ was successfully deposited on the nanostructured SnO_2 electrode without changing its inherent structure. In contrast, the FE-SEM image of the FTO/SnO_2/$(H_2P\text{-ref}+C_{60}\text{-ref})_m$ electrode exhibits dense packing of the small cubic nanograins (Figure 7b).

To evaluate the charge carrier mobility (μ) of the FTO/SnO_2/$(H_2P\text{-}C_{60})_m$ electrode, the author measured the flash-photolysis time-resolved microwave conductivity (TRMC).[13,14] Upon exposure to a laser pulse with an excitation wavelength of 355 nm, the sample reveals a rise of the transient conductivity $<\phi\Sigma\mu>$, in which ϕ is the quantum efficiency of charge separation (CS) and $\Sigma\mu$ is the sum of the mobilities of all the transient-charge carriers (Figure 8 and Table 2). The $\Sigma\mu$ value (0.30 cm^2 V^{-1} s^{-1}) of the FTO/SnO_2/$(H_2P\text{-}C_{60})_m$ electrode is very close to the highest value (2.0 cm^2 V^{-1} s^{-1}) ever reported for analogous D–A arrays utilizing D–A linked systems,[2,14] demonstrating the superior carrier-transporting capability within the nanograins.

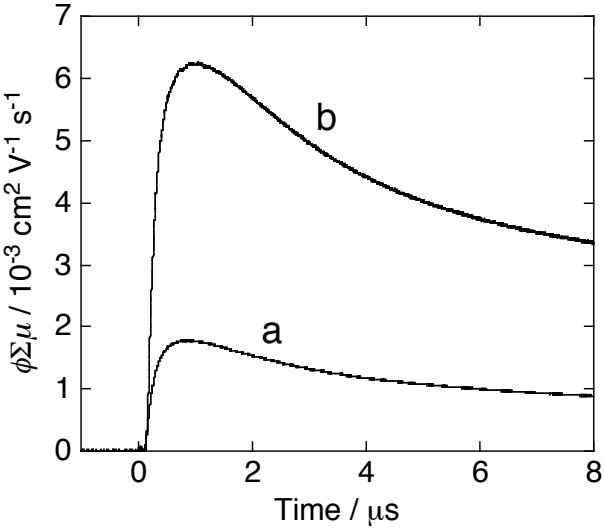

Figure 8. Flash-photolysis TRMC transients for (a) FTO/SnO_2/$(H_2P\text{-}C_{60})_m$ and (b) FTO/SnO_2/$(H_2P\text{-}C_{60}$+f-SWNT$)_m$ electrodes. The transients were recorded at an excitation wavelength of 355 nm with a photon density of 3.0×10^{15} cm^{-2}. All samples were fixed on quartz substrates with poly(methyl methacrylate) matrices.

TABLE 2: Microwave Conductivity, Quantum Efficiency of CS, Electron Mobility, and Maximal IPCE Value.

	$\phi\Sigma\mu^{a,b}$ / cm^2 V^{-1} s^{-1}	$\phi^{a,c}$ / %	$\Sigma\mu^a$ / cm^2 V^{-1} s^{-1}	maximal IPCE / %
$(H_2P\text{-}C_{60}$+f-SWNT$)_m$	6.3×10^{-3}	0.2	3.1	22
$(H_2P\text{-}C_{60})_m$	1.8×10^{-3}	0.6	0.30	11

[a] ϕ = quantum efficiency of CS; $\Sigma\mu$ = sum of mobility of all the transient-charge carriers. [b] Maximum value of the transient conductivity upon photoirradiation at 355 nm (photon density: 3.0×10^{15} cm^{-2}). [c] Determined by conventional DC-current integration technique with a photoexcitation at 355 nm.

Photocurrent Generation Property: To assess the macroscopic charge-transporting properties of the deposited films, the author measured the wavelength dependent incident photon-to-current efficiency (IPCE) spectra. Figure 9A(a) depicts the photocurrent action spectrum of the FTO/SnO_2/$(H_2P\text{-}C_{60})_m$ device under three-electrode photoelectrohemical conditions.[2] The photocurrent action spectrum largely resembles the absorption spectrum of the deposited nanograins on the electrode (Figure 6), implying the involvement of the porphyrin absorption for the photocurrent generation. In contrast, the photocurrent action spectrum of the FTO/SnO_2/$(H_2P\text{-ref}+C_{60}\text{-ref})_m$ device shows structureless photocurrent response resembling the C_{60} absorption owing to the limited incorporation of H_2P-ref into the deposited film (Figure 9A(b)). The maximal IPCE value (11% at 440 nm) of the FTO/SnO_2/$(H_2P\text{-}C_{60})_m$ device is *ca.* three times as large as the corresponding value (4% at 440 nm) of the FTO/SnO_2/$(H_2P\text{-ref}+C_{60}\text{-ref})_m$ device. It should also be emphasized here that the maximum IPCE value (11%) of the FTO/SnO_2/$(H_2P\text{-}C_{60})_m$ device is the highest one ever reported for analogous photoelectrochemical devices utilizing D–A linked systems under three-electrode conditions (4%).[2,14,15]

Effect of Carbon Nanotube Wiring: To examine the wiring effect of SWNTs on the charge-transporting properties, the author attempted to link the ellipsoid-shaped nanograins of $(H_2P\text{-}C_{60})_m$ with f-SWNT to enhance the electric communication. Namely, initial self-assembly of $H_2P\text{-}C_{60}$ with f-SWNT in the same mixed solvent leads to the formation of $H_2P\text{-}C_{60}$–f-SWNT ternary composites (denoted as $(H_2P\text{-}C_{60}\text{+f-SWNT})_m$) and subsequent

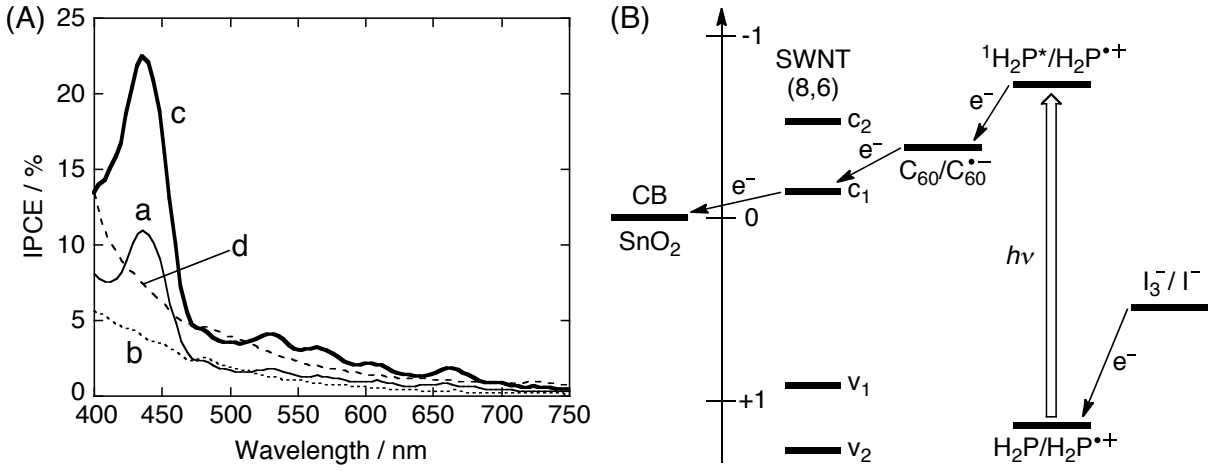

Figure 9. (A) Photocurrent action spectra of (a) FTO/SnO_2/$(H_2P\text{-}C_{60})_m$, (b) FTO/SnO_2/$(H_2P\text{-ref}+C_{60}\text{-ref})_m$, (c) FTO/$SnO_2$/$(H_2P\text{-}C_{60}\text{+f-SWNT})_m$, and (d) FTO/$SnO_2$/$(H_2P\text{-ref}+C_{60}\text{-ref+f-SWNT})_m$ devices. Applied potential: +0.17 V *vs.* SCE. Electrolyte: 0.5 M LiI and 0.01 M I_2 in acetonitrile. (B) Photocurrent generation diagram of the FTO/SnO_2/$(H_2P\text{-}C_{60}\text{+f-SWNT})_m$ device.

electrophoretic deposition of the $(H_2P\text{-}C_{60}\text{+f-SWNT})_m$ onto an FTO/SnO_2 electrode affords the deposited electrode (denoted as FTO/SnO_2/$(H_2P\text{-}C_{60}\text{+f-SWNT})_m$).

The FE-SEM image of the FTO/SnO_2/$(H_2P\text{-}C_{60}\text{+f-SWNT})_m$ electrode disclosed the expected morphology in which the ellipsoid-shaped nanoaggregates of $(H_2P\text{-}C_{60})_m$ are connected with f-SWNT (Figure 7c). It is noteworthy that the self-assembly processes allow f-SWNT to just bridge between the ellipsoid-shaped nanograins without affecting the intrinsic morphology of the $(H_2P\text{-}C_{60})_m$. In accordance with the surface observation, the TRMC measurement on the FTO/SnO_2/$(H_2P\text{-}C_{60}\text{+f-SWNT})_m$ electrode exhibited one order of magnitude higher transient conductivity than that of the FTO/SnO_2/$(H_2P\text{-}C_{60})_m$ electrode (Figure 8) to yield a $\Sigma\mu$ value of 3.1 $cm^2\ V^{-1}\ s^{-1}$, which is comparable to the value (3.2 $cm^2\ V^{-1}\ s^{-1}$)[5b,c] of the FTO/SnO_2/$(f\text{-SWNT})_m$ electrode without $H_2P\text{-}C_{60}$. Note that the rise profile of the transient conductivity for the FTO/SnO_2/$(H_2P\text{-}C_{60}\text{+f-SWNT})_m$ is different from that for FTO/SnO_2/f-SWNT)$_m$[5b,c] but close to that for the FTO/SnO_2/$(H_2P\text{-}C_{60})_m$, reaching the conductivity maxima within 1 μs. Similarity in the photoresponse behavior of the TRMC signals implies that large majority of the photocarriers in the $(H_2P\text{-}C_{60}\text{+f-SWNT})_m$ is generated by the excitation of $H_2P\text{-}C_{60}$, that is, CS between the porphyrin and C_{60}. Therefore, the improved $\Sigma\mu$ value of the FTO/SnO_2/$(H_2P\text{-}C_{60}\text{+f-SWNT})_m$, which is almost the same as that of the FTO/SnO_2/$(f\text{-SWNT})_m$, can be interpreted by the occurrence of charge shift from the resulting $C_{60}^{\bullet-}$ to f-SWNT, followed by bulk recombination of charge carriers during efficient electron transportation through f-SWNT. In accordance with the f-SWNT wiring, the maximum IPCE value (22%) of the FTO/SnO_2/$(H_2P\text{-}C_{60}\text{+f-SWNT})_m$ device is twice as large as that of the FTO/SnO_2/$(H_2P\text{-}C_{60})_m$ device (Figure 9A(c)). On the other hand, the FTO/SnO_2/$(f\text{-SWNT})_m$ device without $H_2P\text{-}C_{60}$ showed an IPCE value of 1% at 440 nm.[5b,c] These results unambiguously corroborate that electric communication between the D–A nanoaggregates is enhanced remarkably by the SWNT wiring.[16]

Photocurrent Generation Mechanism: On the basis of the film structures, TRMC mobilities, and photoelectrochemical properties discussed above, as well as the previous studies on similar photoelectrochemical devices consisting of the porphyrin–fullerene composites[17] and the fullerene–SWNT composites,[5] mechanism of a photocurrent generation for the FTO/SnO_2/$(H_2P\text{-}C_{60}\text{+f-SWNT})_m$ device can be illustrated as Figure 9B. Photocurrent generation is initiated by the photoinduced ET from the porphyrin singlet excited state ($^1H_2P^*/H_2P^{\bullet+}$ = –0.7 V *vs.* NHE) to the C_{60} moiety ($C_{60}/C_{60}^{\bullet-}$ = –0.4 V *vs.* NHE), as evidenced by the time-resolved absorption measurements (Figure 2B) and the photoelectrochemical measurements (Figure 9A). The photoinduced ET occurs with a quantum efficiency of near unity.[2] Then, the C_{60} arrays mediate electrons to a conduction band (CB) of f-SWNT (c_1 =

–0.1 V *vs.* NHE).[5] ET from $C_{60}^{\bullet-}$ to f-SWNT is energetically favorable and demonstrated by results of the TRMC measurements[5b,c] (*vide supra*). In addition, intimate contact between f-SWNT and the nanograins of H_2P-C_{60} disclosed by the microscopic observation (Figures 7c) promotes the electron mediation from $C_{60}^{\bullet-}$ to f-SWNT. The superb electron mobility (3.2 cm^2 V^{-1} s^{-1}) of the f-SWNT facilitates the electron flow toward the SnO_2 electrode ($E_{CB} \approx 0$ V *vs.* NHE)[17] by electrically wiring the ellipsoid-shaped nanograins of H_2P-C_{60}. On the other hand, the porphyrin arrays ($H_2P/H_2P^{\bullet+}$ = 1.2 V *vs.* NHE) shift holes until the oxidized porphyrin accepts electrons from I_3^-/I^- redox couple (I_3^-/I^- = 0.5 V *vs.* NHE)[17] to regenerate the initial state. Finally, the electrons injected into the CB of the SnO_2 nanocrystallines are driven to the counter electrode via external circuit to regenerate the I_3^-/I^- redox couple.

Conclusion

In conclusion, the author has developed a novel self-assembly methodology to build up well-organized D–A nanograins and simultaneous molecular wiring for efficient charge transport. The semiflexible, short methylene linkage of H_2P-C_{60} without conventional, extra self-assembling units successfully allowed the author to form the unique ellipsoid-shaped nanograins in the good–poor solvent mixture by selectively enforcing the porphyrin–porphyrin interactions as well as the C_{60}–C_{60} interactions rather than the porphyrin–C_{60} interactions. H_2P-C_{60} molecules in the nanograins were found to yield highly-aligned D–A structures, making it possible to achieve efficient intra charge transport within the nanograins. More importantly, the f-SWNT wiring between the D–A nanograins also rendered the inter charge transport efficient, leading to the highest IPCE value (22%) ever reported for analogous photoelectrochemical devices utilizing D–A linked systems. The author believes that the self-assembly of D–A linked molecules with molecular wires will be a highly promising method to achieve excellent device performances in organic photovoltaics and transistors.

Experimental Section

General Procedure: ^{1}H NMR spectra were measured with a JEOL JNM-EX400 NMR spectrometer. Matrix-assisted laser desorption/ionization (MALDI) time-of-flight mass spectra were obtained using a SHIMADZU Biotech AXIMA-CFR with 1,8-dihydroxy-9(10H)-anthracenone (dithranol) as a matrix. IR spectra were recorded on a JASCO FT/IR-470 Plus spectrometer using KBr pellets. UV–vis–near infrared (NIR) spectra of solutions and films were measured with a Perkin-Elmer Lambda 900 UV/vis/NIR spectrometer. Steady-state fluorescence spectra were obtained by a HORIBA SPEX Fluoromax-3 spectrofluorometer. Cyclic voltammetry (CV) measurements were performed using an ALS 630A electrochemical

analyzer in benzonitrile containing 0.1 M tetrabutylammonium hexafluorophosphate as a supporting electrolyte. A glassy carbon working electrode (3 mm diameter), $Ag/AgNO_3$ (0.01 M in acetonitrile) reference electrode, and Pt wire counter electrode were employed. FE-SEM observation was carried out with a JEOL JSM-6705F. For preparation of the cluster samples, a mixture of ODCB–acetonitrile containing self-assembled grains was spin-coated on Si wafer (polished wafer; SUMCO TECHXIV) at a rotation speed of 1600 rpm. Except for the samples containing SWNTs, all other spin-coated samples and electrophoretically deposited films were coated with *ca.* 5 nm thick Pt layer using a JEOL JFC-1600 auto fine coater before the measurements. The structures of the clusters were analyzed by X-ray diffraction (XRD) with Cu K_α radiation (MultiFlex DR Powder X-ray diffractometer).

Materials: C_{60} (99.98%) were obtained from MTR Ltd. and used as-received. All other solvents and chemicals were of reagent-grade quality, purchased commercially, and used without further purification unless otherwise noted. Thin layer chromatography (TLC) and column chromatography were performed with Silica gel 60 F254 (Merck) and SiliaFlash F60 (230 – 400 mesh; SiliCycle Inc.), respectively. H_2P-ref and C_{60}-ref were synthesized as a reference compound for spectroscopic and electrochemical measurements.[7,8] Highly soluble functionalized SWNTs (f-SWNT) was prepared by purification and oxidation of commercially available HiPco SWNTs (Carbon Nanotechnologies, Inc., batch P0343) and subsequent treatment with thionyl chloride and 8-aminopentadecane as described elsewhere.[5a] An optically transparent FTO electrode (AGC Fabritech) was washed by sonication in 2-propanol and cleaned in an O_3 atmosphere in advance. A 15% SnO_2 colloidal solution (Alfa Aesar) was deposited on the FTO electrode using doctor blade technique. The electrode was annealed at 673 K to yield 1 μm thick SnO_2 film (denoted as FTO/SnO_2).

Synthetic Procedure: The target compound H_2P-C_{60} was synthesized as illustrated in the scheme below. Starting compound **1** was synthesized according to the literature.[18]

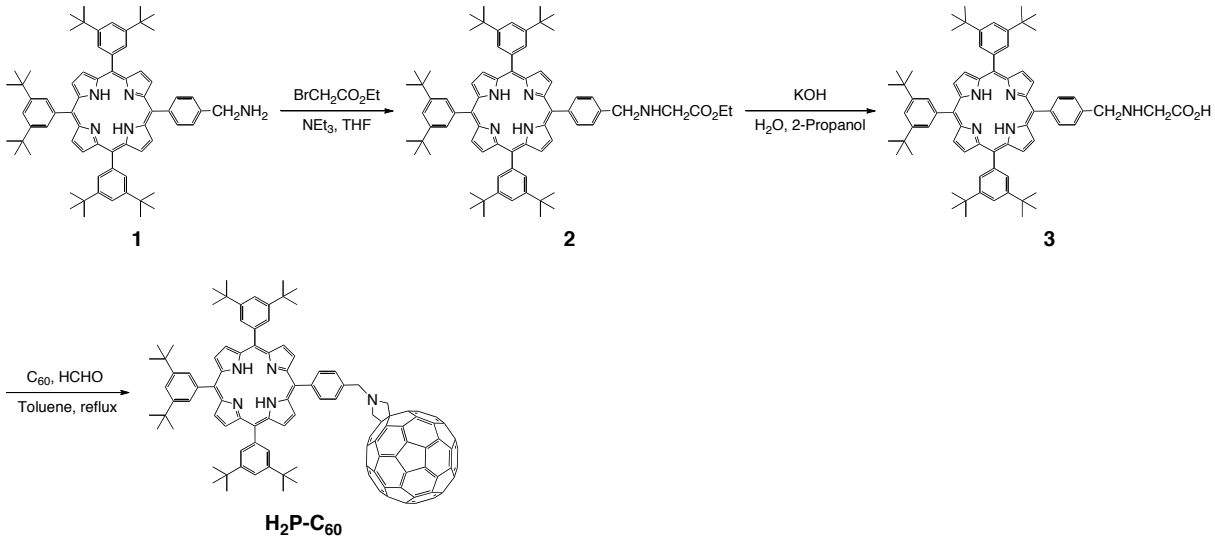

Synthesis of 2: A solution of ethyl bromoacetate (0.12 mL, 1.1 mmol) in dry THF (30 mL) was added dropwise to a stirred solution of **1** (1.1 g, 1.1 mmol) and triethylamine (0.15 mL, 1.1 mmol) in dry THF (30 mL). After additional stirring for 24 h at room temparature, the reaction mixture was evaporated, subjected to silica gel chlomatography (CH_2Cl_2/AcOEt/ hexane = 1/1/5), and reprecipitated from $CHCl_3$/MeOH to afford **2** (0.73 g, 0.68 mmol, 63%). ^{1}H NMR (400 MHz, $CDCl_3$): δ 8.89 – 8.83 (m, 8H), 8.20 (d, J = 8 Hz, 2H), 8.09 – 8.07 (m, 6H), 7.79 (s, 3H), 7.71 (d, J = 8 Hz, 2H), 4.31 (q, J = 7 Hz, 2H), 4.16 (s, 2H), 3.67 (s, 2H), 1.52 (s, 54 H), 1.37 (t, J = 7 Hz, 3H), –2.70 (s, 2H). FTIR (KBr): ν 3315, 3065, 2960, 2903, 2867, 1741, 1592, 1475, 1363, 1247, 1185, 973, 915, 801 cm^{-1}. HRMS (MALDI): *m*/*z* calcd for $C_{73}H_{87}O_2N_5^+$ ([M]$^+$), 1065.6860; found 1065.6826.

Synthesis of 3: Porphyrin **2** (0.73 g, 0.68 mmol) was dispersed in 110 mL of 2-propanol by sonication for 15 min. To this dispersion was added dropwise an aqueous solution of KOH (2.1 M, 25 mL). After refluxing for 15 h, 5.2 mL of *conc.* HCl *aq.* was added to the reaction mixture. The organic layer was separated, washed with saturated $NaHCO_3$ *aq.*, and dried over anhydrous $MgSO_4$. The crude product was purified through column chromatography on silica gel with CH_2Cl_2/MeOH (9/1) as an eluent. Subsequent freeze-drying of the desired fraction gave **3** (0.65 g, 0.63 mmol, 92%). ^{1}H NMR (400 MHz, $CDCl_3$): δ 8.84 – 8.80 (m, 8H), 8.31 (d, J = 8 Hz, 2H), 8.01 (d, J = 12 Hz, 8H), 7.76 (s, 1H), 7.63 (s, 2H), 4.79 (s, 2H), 4.00 (s, 2H), 1.40 (m, 54 H), –2.75 (s, 2H). FTIR (KBr): ν 3316, 3064, 2961, 2904, 2868, 1592, 1475, 1363, 1247, 973, 915, 802, 715 cm^{-1}. HRMS (MALDI): *m*/*z* calcd for $C_{71}H_{83}O_2N_5^+$ ([M]$^+$), 1037.6547; found 1037.6542.

Synthesis of H_2P-C_{60}: C_{60} (0.55 g, 0.76 mmol), paraformaldehyde (0.12 g), and **3** (0.65 g, 0.63 mmol), were disolved in 600 mL of dry toluene by sonication and the resultant mixture was refluxed for 3 days. After cooled to room temparature, the reaction mixture was evaporated and subjected to the repeated cycle of silica gel chromatography (toluene/hexane = 2/3, then 1/1) to completely remove the unreacted C_{60} and any other byproducts. The separated product was further purified by reprecipitation from toluene/MeOH to give H_2P-C_{60} (0.30 g, 0.18 mmol, 28%). ^{1}H NMR (400 MHz, $CDCl_3$): δ 8.97 – 8.87 (m, 8H), 8.37 (d, J = 7 Hz, 2H), 8.08 (s, 8H), 7.78 (s, 3H), 4.59 (s, 2H), 4.40 (s, 4H), 1.51 (s, 54 H), –2.72 (s, 2H). FTIR (KBr): ν 3314, 3060, 2961, 2904, 2866, 1592, 1475, 1428, 1362, 1247, 973, 917, 801, 731 cm^{-1}. HRMS (MALDI): *m*/*z* calcd for $C_{131}H_{83}N_5^+$ ([M]$^+$), 1725.6648; found 1725.6659.

Preparation of Nanograin Solutions and Films: The nanograin solutions of H_2P-C_{60} (0.16 mM) and/or f-SWNT (0.013 g L^{-1}) were prepared in a 1 cm cuvette by injecting 1.14 mL of acetonitrile into a solution of H_2P-C_{60} (0.55 mM) and/or f-SWNT (0.044 g L^{-1}) in 0.46 mL of ODCB (ODCB:acetonitrile = 2:5, v/v).[5] Then, two electrodes (*i.e.*, FTO and FTO/SnO_2) were inserted into a cuvette with keeping at a distance of 0.6 cm by a Teflon spacer. A dc

voltage (200 V) was applied for 120 s between these two electrodes using a power supply (ATTO, model AE-8750). The deposition of the film could be visibly confirmed as the suspension became colorless with simultaneous colorization of the FTO/SnO_2 electrode. After the deposition, the deposited film was dried immediately with a hair dryer. Likewise, the nanograin and the deposited film of H_2P-ref–C_{60}-ref were also prepared.

Molecular Modeling: Computational modeling of the assembly structure of H_2P-C_{60} nanograin was performed using the MM3 force field[19–21] implemented in the TINKER program package.[22] Modified MM3 parameters were used for C–C bonds between porphyrin and aryl to reproduce the molecular structure of H_2P optimized by the B3LYP method which was performed with cc-pVDZ basis set by the Gaussian 03 package.[23] As a representative example, ten H_2P-C_{60} molecules were incorporated for plausible self-assembled structures.

Time-resolved Spectroscopy: A pump-probe method was used to measure transient absorption spectra in sub-picosecond to nanosecond time domain. The measurements were carried out using the instrument described previously.[24] Briefly, the transient spectra were recorded by a CCD detector coupled with a monochromator in the visible and NIR ranges and a second harmonic (420 nm) of Ti:sapphire laser was used for excitation. A typical time resolution of the instrument was 150 fs (full width at half maximum (FWHM)). The excitation energy was adjusted to low enough to avoid the photodegradation of samples and the energy-dependent decay process. All measurements were carried out at room temperature.

Time-resolved Microwave Conductivity Measurements: The instruments setup as descrived in the previous studies[5b,c,13] were used for the measurements. Namely, nanosecond laser pulses at 355 nm (FWHM: 3 – 5 ns) with photon density of 1.6×10^{15} – 3.6×10^{16} cm^{-2} were used as an excitation source. A microwave frequency of 8.6 – 9.4 GHz and a power of 2.1 – 4.6 mW were employed. Other experimental details are described elsewhere.[13]

Photoelectrochemical Measurements: All electrochemical measurements were carried out in a standard three-electrode system using an ALS 630A electrochemical analyzer.[5] The deposited film as a working electrode was immersed into an electrolyte solution containing 0.5 M LiI and 0.01 M I_2 in acetonitrile. A Pt wire covered with a glass Luggin capillary, whose tip was located near the working electrode, was used as a quasi-reference electrode. A Pt coil was employed as a counter electrode. The potential measured was converted to the saturated calomel electrode (SCE) scale by adding +0.05 V. A 500 W xenon lamp (USHIO, XB-50101AAA) was used as a light source. Monochromatic light through a monochromator (Ritsu, MC-10N) was illuminated on the modified area of the working electrode (0.20 cm^2) from the backside. The light intensity was monitored by an optical power meter (Anritsu, ML9002A) and corrected for calculation of IPCE values.

References and Notes

[1] a) H. Klauk, *Organic Electronics*, Wiley-VCH, Weinheim, 2006; b) H. Sirringhaus, *Adv. Mater.* **2005**, *17*, 2411; c) V. Coropceanu, J. Cornil, D. A. da Silva Filho, Y. Olivier, R. Silbey, J.-L. Brédas, *Chem. Rev.* **2007**, *107*, 926.

[2] a) H. Imahori, *Bull. Chem. Soc. Jpn.* **2007**, *80*, 621; b) H. Imahori, *J. Mater. Chem.* **2007**, *17*, 31.

[3] a) P. D. W. Boyd, C. A. Reed, *Acc. Chem. Res.* **2005**, *38*, 235; b) D. M. Guldi, N. Martín, *J. Mater. Chem.* **2002**, *12*, 1978.

[4] a) D. M. Guldi, *Chem. Soc. Rev.* **2002**, *31*, 22; b) S. Fukuzumi, *Phys. Chem. Chem. Phys.* **2008**, *10*, 2283; c) D. Gust, T. A. Moore, A. L. Moore, *Acc. Chem. Res.* **2001**, *34*, 40.

[5] a) T. Umeyama, N. Tezuka, M. Fujita, S. Hayashi, N. Kadota, Y. Matano, H. Imahori, *Chem.-Eur. J.* **2008**, *14*, 4875; b) T. Umeyama, N. Tezuka, S. Seki, Y. Matano, M. Nishi, K. Hirao, H. Lehtivuori, N. V. Tkachenko, H. Lemmetyinen, Y. Nakao, S. Sakaki, H. Imahori, *Adv. Mater.* **2010**, *22*, 1767; c) N. Tezuka, T. Umeyama, S. Seki, Y. Matano, M. Nishi, K. Hirao, H. Imahori, *J. Phys. Chem. C* **2010**, *114*, 3235.

[6] a) D. M. Guldi, G. M. A. Rahman, M. Prato, N. Jux, S. Qin, W. Ford, *Angew. Chem. Int. Ed.* **2005**, *44*, 2015; b) T. Umeyama, M. Fujita, N. Tezuka, N. Kadota, Y. Matano, K. Yoshida, S. Isoda, H. Imahori, *J. Phys. Chem. C* **2007**, *111*, 11484; c) F. D'Souza, A. S. D. Sandanayaka, O. Ito, *J. Phys. Chem. Lett.* **2010**, *1*, 2586.

[7] N. V. Tkachenko, H. Lemmetyinen, J. Sonoda, K. Ohkubo, T. Sato, H. Imahori, S. Fukuzumi, *J. Phys. Chem. A* **2003**, *107*, 8834.

[8] M. Maggini, G. Scorrano, M. Prato, *J. Am. Chem. Soc.* **1993**, *115*, 9798.

[9] C. Luo, D. M. Guldi, H. Imahori, K. Tamaki, Y. Sakata, *J. Am. Chem. Soc.* **2000**, *122*, 6535.

[10] T. J. Kesti, N. V. Tkachenko, V. Vehmanen, H. Yamada, H. Imahori, S. Fukuzumi, H. Lemmetyinen, *J. Am. Chem. Soc.* **2002**, *124*, 8067.

[11] K.-i. Sugiura, K. Iwasaki, K. Umishita, S. Hino, H. Ogata, S. Miyajima, Y. Sakata, *Chem. Lett.* **1999**, 841.

[12] V. Georgakilas, F. Pellarini, M. Prato, D. M. Guldi, M. Melle-Franco, F. Zerbetto, *Proc. Natl. Acad. Sci. U.S.A.* **2002**, *99*, 5075.

[13] T. Amaya, S. Seki, T. Moriuchi, K. Nakamoto, T. Nakata, H. Sakane, A. Saeki, S. Tagawa, T. Hirao, *J. Am. Chem. Soc.* **2009**, *131*, 408.

[14] a) Y. Yamamoto, T. Fukushima, Y. Suna, N. Ishii, A. Saeki, S. Seki, S. Tagawa, M. Taniguchi, T. Kawai, T. Aida, *Science* **2006**, *314*, 1761; b) Y. Yamamoto, G. Zhang, W. Jin, T. Fukushima, N. Ishii, A. Saeki, S. Seki, S. Tagawa, T. Minari, K. Tsukagoshi, T. Aida, *Proc. Natl. Acad. Sci. U.S.A.* **2009**, *106*, 21051; c) F. Würthner, Z. Chen, F. J. M.

Hoeben, P. Osswald, C.-C.You, P. Jonkheijm, J. Herrikhuyzen, A. P. H. J. Schenning, P. P. A. M. van der Schoot, E. W. Meijer, E. H. A. Beckers, S. C. J. Meskers, R. A. J. Janssen, *J. Am. Chem. Soc.* **2004**, *126*, 10611; d) C. Röger, M. G. Müller, M. Lysetska, Y. Miloslavina, A. R. Holzwarth, F. Würthner, *J. Am. Chem. Soc.* **2006**, *128*, 6542; e) W.-S. Li, Y. Yamamoto, T. Fukushima, A. Saeki, S. Seki, S. Tagawa, H. Masunaga, S. Sasaki, M. Takata, T. Aida, *J. Am. Chem. Soc.* **2008**, *130*, 8886; f) R. Charvet, S. Acharya, J. P. Hill, M. Akada, M. Liao, S. Seki, Y. Honsho, A. Saeki, K. Ariga, *J. Am. Chem. Soc.* **2009**, *131*, 18030; g) Y. Hizume, K. Tashiro, R. Charvet, Y. Yamamoto, A. Saeki, S. Seki, T. Aida, *J. Am. Chem. Soc.* **2010**, *132*, 6628.

[15] a) P. V. Kamat, S. Barazzouk, S. Hotchandani, K. G. Thomas, *Chem.-Eur. J.* **2000**, *6*, 3914; b) H. Imahori, T. Hasobe, H. Yamada, P. V. Kamat, S. Barazzouk, M. Fujitsuka, O. Ito, S. Fukuzumi, *Chem. Lett.* **2001**, 784.

[16] Although the photocurrent response from the porphyrin is absent because of the little incorporation of H_2P-ref into the grains, the IPCE value of the FTO/SnO_2/(H_2P-ref+C_{60}-ref+f-SWNT)$_m$ device (Figure 9A(d)) is also larger than that of the FTO/SnO_2/(H_2P-ref+C_{60}-ref)$_m$ device (Figure 9A(b)) as a result of the wiring of the nanograins by f-SWNT (Figure 7d).

[17] a) H. Imahori, M. Ueda, S. Kang, H. Hayashi, S. Hayashi, H. Kaji, S. Seki, A. Saeki, S. Tagawa, T. Umeyama, Y. Matano, K. Yoshida, S. Isoda, M. Shiro, N. V. Tkachenko, H. Lemmetyinen, *Chem.-Eur. J.* **2007**, *13*, 10182; b) P. V. Kamat, S. Barazzouk, K. G. Thomas, S. Hotchandani, *J. Phys. Chem. B* **2000**, *104*, 4014.

[18] H. Imahori, K. Tamaki, Y. Araki, T. Hasobe, O. Ito, A. Shimomura, S. Kundu, T. Okada, Y. Sakata, S. Fukuzumi, *J. Phys. Chem. A* **2002**, *106*, 2803.

[19] N. L. Allinger, Y. H. Yuh, J.-H. Lii, *J. Am. Chem. Soc.* **1989**, *111*, 8551.

[20] J.-H. Lii, N. L. Allinger, *J. Am. Chem. Soc.* **1989**, *111*, 8566.

[21] J.-H. Lii, N. L. Allinger, *J. Am. Chem. Soc.* **1989**, *111*, 8576.

[22] J. W. Ponder, TINKER Version 5.1, 2010 (http://dasher.wustl.edu/tinker/).

[23] M. J. Frisch, G. W. Trucks, H. B. Schlegel, G. E. Scuseria, M. A. Robb, J. R. Cheeseman, J. A. Jr. Montgomery, T. Vreven, K. N. Kudin, J. C. Burant, J. M. Millam, S. S. Iyengar, J. Tomasi, V. Barone, B. Mennucci, M. Cossi, G. Scalmani, N. Rega, G. A. Petersson, H. Nakatsuji, M. Hada, M. Ehara, K. Toyota, R. Fukuda, J. Hasegawa, M. Ishida, T. Nakajima, Y. Honda, O. Kitao, H. Nakai, M. Klene, X. Li, J. E. Knox, H. P. Hratchian, J. B. Cross, V. Bakken, C. Adamo, J. Jaramillo, R. Gomperts, R. E. Stratmann, O. Yazyev, A. J. Austin, R. Cammi, C. Pomelli, J. W. Ochterski, P. Y. Ayala, K. Morokuma, G. A. Voth, P. Salvador, J. J. Dannenberg, V. G. Zakrzewski, S. Dapprich, A. D. Daniels, M C. Strain, O. Farkas, D. K. Malick, A. D. Rabuck, K. Raghavachari, J. B. Foresman, J. V.

Ortiz, Q. Cui, A. G. Baboul, S. Clifford, J. Cioslowski, B. B. Stefanov, G. Liu, A. Liashenko, P. Piskorz, I. Komaromi, R. L. Martin, D. J. Fox, T. Keith, M. A. Al-Laham, C. Y. Peng, A. Nanayakkara, M. Challacombe, P. M. W. Gill, B. Johnson, W. Chen, M. W. Wong, C. Gonzalez, J. A. Pople, *Gaussian 03*, revision C.02; Gaussian, Inc.: Wallingford, CT, 2004.

[24] N. V. Tkachenko, L. Rantala, A. Y. Tauber, J. Helaja, P. H. Hynninen, H. Lemmetyinen, *J. Am. Chem. Soc.* **1999**, *121*, 9378.

Concluding Remarks

This thesis has described the preparation and photoelectrochemical application of novel nanocarbon composites of fullerenes and chemically functionalized single-walled carbon nanotubes (SWNTs). The results and findings in this work are summarized as follows.

1. The author has utilized Bingel reaction for the sidewall modification of the acid-treated, shortened SWNTs with long alkyl chains at the open ends and defect sites. The microwave irradiation was applied to promote Bingel reaction, by which the reaction rate became *ca.* 50 times faster than that under the conventional conditions. The degree of the sidewall functionalization (one diester unit per 75 – 300 carbon atoms of SWNT) was found to be controllable by changing the output power of microwave irradiation. Resonant Raman and UV–vis–near IR absorption spectroscopies revealed that the electronic properties of SWNTs are largely retained after a significant degree of the sidewall modification by Bingel reaction without apparent selective reactivity for metallic and semiconducting SWNTs.

2. The author has synthesized the covalently modified SWNTs with bulky porphyrin moieties to construct the photoelectrochemical devices. The electrophoretically deposited film of the multiporphyrin-linked SWNTs exhibited the incident photon-to-current efficiency (IPCE) values of up to 4.9%. The more uniform film formation and the moderate photocurrent generation in the porphyrin-linked SWNT devices were rationalized by the exfoliation abilities of the bulky porphyrins toword the SWNT bundles. It was revealed that direct electron injection from the excited states of SWNTs to the conduction band of SnO_2 is responsible for the photocurrent generation, despite of the efficient quenching of the porphyrin excited singlet state by SWNTs in the porphyrin-linked SWNTs. The evolution of an exciplex between the porphyrin excited singlet state and the SWNTs and the subsequent decay to the ground state without generating the charge-separated state was proposed to explain the unusual photoelectrochemical behavior.

3. Novel nanohybrids of SWNTs encapsulating C_{60} or C_{70} with poly(3-hexylthiophene) (P3HT) have been constructed and their photophysics and photoelectrochemical properties were investigated. The noncovalent π-π interaction between the SWNT sidewalls and P3HT was harnessed to dissolve the so-called peapods into an organic

solvent. Transient absorption and fluorescence up-conversion techniques elucidated the excited state behavior of the nanohybrids, where exciplex forms from the P3HT singlet excited state with the peapods and subsequently relaxes to the ground state within ~ 1 ps. Significant impact of the encapsulation of C_{60} or C_{70} upon the photodynamics was not observed, suggesting little participation of the fullerenes in the excited state events. Photoelectrochemical devices based on the peapod–P3HT nanohybrids showed almost the same IPCE values as those for the empty SWNT-based device, which agrees well with the results of the time-resolved spectroscopies.

4. The author has systematically studied the good solvent effects of C_{70} cluster formations and their electron-transporting and photoelectrochemical properties. Differently shaped assemblies of C_{70} with nano-to-micrometer dimensions were successfully prepared by rapidly injecting a poor solvent into a solution of C_{70} in various good solvents. The cluster morphology engineering was achieved by changing the good solvent, yielding the spherical, rod-like, or plate-like clusters in the mixed solvents. The electrophoretically deposited cluster films showed significant dependence of the IPCE values on the combination of good–poor solvents. More importantly, the IPCE values were found to correlate with electron mobility of the deposited cluster films, implying the importance of the electron-transporting process in the photocurrent generation mechanism. Furthermore, the underlying molecular packing was suggested to affect strongly the resultant cluster structure and the electron mobility.

5. The author has established a new methodology for the self-assembly of fullerene C_{60} on the sidewalls of SWNTs. The nanocarbon composites of C_{60} and highly soluble, chemically functionalized SWNTs (f-SWNT) were prepared by rapid injection of a poor solvent (*i.e.*, acetonitrile) into a mixed solution of C_{60} and f-SWNT in good solvent (*i.e.*, *o*-dichlorobenzene (ODCB)). Microscopic observation disclosed that the composites are categorized into three groups; i) f-SWNT bundles covered with layers of C_{60} molecules, ii) round, large C_{60} clusters containing f-SWNT, and iii) typical, round C_{60} clusters. The electrophoretic deposition of the composites onto a SnO_2 electrode yielded the hierarchical film with gradient composition depending on the difference in the mobilities of C_{60} and f-SWNT during the electrophoretic process. The composite film demonstrated the IPCE value of 18%, which was the highest among SWNT-based photoelectrochemical devices. The ordered arrangement of C_{60} molecules on f-SWNT accounts for the efficient photocurrent generation.

6. The author has prepared novel nanocarbon composites, where C_{70} molecules are stacked on the sidewall of SWNTs. Enhanced interaction between the flattened-shaped C_{70} and SWNTs provoked the single component cluster formation in the ODCB–acetonitrile mixture, which is in remarkable contract to the case of C_{60}–SWNT composite with three different structures. Time-resolved microwave conductivity technique indicated superb electron mobility through the SWNT network formed in the composite. The C_{70}–SWNT photoelectrochemical device exhibited efficient photocurrent generation resulting from selective formation of the single composite film consisting of the SWNT network covered with C_{70} molecules in addition to the high electron mobility through the C_{70}–SWNT network.

7. The cluster formation in ODCB–acetonitrile mixture, electrophoretically deposited film structures, microwave conductivity, and photoelectrochemical properties of the nanocarbon composites consisting of SWNTs with C_{60}, C_{70}, or C_{84} have been systematically compared. The author found that the higher fullerenes (*i.e.*, C_{70} and C_{84}) form single composite clusters exclusively with highly soluble SWNTs with bulky swallow-tailed substituents (f-SWNT), which marks a sharp contrast with the unselective formation of three different clusters in the C_{60}–f-SWNT composites. The microwave conductivity measurements revealed the charge shift from C_{70} radical anion to f-SWNT, followed by electron transport through f-SWNT, in addition to electron hopping through C_{70} arrays on the sidewalls of f-SWNT in the C_{70}–f-SWNT composite. The C_{70}–f-SWNT photoelectrochemical device disclosed the higher IPCE value (26%) than that of the C_{60}–f-SWNT device (18%). The higher IPCE value was rationalized by selective formation of the single composite film, in which the SWNT network is covered with C_{70} molecules, and the high electron mobility through the C_{70}–SWNT network. In contrast, the C_{84}–f-SWNT photoelectrochemical device showed rather poor photocurrent generation (4.8%) owing to the inefficient electron injection from C_{84} radical anion to the SnO_2 electrode directly or indirectly despite of the exclusive formation of the single composite clusters.

8. The author has successfully developed an unprecedented self-assembly method to build up the ordered donor–acceptor nanoclusters and their efficient molecular wiring that can be detected as photocurrent. The semiflexible methylene linkage of porphyrin (donor)–C_{60} (acceptor) allowed the author to form unique ellipsoid-shaped nanoclusters in a mixed solvent of ODCB and acetonitrile. The porphyrin–C_{60} linked molecules in the nanoclusters were found to yield highly ordered donor–acceptor arrays, resulting in

the efficient intra charge transport within the nanoclusters. Moreover, functionalized SWNT wiring between the nanoclusters also rendered the inter charge transport extremely efficient, leading to the highest IPCE value (22%) ever reported for analogous photoelectrochemical devices utilizing donor–acceptor linked dyads.

List of Publications

The content of this thesis is composed of the following papers.

Chapter 1

Retention of Intrinsic Electronic Properties of Soluble Single-Walled Carbon Nanotubes after a Significant Degree of Sidewall Functionalization by the Bingel Reaction

T. Umeyama, N. Tezuka, M. Fujita, Y. Matano, N. Takeda, K. Murakoshi, K. Yoshida, S. Isoda, H. Imahori

The Journal of Physical Chemistry C **2007**, *111*, 9734 – 9741.

Chapter 2

Electrophoretic Deposition of Single-Walled Carbon Nanotubes Covalently Modified with Bulky Porphyrins on Nanostructured SnO_2 Electrodes for Photoelectrochemical Devices

T. Umeyama, M. Fujita, N. Tezuka, N. Kadota, Y. Matano, K. Yoshida, S. Isoda, H. Imahori

The Journal of Physical Chemistry C **2007**, *111*, 11484 – 11493.

Chapter 3

Photophysics and Photoelectrochemical Properties of Nanohybrids Consisting of Fullerene-Encapsulated Single-Walled Carbon Nanotubes and Poly(3-hexylthiophene)

N. Tezuka, T. Umeyama, Y. Matano, T. Shishido, K. Yoshida, T. Ogawa, S. Isoda, K. Stranius, V. Chukharev, N. V. Tkachenko, H. Lemmetyinen, H. Imahori

Energy and Environmental Science, in press (DOI:10.1039/C0EE00482K).

Chapter 4

Good Solvent Effects of C_{70} Cluster Formations and Their Electron-Transporting and Photoelectrochemical Properties

N. Tezuka, T. Umeyama, Y. Matano, T. Shishido, M. Kawasaki, M. Nishi, K. Hirao, H. Lehtivuori, N. V. Tkachenko, H. Lemmetyinen, Y. Honsho, S. Seki, H. Imahori

The Journal of Physical Chemistry B **2010**, *114*, 14287 – 14297.

Chapter 5

Clusterization, Electrophoretic Deposition, and Photoelectrochemical Properties of Fullerene-Functionalized Carbon Nanotube Composites

T. Umeyama, N. Tezuka, M. Fujita, S. Hayashi, N. Kadota, Y. Matano, H. Imahori

Chemistry – A European Journal **2008**, *14*, 4875 – 4885.

Chapter 6

Selective Formation and Efficient Photocurrent Generation of [70]Fullerene–Single-Walled Carbon Nanotube Composites

T. Umeyama, N. Tezuka, S. Seki, Y. Matano, M. Nishi, K. Hirao, H. Lehtivuori, N. V. Tkachenko, H. Lemmetyinen, Y. Nakao, S. Sakaki, H. Imahori

Advanced Materials **2010**, *22*, 1767 – 1770.

Chapter 7

Comparison of Cluster Formation, Film Structure, Microwave Conductivity, and Photoelectrochemical Properties of Composites Consisting of Single-Walled Carbon Nanotubes with C_{60}, C_{70}, and C_{84}

N. Tezuka, T. Umeyama, S. Seki, Y. Matano, M. Nishi, K. Hirao, H. Imahori

The Journal of Physical Chemistry C **2010**, *114*, 3235 – 3247.

Chapter 8

Carbon Nanotube Wiring of Donor–Acceptor Nanograins by Self-Assembly and Efficient Charge Transport

T. Umeyama, N. Tezuka, F. Kawashima, S. Seki, Y. Matano, Y. Nakao, T. Shishido, M. Nishi, K. Hirao, H. Lehtivuori, N. V. Tkachenko, H. Lemmetyinen, H. Imahori

Submitted to *Angewandte Chemie International Edition*.

Other Publications

Photoinduced Energy Transfer in Composites of poly[(*p*-phenylene-1,2-vinylene)-*co*-(*p*-phenylene-1,1-vinylidene)] and Single-Walled Carbon Nanotubes
T. Umeyama, N. Kadota, N. Tezuka, Y. Matano, H. Imahori
Chemical Physics Letters **2007**, *444*, 263 – 267.

Synthesis and Photophysical and Photovoltaic Properties of Porphyrin–Furan and –Thiophene Alternating Copolymers
T. Umeyama, T. Takamatsu, N. Tezuka, Y. Matano, Y. Araki, T. Wada, O. Yoshikawa, T. Sagawa, S. Yoshikawa, H Imahori
The Journal of Physical Chemistry C **2009**, *113*, 10798 – 10806.

Dispersion of Carbon Nanotubes by Photo- and Thermal-Responsive Polymers Containing Azobenzene Unit in the Backbone
T. Umeyama, K. Kawabata, N. Tezuka, Y. Matano, Y. Miyato, K. Matsushige, M. Tsujimoto, S. Isoda, M. Takano, H. Imahori
Chemical Communications **2010**, *46*, 5969 – 5971.

Formation of Single-Walled Carbon Nanotube Thin Films Enriched with Semiconducting Nanotubes and Their Application in Photoelectrochemical Devices
L. Wei, N. Tezuka, T. Umeyama, H. Imahori, Y. Chen
Nanoscale, in press (DOI:10.1039/C0NR00986E).

Density Functional Theory Studies on Chemical Functionalization of Single-Walled Carbon Nanotubes by Bingel Reaction
T. Umeyama, H. Fueno, E. Kawabata, Y. Kobayashi, K. Tanaka, N. Tezuka, Y. Matano, H. Imahori
Submitted to *Bulletin of the Chemical Society of Japan*.

Review

Construction of the Light Energy Conversion Systems Utilizing Single-Walled Carbon Nanotubes
H. Imahori, N. Tezuka
Chemical Engineering **2008**, *53*, 35 – 40.

Acknowledgment

The studies presented in this thesis have been carried out under the direction of Professor Hiroshi Imahori at Department of Molecular Engineering, Graduate School of Engineering, Kyoto University, during the period of *2005 – 2011*.

First of all, the author would like to express his gratitude to Prof. Hiroshi Imahori for his kind guidance and invaluable suggestions during this study. The author is also deeply grateful to Prof. Yoshihiro Matano and Assistant Prof. Tomokazu Umeyama for their constant advice, helpful discussions, and continuous encouragement throughout the course of this work.

The author is indebted to Prof. Noboru Ono, Assistant Prof. Tatsuya Murakami, Dr. Hiroki Hotta, Dr. Masanobu Tanaka, Dr. Simon Mathew, Dr. Yuki Shibano, Dr. Kohei Hosomizu, Dr. Seunghun Eu, Dr. Soonchul Kang, Dr. Takashi Nakabuchi, and Dr. Aiko Kira for their helpful suggestions and technical assistance.

The author would like to thank Prof. Shu Seki (*Osaka Univ.*), Prof. Shigeyoshi Sakaki (*Kyoto Univ.*), Assistant Prof. Yoshihide Nakao (*Kyoto Univ.*), Prof. Mitsuo Kawasaki (*Kyoto Univ.*), Prof. Tetsuya Shishido (*Kyoto Univ.*), Prof. Kazuyuki Hirao (*Kyoto Univ.*), Assistant Prof. Masayuki Nishi (*Kyoto Univ.*), Prof. Kazuhiro Mae (*Kyoto Univ.*), Assistant Prof. Isao Hasegawa (*Kyoto Univ.*), Prof. Seiji Isoda (*Kyoto Univ.*), Assistant Prof. Tetsuya Ogawa (*Kyoto Univ.*), Dr. Kaname Yoshida (*Kyoto Univ.*), Prof. Naoki Komatsu (*Shiga Univ. of Medical Science*), Prof. Kei Murakoshi (*Hokkaido Univ.*), and Dr. Heli Lehtivuori (*Tampere Univ. of Technology*) for their kind collaborations and valuable suggestions.

The author wishes to express his special gratitude to Prof. Nikolai V. Tkachenko, Prof. Helge Lemmetyinen, Dr. Vladimir Chukharev, and Ms. Kati Stranius at Department of Chemistry and Bioengineering, Tampere University of Technology, for their kind support and valuable suggestions in the author's stay in Finland (June – July, *2010*).

The author acknowledges Research Fellowships of the Japan Society for the Promotion of Science (JSPS) for Young Scientists.

Thanks also go to all the members of Photo-Organic Chemistry laboratory, Department of Molecular Engineering, Graduate School of Engineering, Kyoto University, and the people with whom the author has become acquainted through his research, for their help and

heartwarming friendship. In particular, the author sincerely appreciates Mr. Mitsuru Fujita, Mr. Naoki Kadota, Mr. Kazuhiro Kawabata, and Mr. Fumiaki Kawashima for sharing joys and sorrows arising from exploration of ***the chemistry of carbon nanotubes***.

Finally, the author would like to thank heartily his father, mother, sister, grandfathers, and grandmothers for their encouragements and supports which have been continuing for as long as twenty seven years.

Noriyasu Tezuka

Department of Molecular Engineering
Graduate School of Engineering
Kyoto University

Kyoto, Japan
March, 2011